

**AB INITIO SIMULATIONS AND
EXPERIMENTAL STUDIES ON
IRRADIATION-INDUCED DEFECTS IN Zr &
Al CONTAINING ODS STEELS AND
CONSTITUENT $Y_4Zr_3O_{12}$ PRECIPITATES**

by

SRUTHI MOHAN

(Enrollment No. PHYS02 2015 04 001)

Indira Gandhi Centre for Atomic Research, Kalpakkam, India.

Thesis submitted to the

Board of Studies in Physical Sciences

in partial fulfillment of requirements

for the Degree of

DOCTOR OF PHILOSOPHY

at

HOMI BHABHA NATIONAL INSTITUTE



January, 2021

Homi Bhabha National Institute

Recommendations of the viva voce Board

As members of the Viva Voce Committee, we certify that we have read the dissertation prepared by **Sruthi Mohan** entitled “**Ab initio simulations and experimental studies of irradiation-induced defects in Zr and Al-containing ODS steels and constituent $Y_4Zr_3O_{12}$ precipitates**” and recommend that it may be accepted as fulfilling the thesis requirement for the award of Degree of Doctor of Philosophy.

----- Date:
(Chairman: Dr. B. K. Panigrahi)

----- Date:
(Guide/Convener: Dr. G. Amarendra)

----- Date:
External Examiner:

----- Date:
Member 1: Dr. Divakar Ramachandran

----- Date:
Member 2: Dr. M. Kamaruddin

Final approval and acceptance of this thesis is contingent upon the candidate's submission of the final copies of the thesis to HBNI.

I hereby certify that, I have read this thesis prepared under my direction and recommend that it may be accepted as fulfilling the thesis requirement

Date:

Place: Kalpakkam

Dr. G. Amarendra

(Guide)

STATEMENT BY AUTHOR

This dissertation has been submitted in partial fulfillment of requirements for an advanced degree at Homi Bhabha National Institute (HBNI) and is deposited in the library to be made available to borrowers under the rules of the HBNI.

Brief quotations from this dissertation are allowable without special permission, provided that accurate acknowledgment of the source is made. Requests for permission for extended quotation from or reproduction of this manuscript in whole or in part may be granted by the competent authority of HBNI when in his or her judgment the proposed use of the material is in the interests of scholarship. In all other instances, however, permission must be obtained from the author.

Date:

Place: Kalpakkam

Sruthi Mohan

Declaration

I, hereby declare that the investigation presented in the thesis has been carried out by me. The work is original and has not been submitted earlier as a whole or in part for a degree / diploma at this or any other Institution / University

Date:

Place:

Sruthi Mohan

List of Publications

(a) Published in journals

1. Effect of Zr and Al addition on the nanocluster formation in ODS steel- an *ab-initio* study, **Sruthi Mohan**, Gurpreet Kaur, C. David, B. K. Panigrahi, G. Amarendra, *Journal of Alloys and Compounds*, **2018**, 767, 122-130
2. Ab-initio molecular dynamics simulations on threshold displacement energies and defect formation energies in $Y_4Zr_3O_{12}$, **Sruthi Mohan**, Gurpreet Kaur, C. David, B. K. Panigrahi, G. Amarendra, *Journal of Applied Physics*, **2020**, 127, 235901

(b) Manuscript under preparation

3. Transmission electron microscopy investigation of nanoprecipitates in Zr and Al-containing ODS steels, **Sruthi Mohan et al.** (Submitted to *Journal of Applied Physics*)
4. Role of anion defects in Ion beam induced luminescence of $Y_4Zr_3O_{12}$, **Sruthi Mohan et al.**(*Under preparation*)
5. Positron annihilation study of vacancy defects in self ion irradiated Zr and Al-containing ODS steels, **Sruthi Mohan et al.** (*Under preparation*)

(c) Papers presented in national/international conferences

1. *Ab initio* simulations and experimental studies on precipitate stability in Zr and Al-containing ODS alloy, **Sruthi Mohan**, Gurpreet Kaur, C. David, B. K. Panigrahi, G. Amarendra, International Conference on Nanostructuring by Ion Beams (ICNIB), November 6-8, 2019, IGCAR, Kalpakkam
2. On the relative stability of different structures in Y-Zr-O system, **Sruthi Mohan**, Gurpreet Kaur, C. David, B. K. Panigrahi, G. Amarendra, NEA International Workshop on Structural Materials for Innovative Nuclear Systems (SMINS), July 8-11, 2019, Kyoto, Japan.
3. *Ab initio* simulations and experimental studies on the effect of Zr in Al-containing ODS alloy, **Sruthi Mohan**, Gurpreet Kaur, C. David, B. K. Panigrahi, G.

Amarendra, International Conference on Electron Microscopy (EMSI), July 18-20, 2018, IOP Bhuvanewar.

4. TEM studies in TiC precipitate formation in D9 alloy, **Sruthi Mohan**, S. Balaji, C. David, B. K. Panigrahi, G. Amarendra, Modeling and Simulation of Safety and Materials for Nuclear Applications (MSMNA), December 16-17, 2015, SRI Centre, Anupuram.

(d) Publications not included in the thesis

1. Effect of heavy ion irradiation at low temperature in Fe-14Cr-.2Ti-0.3Y₂O₃, **Sruthi Mohan**, S. Balaji, S. Amirthapandian, S. Chinnathambi, C. David, B. K. Panigrahi, *Advanced Material Letters*, **2015**, 6, 442-445
2. Ion irradiation studies on the void swelling behavior of titanium modified D9 alloy, S. Balaji, **Sruthi Mohan**, S. Amirthapandian, S. Chinnathambi, C. David, B.K.Panigrahi, *Journal of Nuclear Materials*, **2015**, 467, 368 - 372

Sruthi Mohan

Dedicated to my parents

ACKNOWLEDGEMENTS

*It is my privilege to acknowledge **Dr. G. Amarendra**, my guide and mentor, for the constant guidance, enthusiasm, encouragement and affection he showed to me amid his busy schedule. I am thankful to him for the pleasant interactions I had with him.*

*I express my sincere thanks to **Dr. B.K. Panigrahi**, chairman of my DC committee, for proposing this problem of Al and Zr containing ODS steels and introducing me to the theoretical aspects of it. That was the best starting point I could ever ask for.*

*I am extremely grateful to **Dr. Divakar Ramachandran**, for the insightful suggestions during the DC meetings and for helping in interpreting and consolidating TEM data. It is indeed an honor to witness his zest for research.*

*It is a pleasure to thank **Dr. C. David**, for his unconditional support, endless technical discussions and for being a considerate and respectable supervisor. I am thankful for the concern he showed to provide new opportunities that improved me as a researcher.*

*I am indebted to **Dr. Gurpreet Kaur**, for teaching me the DFT simulations from scratch, for bearing with all my silly mistakes and for backing me with her intelligence. I am thankful to her for being a selfless human being whom I could always rely on.*

I convey wish to express sincere gratitude to my collaborators:

- **Dr. R. Vijay**, ARCI, for timely synthesis of the alloys,*
- **Dr. S. Amirthapandian**, for TEM data,*
- **Dr. Renjith Ramachandran**, for positron measurements and technical discussions,*
- **Dr. Sachin Srivastava** and **Mr. P Magudapathy**, for Raman and ionoluminescence experiments, and*
- **Dr. Arindam das** and **Mr. Binaya Kumar Sahoo**, for UV-Vis spectroscopic measurements.*

I thank them for the patience, kindness and wisdom they have showered on me. It is a memorable experience to have interacted with physicists like them.

*I would like to acknowledge all the **colleagues in ARDS and the accelerator lab**, for their constant support, stimulating discussions and for being a second family for me.*

*I owe a deep sense of gratitude to **Ms. Alphy George**, for all the wisdom she imparted, for influencing my writing style, for giving me the much-needed push during*

the difficult times and for her continued presence in my life.

*I will always cherish the moments of camaraderie I shared with my beloved friends, **Ms. Balasaritha and Dr. Rajani P Antony.***

*I am extremely grateful to **Dr. P. A. Manojkumar, Dr. Saravanan, Mr. Giftsondass and Dr. Gururaj** for carefully reading my chapters and correcting it.*

*I take this opportunity to thank **Dr. Kamaruddin**, for painstakingly reading the synopsis and suggesting changes.*

*I would like to thank **Dr. Rajaraman**, Dean Physical Sciences, for helping me during the final year.*

*It is a great pleasure to thank **all my friends**, in and out of Kalpakkam, for their company and the continued presence in my life.*

*Last but not the least, I thank **my beloved family**, for the constant love and freedom they have bestowed on me.*

Contents

Abstract	xix
List of Figures	xxiii
List of Tables	xxxix
List of Abbreviations	xxxv
1 Introduction	1
1.1 Need for radiation-resistant steels	1
1.2 Dispersion Strengthening	4
1.3 Oxide Dispersion Strengthened(ODS) steels	6
1.3.1 Metallurgy of ODS steels	7
1.3.2 Nature of dispersoids	9
1.3.3 Radiation response of ODS steels	15
1.4 Fluorite related structures and their radiation resistance	17
1.4.1 Significance of threshold displacement energies and Defect formation energies	18
1.4.2 Luminescence in fluorite related structures	20
1.5 Overview of the thesis	21
2 Simulation and Experimental Methods	23
2.1 Introduction	23
2.2 Density functional theory	23
2.2.1 Many-body systems	24
2.2.2 Hohenberg and Kohn theorems	24
2.2.3 Kohn-Sham formalism	27
2.2.4 The exchange-correlation functional	29
2.2.5 Hybrid functionals	30

2.2.6	Methods for electronic structure calculations	31
2.3	<i>Ab initio</i> molecular dynamics	33
2.3.1	Born-Oppenheimer molecular dynamics	33
2.3.2	Car-Parrinello molecular dynamics	34
2.4	Transmission electron microscopy	35
2.4.1	Bright-field (BF) and dark-field(DF) imaging	37
2.4.2	Phase-contrast imaging	38
2.5	Ion - implantation systems	40
2.5.1	1.7 MV Tandetron accelerator	40
2.5.2	150 kV accelerator and <i>in situ</i> ionoluminescence	42
2.6	Positron annihilation spectroscopy	44
2.6.1	Positron lifetime spectroscopy	44
2.6.2	Doppler broadening spectroscopy	45
2.6.3	Variable energy slow positron Doppler broadening spectroscopy	45
2.7	X-ray diffraction	47
2.8	Raman spectroscopy	48
3	<i>Ab initio</i> simulations of nanocluster formation in ODS steel containing Zr and Al	49
3.1	Introduction	49
3.2	Details of Calculation	50
3.2.1	Planewave cut-off energy and K-point sampling	50
3.2.2	Equilibrium lattice parameter	51
3.2.3	Formation energy and binding energy	52
3.3	Binding energies of atom clusters in Fe matrix	53
3.3.1	Formation energies and bonding-nature of solute atoms	53
3.3.2	Solute-solute interaction	56
3.3.3	Solute-vacancy interactions and its dependence on the size of the solute atom	57
3.3.4	Solute-oxygen interaction	58
3.3.5	Solute-oxygen-vacancy interactions	60
3.3.6	Effect of yttrium on solute-vacancy-oxygen interactions	63
3.3.7	Relative stability of Y-Zr-O and Y-Al-O phases in bcc Fe-matrix	66
3.4	Relative stability of pyrochlore, δ -phase and disordered fluorite in Y-Zr-O system	67

3.4.1	Crystal structures of pyrochlore, δ -phase and disordered fluorite phases	68
3.4.2	Formation energies of different phases in Y-Zr-O system	70
3.5	Conclusions	72
4	Synthesis and Characterization of ODS steels containing Zr and Al	73
4.1	Introduction	73
4.2	Experimental methods	74
4.2.1	Synthesis of ODS steels containing Zr and Al	74
4.2.2	Transmission Electron Microscopy	75
4.3	Microstructure of Al/Zr ODS steels	76
4.3.1	Nanocrystalline grain size and its contribution to strength and radiation tolerance	76
4.3.2	Nature of dispersoids and verification of DFT simulations	78
4.4	Strengthening mechanisms in Zr/Al-ODS steels	83
4.5	Crystal structure and orientation relationships of dispersoids	85
4.5.1	Existence of novel bcc/trigonal orientation relationship in Zr-containing ODS steels	85
4.5.2	Orientation related by rotation to preferred orientation	89
4.5.3	Random orientations of precipitates in the matrix	90
4.5.4	Chemistry of dispersoids in Al-ODS	100
4.6	Conclusions	109
5	Study of vacancy defects in self-ion irradiated Zr and Al containing ODS steels	111
5.1	Introduction	111
5.2	Experimental methods	112
5.3	Estimation of defect concentration in as-prepared Zr/Al - ODS alloys using positron annihilation lifetime spectroscopy	114
5.4	Coincidence Doppler broadening spectroscopy	118
5.5	VLEPB studies in Zr/Al-ODS steels	119
5.6	Conclusions	125
6	Threshold displacement energies and defect formation energies of $Y_4Zr_3O_{12}$	127
6.1	Introduction	127
6.2	Computational Details	128

6.3	distribution of Y and Zr in $Y_4Zr_3O_{12}$ unitcell	130
6.4	Threshold displacement energies of $Y_4Zr_3O_{12}$	132
6.5	Nature of defects produced during threshold displacement events	135
6.6	Defect formation energies in $Y_4Zr_3O_{12}$ and its role in radiation resistance	140
6.7	Discussions	143
6.8	Conclusions	146
7	Ion beam induced luminescence in $Y_4Zr_3O_{12}$ and the role of anion defects	149
7.1	Introduction	149
7.2	Experimental methods	150
7.2.1	Synthesis of $Y_4Zr_3O_{12}$	150
7.2.2	Ionoluminescence	150
7.2.3	Calculation of defect-levels	151
7.3	X-Ray Diffraction of as-prepared $Y_4Zr_3O_{12}$	152
7.4	Raman modes in $Y_4Zr_3O_{12}$	153
7.5	Bandgap energy of $Y_4Zr_3O_{12}$	157
7.5.1	Estimation of bandgap using UV-Vis spectroscopy	157
7.5.2	Calculation of bandgap using PBE-GGA and HSE06 xc functionals	159
7.6	Ionoluminescence spectroscopy of $Y_4Zr_3O_{12}$	160
7.7	<i>Ab initio</i> simulation of anion-related defect levels in $Y_4Zr_3O_{12}$ using HSE06 functional	162
7.8	Correlation between IL spectra and simulated defect levels	166
7.9	Conclusions	169
8	Summary and scope for future work	171
8.1	Summary of the thesis	171
8.2	Future scope	173
	Bibliography	177

ABSTRACT

Oxide Dispersion Strengthened (ODS) steels, characterized by thermally stable nano-sized dispersions in Fe-matrix, are promising materials for future fission and fusion reactor applications, due to their potential to withstand elevated temperature and high radiation dose. The small dispersions in ODS matrix act as pinning sites to dislocations, sinks for irradiation induced point defects and play a role in limiting the grain growth. Typically ODS alloys are prepared by ball milling elemental powders (Fe, Cr, Ti, *etc*) and Y_2O_3 together into fine-sized powders with dissolved Y, O and minor elements in supersaturation. These mechanically alloyed powders are further consolidated by hot-extrusion or hot-isostatic pressing, during which high density of Y-Ti-O precipitates form from the dissolved elements. There have been many attempts to understand the radiation stability of these dispersoids, which is critical for the future deployment of the alloys, and outstanding stability at elevated temperatures and doses have been reported by many groups. However, when Al is added in Ti-containing conventional ODS alloys to guarantee enhanced corrosion resistance during reprocessing, the chemistry and size of the dispersoids undergo a change - the fine Y-Ti-O dispersoids are replaced by relatively coarse Y-Al-O dispersoids, thereby deteriorating the ultimate tensile strength of the alloy containing Al. Nullifying these adverse effects of Al by considering Zr as a replacement for Ti in Al-containing ODS alloys is the central theme of this thesis.

To assess the suitability of Zr as an alternative for Ti in ODS alloys with Al, density functional theory (DFT) calculations have been carried out in a bcc supercell containing atomic clusters made of Zr, O, vacancy, Al and Y. The vacancy has to be considered as a constituent of nanocluster nuclei because enormously high number density of vacancies gets trapped in the matrix during the ball milling process. The binding energy calculations in different configurations of these atomic clusters show that during all the stages of formation, Y-Zr-O-vacancy clusters have higher binding energy than Y-Al-O-vacancy clusters. This signifies accelerated formation of high number densities of Y-Zr-O nuclei in Fe-matrix containing Zr and Al. Further, the formation energy calculations on pyrochlore ($Fd\bar{3}m$, $Y_2Zr_2O_7$), defect fluorite ($Fm\bar{3}m$, $Y_2Zr_2O_7$) and the δ phase ($R\bar{3}$, $Y_4Zr_3O_{12}$) indicate the propensity to form δ phase than other structures. Therefore, the initial simulations predicted a $Y_4Zr_3O_{12}$ dispersoid-rich microstructure in ODS alloys containing Zr and Al.

These predictions are further experimentally validated by synthesizing and characterizing alloys containing Zr and Al : (i) Fe-14Cr-0.3Y₂O₃-0.63Zr (a.k.a. Zr-ODS) and (ii) Fe-14Cr-0.3Y₂O₃-0.63Zr-4Al (a.k.a. Al-ODS). These alloys, synthesized by ball

milling and hot extrusion, showed high density ($1.7 \times 10^{24}/\text{m}^3$ in Zr-ODS and $3.8 \times 10^{23}/\text{m}^3$ in Al-ODS) of nano-sized (diameter = 4 nm for Zr-ODS and 8 nm for Al-ODS) dispersoids in transmission electron micrographs. All the dispersoids in Zr-ODS and $\sim 78\%$ dispersoids in Al-ODS were structurally consistent with trigonal rhombohedral $\text{Y}_4\text{Zr}_3\text{O}_{12}$ with a few dispersoids in Al-ODS possessing tetragonal, cubic and monoclinic ZrO_2 structures. However, the Al-containing precipitates were completely absent in both alloys, substantiating earlier ab-initio simulation results. In high resolution transmission electron micrographs exist a novel, predominant precipitate(δ)/matrix(α) orientation relationship, $[2\bar{1}0]_\delta || [111]_\alpha$ and $(122)_\delta || (011)_\alpha$ and a rotation of this OR by 5.26° gives rise to yet another co-existing OR, $[2\bar{1}0]_\delta || [111]_\alpha$ and $(122)_\delta || (011)_\alpha$. These trigonal/bcc OR is similar to Pitsche-Shrader and Burger orientation relationships in hcp/bcc systems, that are related by a rotation of 5.26° .

Since the information on the radiation tolerance of as-prepared alloys is critical for their future deployment, the radiation response of these alloys is assessed using ion-beam irradiation, which is a convenient analogue for neutron irradiation. The positron annihilation spectroscopy studies indicate that the Al-ODS exhibits formation and clustering of vacancy-defects for a self-ion irradiation induced displacement damage of 100 dpa, whereas Zr-ODS doesn't show any change. This can be attributed to the higher number density and finer size of the dispersoids in Zr-ODS, which successfully act as sinks for point defects. The presence of vacancy defects is evident in Zr-ODS only for a displacement damage of 150 dpa. For a high temperature irradiation at 340°C , the alloys are free from open volume defects.

The long-term radiation tolerance of the ODS alloys relies on the radiation response of its dispersoids. The behaviour of major dispersoid phase $\text{Y}_4\text{Zr}_3\text{O}_{12}$ under irradiation can be predicted by calculating its threshold displacement energies and defect formation energies. $\text{Y}_4\text{Zr}_3\text{O}_{12}$ is a fluorite related structure belonging to $R\bar{3}$ space group with Zr atom in $3a$ positions, Zr and Y distributed in one set of $18f$ positions and two sets of oxygen, O_I and O_II occupying two sets of $18f$ positions. The threshold displacement energies computed using *ab initio* molecular dynamics simulations are found to be strongly dependent on crystallographic directions. The anions possess lower threshold displacement energies and their recoil events involve less disorder in the crystal compared to cation displacement. This infers that the anion-related defects are more probable than cation-related defects in irradiated $\text{Y}_4\text{Zr}_3\text{O}_{12}$. The Y – Zr $_{18f}$ antisite formation energy has the least value among defect formation energies considered in this study. Therefore, upon irradiation, the $18f$ atoms can interchange position and continue to be in the δ - phase structure before transforming into the disordered fluorite

phase. The defect reaction pair energy, the sum of cation antisite formation energy and anion Frenkel pair formation energy, is known to scale up with the decrease in irradiation stability of fluorite related structures. The defect reaction pair energy of $Y_4Zr_3O_{12}$ is smaller than that of pyrochlore and other δ - phase structures available in the literature, indicating its high radiation tolerance.

The ion beam induced luminescence spectroscopy is an effective tool to understand the nature of radiation induced defects in $Y_4Zr_3O_{12}$. The ionoluminescence (IL) spectra of as-prepared $Y_4Zr_3O_{12}$ is comprised of two wide bands, centered at 330 nm and 415 nm respectively. The bandgap value measured using UV-Vis absorption spectroscopy and calculated using HSE06 hybrid exchange-correlation functionals are 5.47 and 5.27 respectively. The HSE06 hybrid functionals are chosen in order to compensate the underestimation of bandgap in GGA functionals. It is obvious that the bands in IL spectrum are at lower energy than the bandgap emission and hence can be attributed to deep band emissions (DBE) from defect-related levels within the bandgap. The IL bands of fluorite related structures are usually ascribed to anion vacancies and related color centers (anion vacancies with trapped charge). The positions of defect levels created by O_I (F center), O_I^+ (F^+ center), O_I^- (F^- center), O_I^{2+} , O_I^{2-} , O_{II} (F center), O_{II}^+ (F^+ center), O_{II}^- (F^- center), O_{II}^{2+} , O_{II}^{2-} vacancy defects are calculated using DFT-HSE06 calculations. By comparing the experimental IL spectra and the calculated defect levels, it can be concluded that the O_I (F center), O_I^+ and O_{II}^+ vacancy defects contribute to the peak at 330 nm and O_{II} and O_I^- vacancies and O interstitial at $6c$ site contribute to the peak at 415 nm. This result is in agreement with the previous *ab initio* molecular dynamics simulation results, that anion vacancies are more probable defects in ion irradiated $Y_4Zr_3O_{12}$.

List of Figures

1.1	(a) TEM micrograph showing shearing of Ni ₃ Si in a Ni-based alloy, figure taken from [14] (b) Schematic of a dislocation cutting through a coherent particle on the same slip plane as in the matrix.	5
1.2	(a) Orowan looping of Ni ₃ Si particles in a Ni-base alloy, figure taken from [14]. (b) Stages on Orowan’s mechanism of dispersion hardening [12].	6
1.3	Different stages of ODS fabrication	8
1.4	The binding energies of Ti and Zr atoms with a vacancy (V), O, O–V and Y–V–O cluster in bcc Fe supercell, reproduced from Murali <i>et al.</i> [71]. The Zr containing atomic- clusters have more binding energy than Ti containing clusters	14
2.1	Carl Zeiss LIBRA 200FE HRTEM (left) and schematic of its cross-sectional view (right).	36
2.2	Basic operating modes in TEM (a) diffraction mode and (b) image mode. [169]	37
2.3	(a) $\sin \chi(u)$ versus u without damping of the higher spatial frequencies (b) $T(u)$ versus u modified by the damping envelope (dashed line); $\Delta f = -100$ nm, $C_s = 2.2$ nm. (Reproduced from [169])	39
2.4	(a) Photograph of 1.7 MV accelerator (b) The beamlines connected to the analyzing magnet of the accelerator, reproduced from [171] . . .	41
2.5	(a) Photograph and (b) Schematic diagram of 150 kV accelerator . .	43
2.6	(a) Schematic of the coupling of spectrometer with the accelerator for IL spectroscopy (Legends: 1, 2: optical absorption ports; 3: coupler optics for IL measurements; 4: vacuum chamber; 5-7: optical fiber assemblies; 8: spectrometer) (b) Photograph of FLS 980 UV-Vis absorption spectrometer.	43
2.7	A schematic diagram of variable energy slow positron beam spectroscopy [176]	46

2.8	Photograph of the variable low-energy positron beam based Doppler broadening spectroscopic instrument in IGCAR, Kalpakkam [175, 176]	47
2.9	A photograph of INEL Equinox3000 XRD system	48
3.1	Total energy of a bcc Fe unitcell as function of (a) E_{cut} (b) k-grid size	51
3.2	Total energy of a unitcell of bcc Fe as a function of volume of the cell	52
3.3	The differential charge density plot of Al, Zr, Y and O in Fe matrix in $(1\bar{1}0)$ plane of 128 atom bcc Fe supercell. Blue colour is $-0.006 e/\text{Bohr}^3$ and red is $+0.006 e/\text{Bohr}^3$. Al, Y and Zr are in substitutional position while oxygen is in octahedral interstitial site. Al, Y and Zr bind covalently with surrounding Fe atoms. Oxygen – Fe binding is ionic in nature which is evident from the polarization of Fe-O bond. .	56
3.4	The $(1\bar{1}0)$ slice of charge density difference plot of interaction of Zr and Al with a vacancy. (Vacancy is marked by a white square.)	59
3.5	Differential charge density plot of Zr with oxygen in 128 atom Fe matrix. (a) $(02\bar{1})$ plane (b) $(1\bar{1}0)$ plane	61
3.6	Differential charge density plot of Al with oxygen in 128 atom Fe matrix. (a) $(02\bar{1})$ plane (b) $(1\bar{1}0)$ plane	61
3.7	The $(1\bar{1}0)$ slice of charge density difference plot of interaction of Zr/Al with O and vacancy for the most stable configuration of Table 3.6. The vacancy is represented by a \square	63
3.8	The $(1\bar{1}0)$ and $(02\bar{1})$ slices of charge density difference plot Y-Zr- \square -O configuration with maximum binding energy. It can be seen that Y-O and Zr-O binding is much stronger than Fe-O binding. Also, the interaction of Fe with \square is negligible compared to the interaction of Zr and Y with vacancy.	64
3.9	The $(1\bar{1}0)$ and $(02\bar{1})$ slices of charge density difference plot of Y-Al-O-vacancy cluster configuration with maximum binding energy. It can be seen that Y-O and Fe-O interactions are stronger than Al-O interactions.	66
3.10	Absolute values of binding energies of Zr and Al containing clusters in bcc Fe (here S is solute: Zr/Al). The binding energy of Zr containing clusters are always higher than that of Al containing clusters.	67
3.11	$Y_4Zr_3O_{12}$ unitcell	68
3.12	An 88 atom unitcell of pyrochlore structure.	69
3.13	A defect fluorite unitcell. The anion positions have 50% occupancy and one-eighth of the cation position is vacant.	70

3.14	The formation energy/atom of delta-phase, pyrochlore and disordered fluorite structure in Y-Zr-O system.	71
4.1	As prepared (a) Fe-14Cr-0.63Zr-4Al-0.3Y ₂ O ₃ (Al-ODS) and (b) Fe-14Cr-0.63Zr-0.3Y ₂ O ₃ (Zr-ODS) rods	75
4.2	Bright Field TEM images of (a) Al - ODS and (b) Zr - ODS. (c)SAED pattern of Al-ODS sample, indexed for bcc Fe. (d) SAED pattern of Zr-ODS, indexes correspond to planes of bcc Fe. (e) Grain size distribution of Zr-ODS and Al-ODS.	80
4.3	(a) Bright Field image and (b) Dark Field image of oxide particles in the carbon extraction replica of Al-ODS. (c) The SAED pattern of the extraction replica, which can be indexed for trigonal Y ₄ Zr ₃ O ₁₂ (ICDD : 01-077-0743) (d) Particle size distribution in Al-ODS.	81
4.4	(a) Bright Field and (b) Dark Field images and (c) the SAED pattern of the extraction replica of Zr-ODS, which can be indexed for trigonal Y ₄ Zr ₃ O ₁₂ (ICDD : 01-077-0743) and (d) particle size distribution of Zr - ODS	82
4.5	(a) HRTEM image showing distribution of dispersoids in the matrix of as prepared Zr-ODS steel. The dispersed precipitates in the micrograph have diameter ranging from 1.6 nm to 8 nm (b) Power spectrum of the micrograph in (a). Matrix spots are marked with red arrows and indexed for [111] zone axis of Fe. The diffraction spots corresponding to precipitates are marked with yellow arrows. (c) The image reconstructed using diffraction spots corresponding to precipitates. The nanoclusters are indicated by yellow arrows in (a) and (c).	86
4.6	(a) HRTEM micrograph of a faceted Y ₄ Zr ₃ O ₁₂ precipitate in Zr-ODS matrix.(b) Power spectrum of the image. The spots corresponding to the matrix are indexed with subscript Fe. (c) Simulated diffraction pattern corresponding to the orientation relationship (10 $\bar{1}$) _α (122) _δ and [111] _α [2 $\bar{1}$ 0] _δ which can be derived from the power spectrum. The open circles indicate matrix-spots and filled circles indicate precipitate-spots. (d) The image reconstructed using precipitate spots of (b).	94
4.7	Combined stereographic projection of [2 $\bar{1}$ 0] _δ and [111] _α with (122) _δ (1 $\bar{1}$ 0) _α . Blue spots indicate [2 $\bar{1}$ 0] zone axis of Y ₄ Zr ₃ O ₁₂ and black spots correspond to [111] zone axis of Fe	95

4.8	The precipitate matrix interface of precipitate in Figure 4.6. The simulated HREM map of precipitate and matrix is shown in regions marked (a) and (b) respectively. The precipitate matrix interface has a periodic array of dislocations, marked in yellow.	96
4.9	(a) HRTEM micrograph of a $Y_4Zr_3O_{12}$ precipitate (b) The power spectrum of (a). (c) A combined diffraction pattern of $[111]_{Fe} [2\bar{1}0]_{\delta}$ with $(110)_{Fe} (\bar{0}0\bar{3})_{\delta}$. The matrix spots are shown as open circles. (d) The inverse FFT generated using the precipitate spots of the power spectrum.	97
4.10	(a) HRTEM micrograph of a $Y_4Zr_3O_{12}$ particle in Zr-ODS. (b) Power spectrum of the micrograph with corresponding (hkl) values. The zone axis is $[\bar{4}7\ 10]$ (c) Simulated diffraction pattern of the $[\bar{4}7\ 10]$ zone axis of $Y_4Zr_3O_{12}$ with $[111]$ zone axis of α -Fe. The open circles corresponds to matrix spots and the filled circles corresponds to precipitate spots (d) IFFT constructed from power spectrum using precipitate spots.	98
4.11	The HRTEM micrograph and its power spectrum of a precipitate in Zr-ODS is shown in (a) and (b). The spots marked in (b) correspond to $[\bar{4}1\ \bar{1}1]$ zone axis of $Y_4Zr_3O_{12}$. The theoretical diffraction pattern and noise-filtered image (inverse FFT) is shown in (c) and (d).	99
4.12	(a) HRTEM micrograph of a tetragonal ZrO_2 precipitate in Al-ODS, (b) power spectrum of micrograph with corresponding (hkl) values, zone axis is identified to be $[201]$ (c) IFFT constructed using the spots in (b) and (d) The simulated diffraction pattern of $[201]$ zone axis of tetragonal ZrO_2 as per ICDD: 00-065-0729.	102
4.13	The HRTEM image of a $Y_4Zr_3O_{12}$ nanoprecipitate of diameter ~ 13 nm found in Al-ODS steel. The power spectrum of precipitate in (a) is shown in (b). The power spectrum is compared with simulated diffraction pattern shown in (c) and zone axis is $[2\bar{1}0]$. The precipitate image reconstructed using spots in (b) is shown in (d).	103
4.14	HRTEM micrograph of a nearly spherical tetragonal ZrO_2 precipitate in Al-ODS. The power spectrum of the precipitate shown in (b) matches well with the simulated diffraction pattern of tetragonal ZrO_2 structure along $[101]$ zone axis (ICDD: 00-065-0729). The precipitate image reconstructed using spots in (b) is shown in (d).	104

4.15	HRTEM micrograph of a nearly spherical cubic -ZrO_2 precipitate of diameter ~ 10 nm. The power spectrum of the precipitate shown in (b) matches well with the simulated diffraction pattern of cubic ZrO_2 structure along $[001]$ zone axis. The precipitate image reconstructed using spots in (b) is shown in (d).	105
4.16	(a) shows a $\text{Y}_4\text{Zr}_3\text{O}_{12}$ precipitate of diameter ~ 28 nm. The power spectrum can be identified as $[0\bar{5}2]$ zone axis and is in agreement with the simulated pattern shown in (c). The FFT filtered image is presented in (d).	106
4.17	(a) shows a $\text{Y}_4\text{Zr}_3\text{O}_{12}$ precipitate of diameter ~ 13 nm. The power spectrum can be identified as $[\bar{4}1\ \bar{1}1]$ zone axis and is in agreement with the simulated pattern shown in (c). The FFT filtered image is presented in (d).	107
4.18	(a) HRTEM micrograph of a monoclinic ZrO_2 precipitate in Al-ODS steel. (b) The power spectrum generated from (a). The zone axis is identified to be $[111]$. (c) Simulated diffraction spots along $[111]$ direction of monoclinic ZrO_2 (ICDD 00-036-0420). (d) The inverse FFT generated using the spots in (b).	108
5.1	Depth distribution of displacement damage and implanted ions in 1.6 MeV Fe^+ irradiated Fe, calculated using SRIM. The peak damage is 100 dpa at 480 nm.	113
5.2	CDB ratio curves for Al-ODS and Zr-ODS alloys, normalized with respect to the pure Fe. The ratio curves for Zr, Cr and Al are also shown for comparison.	118
5.3	The variation of S-parameter with mean positron implantation depth for pristine Zr-ODS and Al-ODS alloys. The solid lines are obtained from VEPFIT analysis. The S-parameter values for both the alloys decrease with depth and attain bulk value.	120
5.4	The S-W plot of the Al-ODS and Zr-ODS, which allows a direct comparison of defect types. The nature of defects in Zr-ODS and Al-ODS are dissimilar.	121

5.5	Depth distribution of vacancy defects in pristine and 1.6 MeV Fe ⁺ ion irradiated Al-ODS samples obtained by VLEPB studies. The solid lines are obtained by VEPFIT analysis. There is an increment in the S-parameter value for 100 dpa, RT irradiated specimens. Whereas, the 100 dpa HT irradiated specimens do not show any change in S-parameter.	122
5.6	(a) S-W correlation plot for pristine and ion-irradiated Al-ODS. The 100 dpa, RT- irradiated specimen shows 3 slopes in the S-W plot (b) The depth profile obtained from VEPFIT analysis. R ₁ is the surface layer, R ₂ and R ₃ are defect layers.	122
5.7	The S - parameter as a function of positron implantation depth in pristine and self ion- irradiated Zr-ODS alloy. There is no change in S-parameter for displacement damage of 100 dpa at room temperature as well as high temperature. An increment in S-parameter is observed for a damage of 150 dpa at room temperature.	124
5.8	(a) S-W correlation plot for pristine and ion irradiated Zr-ODS steels. The 150 dpa, RT irradiated specimen show 3 slopes. (b) The depth profile obtained from VEPFIT analysis. R ₁ and R ₂ are the defect levels	124
6.1	Convergence of energy in Y ₄ Zr ₃ O ₁₂ supercell. Variation of total energy with respect to (a) k-point mesh and (b) cut-off energy.	128
6.2	Orthogonal cell of the Y ₄ Zr ₃ O ₁₂ , containing 456 atoms. It is constructed from rhombohedral unitcell using the transformation matrix: (-2,1,2; 2,1,2; 0,-2,2). The lattice parameters are: a= 19.44 Å, b = 16.84 Å, c= 18.18 Å, α = β = γ = 90°. This cell is used for AIMD calculations. . .	129
6.3	Variation in temperature of Y ₄ Zr ₃ O ₁₂ supercell with time steps. The equilibrated temperature remains in the range of 300±20 K.	130
6.4	Formation energies for different configurations of Y ₄ Zr ₃ O ₁₂ unitcell .	131
6.5	Defects produced when Zr _{3a} atom is given energy along (a) [100], (b) [110] and (c) [111] directions. The direction in which energy is given, is marked by a black arrow. The purple arrow indicates Zr displacement direction, the blue arrow indicates Y displacement direction and the yellow arrow indicates oxygen displacement direction. Here, the green atoms are Zr _{3a} , the yellow atoms are Zr _{18f} , the blue atoms are Y _{18f} , and the red atoms are oxygen.	136

6.6	Defects generated by imparting threshold displacement energy to Zr_{18f} atom along (a) [100] (b) [110] and (c) [111] directions. The purple arrow indicates Zr displacement direction, the blue arrow indicates Y displacement direction and the yellow arrow indicates oxygen displacement direction. Here, the green atoms are Zr_{3a} , the yellow atoms are Zr_{18f} , the blue atoms are Y_{18f} , and the red atoms are oxygen.	138
6.7	Defects generated by imparting energy to Y atom along (a) [100] (b)[110] and (c)[111] directions. (a) $Y[100] \rightarrow Y_Y + Y_{int} + Y_{vac} + O_{I, int} + O_{II, int} + O_{I, vac} + O_{II, vac}$ (b) $Y[110] \rightarrow Y_{3a} + Zr_{int} + Y_{vac}$ (c) $Y[111] \rightarrow Y_Y + Y_{int} + Y_{vac} + O_{int} + O_{II, int} + O_{vac} + O_{II, vac}$	139
6.8	The displacements of O_I atom when incident energy is given along [100] (Blue arrow), [110] (Yellow arrow) and [111] (Purple arrow) directions. The first two result in FP with interstitial occupied in $6c$ site and third one results in an anion antisite pair and FP with interstitial in $6c$ site. Here green atoms are Zr_{3a} , Yellow atoms are Zr_{18f} , blue atoms are Y and red atoms are oxygen.	140
7.1	The vacancy profile of Y, Zr and O in 100 keV He^+ ion irradiated $Y_4Zr_3O_{12}$, calculated using SRIM.	151
7.2	The XRD spectrum of as-prepared $Y_4Zr_3O_{12}$. Corresponding ICDD data (ICDD 01-077-0743) is also shown.	152
7.3	The Raman spectrum of $Y_4Zr_3O_{12}$. The spectrum can be divided into three bands I, II, and III. The band-I, II and III have 6, 7 and 4 sub bands respectively. (<i>refer to</i> Table 7.1)	154
7.4	(a) The UV-vis absorption spectrum of $Y_4Zr_3O_{12}$. The absorption edge is at 226 nm. (b) The Tauc plot. The bandgap calculated from the Tauc plot is 5.47 eV.	158
7.5	Total Density of states (TDOS) of $Y_4Zr_3O_{12}$, calculated using PBE-GGA(blue, dashed line) and HSE06 hybrid functional(black solid line). The red line indicates the Fermi level. The calculated bandgap is 5.27 eV for HSE06 and 3.55 eV for PBE-GGA calculations.	159
7.6	The ionoluminescence spectra of $Y_4Zr_3O_{12}$ aquired during irradiation with 100 keV He^+ ion at various fluences. The two bands observed in the spectra are marked as I_1 and I_2	161

7.7	(a) Intensity variation of ionoluminescence bands with fluence. I_1 is the intensity of band centered at 330 nm and I_2 is the intensity of band centered at 415 nm. Both intensities decrease exponentially with fluence. (b) The ratio of intensities of first and second peaks. It shows that the second band is quenching faster than the first band.	161
7.8	Total density of states for O vacancy in $Y_4Zr_3O_{12}$, in GGA(blue, dashed line) and HSE06 (black, solid line) functionals. O vacancy creates a localized defect state at 3.51 eV above the valence band maximum. . .	162
7.9	The DOS plot for O_{II} vacancy in $Y_4Zr_3O_{12}$. It produces a localized defect level at 2.9 eV from the valence band maximum.	163
7.10	Total density of states for O vacancy with a trapped negative charge in $Y_4Zr_3O_{12}$, in GGA and HSE06 functionals. There are two defect levels at 3 eV and 4.5 eV above the valence band, marked using red arrows.	163
7.11	TDOS plot for O_{II}^- vacancy in $Y_4Zr_3O_{12}$, calculated using GGA and HSE06 functionals. There are two defect levels at 3.2 eV and 4.6 eV respectively. The red arrows indicate the position of defect levels. . .	164
7.12	TDOS plot for O_1^+ vacancy. The defect band created by O_1^+ vacancy is situated at 3.55 eV from the valence band maximum.	165
7.13	TDOS plot for O_2^+ vacancy. The defect band created by O_2^+ vacancy is half filled and is situated at 3.46 eV from the conduction band edge. . .	165
7.14	TDOS plot for Oxygen interstitial in $6c$ site in $Y_4Zr_3O_{12}$, calculated using GGA and HSE06 functionals. The defect level is at 2.9 eV from valence band edge.	166
7.15	The defect levels in $Y_4Zr_3O_{12}$ simulated using HSE06 hybrid functional for two types of oxygen, O_I and O_{II} , in different charge states. E_V and E_C are valence band maximum and conduction band minimum respectively.	168
7.16	The simulated defect levels in $Y_4Zr_3O_{12}$, scaled-up to experimentally observed bandgap, $E_g = 5.47$ eV	168

List of Tables

1.1	Summary of the nature of dispersoids in Al and Zr containing ODS steels	12
1.2	Processing parameters of Zr/Al ODS steels from literature	13
1.3	Threshold displacement energies of fluorite and pyrochlore structures, obtained from literature.	19
3.1	Formation energies of Zr, Y, Al, and O in the bcc Fe matrix. The more positive formation energy corresponds to less solubility and vice-versa. Aluminum is the most soluble element in Fe matrix, followed by Zr, Y and then O. The data available in the literature is given in parentheses. ^a - Murali <i>et al.</i> [71], ^b - Jiang <i>et al.</i> [69], ^c - Claisse <i>et al.</i> [72], ^d - Posselt <i>et al.</i> [187], ^e - Kim <i>et al.</i> [188], ^f - Olsson <i>et al.</i> [189].	55
3.2	Nearest neighbor distances in Fe matrix with and without impurity atoms. (nn denotes nearest neighbor).	55
3.3	Binding energies of two metallic atoms in Fe matrix at first and second nearest neighbor (nn) positions. (^a - Jiang <i>et al.</i> [69], ^b - Murali <i>et al.</i> [71], ^c - Posselt <i>et al.</i> [187])	57
3.4	The binding energy of Y, Al and Zr with a vacancy.(^a - Fu <i>et al.</i> [68], ^b - Posselt <i>et al.</i> [187])	58
3.5	Solute–oxygen binding energy in bcc Fe matrix.(^a - Jiang <i>et al.</i> [69], ^b - Murali <i>et al.</i> [71]))	60
3.6	The solute–oxygen -vacancy binding energy in bcc Fe matrix. In the defect configurations, solute (Zr or Al) is represented by green sphere. Oxygen and vacancy are represented by red sphere and blue cube respectively.	62

3.7	Binding energies of different yttrium–solute– oxygen–vacancy combinations in bcc Fe. Here, the O – vacancy positions are fixed and different configurations of Yttrium and solute around this O – vacancy pair are considered. (green circle is solute atom(Zr or Al), orange is yttrium, red is oxygen and blue cube is the vacancy.)	65
3.8	The formation energy/atom for pyrochlore, δ -phase and SQS structures.	71
4.1	Details of starting elemental and Y_2O_3 powders used for ball milling.	74
4.2	Microstructural information of as-prepared Zr ODS and Al-ODS alloys	79
4.3	Microstructural information of Zr and Al-ODS, used for calculating different strength contributions.	83
4.4	The details of crystal structures used for analyzing HRTEM micrographs.	86
4.8	Summary of the orientation relationships found in as prepared Zr-ODS steel.	93
4.5	Inter-planar distances (d) and angles (α) of the nanoparticle of Figure 4.6	94
4.6	Inter-planar distances (d) and angles (α) of the nanoparticle of Figure 4.9	97
4.7	Inter-planar distances (d) and angles (α) of the nanoparticle of Figure 4.10	98
4.9	Inter-planar distances (d) and angles (α) of the nanoparticle of Figure 4.11	99
4.10	Inter-planar distances (d) and angles (α) of the monoclinic ZrO_2 nanoparticle of Figure 4.12. The zone-axis is $[201]$	102
4.11	Inter-planar distances (d) and angles (α) of the $Y_4Zr_3O_{12}$ nanoparticle in Figure 4.13 with zone-axis $[2\bar{1}0]$	103
4.12	Inter-planar distances (d) and angles (α) of the ZrO_2 nanoparticle in Figure 4.14. The structure is tetragonal with zone-axis $[101]$	104
4.13	Inter-planar distances (d) and angles (α) of the ZrO_2 nanoparticle in Figure 4.15. The structure is face centered cubic with zone-axis $[001]$	105
4.14	Inter-planar distances (d) and angles (α) of the $Y_4Zr_3O_{12}$ nanoparticle in Figure 4.16.	106
4.15	Inter-planar distances (d) and angles (α) of the $Y_4Zr_3O_{12}$ nanoparticle in Figure 4.17.	107
4.16	d-spacings and angles of the monoclinic ZrO_2 nanoparticle of Figure 4.18.	108
4.17	The chemistry of precipitates in Al-ODS steel.	109
5.1	PALS lifetimes and corresponding intensities of Zr-ODS and Al-ODS steels.	115

5.2	Rate constants, dislocation densities, vacancy cluster densities and individual fractions of positron trapping values calculated from PALS lifetime using standard trapping model.	117
6.1	Formation energies/unitcell for different configurations of Y and Zr in $18f$ positions of $Y_4Zr_3O_{12}$ structure.	132
6.2	The threshold displacement energies of O_I and O_{II} in $Y_4Zr_3O_{12}$ structure along with final defect configurations and separation between defects after simulation for 2 ps. (A_B is A atom occupying site of B atom.) .	133
6.3	The threshold displacement energies of Y and Zr in $Y_4Zr_3O_{12}$ structure along with final defect configurations and separation between defects after simulation for 2 ps. (A_B is A atom occupying site of B atom.) .	134
6.4	Formation energies of vacancy and interstitial defects in $Y_4Zr_3O_{12}$. .	142
6.5	Antisite and Frenkel pair formation energies of $Y_4Zr_3O_{12}$	143
6.6	O-D defect reaction pair energies of Zr containing δ – phases. (* - current study; ** - values obtained from Figure 3. of reference [102]) .	145
7.1	The calculated vibrational modes, their frequencies and Raman activity in $Y_4Zr_3O_{12}$	156

List of Abbreviations

AIMD	- <i>Ab initio</i> Molecular Dynamics
Al-ODS	- ODS steel containing Al
<i>appm</i>	- atomic parts per million
APT	- Atom Probe Tomography
APW	- Augmented Plane Wave
APW + lo	- Augmented Plane Wave plus local orbitals
AS pair	- Antisite pair
B3LYP	- Becke, 3-parameter, Lee–Yang–Parr
BCA	- Binary Collision Approximation
bcc	- body centered cubic
BO	- Born-Oppenheimer
BOMD	- Born Oppenheimer Molecular Dynamics
BF/DF	- Bright Field/Dark Field
CCD	- Charged Coupled Device
CDB	- Coincidence Doppler Broadening
CL	- Cathodoluminescence
CPMD	- Carr Parinello Molecular Dynamics
CS/MS/OS	- Coherency Strengthening/ Modulus Strengthening/Order Strengthening
CTF	- Contrast Transfer Function
DFPT	- Density Functional Perturbation theory
DFT	- Density Functional Theory
DOS	- Density of States
dpa	- Displacement Per Atom
EM lens	- ElectroMagnetic lens
fcc	- face centered cubic
FEG	- Field Emission Gun
FFT	- Fast Fourier Transform
FP	- Frenkel Pair

LIST OF ABBREVIATIONS

fs	- femtosecond
GGA	- Generalized Gradient Approximation
HF	- Hartree Fock
HK	- Hohenberg-Kohn
HPGe	- High Pure Germanium
HRTEM	- High Resolution Transmission Electron Microscopy
HSE	- Heyd-Scuseria-Ernzerhof
ICDD	- International centre for diffraction data
IFFT	- Inverse Fast Fourier Transform
IL	- Ionoluminescence
KS	- Kohn-Sham
LBE	-Lead Bismuth Eutetic
LDA	- Local density approximation
LD	- Lattice Dynamics
LT	- Lifetime
MC	- Monte Carlo
MD	- Molecular dynamics
NN or nn	- Nearest Neighbor
NVE	- Number of particle(N), volume(V) and energy(E) are fixed
NVT	- Number of particle(N), volume(V) and temperature(T) are fixed
O-D	- Order to Disorder
OR	- Orientation Relationship
ODS	- Oxide Dispersion Strengthened Steel
PAS	- Positron Annihilation Spectroscopy
PALS	- Positron Annihilation Lifetime Spectroscopy
PAW	- Projector augmented wave
PBC	- Periodic boundary condition
PBE	- Perdew-Burke-Ernzerhof
PBoS	- Programmable System on Chip
PDOS	- Phonon density of states
PKA	- Primary Knock-on Atom
PL	- Photoluminescence
PP	- pseudo-potential
ps	- picosecond
RAFM	- Reduced Activation Ferritic Martensitic
RF	- Radio Frequency

SAED	- Selected Area Electron Diffraction
SANS	- Small Angle Neutron Scattering
SCW	- Supercritical Pressurized Water
SNICS	- Source of Negative Ions by Cesium Sputtering
SPS	- Spark Plasma Sintering
SQS	- Special Quasirandom Structure
SRA	- Self Recoil Atom
SRIM	- Stopping Range of Ions in Matter
STE	- Self Trapped Exciton
STEM	- Scanning Transmission Electron Microscopy
TDE	- Threshold Displacement Energy
TDOS	- Total Density of States
TEM	- Transmission Electron Microscopy
TRIM	- Transport of Ions in Matter
UHV	- Ultra High Vacuum
VASP	- Vienna <i>ab initio</i> Simulation Package
VESTA	- Visualization for Electronic STructural Analysis
XC	- Exchange Correlation
XRD	- X-ray Diffraction
YAM	- Yttrium Aluminum Monoclinic ($Y_4Al_2O_9$)
YAP	- Yttrium Aluminum Perovskite ($YAlO_3$)
YAG	- Yttrium Aluminum Garnet ($Y_3Al_5O_{12}$)
YSZ	- Yttria Stabilized Zirconia
Zr-ODS	- ODS steel containing Zr

Introduction

1.1 Need for radiation-resistant steels

Identifying and utilizing clean, affordable, abundant and sustainable energy resources that satisfy ever-increasing needs of the growing global population is one of the greatest technological challenges of the twenty-first century. Recently, nuclear energy has emerged as a secure and environment-friendly alternative to depleting fossil fuels. Nuclear power is responsible for nearly 10% of global electricity generation and is the second-largest low carbon power source after hydroelectricity. The future of nuclear power varies greatly between countries and is determined by government policies. India is looking forward to rapid expansion of nuclear power generation along with other renewable energy sources.

India's nuclear energy program was carefully designed by Dr. Homi Bhabha in the 1950s, towards achieving its energy requirements by utilizing the thorium reserves in the country through a three-stage program. According to this program, nuclear power is expected to contribute 20% of India's overall energy production by 2050 [1]. The Prototype Fast Breeder Reactor (PFBR), being constructed at Kalpakkam is a crucial step in the second stage of the three-stage program. It is expecting to generate 500 MWe of electrical power for an operational life of 40 years. The target burn-up

(*ie.*, the total amount of thermal energy generated per unit quantity of fuel loaded) of PFBR is ~ 100 GWd/t.

The reactor core of Fast Breeder Reactor (FBR) has an environment of high temperature, large time-varying stresses and high irradiation fluxes [2]. The core of a fast reactor consists of a large number of fuel sub-assemblies. Each sub-assembly consists of a hexagonal wrapper tube in which many circular clad tubes (or fuel pins) filled with fuel are assembled. In PFBR, the clad tubes experience temperatures in the range of $400\text{ }^{\circ}\text{C}$ - $700\text{ }^{\circ}\text{C}$ under steady-state operating conditions and up to $1000\text{ }^{\circ}\text{C}$ under transient conditions [2]. Wrapper operates at a relatively low temperature than the clad ($400\text{ }^{\circ}\text{C}$ - $600\text{ }^{\circ}\text{C}$). During transient conditions, it may rise up to $900\text{ }^{\circ}\text{C}$. The clad tube experiences an internal pressure of around 100 MPa due to the fission gas released from the fuel matrix for an in-service time between $50,000$ and $80,000$ hours. For similar conditions, the wrapper experiences an internal pressure of $\sim 12\text{ MPa}$ due to sodium coolant.

Both clad and wrapper are also subjected to a high neutron flux of $\sim 10^{15}$ neutrons/cm²/s for a burn-up of 100 GWd/t , due to which atoms in structural materials get displaced up to 85 times, creating a large number of vacancies and interstitials, and is characterized by the unit of radiation damage, displacements per atom (dpa). Neutrons also produce solid transmutation products, such as Mn, from reactions with Fe, along with gaseous products like H and He from (n,p) and (n, α) reactions. Helium is insoluble in steel and its concentration increases at $\sim 1\text{ appm/dpa}$ for fast neutron spectrum [3]. At elevated temperatures, local vacancy supersaturation and accumulation cause volumetric changes in the core reactor components and this phenomenon is called void swelling [4]. The void swelling results in dimensional instability and operational difficulties in these components and therefore plays a crucial role in determining the reactor lifetime. Thus the successful operation of PFBR and future FBRs are strongly dependent on the design of materials exhibiting good mechanical, physical, and radiological stability under long-term service in these extreme conditions.

Void swelling is dependent on the fluence and it is insensitive up to certain fluence called incubation dose, followed by a transient regime of low swelling and then an accelerated regime of nearly linear swelling rate [4]. The first generation materials like SS316 and SS304 have unacceptable swelling even at fluences less than 50 dpa [5, 6].

Modification of alloying elements and engineering of metallurgical structures by cold working help to increase the incubation dose. Austenitic steels have peak swelling temperature in the range 400 °C-700 °C [7], which coincides with the reactor operating temperature range. The steady-state swelling rate is constant for most austenitic SS alloys, $\sim 1\%$ per dpa, for a wide range of irradiation temperatures [2]. Ni is an inevitable element in austenitic steels and will be transmuted to He by thermal neutrons, thereby accelerating the void growth [3].

Ferritic steels and ferritic martensitic steels having bcc structure possess high tolerance towards void swelling compared to austenitic steels owing to their low concentration of Ni, high self-diffusion coefficient, etc [8]. However, any metallic alloy subjected to constant tensile load at elevated temperature and radiation environment will undergo a time-dependent elongation called *creep*. Since the diffusion coefficient of ferritic steel is higher than that of austenitic steel, they are more susceptible to creep. Therefore, when we consider ferritic steel for reactor core applications because of its swelling resistance, the high-temperature strength of these core components is compromised. The addition of carbide forming elements like Mo or V into high Cr (9-12 wt%) alloyed ferritic martensitic steels helped in achieving creep resistance up to 600 °C. Later it was recognized that the residual activity at the end of the steel's lifespan can be considerably reduced by limiting the amount of elements like Mo, Nb and Ni [9], making the steel more suitable for FBRs and fusion reactors. Thus the reduced activation ferritic martensitic (RAFM) steels came into the picture. In these steels, Mo and Nb are replaced by W and Ta respectively [10]. The amount of minor alloying elements like Ni, Co, Cu and B were strictly controlled. The F82H (Japan), EUROFER97 (Europe), CLAM steel (China) and INRAFM (India) belong to RAFM class. Despite slightly varying chemical compositions, all of them have very similar microstructures: tempered martensite with fine carbide precipitates.

Further, in the 1960s the first ferritic oxide dispersion strengthened steel was developed by SCK CEN [11]. The fine, stable oxide dispersions in ODS steels were superior to the carbide precipitates in RAFM steels and ODS steels showed exceptional creep properties and swelling resistance. Till now, these ODS steels are considered a promising candidate material for reactor core structural materials and abundant research is going on the synthesis, characterization and simulation of ODS steels emphasizing on their thermal and radiation resistance. This thesis is one such attempt

towards the mechanistic understanding of the tailored microstructure and exceptional radiation resistance of two specific ODS alloys. As an introduction, the dispersion strengthening mechanism, which is crucial in tailoring the microstructure of ODS steels is explained below.

1.2 Dispersion Strengthening

The strength of a material is inversely proportional to the mobility of its dislocations. The movement of dislocations can be interrupted by introducing grain boundaries, solute atoms, second phase precipitates, or fibers into the matrix, which will strengthen the material [12]. Corresponding strengthening mechanisms are termed grain boundary strengthening, solid solution strengthening, precipitate(or dispersion) strengthening, and fiber strengthening respectively. The high-temperature strength of the RAFM and ODS steels mentioned in the previous section is ensured by precipitation or dispersion strengthening. In these alloys, fine precipitates in the metal matrix impede the dislocation movement and thereby resist the deformation. The degree of strengthening depends upon the coherency, shape, volume fraction, average particle diameter and mean inter-particle spacing of the dispersed precipitates [13].

There are two mechanisms by which dislocations interact with the dispersed precipitates in the matrix. If there is an atomic matching or *coherency* between the precipitates and matrix, the dislocations tend to shear through the precipitate. In an incoherent precipitate (or when coherent particle size exceeds a critical value), the dislocations bend to avoid the particles by a process of cross-slip. In both cases, the stress required to move the dislocations is higher than that of the pure matrix, though hard impenetrable particles provide generally a higher strengthening effect. Among these two processes, the one leading to smaller strength increment is the operative mechanism.

The mechanism of dispersion shearing is shown in Figure 1.1. As per the Friedel effect, dislocation shearing forms an anti-phase boundary. The ease with which a particle can be sheared depends on coherency strain, stacking fault energy, modulus effect, interfacial energy and lattice friction stress.

It is difficult for a dislocation to overcome the boundary between the lattice and

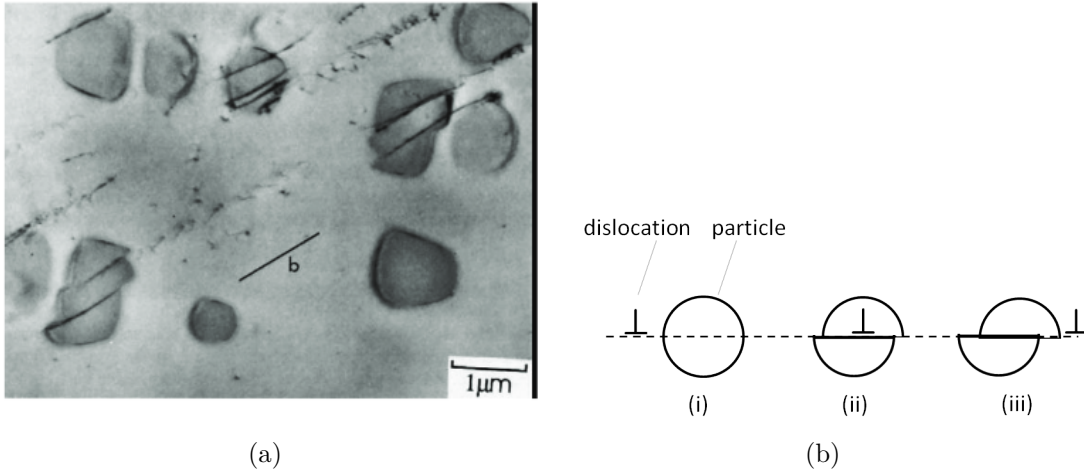
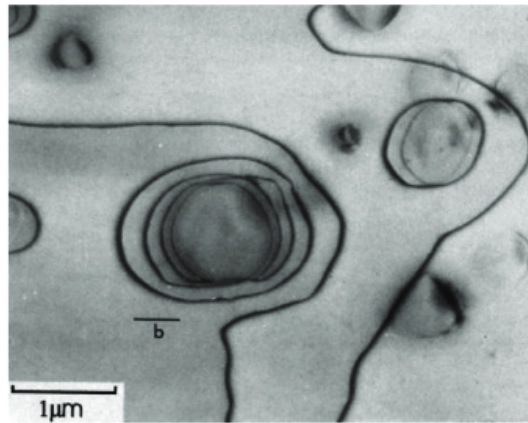


Figure 1.1: (a) TEM micrograph showing shearing of Ni_3Si in a Ni-based alloy, figure taken from [14] (b) Schematic of a dislocation cutting through a coherent particle on the same slip plane as in the matrix.

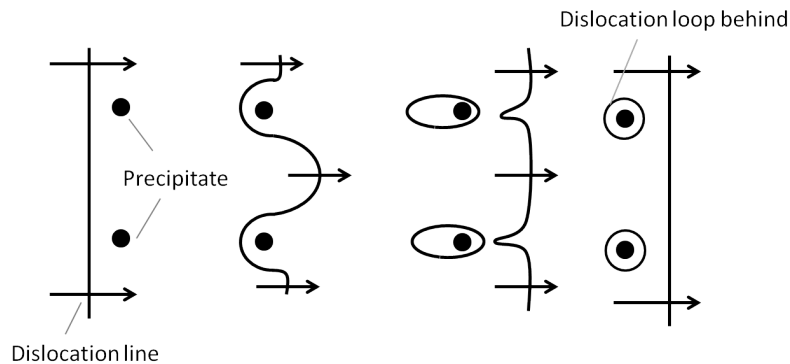
the incoherent precipitation, therefore they bow out the precipitates by leaving a dislocation ring around it. This is called ‘Orowan mechanism’ which is depicted in Figure 1.2(a) and (b). The yield stress is determined by the shear stress required to bow a dislocation line between two particles. In stage 1 of Figure 1.2, a dislocation approaches two precipitates, in stage 2., it starts to bend and reaches a critical curvature. The dislocation can now move forward without further reducing its radius of curvature. The segments of dislocations that meet on the other side of the precipitate are of opposite signs. So they annihilate and form a loop around the precipitates, leaving the original dislocation free to move on. Due to the existing dislocation loop around the precipitates, the stress required to cross these precipitates has further increased.

Since the shearing and bypassing mechanisms occur concurrently and independently of each other, the strengthening is determined by the smaller of $\Delta\sigma_{shearing}$ or $\Delta\sigma_{orowan}$. That means, the softer mechanism initiates the plastic deformation. For a given volume fraction f , the maximum strength increment could be reached when $\Delta\sigma_{shearing} = \Delta\sigma_{orowan}$ at a critical particle size, r_0 .

Besides the enhanced creep strength, the fine dispersions will help to increase the radiation tolerance of the material. The high density of dispersoids will not only act as stable sinks for point defect annihilation but also play a role in trapping fine He bubbles. They help in controlling the grain growth by ‘Zener pinning’ mechanism [15, 16] and



(a)



(b)

Figure 1.2: (a) Orowan looping of Ni_3Si particles in a Ni-base alloy, figure taken from [14]. (b) Stages on Orowan's mechanism of dispersion hardening [12].

thus indirectly contribute to the radiation resistance and strengthening caused by increased grain boundaries.

1.3 Oxide Dispersion Strengthened(ODS) steels

The history of Oxide Dispersion Strengthened(ODS) steels traces back to the invention of powder metallurgy by Benjamin *et al.* [17,18] and its subsequent application by Fisher *et al.* [19]. Initial ODS ferritic steels used Y_2O_3 as dispersoids. They were found to be dissolved in the matrix during the milling process and re-precipitated during consolidation [20]. Later it was found that the addition of Ti results in Y-Ti-O nanoprecipitates (Y_2TiO_5 and $\text{Y}_2\text{Ti}_2\text{O}_7$) which are finer and more coherent than

Y_2O_3 , resulting in high tensile and creep strengths [21]. The creep rupture strength of Y-Ti-O dispersed steels are found to be 1.6 times larger than the Y_2O_3 dispersed version and nearly 3 times larger than the conventional heat resistant steels of the same Cr content. Since the yttrium is found to be dissolving during milling and precipitating as Y-Ti-O dispersoids, the terms precipitate, dispersion and dispersoid are used synonymously in the case of ODS steels. One of the primary types of ODS steels was with ferritic/martensitic structure (Cr<12 wt%) [22,23]. But the tolerance to internal corrosion and behavior during fuel reprocessing was at stake due to the low Cr content [24,25]. Therefore, high Cr (Cr>12 wt%) ODS steels were widely developed. Thereafter, ODS EUROFER [26,27], J12YWT [28], U14Y, U14YT and U14YWT [20,29] were manufactured and studied extensively for their suitability for nuclear reactor applications. The ultra-high number density ($\sim 10^{23}/m^3$) of small (2-10 nm) coherent dispersoids with uniform nano-sized grain size distribution are the main characteristics that make the ODS alloy suitable for such applications. A prompt literature review on the manufacturing of ODS steels, the characteristic of the dispersions and their radiation response are presented below.

1.3.1 Metallurgy of ODS steels

ODS steels are fabricated by mechanical alloying, followed by Hot Isostatic Pressing (HIP) or hot extrusion. Then they are made into tubes by various sequences of re-crystallization and cold/warm working.

Powder Production

Conventionally, alloys are produced by smelting and casting. The alloying elements are added to the material during smelting. But the elements of ODS steels, Y, Zr, O, Ti, etc., have extremely poor solubility in molten steel. So in the process of casting, they tend to form bulk aggregates rather than fine dispersions. Mechanical alloying helps to dissolve these elements in the Fe matrix [17]. In this process, the constituent elemental powders are repeatedly deformed, broken and cold-welded into small particle sizes with the help of a ball mill or an attritor [18]. The balance between fracturing and cold welding is maintained with the help of a surfactant. The process is carried out in a vacuum or inert gas atmosphere. The resulting powder is typically 20 -100

nm in size with dissolved Y, O, etc in supersaturation. The final size of the powder is strongly dependent on the initial size, milling time, ball to powder ratio and milling temperature [30, 31].

High-temperature Consolidation

Fully dense material is obtained from milled powder by high-temperature consolidation. The most popular consolidation methods are hot isostatic pressing (HIP) and hot extrusion (HE). The milled powders are canned and vacuum degassed prior to consolidation. In the HIP process, the canned powder is subjected to elevated temperature and isostatic gas pressure in a high-pressure containment vessel. In hot extrusion, the canned powder is heated and subsequently drawn through a reduced section to obtain a rod of a fixed cross-section. Extrusion results in anisotropic grain distribution, with a grain size of few micrometers along the extrusion direction and few hundreds of nanometers in the transverse direction [32]. Whereas, HIP results in bimodal grain distribution, with both ultra-fine and coarse grains. A decrease in HIPing temperature from 1150 °C to 850 °C causes mean particle size to decrease from 1.7 nm to 1.25 nm, with number densities increasing from $3 \times 10^{23} \text{m}^{-3}$ to $2.6 \times 10^{24} \text{m}^{-3}$ [29]. Thus the nature of dispersoids can be tuned by controlling the consolidation temperature history. The size and density of the dispersoids are similar in both HIP and hot extrusion at the same temperature. A schematic view of the ODS fabrication process used in this thesis is given in Figure 1.3.

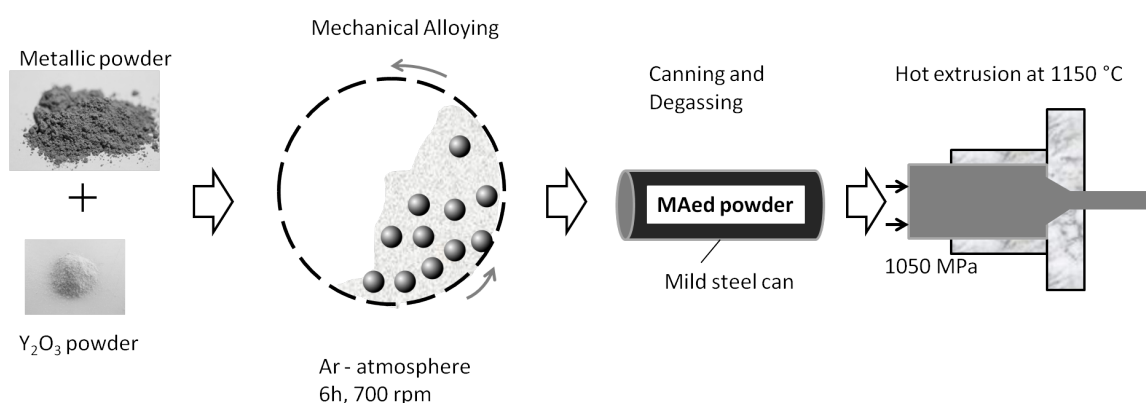


Figure 1.3: Different stages of ODS fabrication

1.3.2 Nature of dispersoids

A typical composition of ODS steel is Fe with 0.2-0.5 wt% of Y_2O_3 , 0.1-0.4 wt% Ti, 9-19 wt% of Cr and 1-3 wt% of W [29]. Cr forms a corrosion-resistant oxide layer on the alloy surface and also acts as the ferrite stabilizer. Cr content is optimized to be 9-19 wt% from the Fe-Cr phase diagram [33], in order to achieve ferritic structure over the whole temperature range without any harmful effect of the intermetallic FeCr compound, σ -phase [34–36]. The low activation W provides solid solution strengthening. In some cases, W is replaced by Mo, V and Ta [37, 38].

The elements in group IVb of the periodic table, mainly Ti, Zr, and Hf are widely used as reactive alloying elements. These elements get dissolved in Fe during mechanical alloying along with Y_2O_3 and re-precipitate as oxides during hot consolidation process. Nearly, 0.1-0.4 wt % of Ti is necessary to form fine dispersions [39–41]. Transmission electron microscopy (TEM) and small-angle neutron scattering (SANS) studies in Y and Ti containing ODS steels consistently show that the precipitates are ~ 2 nm sized Y_2TiO_5 and $Y_2Ti_2O_7$, which are the major and most stable Y-Ti oxides [21, 39, 42]. The $Y_2Ti_2O_7$ belongs to the pyrochlore class, a cubic fluorite related structure and Y_2TiO_5 is an orthorhombic phase. These precipitates are either semi-coherent or incoherent with the matrix. Partial coherency is preferred as it reduces the strain energies and interfacial energies while effectively blocking the dislocations. Pyrochlore type oxides are reported to have cube on cube orientation $[110]_{YTO}||[100]_{Fe}$ and $[001]_{YTO}||[010]_{Fe}$ with $8d_{110,Fe}=9d_{440,Y_2Ti_2O_7}$. The misfit, $\epsilon = 12.6\%$ is accommodated by misfit dislocations [43]. The atom probe tomography (APT) studies show the presence of Y, Ti and O in the nanoclusters as well. However, they were not necessarily stoichiometric oxides, rather non-equilibrium sub-oxide transition phases, which are coherent with the matrix with a Cr-rich shell and Y-Ti-O rich core [28, 44–47].

Furthermore, the performance of ODS ferritic steel in a corrosive environment can be improved by the addition of 4–6 wt% of Al that results in the formation of a continuous protective layer of Al_2O_3 [48–51]. Zr is a suitable replacement for Ti in ODS alloy containing Al. Being the main scope of the present thesis, the effect of Al and Zr addition has to be discussed in detail.

Effect of Al addition

Thermodynamically, aluminum oxide is one of the most stable oxide layers and one with the lowest kinetic growth rate [52]. The formation of Al_2O_3 protective layer begins with the adsorption of oxygen molecules from the atmosphere, which then nucleates the oxide product, extending to the formation of a thin continuous layer, followed by its growth to a thicker scale [53]. It is easy to establish and maintain Al_2O_3 scales on Fe-Cr-Al alloys than on Fe-Al alloys [54]. Cr reduces the entry of oxygen in the alloy thereby promoting a complete external layer of Al_2O_3 scale rather than its precipitation as internal oxide [24]. At very high temperatures, alloys capable of developing external Al_2O_3 -rich scales have greater potential for oxidation resistance than those developing other oxides like Cr-oxide [54]. It is reported that nearly 4-6% of Al and greater than about $\sim 5\%$ Cr are required to stabilize Al_2O_3 with Cr_2O_3 in ferritic alloys.

In ODS steels 4-6 wt% of Al helps to keep the alloy intact in liquid metal, Lead Bismuth Eutectics (LBE) and supercritical pressurized water (SCW) environments, where the Al-free alloys with Cr content up to 19 wt% fail [55]. The addition of Al is found to be effective in 16Cr-ODS steel but not in 19Cr-ODS steel. Thus according to Lee *et al.*, 14-16 wt% of Cr and 3.5-4.5 wt% of Al is adequate for ODS steel in these environments [56].

However, Al addition changes the chemistry of dispersoids in ODS steels. The initial Ti-rich Y-Ti-O complexes are replaced by Al-rich Y-Al-O complexes on Al-addition [50]. In Fe-16Cr-4Al-2W-0.3Ti-0.3 Y_2O_3 (extrusion temperature 1150 °C) and Fe-20Cr-4.5Al-0.34Ti-0.5 Y_2O_3 (extrusion temperature 1107 °C) model ODS alloys, the dispersed phases are $\text{Y}_4\text{Al}_2\text{O}_9$ (Yttrium Aluminum Monoclinic - YAM) and YAlO_3 (Yttrium Aluminum Perovskite - YAP). These nanoprecipitates were partially coherent with the matrix (α). The orientation relationships observed are: $[011]_\alpha \parallel [100]_{\text{YAM}}$ with $(011)_\alpha \parallel (004)_{\text{YAM}}$, $[011]_\alpha \parallel [012]_{\text{YAM}}$ with $(011)_\alpha \parallel (2\bar{4}2)_{\text{YAM}}$, $[011]_\alpha \parallel [432]_{\text{YAM}}$ with $(0\bar{1}1)_\alpha \parallel (2\bar{4}2)_{\text{YAM}}$ and $[011]_\alpha \parallel [221]_{\text{YAM}}$ with $(0\bar{1}1)_\alpha \parallel (2\bar{4}2)_{\text{YAM}}$. The lattice mismatch varies from 2% to 30%, which are accommodated by a periodic array of dislocations [51, 57]. The Y-Al-O phases are coarser with a size range of 20-100 nm than Y-Ti-O phases with a size range of 2-10 nm. The number density of Y-Al-O is fewer by one order of magnitude. The large-sized dispersoids with lower number density result in a significant reduction of the ultimate tensile strength of

Al-containing ODS alloys. The role of Ti is insignificant in the formation of oxide nanoparticles in the presence of Al [50] and Zr is considered as a potential replacement for Ti in Al-containing alloys.

Effect of Zr addition

It has been observed that the addition of a small amount of Zr or Hf results in a significant increase in creep strength and yield strength at elevated temperatures in Al-added ODS steels, which was attributed to the decrease in precipitate size [48, 58, 59]. Yu *et al.* [60] found $Y_2Zr_2O_7$ oxide in Fe-16Cr-4Al-0.63Zr-0.35 Y_2O_3 alloy, while Ohnuki *et al.* [61] detected Y_6ZrO_{11} and $Y_4Zr_3O_{12}$ oxides in Fe-16Cr-4Al-2W-(0.3-0.5) Y_2O_3 -(0.3-0.45)Zr alloy. In both cases there was a reduction in precipitate size and an increase in number density. The size and number densities of precipitates were close to 16Cr-Ti ODS steel. Further, Dou *et al.* [62], found that 98% of oxides in Fe-15Cr-2W-0.1Ti-4Al-0.63Zr are with $Y_4Zr_3O_{12}$ structure and they are coherent with the matrix. A few cubic and tetragonal ZrO_2 and Y_2TiO_5 precipitates were detected. However, the Al-containing phases were completely absent [62–64]. The Y-Zr-O phases were \sim (4-25) nm in diameter and their number densities were higher than Y-Al-O phases, causing increment in tensile strength. Hf addition gives similar results as Zr addition. It produces \sim 3 nm-sized, coherent $Y_2Hf_2O_7$ precipitates [65, 66]. The internal oxidation reactions causing this precipitation are: $2Y_2O_3 + 3ZrO_2 \rightarrow Y_4Zr_3O_{12}$ and $Y_2O_3 + 2HfO_2 \rightarrow Y_2Hf_2O_7$.

Nearly 96% of reported Y-Zr-O precipitates are at least partially coherent with the matrix. The orientation relationships $[001]_{\alpha} \parallel [2\bar{1}0]_{\delta}$ with $(0\bar{2}0)_{\alpha} \parallel (12\bar{4})_{Y_4Zr_3O_{12}}$ and $[111]_{\alpha} \parallel [102]_{Y_4Zr_3O_{12}}$ with $(43\bar{2})_{\alpha} \parallel (10\bar{1})_{Y_4Zr_3O_{12}}$ are reported [62, 67]. The lattice mismatch between different planes varies from 2% to 17%. These studies sum up the possibility of Zr/Hf as an effective alternative to Ti for refining precipitates in ODS steels containing Al. However, the mechanistic understanding behind such a proposition is yet to be explored in detail. The size, number density and structure of nanoprecipitates in ODS steels containing Zr and Al, available in the literature are summarized in Table 1.1. The processing parameters of these steels are tabulated in Table 1.2. It is evident that the Y-Al-O phase is the predominant precipitate phase in Al-containing ODS steels without Zr, irrespective of the amount of Ti. But Zr addition changes the phase into Y-Zr-O structure. Atomistic simulations based on density functional theory (DFT) is a

powerful tool for understanding this preferential precipitation of Y-Zr-O nanoclusters in presence of Al and Ti. Several detailed first principle calculations have been carried out for developing a comprehensive understanding of the effect of the addition of Ti and Zr in bcc ODS [68–74]. But studies in the presence of Al are scarce. This is the starting point of this thesis and a brief overview of DFT simulations carried out so far in this direction is essential.

Table 1.1: Summary of the nature of dispersoids in Al and Zr containing ODS steels

Alloy	Cr	Ti	Y ₂ O ₃	Al	W	Others	Particle diameter(nm)	Number Density	Composition
K3-ODS [57]	16	0.3	0.37	4.5	2		8.07	1.3×10 ²²	YAM (Y ₄ Al ₂ O ₉) YAP(YAlO ₃) YAG(Y ₃ Al ₅ O ₁₂)
MA956 [51, 57]	20	0.34	0.5	4.5	2		5.9	1×10 ²⁰	YAM (Y ₄ Al ₂ O ₉) YAP (YAlO ₃)
SOC-9 [62, 75]	15.5	0.1	0.35	4	2		6.8	1.72×10 ²²	YAH (YAlO ₃) YAM (Y ₄ Al ₂ O ₉)
SOC9-ET [75]	15.5	0.1	0.35	4	2		3.21	9.38×10 ²²	YAP (YAlO ₃) YAH (YAlO ₃) YAM (Y ₄ Al ₂ O ₉)
Gao <i>et al.</i> [50]	16	0.5	0.4	4	2		40-100	10 ¹⁹	Y-Al-O Y-Ti-O
Gao <i>et al.</i> [50]	16	0.5	0.4	4	2	1Zr	20	2.6×10 ²¹	Y-Al-O Y-Zr-O
Zhang <i>et al.</i> [76]	19.4	0.38	0.51	4.8		0.1Mn	10	5×10 ¹⁸	YAP YAG
Zhang <i>et al.</i> [76]	16	0.1	0.34	3.4			6	3×10 ¹⁹	YAP YAM
SOC-14 [62]	15	0.1	0.35	4	2	0.63Zr	4.75	7.16×10 ²²	Y ₄ Zr ₃ O ₁₂

DFT simulation: A tool for predicting nanocluster formation

One of the first studies using DFT about the effect of a foreign atom in Fe matrix was by C. L. Fu *et al.* [68]. They found that oxygen has high formation energy (and low solubility) in defect-free Fe lattice, but the formation energy of O–vacancy pairs

Table 1.2: Processing parameters of Zr/Al ODS steels from literature

Alloy	MA parameters	Hot consolidation method
K3-ODS [51]	Argon gas atomized powder alloyed using attritor, 290rpm/48h	HE at 1150 °C Tempering at for 1h air cooling
SOC-9 [75]	Ball milling,	HE at 1150C
SOC-9 ET [62, 75]	220rpm/48h	HE at 1050 °C
Gao <i>et al.</i> [50]	Ball milling, 350 rpm/20h	Consolidated by SPS
SOC-14 [62]	Attritor, 220 rpm/48h	HE at 1150 °C Heat treatment at 1050C air cooling
Zhang <i>et al.</i> [76]	Ball milling 220 rpm/48h	HE at 1150 °C

becomes surprisingly small if the vacancies pre-exist in the matrix [68]. This behavior is different from interstitial C and N atoms in bcc Fe. Oxygen-vacancy binding significantly reduces the oxygen mobility in Fe. It is well-known that mechanical alloying introduces an ultra-high amount of vacancies, dislocations, self interstitial atoms and voids into the steel matrix. Later, the nanoclusters in ODS steels are formed during the high-temperature consolidation process. Thus trapped vacancies can be a crucial element of these nanoclusters and the reduction in the formation energy of O-vacancy pairs can be a starting point of nanocluster formation. This argument has been supported as well as contradicted by many studies in subsequent years.

Further calculations on the total energy cost of dissolving Y_2O_3 and Ti in Fe suggested that a high energy process like mechanical alloying is needed to achieve the dissolution of elements in Fe host and the dissolved state will consist of substitutional Y and Ti, excess vacancies and an unknown mixture of interstitial oxygen and lower energy O-O pairs [69]. They were in agreement with the critical role of vacancies

in the kinetics of nucleation and growth of the Y–Ti–O enriched clusters. Murali *et al.* [71] calculated the role of minor alloying elements like Ti and Zr on the stability and dispersion of nanoclusters considering vacancy as a constituent element. Their main conclusion was that the binding energies of Y–O–vacancy clusters increase when Ti is replaced with Zr, thereby leading to higher stability (Figure 1.4). The higher stability of clusters enhances the nucleation rate, which will result in finer dispersions.

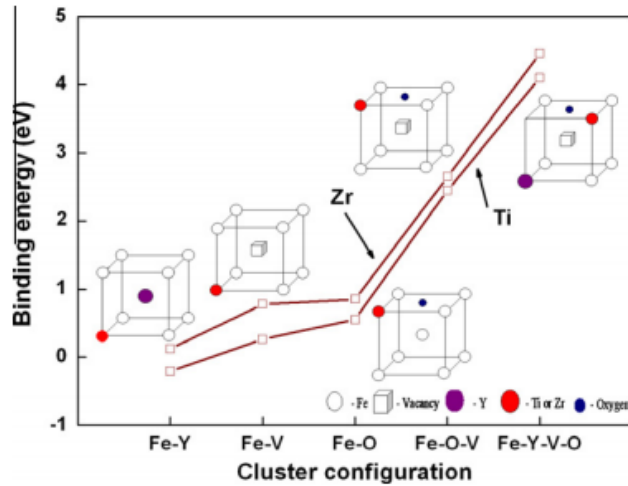


Figure 1.4: The binding energies of Ti and Zr atoms with a vacancy (V), O, O–V and Y–V–O cluster in bcc Fe supercell, reproduced from Murali *et al.* [71]. The Zr containing atomic- clusters have more binding energy than Ti containing clusters

However, Claisse *et al* [72] calculated that the Y–Ti–O clusters do not need a vacancy to stabilize in the bcc Fe matrix and the repulsion between Y and Ti can be overcome by their strong attraction to oxygen. L. Barnard *et al.* [73,74] proposed that strained variants of bulk Y and Ti oxides are more stable compared to nanoclusters that are restricted to body-centered Fe lattice. In these cases, the equilibrium concentration of vacancies is enough to enable nucleation and clustering.

Experimental studies using positron annihilation spectroscopy have reported the presence of vacancy clusters inside Y–Ti–O complexes in ODS alloys [77,78]. Therefore, vacancies can be considered as a constituent element of nanoclusters especially when the alloys are made in a ball milling atmosphere, where alloys containing high dislocation densities [20] and excess vacancies [79] are produced. Chapter 4 of this thesis deals with the energetics of Y–Zr–O and Y–Al–O nanoclusters in Fe matrix with vacancy as

a constituent element.

1.3.3 Radiation response of ODS steels

The behavior of ODS steels under neutron and self-ion irradiation is necessary to comprehend the possible structural changes that occur during in-service conditions. Several irradiations using neutron, heavy-ion single beam, He, dual and triple beam, etc have been carried out in ODS steels of various compositions. The dispersoids and grain structure of Ti containing ODS steels are found to withstand neutron irradiation up to 100 dpa and self-ion irradiation up to 150 dpa at 700 °C. Irradiation-induced defect clusters, dislocations or voids are not visible up to 100 dpa of self-ion irradiation and 25dpa/40ppm He ion irradiation at 500 °C [80]. Above 150 dpa the nanoparticles showed a decrease in number density and increase in size, which is attributed to the Ostwald ripening process. Nevertheless, the precipitates are amorphized completely by swift heavy ion irradiation (74 MeV Kr) at room temperature as well as low temperature, due to the high electronic energy deposition and subsequent ion track formation. But such studies are rare for Zr and Al containing ODS steels.

The radiation resistance of ODS steels with Y-Al-O precipitates is inferior to steels with Y-Ti-O precipitates. The Fe/He dual ion irradiation produces nanovoids uniformly in the grains, in ODS alloy with Y-Al-O dispersoids after 25dpa/500 °C irradiation [81]. The void growths are delayed with an increase in number density and a decrease in size of the Y-Al-O nanoparticles [82]. Irradiation-induced hardening and embrittlement are observed in these steels. The smaller precipitate size corresponds to a larger increment in hardness and vice-versa [83]. The swelling of non-Al-ODS is in the range of 0.3-0.5 vol%. In ODS alloys with Al, it is temperature sensitive and peaks to 0.9-1.1 vol% at ~ 600 °C. After irradiation of 60dpa Fe/900appm He ion at 500 °C, cavities were found in ODS steels containing 4.5 wt% of Al. These cavities were half the size and twice the density of those formed in the RAFM steel, indicating that it is still better than RAFM because of lower dislocation bias and high number density of particles, acting as effective traps for He atoms and vacancies [84].

Zr addition in ODS steels containing Al is found to be beneficial in reducing the void swelling. The mean diameter and number density of He nanobubbles in Y-Ti-ODS, Y-Al-ODS and Y-Al-Zr-ODS after He+Fe dual ion implantation are 2.8 nm/ $1.1 \times 10^{23} \text{m}^{-3}$, 6.6 nm/ $2.7 \times 10^{22} \text{m}^{-3}$ and 4.5 nm/ $3.6 \times 10^{22} \text{m}^{-3}$ respectively [80].

The corresponding swelling is estimated to be 0.13%, 0.53% and 0.20% respectively [85]. Nearly 80% of the He bubbles were formed near the nanoprecipitates. This indicates that the precipitates are effective in delaying void formation. The nucleation and growth of radiation-induced dislocation loops are high in ODS steels with only Al, compared to its Zr and Hf-added versions [60]. In a recent study, upon 6.4 MeV Fe ion irradiation at 200 °C, Y-Al-O precipitates are found to lose ‘Moire’ fringe because of the amorphization of oxide particles, while the δ -phase $Y_4Zr_3O_{12}$ in (Y, Zr) ODS remained crystalline indicating that Y-Zr-O particles are more stable than Y-Al-O and possibly Y-Ti-O particles [86]. The radiation behaviour of Zr containing ODS steels with and without Al form Chapter 6 of the thesis. Positron annihilation spectroscopy is utilized to compare the evolution of vacancy defects of these alloys irradiated by Fe^+ ions.

Positron Annihilation Spectroscopy studies in ion-irradiated ODS steels

Positron annihilation spectroscopy studies can be used to understand the solute clustering mechanism [87] and the nature of irradiation-induced open volume defects in ODS steels. Positron lifetime results give information on the size and number density of vacancy clusters. Coincidence Doppler broadening (CDB) spectroscopy provides information about its surroundings whereas, the depth-resolved positron spectroscopy gives depth distribution of vacancy defects created by irradiation.

Generally, two lifetime components are observed in as-prepared ODS steels. The first one (τ_1) is usually larger than the pristine matrix but smaller than mono-vacancies. Thus they can be attributed to dislocations in the matrix. The second lifetime component (τ_2) is larger than the first one. The τ_2 arises from the combined effects of vacancy clusters and nano dispersoids [78,88]. The second lifetime component is absent in ODS base material without dispersoids. This indicates its close correlation with precipitates and processing parameters. Fitting the lifetimes in the two-component trapping model of positron annihilation can provide information on the nature and number density of trapping sites. The average lifetime values remain constant during isochronal annealing up to 1000 °C [89].

Ion irradiated ODS samples show irradiation-induced accumulation of defects resulting in strengthening and hardening [90]. The number of irradiation-induced open volume defects in ODS alloys is much lower than that in non-ODS alloys. The

CDB profile of self-ion irradiated ODS steel suggests the existence of traps associated with the Y atoms. In He-implanted ODS specimens, He-vacancy complexes (He_nV_m) are also detected along with vacancy clusters [91] and some of the studies found them to be associated with Al and Cr atoms [91, 92]. Majority of the bubbles in He-implanted specimen are in the matrix. However, the presence of dispersoids is effective in reducing the coarsening of bubbles created under irradiation at different temperatures. The mean diameter of the bubbles in ODS steels is smaller than that in the Fe-Cr alloy without dispersoids [93]. In sequential Fe^+ -He ion irradiation the He is trapped in the open-volume defects created by Fe, but not as predominant as in Fe-Cr non-ODS alloy [94]. Simultaneous Fe^+ -He ion irradiations also produces nanometer-sized cavities resulting in increased hardness, above 300 °C [95].

The superior radiation resistance of ODS alloys depends on the size, structure and radiation response of its constituent precipitates. Therefore, Chapters 7 and 8 of this thesis are dedicated to the comprehensive understanding of the structure and radiation response of the precipitate phase, which belongs to the class of ‘fluorite related structures’.

1.4 Fluorite related structures and their radiation resistance

The nanoprecipitates in ODS steels containing Zr and Al are identified to be rhombohedral $\text{Y}_4\text{Zr}_3\text{O}_{12}$. $\text{Y}_4\text{Zr}_3\text{O}_{12}$ belongs to a class known as delta (δ) phase ($\text{A}_4\text{B}_3\text{O}_{12}$, $\text{R}\bar{3}$), which is an oxygen-deficient fluorite derivative structure with general formula $\text{A}_2\text{B}_2\text{O}_{8-\delta}$, where A^{3+} and B^{4+} are rare-earth or transition metal species. The cubic pyrochlore ($\text{A}_2\text{B}_2\text{O}_7$, $\text{Fd}\bar{3}\text{m}$), disordered fluorite ($\text{A}_2\text{B}_2\text{O}_7$, $\text{Fm}\bar{3}\text{m}$), and monoclinic pyrochlore ($\text{A}_2\text{B}_2\text{O}_7$, $\text{P}2_1$) are the other structures of this family. These structures are well known for their exceptional radiation tolerance and phase stability at elevated temperatures [96].

The properties of pyrochlores have been explored in depth over a wide compositional range. Upon irradiation, most of the pyrochlores transform into disordered fluorite structures before they are fully amorphized [97]. The critical amorphization doses are less than 1 dpa for titanate pyrochlores [98]. Zirconate pyrochlores are more radiation-

resistant than titanate pyrochlores. The experimentally determined amorphization dose of zirconate pyrochlore has been found to range from ~ 5.5 dpa (for $\text{La}_2\text{Zr}_2\text{O}_7$) to more than 100 dpa ($\text{Gd}_2\text{Zr}_2\text{O}_7$). The radiation stability of a pyrochlore depends on its degree of deviation from the ideal fluorite structure [99].

However, there are only few studies discussing the radiation stability of delta (δ) phase compounds. The rhombohedral to disordered fluorite transformation has been observed in $\text{Sc}_4\text{Zr}_3\text{O}_{12}$ upon swift heavy ion irradiation at room temperature (185 MeV Au^{13+} ions, 1×10^{13} ions/cm², ~ 0.2 dpa) [100] and low energy ion irradiation at cryogenic temperature (300 keV Kr^{2+} ions, 3×10^{16} ions/cm², 23 dpa, -173 °C) [98, 101]. K. E. Sickafus *et al.* [102] irradiated $\text{Dy}_4\text{Zr}_3\text{O}_{12}$, $\text{Lu}_4\text{Zr}_3\text{O}_{12}$ and $\text{Sc}_4\text{Zr}_3\text{O}_{12}$ with 300 keV Kr^{2+} ions at -173 °, and found that $\text{Dy}_4\text{Zr}_3\text{O}_{12}$, which is the most radiation-resistant phase, did not amorphize up to 55 dpa. Uranium containing δ -phase oxides Y_6UO_{12} , $\text{Gd}_6\text{UO}_{12}$, $\text{Ho}_6\text{UO}_{12}$, $\text{Yb}_6\text{UO}_{12}$, and $\text{Lu}_6\text{UO}_{12}$ showed resistance to amorphization up to 65 dpa of Kr^{2+} , Ne^{2+} and He^+ at cryogenic temperature (~ -173 °C), but all of them showed partial or full ordered rhombohedral to disordered fluorite phase transformation [103]. Nevertheless, there is no experimental or simulation study on the irradiation response of $\text{Y}_4\text{Zr}_3\text{O}_{12}$, which is the material of our interest. As threshold displacement energy (TDE) is the most fundamental quantity governing the creation and evolution of radiation cascade in a material [104], the calculation of TDE and defect formation energies is a good starting point to predict the radiation stability of $\text{Y}_4\text{Zr}_3\text{O}_{12}$.

1.4.1 Significance of threshold displacement energies and Defect formation energies

In order to produce a point defect by an energetic projectile, a sufficient amount of energy has to be transferred to a lattice atom. Threshold displacement energy (TDE) is the minimum kinetic energy required to displace an atom from its lattice site to create a stable defect [105]. It is a key parameter in Kinchin – Pease [20] and Norgett – Torrens – Robinson (NRT) [106] models used for estimating the number of Frenkel pairs that an energetic primary knock-on atom (PKA) will create in a material. TDE is a critical factor for determining damage production profiles using Monte Carlo simulations and normalizing doses from various irradiation sources [107]. Most experimental results

in TDE are obtained by irradiating with energetic electrons [108, 109]. However, the short time and length scales of the radiation damage processes make these experiments challenging. Therefore, atomistic modeling is a promising tool for understanding the underlying mechanisms involved in primary defect production.

Table 1.3: Threshold displacement energies of fluorite and pyrochlore structures, obtained from literature.

Material	Threshold Displacement Energy (eV)
Y ₂ Ti ₂ O ₇ [124]	Y – 35.1, Ti – 35.4, O _{8b} – 13, O _{48f} – 20
Gd ₂ Ti ₂ O ₇ [122]	Gd – 28.5, Ti – 43, O _{8b} – 19, O _{48f} – 15
Gd ₂ Zr ₂ O ₇ [122]	Gd – 31, Zr – 39, O _{8b} – 13, O _{48f} – 15
La ₂ Zr ₂ O ₇ [123]	La – 29.5, Zr – 39.5, O _{8b} – 15.5, O _{48f} – 5.5
Nd ₂ Zr ₂ O ₇ [123]	Nd – 21.5, Zr – 27, O _{8b} – 6.5, O _{48f} – 3.0
Sm ₂ Zr ₂ O ₇ [123]	Sm – 21.5, Zr – 26.5, O _{8b} – 7.0, O _{48f} – 3.0
ThO ₂ [119]	Th – 53.5, O – 17.5
CeO ₂ [119]	Ce – 46, O – 20

Classical Molecular Dynamics (MD) simulations have been used extensively to compute threshold displacement energies and evaluate recoil events in materials [110, 111]. However, the results of classical MD simulations are highly dependent on the quality of the empirical interatomic potential chosen and it is likely to overestimate the value by ignoring the effects of partial charge transfer [110]. Recently, *ab initio* molecular dynamics (AIMD) has been employed as an alternative tool to study the low energy radiation response of metals [112], semiconductors [113–117], and ceramics. The advantage of AIMD is that since the forces are obtained by electronic structure calculations, the errors related to empirical potentials and partial charge transfer are avoided. There are many reports on AIMD simulations of oxides [118–121], including pyrochlores [119, 122–124]. The available AIMD simulation data on TDE of different pyrochlores and fluorite structures available in the literature are summarized in Table 1.3. Similar data in δ -phase compound will be beneficial to understand their radiation behaviour compared to pyrochlores.

Defect formation energies in pyrochlore are important in understanding the radiation and luminescence behavior of fluorite related structures. The cation antisite and anion Frenkel pair are the two main point defects in the pyrochlore structure.

The sum of these two defect formation energies is called ‘defect reaction pair energy’ and this quantity is the determining factor in assessing the radiation resistance of fluorite related compounds [102,125]. The resistance to amorphization increases with a decrease in defect reaction pair energy. This is experimentally verified in zirconate and titanate pyrochlores. Recently, Sickafus *et al.* has extended this concept to different δ -phase structures as well [96]. However, the defect reaction pair energy values for $Y_4Zr_3O_{12}$ are yet to be computed. Therefore ab-initio MD simulations are carried out in the thesis to find the threshold displacement energies and defect formation energies of $Y_4Zr_3O_{12}$ and the values obtained are used for comparing its radiation stability with pyrochlores and other δ -phase compounds. The primary conclusion of this study was that in $Y_4Zr_3O_{12}$ under irradiation, the anion defects are more probable to form than cation defects. The luminescence studies are effective tools for verifying this simulation result.

1.4.2 Luminescence in fluorite related structures

Luminescence is a very effective tool in analyzing the intrinsic and radiation induced defects in a material. Ideally, pure and perfect fluorite, pyrochlore or delta phase do not show luminescence because of their wide bandgap. But in presence of structural defects, new electronic levels are introduced in the bandgap leading to luminescence. The luminescence spectrum can be explained using *ab initio* methods. Since normal DFT tend to underestimate the bandgap, hybrid potentials like HSE06, B3LYP and GW are used for getting a better agreement with the bandgap [126–128].

Ionoluminescence

As the name implies, ionoluminescence (IL) is the photon emission caused by excitation using ion beams. The IL signal contains information about the electronic structure of the target. The ionoluminescence spectra range from ultraviolet to infrared and carry information regarding band structure and defect states in the material [129,130]. For inorganic materials, the spectrum can be explained using crystal band structure and additional levels in the bandgap due to defects, like in the case of photoluminescence (PL).

Usually the IL intensity increases with an increase in fluence in the initial stages

and then decreases upon prolonged irradiation [131]. The initial increase is due to radiation induced defect production and the decrease in intensity in the later stage is due to the accumulation and annihilation of the emission centers due to extended defect formation [130]. The intensity of the IL band is proportional to the number density of the defects associated with it [132].

The ionoluminescence spectrum of calcium fluoride (CaF_2) has two broad bands [129,130]. The band at 300 nm is attributed to intrinsic crystal defects and self-trapped excitons (STEs). A wide emission band of M-centers (or F_2^- -centers) is also observed at ~ 580 nm [133]. There are some literatures on ionoluminescence properties of ZrO_2 [134], Al_2O_3 [135], ZnO [136], MgO [137] etc discussing the correlation between irradiation-induced defects and the ion beam induced luminescence. But there is no reported data on the ionoluminescence and underlying processes in any δ -phase compound. Such studies will be beneficial in understanding the irradiation-induced defects, phase transformation and amorphization in δ -phase structures. Therefore this work concludes with the ionoluminescence spectroscopy and simulation of defect levels in He irradiated $\text{Y}_4\text{Zr}_3\text{O}_{12}$.

1.5 Overview of the thesis

The present thesis is aimed at addressing the following important issues:

1. First-principle calculations on the effect of Zr addition in nanocluster composition of ODS steels containing Zr and Al.
2. Synthesis of ODS steels containing Zr and Al and study of their radiation response by evaluation of vacancy defects produced during self-ion irradiation.
3. Application of *ab initio* molecular dynamics simulations to evaluate low energy recoil events in the precipitate phase ($\text{Y}_4\text{Zr}_3\text{O}_{12}$) and thereby predict its radiation stability.
4. Evaluate the nature of defects in bulk $\text{Y}_4\text{Zr}_3\text{O}_{12}$ oxide phase using *in situ* ionoluminescence and *ab initio* studies.

The remainder thesis is divided into seven chapters.

Chapter 2 summarizes the simulation and experimental methods used in the thesis.

In **Chapter 3**, the effect of Zr and Al addition in the nanocluster formation in ODS steels is evaluated using *ab initio* calculations. The binding energies of different configurations of Y-Al-O-vacancy and Y-Zr-O-vacancy clusters are computed and compared to predict the configuration having maximum binding energy. Further, the formation energies of different Y-Zr-O compounds are compared to find the most energetically favored structure.

Chapter 4 focuses on the synthesis and the transmission electron microscopic characterization of two types of ODS steels: (i) ODS alloy containing Zr and (ii) ODS alloy with both Zr and Al. The compositions are Fe-14Cr-0.2 Ti-0.3Y₂O₃-0.63Zr (Zr-ODS) and Fe-14Cr-0.2Ti-0.3Y₂O₃-0.63Zr-4Al (Al-ODS). Bright field and dark field diffraction contrast imaging and high resolution phase contrast imaging are extensively used to investigate the crystal structure of the dispersoids and their orientation relationships with the matrix. The information drawn from the analysis is compared with the predictions given in Chapter 4.

In **Chapter 5**, variable energy slow positron beam Doppler broadening spectroscopy is employed to investigate vacancy defects created by self-ion irradiation in Zr-ODS and Al-ODS. Positron annihilation spectroscopy is used for understanding the defects in pristine material. Further variable energy positron beam studies are utilized to explore the distribution of vacancy defects in irradiated alloys

The **sixth chapter** is devoted to the *ab initio* molecular dynamics simulations of threshold displacement energies and defect formation energies in Y₄Zr₃O₁₂, which are the dispersoids in the as-prepared alloys. The simulation results are used to predict the radiation response of Y₄Zr₃O₁₂.

Finally, for the in-depth information of point defects in Y₄Zr₃O₁₂, the ionoluminescence spectrum of this compound is acquired for various fluences and compared with defect levels simulated by first principle calculations, the details of which form **Chapter 7** of the thesis.

In **Chapter 8** the suitability of ODS steels containing Zr and Al as a candidate material for nuclear reactor applications is evaluated based on the results of Chapters 3-7. More irradiation experiments and simulations are suggested for future work.

Simulation and Experimental Methods

2.1 Introduction

This chapter outlines the simulation and experimental methods used in the thesis. A brief introduction to Density functional theory along with an overview of exchange-correlation functionals are presented. Then the principles of *ab initio* molecular dynamics methods are summarized. It is followed by a summary of ion implantation systems used. The chapter ends with a concise review of the characterization systems used: transmission electron microscopy, positron annihilation spectroscopy, Raman spectroscopy and ionoluminescence spectroscopy.

2.2 Density functional theory

In multi-scale modeling scheme, electronic structure calculations are important not only because they provide accurate information about the physical and chemical properties of materials but also because they help to formulate parameters in higher-scale methods such as molecular dynamics, kinetic Monte Carlo, etc. Density Functional Theory (DFT) uses quantum mechanics to predict the electronic structure of a material and does not use any empirical parameter, thus it is often called as *ab initio* method.

The history of DFT dates back to Thomas and Fermi in the 1920s but its successful implementation was achieved by Hohenberg, Kohn and Sham in 1960s. After that, DFT has been successfully applied to predict many properties (lattice structure, charge density, magnetization, phonon spectra, etc.) of a wide variety of solids. Followed by the massive success of DFT, one of its authors, Walter Kohn, was awarded Nobel Prize in Chemistry in 1998. A brief introduction to DFT is presented below.

2.2.1 Many-body systems

The dynamics of a quantum system is governed by the Hamiltonian, \hat{H} . Stationary states with definite energies, particularly the ground state of the system, are obtained as the solutions of the time-dependent Schrodinger equation equation:

$$\hat{H}|\Psi\rangle = |\Psi\rangle E, \quad \langle\Psi|\Psi\rangle = 1 \quad (2.1)$$

In other words, they are obtained as the stationary solutions of the vibrational problem:

$$\frac{\langle\Psi|\hat{H}|\Psi\rangle}{\langle\Psi|\Psi\rangle} \Rightarrow \text{Stationary.} \quad (2.2)$$

The approximate ground-state electronic Hamiltonian which describes the motion of N electrons in the field of M nuclei is:

$$H = -\frac{1}{2} \sum_{i=1}^N \nabla_i^2 - \sum_{i=1}^N \sum_{A=1}^M \frac{Z_A}{r_{A_i}} + \sum_{i=1}^N \sum_{j>i}^N \frac{1}{r_{ij}}, \quad r_{ij} = |r_i - r_j| \quad (2.3)$$

Here, Z_A is the number of protons of i^{th} ion located at r_{A_i} . The Born Oppenheimer approximation [138] is valid here because the time scale for movement of nuclei is much larger than that of electrons. $\left(\frac{\tau_N}{\tau_e} = \sqrt{\frac{m_N}{m_e}} \approx 100\right)$.

2.2.2 Hohenberg and Kohn theorems

All modern-day density functional theories are based on the landmark paper published by Hohenberg and Kohn in 1964 [139]. The fundamental question which existed ever after Thomas – Fermi used electron density as a basic variable in their approach is that: is it possible to describe the electronic properties (at least ground state properties) of a

many-electron system by means of electron density? The answer lies in two Hohenberg and Kohn theorems [140, 141].

Theorem.1. The first Hohenberg and Kohn theorem states that: ‘*The external potential $V_{ext}(r)$ is (to within a constant) a unique functional of $n(r)$; since, if $V_{ext}(r)$ fixes \hat{H} we see that the full many particle ground state is a unique functional of $n(r)$* ’.

Let us assume that there exist two external potentials V_{ext} and V'_{ext} , which differ by more than a constant and give rise to the same electron density $n(r)$, associated with the corresponding non-degenerate ground states of N particles. These two external potentials also define two Hamiltonians \hat{H} and \hat{H}' , and two ground states Ψ and Ψ' with ground state energies E_0 and E'_0 , where $E_0 \neq E'_0$. Then,

$$E_0 = \langle \Psi | \hat{H} | \Psi \rangle = \int V_{ext}(r) n(r) d^3(r) + \langle \Psi | \hat{T} + \hat{U} | \Psi \rangle \quad (2.4)$$

$$E'_0 = \langle \Psi' | \hat{H}' | \Psi' \rangle = \int V'_{ext}(r) n(r) d^3(r) + \langle \Psi' | \hat{T} + \hat{U} | \Psi' \rangle \quad (2.5)$$

By virtue of the variational principle:

$$\begin{aligned} E_0 &< \langle \Psi' | \hat{H} | \Psi' \rangle \\ &< \int V_{ext}(r) n(r) d^3(r) + \langle \Psi' | \hat{T} + \hat{U} | \Psi' \rangle \\ &< E'_0 + \int [V_{ext}(r) - V'_{ext}(r)] n(r) d^3(r) \end{aligned} \quad (2.6)$$

Similarly,

$$\begin{aligned} E'_0 &< \langle \Psi | \hat{H}' | \Psi \rangle \\ &< E_0 + \int [V'_{ext}(r) - V_{ext}(r)] n(r) d^3(r) \end{aligned} \quad (2.7)$$

After adding Eq. 2.6 and Eq. 2.7, we get a clear contradiction;

$$E_0 + E'_0 < E'_0 + E_0 \quad (2.8)$$

Therefore, the assumption of the existence of two external potentials corresponding to the same ground-state density $n(r)$ is invalid. In other words, ground-state density uniquely specifies the external potential V_{ext} .

Now that the ground state energy is a functional of electron density, we can write:

$$E_0[n_0] = T[n_0] + U_e[n_0] + V[n_0] \quad (2.9)$$

where $T[n_0]$ is the kinetic energy functional, $V[n_0] = \int V_{ext}(r)n(r)d^3r$ is the total electronic energy due to external potential and $U_e[n_0]$ represents the electron electron interaction energy.

The energy functional can be separated into two parts viz,: (i) that depends on the system ie., the potential energy due to the nuclei-electron attraction and (ii) that which is independent of the system.

$$E[n_0] = \underbrace{\int n(r)V_{ext}(r)d^3r}_{\text{system dependant}} + \underbrace{T[n_0] + U_e[n_0]}_{\text{universally valid}} \quad (2.10)$$

Collecting system independent part in to a new quantity, the *Hohenberg - Kohn functional*, F_{HK} , we arrive at:

$$E[n_0] = \int n(r)V_{ext}(r)d^3r + F_{HK} \quad (2.11)$$

The explicit form of F_{HK} is unknown. But we can extract the classical part of $U_e[n_0]$ and write:

$$\begin{aligned} F_{HK}[n] &= T[n] + \frac{1}{2} \int \int \frac{n(r_1)n(r_2)}{r_{12}} dr_1 dr_2 + U_{ncl}[n] \\ &= T[n] + J[n] + U_{ncl}[n] \end{aligned} \quad (2.12)$$

U_{ncl} is the non-classical contribution to the electron-electron interaction including self-interaction correction, exchange and Coulomb correlation.

Theorem.2. Second Hohenberg – Kohn theorem states that: ‘*The ground-state energy can be obtained variationally: the density that minimizes the total energy is the exact ground-state density*’.

That means, any trial density, $\tilde{n}(r)$ which satisfies the conditions $\tilde{n}(r) \geq 0$, $\int \tilde{n}(r)d^3r = N$ and that is associated with an external potential \tilde{V}_{ext} , the energy functional $E[\tilde{n}]$ defined in Eq. 2.9 is an upper bound to the true ground state energy, E_0 . We know that for any trial density $\tilde{n}(r)$, there is a Hamiltonian, \tilde{H} and a

wavefunction, $\tilde{\Psi}$. This wavefunction can now be used as the trial wavefunction for the Hamiltonian generated from the true external potential V_{ext} . In short:

$$\langle \tilde{\Psi} | \tilde{H} | \tilde{\Psi} \rangle = T[\tilde{n}] + U_e[\tilde{n}] + V[\tilde{n}] = E[\tilde{n}] \geq E_0[n_0] = \langle \Psi_0 | \hat{H} | \Psi_0 \rangle \quad (2.13)$$

Although the first Hohenberg-Kohn theorem requires a non-degenerate ground state, the Levy formulation [142] allows degenerate ground states are also. These theorems can also be generalized to include spin [143]. However, the explicit form of the functionals $T[n]$ and U_{ncl} of Eq. 2.12 is a major challenge of DFT. In 1965, Kohn and Sham proposed an approach to solve this problem.

2.2.3 Kohn-Sham formalism

The Kohn-Sham approach [144] made DFT a practical tool. They introduced the concept of orbitals into the problem in such a way that the kinetic energy can be computed to good accuracy, leaving a small residual correction that can be handled separately. They provided one-electron equations for describing many-electron systems as in the case of Hartree and Hartree-Fock methods, but in an exact manner.

The Kohn - Sham approach starts by calculating the exact kinetic energy of a non-interacting reference system with a Hamiltonian containing an effective local potential $V_S(r)$:

$$\hat{H}_S = -\frac{1}{2} \sum_i^N \nabla_i^2 + \sum_i^N V_S(r_i) \quad (2.14)$$

Its ground state wave function is represented by a Slater determinant,

$$\Theta_S = \frac{1}{\sqrt{N!}} \begin{vmatrix} \phi_1(x_1) & \phi_2(x_1) & \dots & \phi_N(x_1) \\ \phi_1(x_2) & \phi_2(x_2) & \dots & \phi_N(x_2) \\ \vdots & \vdots & \dots & \vdots \\ \phi_1(x_N) & \phi_2(x_N) & \dots & \phi_N(x_N) \end{vmatrix} \quad (2.15)$$

where the spin orbitals, ϕ_i , also known as *Kohn - Sham(KS) Orbitals*, are the eigenstates of one-electron Hamiltonian:

$$\hat{h}\phi_i = \left[-\frac{1}{2} \nabla^2 + V_S(r) \right] \phi_i = \epsilon_i \phi_i \quad (2.16)$$

The potential V_S is chosen in such a way that:

$$n_S(r) = \sum_i^N \sum_s |\phi_i(r, s)|^2 = n_0(r) \quad (2.17)$$

And the kinetic energy,

$$T_S[n] = -\frac{1}{2} \sum_i^N \langle \phi_i | \nabla_i^2 | \phi_i \rangle \quad (2.18)$$

T_S not equal to the true kinetic energy of the interacting system. Kohn - Sham accounted for that by separating Eq. 2.12 as below:

$$F_{HK}[n] = T_S[n] + J[n] + E_{XC}[n] \quad (2.19)$$

where $E_{XC}[n]$ is the ‘exchange-correlation functional’ defined as the part of kinetic energy which is not covered by T_S added to the non classical contribution to electron electron interaction. ie.,

$$E_{XC}[n] = T[n] - T_S[n] + U_{ncl}[n] \quad (2.20)$$

Now, the energy functional:

$$\begin{aligned} E[n] &= T_S[n] + J[n] + E_{XC}[n] + V[n] \\ &= T_S[n] + \frac{1}{2} \int \int \frac{n(r_1)n(r_2)}{r_{12}} dr_1 dr_2 + E_{XC}[n] + \int n(r)V_{ext}(r)d^3r \\ &= -\frac{1}{2} \sum_i^N \langle \phi_i | \nabla_i^2 | \phi_i \rangle + \frac{1}{2} \sum_i^N \sum_j^N \int \int |\phi_i(r_i)|^2 \frac{1}{r_{12}} |\phi_j(r_j)|^2 dr_1 dr_2 \\ &\quad + E_{XC}[n] + \sum_i^N \int \sum_A^M \frac{Z_A}{r_{1A}} |\phi_i(r_i)|^2 dr_i \end{aligned} \quad (2.21)$$

Now we have to variationally search for minimum $E[n]$ with the constraint $\langle \phi_i | \phi_j \rangle = \delta_{ij}$. Define the functional of N orbitals:

$$\Omega[\{\phi_i\}] = E[n] - \sum_i^N \sum_j^N \epsilon_{ij} \int \phi_i(x)^* \phi_j(x) dx \quad (2.22)$$

where ϵ_{ij} are Lagrangian multipliers. For $E[n]$ to be minimum,

$$\delta\Omega[\{\phi_i\}] = 0 \quad (2.23)$$

which leads to the equations:

$$\begin{aligned}
 & \left(-\frac{1}{2}\nabla^2 + \left[\int \frac{n(r_2)}{r_{12}} dr_2 + V_{XC}(r_1) - \sum_A^M \frac{Z_A}{r_{1A}} \right] \right) \phi_i \\
 &= \left(-\frac{1}{2}\nabla^2 + V_{eff}(r_1) \right) \phi_i \\
 &= \hat{h}\phi_i = \epsilon_i\phi_i
 \end{aligned} \tag{2.24}$$

These equations 2.24 are the *Kohn-Sham (KS) orbital equations*. The KS equations will give exact n and E if we know E_{XC} precisely.

2.2.4 The exchange-correlation functional

The quality of the density functional approach rests solely on the accuracy of the chosen approximations for E_{XC} . One of the simplest approach is *Local Density Approximation(LDA)*, in which, a uniform electron gas, the only system for which we know the exact form of exchange correlation functional is known, is used [144, 145]. If ϵ_{XC} denotes the exchange and correlation energy of a uniform electron gas of density(n),

$$E_{XC}^{LDA}[n] = \int n(r)\epsilon_{XC}(n)d^3r \tag{2.25}$$

The ϵ_{XC} can be further divided into exchange and correlation contributions:

$$\epsilon_{XC} = \epsilon_X + \epsilon_C \tag{2.26}$$

The exchange part is already known, given by the Dirac exchange energy functional:

$$\epsilon_X = -\frac{3}{4}\sqrt[3]{\frac{3n}{\pi}} \tag{2.27}$$

The accurate values of ϵ_C is available by quantum Monte-Carlo calculations, which have been interpolated to give an analytical form [145]. The LDA is applicable to slowly varying densities, but cannot be justified for in-homogeneous systems such as atoms and molecules.

In order to include the non - homogeneity of the true electron density, the functional can be supplemented with gradient of the electron density, ∇n . In other words, the functional is a Taylor expansion of the uniform density with local density approximation

as the first term. This form of functional is termed as the *Generalized Gradient Approximation* [146].

$$E_{XC}^{GGA}[n] = \int f(n(r), \nabla n(r)) d^3r \quad (2.28)$$

Compared to LDA, GGA gives reliable atomic bond strength. In recent days GGA is the most popular as well as widely used functional proposed by Perdew, Burke and Ernzerhof [147]. But, both LDA and GGA fail to predict the bandgap of a solid properly. A major contribution to bandgap error comes from the electrostatic electron-electron contribution to the Hamiltonian, known as Hartree energy, which includes the Coulomb repulsion between an electron and its own charge density. This residual self-interaction term is one of the major reasons for the underestimation of bandgap in LDA or GGA based DFT calculations [148].

2.2.5 Hybrid functionals

In the Hartree-Fock method, the exchange energy depends on the single-particle states, but takes no account of correlation. The long-ranged, unscreened nature of HF-exchange severely over-estimates the bandgap. Consequently, a hybrid XC functional, which is a combination of an empirical fraction HF and LDA (or GGA) will mitigate the self-interaction problem and provide a more realistic bandgap [149]. B3LYP(Becke, 3-parameter, Lee-Yang-Parr) [151–153], PBE0 [154, 155], HSE (Heyd-Scuseria-Ernzerhof) [150] and meta-hybrid GGA(M06) [156] are examples for hybrid functionals. All hybrid functionals introduce at least one empirical parameter, the relative fractions of LDA/GGA and HF, which is usually specified by fitting the functionals to accurately calculated thermochemical data. The resulting calculations are no longer *ab-initio* and have limited power for predicting properties other than bandgap. In this thesis HSE06 functional is used for calculation of bandgap for $Y_4Zr_3O_{12}$ in Chapter 7.

HSE06 functional

HSE class (HSE06 and HSE03) uses an error-function screened Coulomb potential to calculate the exchange portion of the energy [150, 154]. There is a partitioning between long and short-ranged contributions, introducing screening into the HF term

itself. The resulting expression for XC energy is given by [150]:

$$E_{XC}^{HSE} = \frac{1}{4}E_X^{SR}(\mu) + \frac{4}{3}E_X^{PBE,SR}(\mu) + E_X^{PBE,LR}(\mu) + E_C^{PBE} \quad (2.29)$$

where SR and LR are short-range and long-range parts respectively. E_C^{PBE} is the electronic correlation part. The parameter μ defines the range separation and is related to the characteristic distance, $2/\mu$ at which the short range interactions become negligible. μ is 0.2 Å for HSE06 functional and 0.3 Å for HSE03 functional [157].

2.2.6 Methods for electronic structure calculations

Real crystalline solids contain roughly 10^{24} electrons and ions per cm^3 and all of them should be considered to construct the Kohn-Sham Hamiltonian. The periodicity of the crystal structure shall be used to solve the problem. The periodic symmetry of the crystal lattice allows reduction of the problem to only those electrons and ionic cores that are contained in the unitcell. By solving the Kohn-Sham Hamiltonian for the atoms in the unitcell, the electron Eigen states of solid can be obtained. The effective potential V_{eff} , in the Kohn-Sham equation, Eq. 2.24, will now be periodic i.e., $V_{eff}(r) = V_{eff}(r + R)$ for all lattice vectors R of the crystal.

Plane waves offer a natural choice of wave functions for solving the KS equations. They are solutions of the Schrodinger equation for free particle and have the form:

$$\eta^{PW} = e^{i\vec{k} \cdot \vec{r}} \quad (2.30)$$

They go well with the concept of periodic boundary conditions. But the number of plane waves required to arrive at an acceptable accuracy is daunting. One way to solve this problem is to define the collective system of nuclei and core electrons by an effective smooth potential, called *pseudopotential* and then solving KS equations only for valence electrons. This reduces the number of wavefunctions to be calculated. This method is called *Plane wave pseudopotential method* [158]. The drawback of the method is that all information on the full wave function close to the nuclei is lost.

The shortcomings of plane wave method is overcome by implementing *Augmented Plane Wave (APW) method*. Since the effective crystal potential is constant in most of the open spaces between the cores, the augmented plane wave (APW) method

assumes a Muffin - tin potential defined by:

$$\eta^{APW} = \begin{cases} e^{i\vec{k}\cdot\vec{r}} ; & \text{when } |\vec{r} - \vec{R}| \geq r_0 \\ \text{atomic function} ; & \text{when } |\vec{r} - \vec{R}| < r_0 \end{cases} \quad (2.31)$$

where r_0 is the core radius. The atomic function inside the core radius is found by solving appropriate free-particle Schrodinger equation. Moreover, the chosen atomic function is such that it joins continuously to the plane wave at the surface of the sphere forming the core. So we expand plane waves in terms of spherical harmonics,

$$e^{i\vec{k}\cdot\vec{r}} = 4\pi \sum_{l=0}^{\infty} \sum_{m=-l}^l i^l j_l(kr) Y_{lm}^*(\theta_k, \zeta_k) Y_{lm}(\theta, \zeta) \quad (2.32)$$

where (r, θ, ζ) represent the polar representation of \vec{r} , j_l is the Bessel function of order l and Y_{lm} is the spherical harmonics. Inside the sphere, the wavefunction is:

$$\eta^{APW} = 4\pi \sum_{lm} i^l \frac{j_l(kr_0)}{R_l(r_0)} R_l(r) Y_{lm}^*(\theta_k, \zeta_k) Y_{lm}(\theta, \zeta) \quad (2.33)$$

The augmentation function R_l depends on muffin - tin potential eigen state and energy. Because of this energy dependence, the eigen value problem will be non-linear in energy and has to be solved iteratively. To solve this problem, linearized versions of APW methods are developed, such as Linearized PAW (LPAW) and the APW+local orbitals (APW+lo).

In *Linearized Augmented Plane Wave (LAPW) method*, the radial wave function, R_l can be approximated around a reference energy ϵ_p as:

$$R(r, \epsilon) = R(r, \epsilon_p) + (\epsilon - \epsilon_p) \dot{R}(r, \epsilon_p) \quad (2.34)$$

The LAPW wavefunction thus reads:

$$\eta^{LAPW} = \begin{cases} 4\pi \sum_{lm} i^l \frac{j_l(kr_0)}{R_l(r_0)} \left(R(r, \epsilon_p) + (\epsilon - \epsilon_p) \dot{R}(r, \epsilon_p) \right) Y_{lm}^*(\theta_k, \zeta_k) Y_{lm}(\theta, \zeta); & \text{when } |\vec{r} - \vec{R}| < r_0 \\ e^{i\vec{k}\cdot\vec{r}} ; & \text{when } |\vec{r} - \vec{R}| \geq r_0 \end{cases} \quad (2.35)$$

Now the wavefunction is independent of energy. But the solutions obtained are reliable only within some range around the pivot energy.

The *Projector Augmented Wave (PAW) method* is a combination of LAPW and the pseudo potential methods [159, 160]. This uses a decomposition of the all-electron wave function in terms of pseudo-wave functions, which are smooth everywhere and a rapidly varying contribution localized within the core region. The PAW wave functions are given by:

$$\eta^{PAW} = \tilde{\phi}_n + \sum_a \sum_i \left(\psi_i^a(\mathbf{r}) - \tilde{\psi}_i^a(\mathbf{r}) \right) \langle \tilde{p}_i^a | \tilde{\phi}_n \rangle ; \sum_i |\tilde{\phi}_i^a\rangle \langle \tilde{p}_i^a| = 1 \quad (2.36)$$

The localized atom centered part is represented by superscript a and the smooth functions are indicated by a \sim . The p_i s are some fixed functions termed projector functions. The ψ_i s are solutions of the spherical scalar relativistic Schrodinger equation for a non-spin-polarized atom at reference energy ϵ_i and angular momentum l_i in the valence regime. The PAW approach implemented in VASP [161–163] is used for DFT simulations in this thesis.

2.3 *Ab initio* molecular dynamics

In classical MD, equilibrium thermodynamic and dynamical properties of many-body systems at finite temperature are computed by numerically solving Newton’s equation of motion, using a pre-defined interatomic potential. Though these interatomic potentials are derived from elaborate theoretical models, they are restricted to the systems to which they have been fitted. Thus the MD fails to track the change of electronic structure and hence the chemical bonding of the species during the course of the simulation. These limitations can be overcome by adopting a first principle based approach, called *Ab initio* Molecular Dynamics (AIMD), where the forces are calculated on-the-fly using DFT [164, 165]. AIMD is mainly of two types which are outlined below.

2.3.1 Born-Oppenheimer molecular dynamics

In Born-Oppenheimer MD [166, 167], static electronic structure problem is solved in each molecular dynamics step with respect to the set of fixed nuclear positions at that instant of time. Thus, the electronic structure part is reduced to solving a

time-independent quantum problem, and at the same time nuclei will evolve according to classical mechanics. Thus the Born-Oppenheimer Lagrangian is:

$$L_{BO} = -\langle \Psi_0 | H_e | \Psi_0 \rangle + \sum_{i,j} \Lambda_{ij} \left(\langle \phi_i | \phi_j \rangle - \delta_{ij} \right) \quad (2.37)$$

where Λ is a Hermitian Lagrangian multiplier matrix. Corresponding equations of motion in DFT framework are:

$$M_I \ddot{\mathbf{R}}_I(t) = -\nabla_{I\{\phi_i\}}^{\min} \langle \Psi_0 | H_e^{KS} | \Psi_0 \rangle \quad (2.38)$$

$$0 = -\hat{H}_e^{KS} \phi_i + \sum_j \Lambda_{ij} \phi_j \quad (2.39)$$

The high computational cost required to minimize the energy at each time step is a major drawback of the BOMD method.

2.3.2 Car-Parrinello molecular dynamics

Car-Parrinello MD (CPMD) is a computational-friendly version of BOMD. In CPMD, the explicit electronic structure minimization using matrix diagonalization methods is not required in each time step. Instead, the electronic degrees of freedom are introduced as fictitious dynamical variables from which a Lagrangian can be derived as [168]:

$$L_{CP} = \underbrace{\sum_i M_I \dot{\mathbf{R}}_I^2}_{\text{Kinetic Energy}} + \underbrace{\sum_i \mu \langle \dot{\phi}_i | \dot{\phi}_i \rangle}_{\text{Potential Energy}} - \underbrace{\langle \Psi_0 | H_e^{KS} | \Psi_0 \rangle}_{\text{Potential Energy}} + \underbrace{\left(\Lambda_{ij} \langle \phi_i | \phi_j \rangle - \delta_{ij} \right)}_{\text{Orthonormality}} \quad (2.40)$$

which leads to a system of coupled equations of motion for both ions and electrons given by:

$$M_I \ddot{\mathbf{R}}_I = -\nabla_I \langle \Psi_0 | H_e^{KS} | \Psi_0 \rangle; \quad (2.41)$$

$$\mu \ddot{\phi}_i(t) = -H_e^{KS} \phi_i + \sum_j \Lambda_{ij} \phi_j \quad (2.42)$$

Nuclei evolve in time at a certain physical temperature $\propto \sum_I M_I \dot{\mathbf{R}}^2$, while the electrons evolve associated to a fictitious temperature $\propto \sum_i \langle \dot{\phi}_i | \dot{\phi}_i \rangle$. The energy transfer from ‘hot nuclei’ to ‘cold electrons’ is limited, which is called adiabatic decoupling. $\Delta t \propto \left(\frac{\mu}{E_{cut}} \right)^{\frac{1}{2}}$

is the largest time step possible keeping the adiabaticity intact. Typical values for large-gap systems are $\mu = 500\text{-}1000$ a.u., which allows for a time step of about 5-10 a.u. (0.12-0.24 fs). depending on the mass of the lightest nuclei.

2.4 Transmission electron microscopy

Transmission electron microscopy is one of the most powerful tools for evaluating the microstructure of materials. The principles of TEM are similar to that of the optical microscope. In the electron microscope, light is substituted by high energy electron beam and optical lenses are replaced by electromagnetic lenses. The high energy electrons are produced by processes thermionic (LaB₆, ZrO/W etc) or field emission. The wavelength of the electron beam for an acceleration potential U is:

$$\lambda = \frac{h}{\sqrt{2m_0eU(1 + \frac{eU}{2m_0c^2})}} \quad (2.43)$$

Here, m_0 is the rest mass and e is the charge of the electron; c is the velocity of light and h the Planck constant. When $U=200$ kV the electron beam has a wavelength of 2.51 pm.

The beam from the source is converged or diverged using a series of electromagnetic lenses. A simple EM lens consists of a copper coil placed inside an iron cylinder. The electric current through the coil creates a magnetic field that is rotationally symmetric but radially in-homogeneous. ie., the magnetic field is weak at the center but strong in the edges, near the Fe cylinder. Consequently, the electron beam moving close to the lens center are less deflected than the beam moving near to the edge. Thus the beam gets focused to a spot (called the *cross over*). The magnetic field and hence the strength of the lens, can be controlled by varying current in the Cu coil. The beam from the source is made into parallel (for normal TEM) or convergent (for STEM) and focused onto the specimen using a system of condenser lenses. The objective lens creates the first immediate image and diffraction pattern of the specimen. The quality of this image determines the resolution of the microscope. A system of projector lenses magnify the image (or diffraction pattern) and projects it into a photographic film or CCD camera [169].

The electromagnetic lenses also suffer from various aberrations, like optical lenses.

When the iron-based pole pieces are not perfectly circular, the image tends to be distorted and deviated from its rotational symmetry. This is similar to *astigmatism* in optical lenses and can be corrected using quadrupole corrector lenses. Due to the energy spread of the ion gun, different wavelengths of the incident beam can get focused on different points in the focal plane leading to *chromatic aberration*, C_c . The energy spread is high ($\Delta E > 1 eV$) in thermionic electron guns and can be limited by using FEG ($\Delta E \sim 0.35 eV$) and monochromators ($\Delta E \sim 0.1 eV$). Another defect of the EM lens, called *spherical aberration*, C_s , is caused by the magnetic field gradient. The result is a spread focal point of the beam and is corrected using an aberration corrector, which compensates the magnetic field gradient. The photograph of Carl Zeiss LIBRA200FE TEM which is used for characterization of ODS steels in this thesis is shown in Figure 2.1.

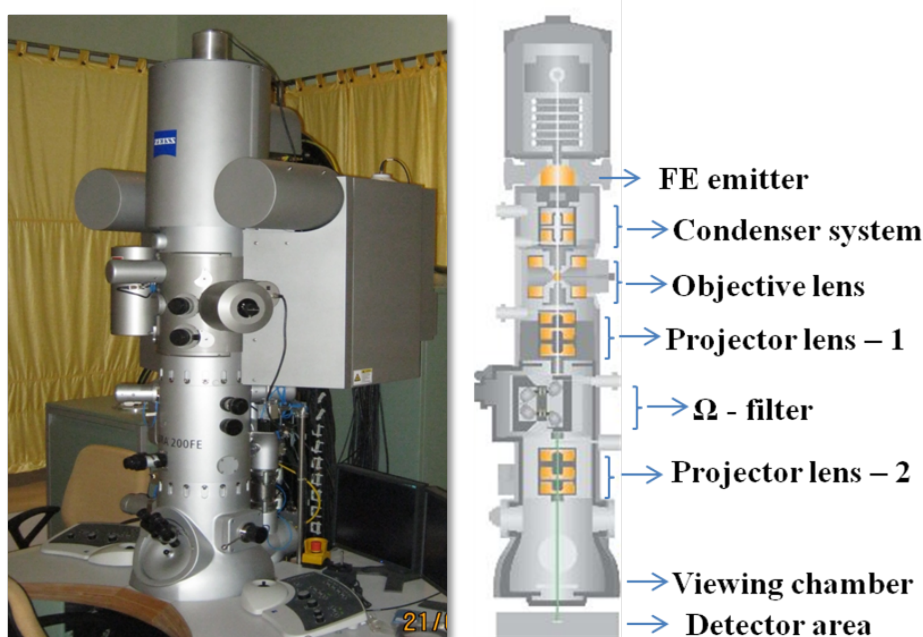


Figure 2.1: Carl Zeiss LIBRA 200FE HRTEM (left) and schematic of its cross-sectional view (right).

The TEM can work in both image mode and diffraction mode as shown in Figure 2.2. The diffraction pattern is formed at the back focal plane of the objective lens and the image is formed at the image plane of the objective lens. An aperture in TEM is a metal plate with holes in it and it helps to filter out stray electrons and improve the image quality. With the help of an aperture (SAD Aperture) and intermediate

lens, whose strength can be varied, the diffraction pattern can be focused into the object plane of the projector lens. Similarly, in the image mode, objective aperture and intermediate lens help to focus the image into the object plane of the projector lens. The projector lens system magnifies the image into the camera.

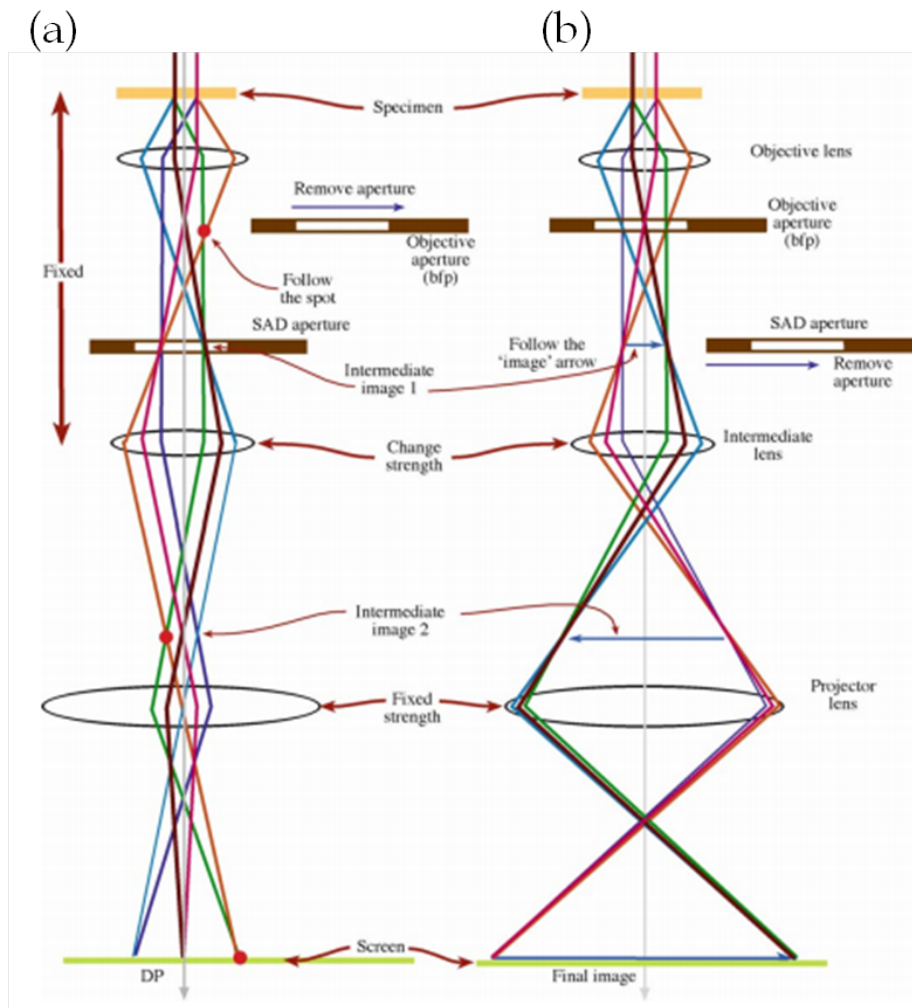


Figure 2.2: Basic operating modes in TEM (a) diffraction mode and (b) image mode. [169]

2.4.1 Bright-field (BF) and dark-field(DF) imaging

BF and DF imaging are the two most basic imaging modes in TEM. In bright-field TEM, the transmitted electron beam is used to produce the image. The dark/bright contrast in the image is due to the high mass density or the crystalline structure of the feature, compared to its surroundings.

When the selected area diffraction pattern (SADP) is projected onto the screen, it has a bright central spot from the direct beam of electrons. This is surrounded by the scattered electrons, the distribution of which depends on the nature of the specimen. If we block the direct beam using an aperture and create the image using only the scattered electrons, a DF image shall be obtained which is the inverse of the BF image. DF images have high contrast and low noise level than BF images.

2.4.2 Phase-contrast imaging

The phase of the incident electron beam changes when it gets diffracted by atoms. The amount of phase change depends on the type of atom diffracting the beam. Thus there is a diffraction contrast in addition to the amplitude/mass thickness contrasts. Phase contrast imaging is the highest resolution imaging, with a resolution up to 1 Å, enabling us to see the atomic columns in a crystalline material.

The phase contrast image, also known as high resolution transmission electron microscopic (HRTEM) image and the atoms in the material do not have a one-to-one correspondence. They are related in such a way that the Fourier transform of the image is the product of fourier transform of point spread function, $h(x,y)$ and specimen function, $f(x,y)$ [169].

$$G(u) = H(u)F(u) \quad (2.44)$$

$H(u)$ is the contrast transfer function, which is the product of three terms, the aperture function $A(u)$, the envelope function $E(u)$ which is related to attenuation of wave and the aberration function $B(u)$.

$$H(u) = A(u)E(u)B(u) \quad (2.45)$$

The aperture function implies that all values of u (spatial frequencies) greater than some selected value determined by the radius of the aperture are cut-off by the objective aperture. The envelope function has the same effect and is a property of the lens itself. $B(u)$ is usually expressed as:

$$B(u) = \exp(i\chi(u)) \quad \chi = \pi\Delta f\lambda u^2 + \frac{1}{2}\pi C_s\lambda^3 u^4 \quad (2.46)$$

Now, a general model for specimen function is:

$$f(x, y) = A(x, y) \exp(-i\phi_t(x, y)) \quad (2.47)$$

where $A(x, y)$ is the amplitude and $\phi_t(x, y)$ is the phase which depends on the thickness of the specimen or the potential $V(x, y, z)$ which the electron experiences as it passes through the specimen.

$$d\phi = \sigma \int V(x, y, z) dz = \sigma V_t(x, y) \quad (2.48)$$

where σ is the interaction constant and $V_t(x, y)$ is the projected specimen potential in the z -direction. In weak-phase object approximation [170] ($V_t(x, y) \ll 1$), $f(x, y)$ is approximated as:

$$f(x, y) = 1 - i\sigma V_t(x, y) \quad (2.49)$$

A transfer function $T(u)$, which is identical to $H(u)$ is also defined:

$$T(u) = A(u)B(u) \sin \chi(u) \quad (2.50)$$

$T(u)$ versus u modified by the damping envelope (dashed line) for $\Delta f = -100$ nm and $C_s = 2.2$ nm is presented in Figure 2.3. The crossover point of $T(u)$ with the

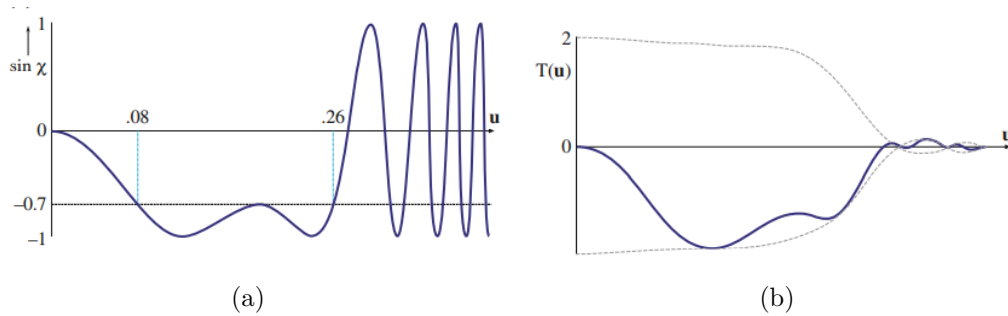


Figure 2.3: (a) $\sin \chi(u)$ versus u without damping of the higher spatial frequencies (b) $T(u)$ versus u modified by the damping envelope (dashed line); $\Delta f = -100$ nm, $C_s = 2.2$ nm. (Reproduced from [169])

zero axis is defined as the instrumental resolution limit. The information about the transfer function helps to choose the instrumental parameters for HRTEM imaging and interpret the image accurately.

2.5 Ion - implantation systems

An ion implantation system comprises of an ion accelerator with an ion source coupled to one or several beamlines. The two ion implantation systems in our centre: a 1.7 MeV Tandetron accelerator and 150 keV ion accelerator with *in situ* ionoluminescence are used for implantations relevant to this thesis.

2.5.1 1.7 MV Tandetron accelerator

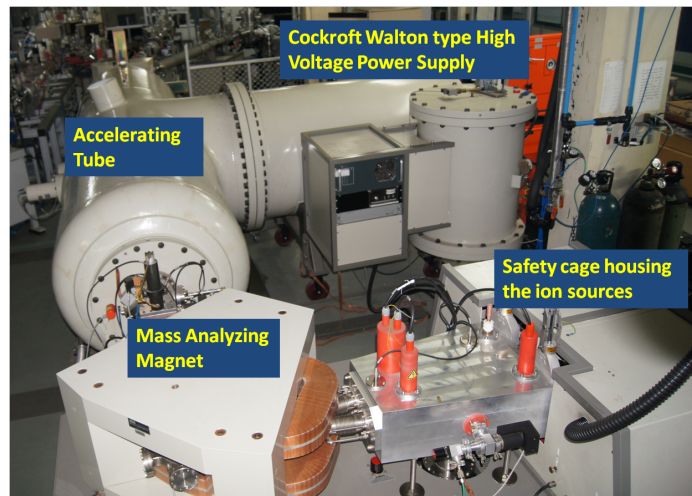
The self-ion (Fe^+) irradiations in Zr-ODS and Al-ODS were carried out using a 1.7 MV Tandetron (M/s. HVEE, Netherlands) accelerator. This accelerator is equipped with two ion sources - a duo-plasmatron source, for the production of H^+ and He^+ ions and a SNICS (Source of Negative Ions by Cesium Sputtering) source for the production of other negatively charged ions. The positive ions from the duoplasmatron source get converted into positive ions by the ion exchange reaction with Li vapor. The negative ions are injected into the accelerator column using a mass analyzing magnet with resolution $M/\Delta M \sim 190$ [171].

The high voltage terminal, located at the middle of the stripper canal has superior energy stability of ~ 250 eV. When a high voltage (V_T) is applied at the terminal, the negative ions get accelerated towards it. At the high voltage terminal, negative ions are converted into positive ions by passing through a stripper gas (N_2). The positive ions get further accelerated to the end of the canal. A high energy switching magnet is used to separate different charge states. The final energy of the ions is:

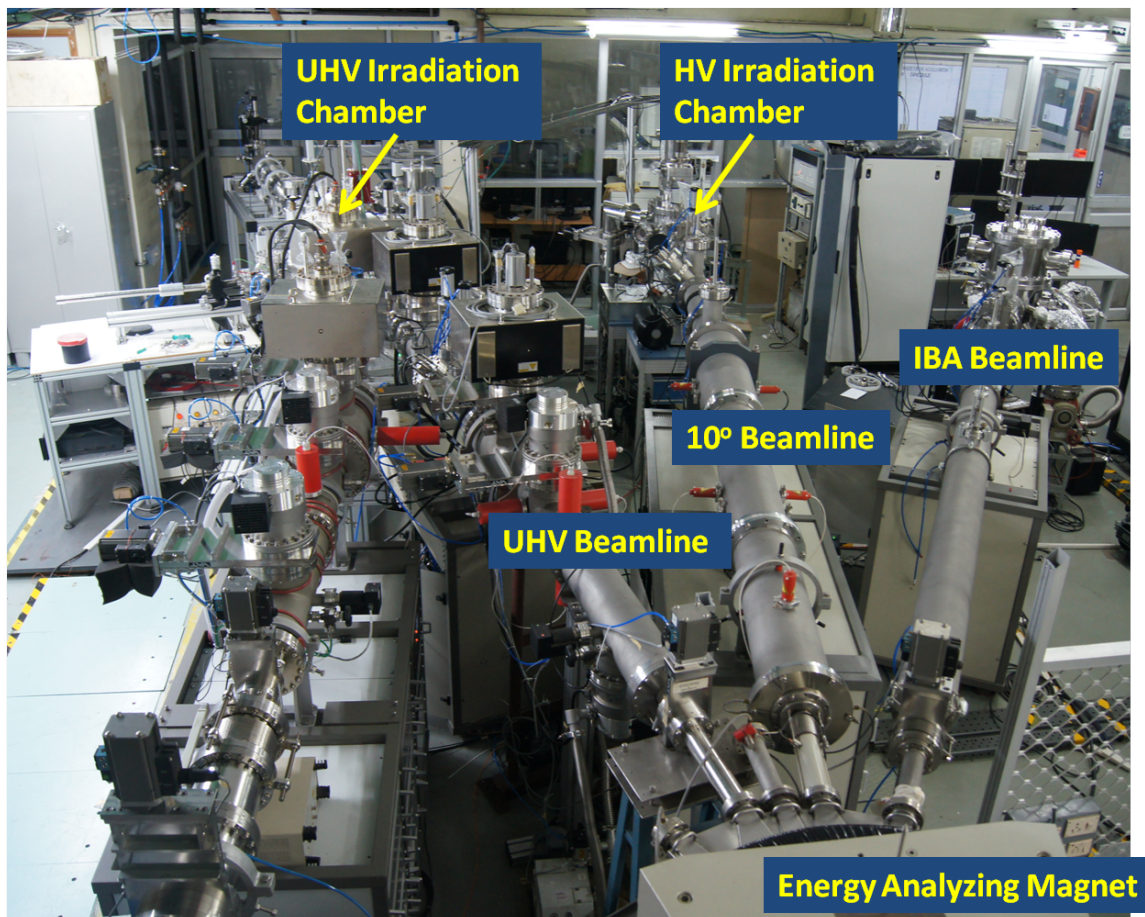
$$E = E_i + (q + 1)eV_T \quad (2.51)$$

Here, E_i is the acceleration from the source side and q is the charge state of the positive ion.

Three beamlines are connected to the energy analyzing magnet, as shown in Figure 2.4(b). The room temperature irradiations are carried out in the implantation chamber which is kept at a vacuum of $\sim 10^{-8}$ mbar. The high-temperature irradiation is carried out in the UHV chamber at a vacuum of $\sim 10^{-9}$ mbar.



(a)



(b)

Figure 2.4: (a) Photograph of 1.7 MV accelerator (b) The beamlines connected to the analyzing magnet of the accelerator, reproduced from [171]

2.5.2 150 kV accelerator and *in situ* ionoluminescence

The 150 kV accelerator in which the *in situ* ionoluminescence is incorporated, has a radio frequency (RF) plasma source, which generates gaseous ions. A photograph and schematic of the accelerator is shown in Figure 2.5. The He or H gas is filled in a bottle at ~ 2 mbar and the bottle is fed into a quartz tube maintained at a vacuum of $\sim 10^{-4}$ mbar and an RF potential of 100 MHz frequency at a power of 100W, is applied to generate the plasma. The ions in the plasma are extracted and then they are accelerated by a high voltage, which can be varied from 30 kV to 150 kV. The accelerated ions are then mass analyzed using a 45° magnet and focused onto the beam line. The beamline of the accelerator is maintained at a vacuum of $\sim 10^{-6}$ mbar. The sample is attached to an electrically isolated copper block. The suppressor with a voltage of -40V helps to extract secondary electrons produced during irradiation. The beam current is maintained at $1 \mu\text{A}$ with the help of a current integrator. More details about the 150 kV accelerator at IGCAR, Kalpakkam can be found in the references [172, 173].

Ionoluminescence(IL) spectroscopy

Ionoluminescence(IL), also known as Ion Beam Induced Luminescence(IBIL) is a luminescence phenomenon originating from the interaction of energetic ions with solid matter. For excitation by energetic particles, the processes leading to luminescence take place in three steps. At first, an excitation volume is formed. In this phase, the energy of the implanted ion gets transferred to excitation volume by electronic or nuclear stopping processes. Ionization takes place in the excitation volume. Recombination of the electrons and the excited ions allows the crystal lattice to absorb the energy released, and the optical system becomes highly excited. The second stage involves the de-excitation of the states of high excitation through radiation-less transitions. The third stage, luminescence emission, occurs when the atoms de-excite from a low excitation state to the ground level.

A set of collimating lenses are connected to the optically isolated irradiation chamber of 150 kV accelerator. These lenses collect the luminescence signals from the sample during irradiation. This lens assembly is connected to the FLS 980 UV-Vis absorption spectrometer using OFC bundles. A schematic of this arrangement in the

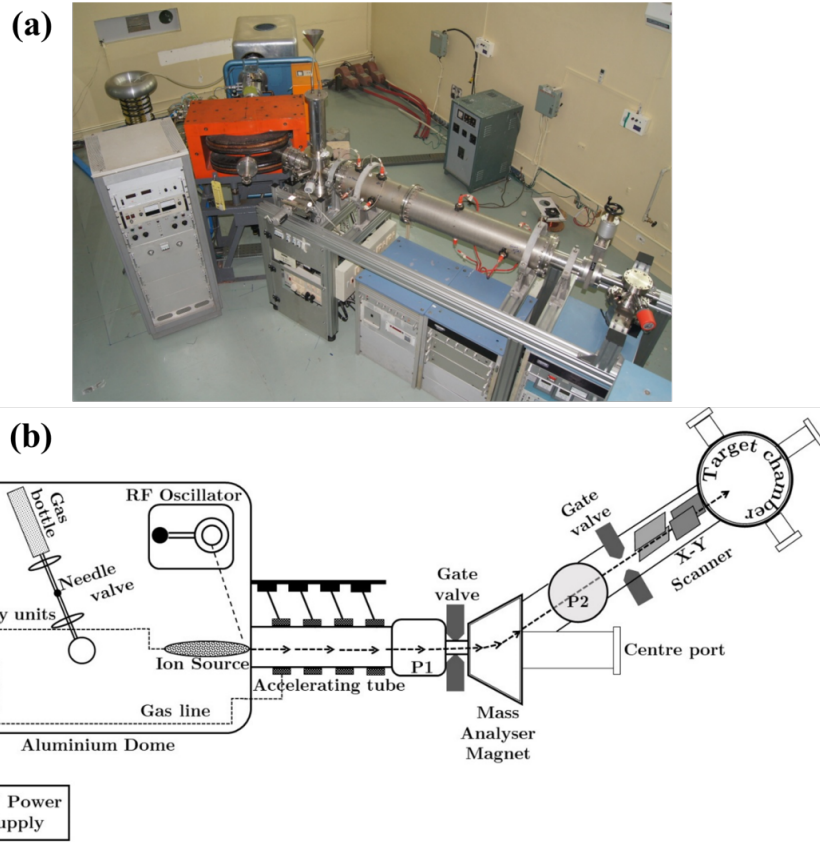


Figure 2.5: (a) Photograph and (b) Schematic diagram of 150 kV accelerator

irradiation chamber and a photograph of FLS 980 spectrometer can be seen in Figure 2.6. Details of the experimental set up is reported in [134]

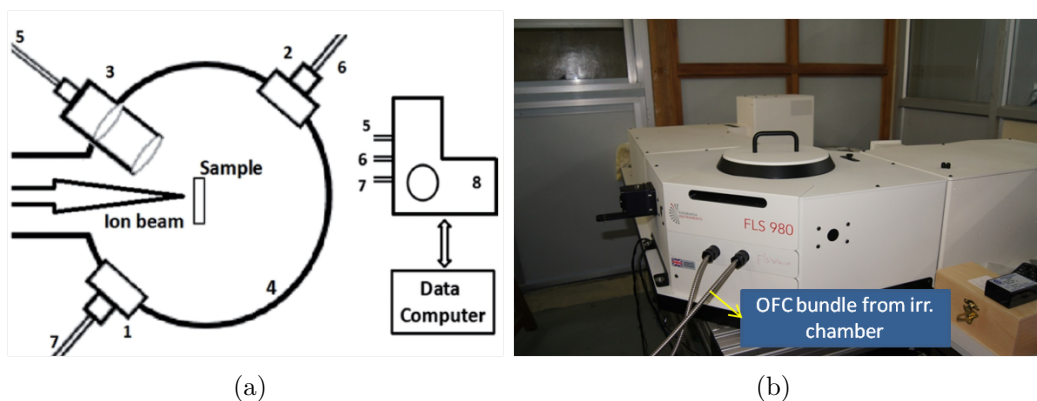


Figure 2.6: (a) Schematic of the coupling of spectrometer with the accelerator for IL spectroscopy (Legends: 1, 2: optical absorption ports; 3: coupler optics for IL measurements; 4: vacuum chamber; 5-7: optical fiber assemblies; 8: spectrometer) (b) Photograph of FLS 980 UV-Vis absorption spectrometer.

2.6 Positron annihilation spectroscopy

Positron annihilation spectroscopy is a non-destructive technique for the characterization of open volume defects. It uses positrons, which are anti-particles of electrons, generated by a ^{22}Na source. These positrons annihilate with electrons in the material. The lifetime of the positron is a strong function of electron density at the annihilation site [174].

Positrons are sensitive to open volume defects like vacancies, vacancy clusters and dislocations due to the absence of nuclei in such sites. The sensitivity of positron annihilation spectroscopy to detect vacancy defect is 1 in 10^7 atoms. When a positron annihilates with an electron, it results in energy equivalent to their combined mass, i.e., 1.002 MeV. Since the total energy of the system needs to be conserved, electron-positron annihilation produces two photons of energy 511 keV each, emitted at an angle of 180° . The rate of the annihilation of the positron in a material is proportional to the local electron density at the annihilation site of the material.

2.6.1 Positron lifetime spectroscopy

The lifetime of a free positron in metals is $\sim 100 - 200$ ps and in ionic solids, it is $100 - 400$ ps. In a metal containing defects, the annihilation of positrons in the defects cause an increased lifetime.

In positron lifetime spectroscopy measurements, the source, usually $10 \mu\text{Ci}$ of ^{22}Na deposited in a thin Ni foil, is sandwiched between two identical samples. The time delay between the 1.28 MeV birth γ ray, simultaneously emitted from the source along with positron and one of the 511 keV γ rays resulting from the positron – electron annihilation process is measured. A typical experimental lifetime spectrum will have an exponential tail, convoluted with the instrument's time resolution function. Complete deconvolution analysis of positron annihilation spectra (using the LT09 program) gives the positron lifetime or lifetimes and relative intensities in which distinguishable positron states occur. It is done by fitting the positron lifetime spectrum with a sum of decaying exponential functions.

$$F(t) = \sum_{i=1}^k \frac{I_i}{\tau_i} e^{-\frac{t}{\tau_i}} \quad (2.52)$$

Where $F(t)$ is the count at time t , k is the number of exponential decays, I_i and τ_i are the intensity and lifetime of the i th component.

2.6.2 Doppler broadening spectroscopy

The two gamma rays originating from positron-electron annihilation have an energy increment ΔE ($E=511 \text{ keV} \pm \Delta E$) and an angular deviation $\theta(180 \pm \theta)$. These values correspond to the momentum of electrons, either core or valance, in the region of annihilation. Therefore, the angular correlation curve ($N(\theta)$ vs. θ) and Doppler broadening curve ($P(\Delta E)$ vs. ΔE), both peak sharply for materials containing defects compared to defect-free materials. In a typical Doppler broadening spectrum, a variety of line-shape parameters can be identified and their ratios can yield defect-specific information.

2.6.3 Variable energy slow positron Doppler broadening spectroscopy

Variable energy slow positron Doppler broadening studies are used to study the depth-dependent distribution of open volume defects in a material. A schematic diagram of the method is given in Figure 2.8. The positron beam is produced by a ^{22}Na source of strength 50 mCi. A W(100) thin film moderator of thickness 100 μm slows down the positrons, which are then transported using a solenoid magnetic field of strength 70 Gauss. The slow positrons are extracted using a U-shaped solenoid bend. The energy of extracted positrons is varied by applying sufficient negative voltage (0.2-22 kV) to the sample. The measurements are carried out using a high purity Ge detector having energy resolution 1.4 keV at 662 keV gamma line of ^{137}Cs . The beam automation is done using a Programmable System on Chip (PSoC) along with LabVIEW program [175]. The implanted positrons follow the Makhovian profile inside the sample.

$$P(z, E) = \frac{mz^{m-1}}{z_0^m} e^{-\left(\frac{z}{z_0}\right)^m}; \quad z_0 = \frac{\langle z \rangle}{\Gamma\left(1 + \frac{1}{m}\right)} \quad (2.53)$$

Where z is the positron penetration depth, E is the positron energy, m is a material dependent empirical parameter, $\langle z \rangle$ is the mean implantation depth and Γ is the

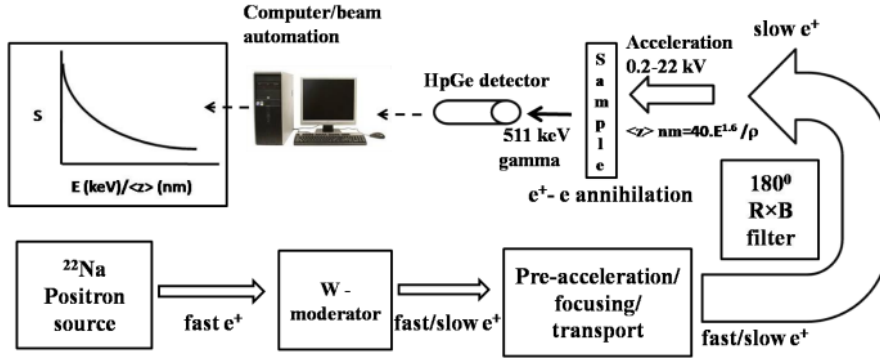


Figure 2.7: A schematic diagram of variable energy slow positron beam spectroscopy [176]

gamma function. Mean implantation depth $\langle z \rangle$ is calculated as:

$$\langle z \rangle = \frac{40E^{1.6}}{\rho} nm \quad (2.54)$$

where ρ is the density of the material in g/cm^3 . Due to the spread in implantation profile at higher incident positron energies, the resolution is better at lower energies. The spectrum is characterized by two parameters, S – parameter and W – parameter. The S – parameter is the ratio of counts in the central energy region (511 ± 1 keV) to the total counts under the peak (511 ± 10 keV). It is closely related to the concentration of defects in the material. W – parameter is defined as the ratio of the wing area ($506 - 508$ keV and $514 - 516$ keV) to the total area under the spectrum (511 ± 10 keV). It is related to the annihilation of the positrons with high momentum electrons and gives information about the chemical environment of the defect. The simultaneous analysis of the S and W parameters (S – W correlation) as a trajectory in the S – W plane using implantation energy as the running parameter gives direct information about the number of trapping layers and their nature in the material.

By assuming a two-state (bulk and defect states) trapping model, the S and W-parameters can be written as:

$$\begin{aligned} S - S_b &= \eta_d(S_d - S_b) \\ W - W_b &= \eta_d(W_d - W_b) \end{aligned} \quad (2.55)$$

Where, η_d is the fraction of positrons trapped at the defect state, S_b , S_d and W_b , W_d

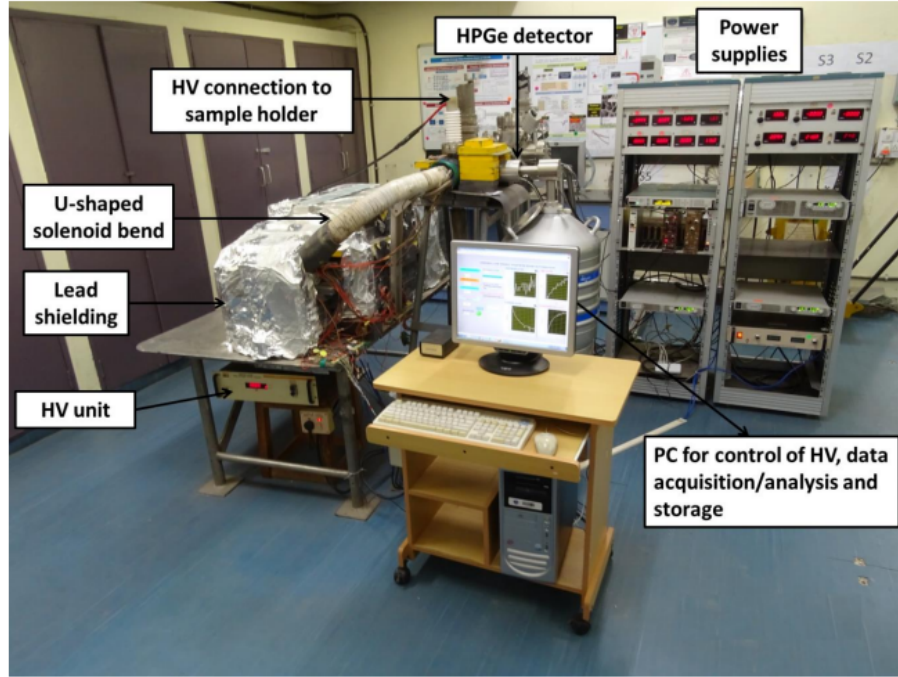


Figure 2.8: Photograph of the variable low-energy positron beam based Doppler broadening spectroscopic instrument in IGCAR, Kalpakkam [175, 176]

are the S and W -parameters of the bulk and defect state. Thus:

$$\frac{S - S_b}{W - W_b} = \frac{S_d - S_b}{W_d - W_b} \quad (2.56)$$

The Eq. 2.56 is independent of η_d , the concentration of defects. All the (W, S) coordinates lying on the line connecting (S_d, W_d) and (S_b, W_b) have same nature.

2.7 X-ray diffraction

X-ray crystallography is a fundamental technique used to obtain the structures, phases, crystal orientations, grain size, etc. of a material. Each atom acts as a diffraction center for the x-rays and thus the entire crystal acts similar to a diffraction grating [177]. The XRD pattern obtained is explained using Bragg's law:

$$n\lambda = 2d \sin \theta \quad (2.57)$$

where n is the order of diffraction, λ the wavelength of x-rays, d is the inter-planar spacing of the crystal and 2θ is the collection angle. The XRD measurements of this thesis are done using INEL Equinox 3000 XRD system, which is shown in Figure 2.9. This was operated in powder mode.

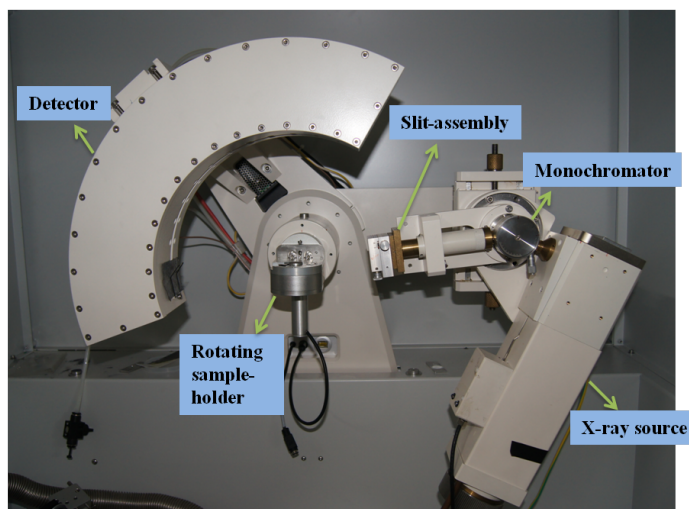


Figure 2.9: A photograph of INEL Equinox3000 XRD system

2.8 Raman spectroscopy

Raman spectra of this thesis are obtained by WITec RA 300 confocal Raman imaging system. It can produce laser beams of two wavelengths: 532 nm and 355 nm. The laser produced goes through a filter, a dichroic beam splitter and gets focused by an objective lens onto the sample. The scattered spectrum is recorded using a CCD camera, after filtering the excitation wavelength using a laser line filter. The WITec RA 300 can also be used for photoluminescence experiments [173].

Ab initio simulations of nanocluster formation in ODS steels containing Zr and Al

3.1 Introduction

The constituent elements of the dispersoids in a typical ODS alloy containing Fe-(0.2-0.5)wt% Y_2O_3 -(0.1-0.4)wt% Ti-(9-19)wt% Cr are Y, Ti and O, along with some vacancies incorporated during the ball-milling process [3]. As already discussed in Section 1.3.2, the density functional theory calculations on the formation and binding energies of these constituents in the Fe matrix can be used to forecast the chemistry of dispersoids in ODS alloys. Murali *et al.* [71] have compared the binding energies of atomic-clusters with compositions Y-Ti-O-vacancy and Y-Zr-O-vacancy in Fe matrix and found that the Zr-containing clusters are more probable to nucleate than Ti-containing clusters in bcc Fe-matrix.

Moving on to Al-containing ODS alloys, when Al is added into the Ti-containing ODS alloys, the chemistry of the dispersoids changed from Y-Ti-O to Y-Al-O and the coarser Y-Al-O precipitates are undesirable due to their detrimental role in reducing the ultimate tensile strength of the alloy [50]. Though Zr is often suggested as a potential substitution to Ti in Al-containing alloy to refine the precipitate size, a detailed first-principle study comparing the energetics of Y-Al-O and Y-Zr-O clusters

in Fe is absent, which is crucial in the development of ODS steels containing Zr and Al.

In this chapter the role of Zr in Al-containing ODS alloys is evaluated by comparing the binding energies of Y–Al–O–vacancy and Y–Zr–O–vacancy atom-clusters in Fe matrix using density functional theory. The binding energies of Zr and Al in Fe matrix in several configurations with oxygen, vacancy, oxygen–vacancy and yttrium–oxygen–vacancy are evaluated. The basic interactions involved in cluster formation are discussed using charge density difference plots. The binding energies of clusters are used to predict the feasibility of Y-Zr-O and Y-Al-O nanoclusters in the Fe matrix. Further formation energy calculations are carried out for different fluorite-related Y-Zr-O structures, to find the most energetically favored Y-Zr-O phase.

3.2 Details of Calculation

The calculations are done using Vienna *ab initio* simulation package (VASP) [161,162] within the density functional theory. All the calculations are done with pseudopotentials generated with the projected augmented wave approach (PAW) [161]. For exchange-correlation functional, the generalized gradient approximation as parameterized by Perdew, Burke and Ernzerhof (PBE) is used [147]. Plane wave cut-off energy and k-point sampling are determined using the convergence tests.

3.2.1 Planewave cut-off energy and K-point sampling

The accuracy of DFT calculations depends on the value of planewave cut-off energy (E_{cut}) and the k-grid used. Therefore, it is advisable to check the sensitivity of physical properties with respect to the size of the basis set and the k-point sampling used. The variation of energy with E_{cut} and k-grid are shown in Figures.3.1(a) and (b) respectively. It can be seen from the plot in Figure 3.1(a), that to achieve an energy convergence of 0.01 meV/atom, the magnitude of the E_{cut} should be at least 300 eV for bcc Fe. In our calculations, cut-off energy of 500 eV is used.

For k-point sampling, Monkhorst pack [178] is used. Usage of special point schemes introduces an approximation in the DFT calculations. Hence it is important to check the convergence of physical properties with respect to the k-grid. As seen in the

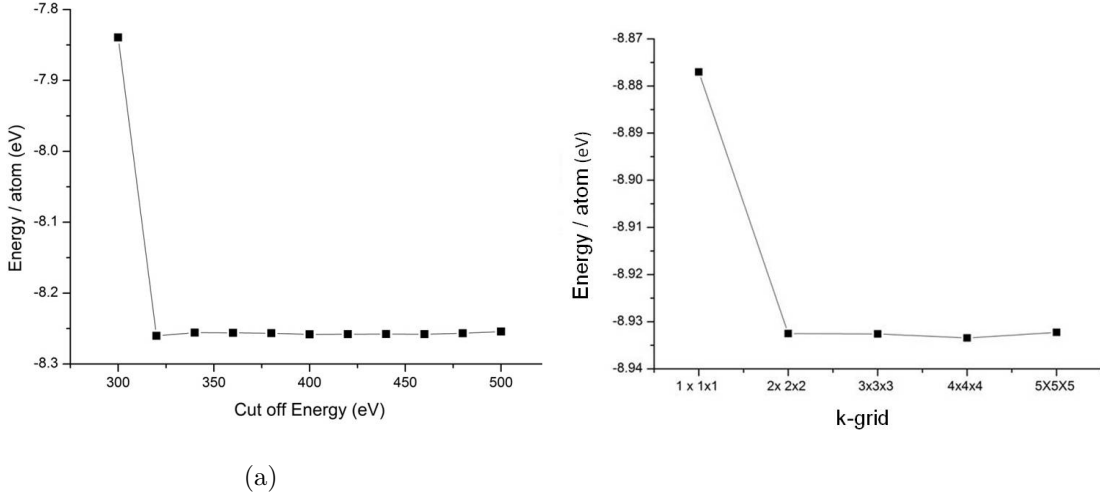


Figure 3.1: Total energy of a bcc Fe unitcell as function of (a) E_{cut} (b) k-grid size

Figure 3.1(b), the difference in total energy between $2 \times 2 \times 2$ and $3 \times 3 \times 3$ K points is 0.01 meV/atom, which is our intended accuracy. Therefore, the k-point mesh is fixed to be $3 \times 3 \times 3$.

3.2.2 Equilibrium lattice parameter

To check whether the pseudopotential, energy cut-off and k point sampling values are optimum, equilibrium lattice parameter values can be calculated and compared with the experimental value. The total energy for Fe is calculated with 10 different values of lattice parameters using cut-off energy 500 eV and k grid size 17^3 . The equilibrium lattice parameter can be found by fitting the data into Murnaghan equation of state [179] representing the relaxation between energy E and volume V :

$$E(V) = \frac{B_0 V}{B'_0} \left[\left(\frac{V_0}{V} \right)^{B'_0} \frac{1}{B'_0 - 1} + 1 \right] + C_0 \quad (3.1)$$

The calculated lattice constant of bcc Fe is 2.82 Å and it is in agreement with the experimental value (2.86 Å) [180].

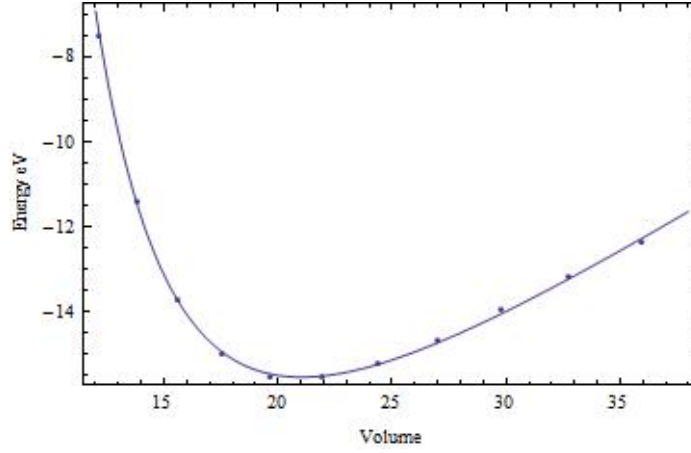


Figure 3.2: Total energy of a unitcell of bcc Fe as a function of volume of the cell

3.2.3 Formation energy and binding energy

The formation energy or mixing energy of a substitutional impurity X in bcc iron supercell of size N atoms is [181]:

$$E_X(Fe) = [E(N-1)Fe + 1X] - (N-1)E(Fe) - E_{ref}(X) \quad (3.2)$$

And if X is an interstitial impurity :

$$E_X(Fe) = E(N.Fe + 1X) - N.E(Fe) - E_{ref}(X) \quad (3.3)$$

where $E_{ref}(X)$ is the reference energy calculated with respect to equilibrium phases. (fcc for Al, hcp for Y and Zr). The $E_{ref}(X)$ of oxygen is calculated with respect to FeO as it forms stable equilibrium compound for the Fe–O system. If formation energy is positive, the process is endothermic and if it is negative, the process is exothermic. Elements with high positive formation energy are expected to have low solubility in the Fe matrix.

Similarly, the binding energy between substitutional impurities X and Y in Fe matrix is [181]:

$$E_{X,Y}(Fe) = E[(N-2)Fe + 1X + 1Y] + E(N.Fe) - E[(N-1)Fe + 1X] - [E((N-1)Fe + 1Y)] \quad (3.4)$$

For an interstitial impurity X and substitutional impurity Y :

$$E_{X,Y}(Fe) = E[(N-1)Fe + 1X + 1Y] + E(N.Fe) - E(N.Fe + 1X) - E[(N-1)Fe + 1Y] \quad (3.5)$$

In both Eq.3.4 and Eq.3.5 if X and Y attract, binding energy will be negative and if they repel, binding energy will be positive.

Differential charge density plots of defect species in Fe matrix are plotted. Differential charge density for a system AB is:

$$\Delta\rho = \rho_{AB} - \rho_A - \rho_B \quad (3.6)$$

where, ρ_{AB} is the electronic charge density of combined system, ρ_A and ρ_B being that of individual systems. In the contour plots, the minimum value of charge density is -0.006 e/Bohr^3 and the maximum value is $+0.006 \text{ e/Bohr}^3$ with an interval 0.001 e/Bohr^3 . The contour lines are plotted in a linear way such that the numerical value of Nth contour line is :

$$F(N) = Min + N \times Interval \quad (3.7)$$

where *Min* is the minimum value. The dashed line indicates negative contours and solid lines indicate positive contours. The higher the density of lines, the change is drastic. Positive contours increase from periphery to center starting from zero to maximum by the interval mentioned. Similar way negative contours decrease from zero to the minimum on moving towards the center.

3.3 Binding energies of Zr and Al containing clusters in bcc Fe matrix

3.3.1 Formation energies and bonding-nature of solute atoms

Formation energies are calculated for solute atoms in tetrahedral, octahedral and substitutional interstitial sites of bcc Fe supercell. It is observed that oxygen prefers

the octahedral interstitial site in Fe matrix while Y, Al and Zr prefer substitutional position. The calculated formation energies for Y, Zr, Al, O and vacancy in defect-free Fe matrix and the existing literature data on the same are tabulated in the Table 3.1. The formation energy of Al in the octahedral site, tetrahedral site and substitutional sites are +5.10 eV, +1.22 eV and -0.74 eV, respectively. So, Al prefers substitution position in the iron matrix.

Formation energies also give insight into the solubilities of elements in the matrix. In the bcc Fe matrix, up to 45 at% of Al can be dissolved depending on the temperature [182]. The solubility of Zr is limited to less than 0.16 at% [183, 184], and for Y, it is less than 1 at% [184]. The reported solubilities of oxygen in Fe have considerable discrepancies because of the strong influence of impurities like Si and Al on the solubility [185]. The purer the iron sample used, the lower the solubility of oxygen. The tentative solubility as per reference [186] is 2.4×10^3 at%. So, more positive formation energy corresponds to less solubility and vice-versa. Although all these elements have limited solubility in Fe matrix, the process of high energy milling helps in achieving high solubility, for instance, ~ 0.13 at% of oxygen is found in as milled ODS powders [47].

The difference in charge density when Al, Zr, Y and O are introduced into Fe matrix is plotted in Figure 3.3. (a), (b), (c) and (d) respectively. The 2D slice shown is $(1\bar{1}0)$ plane of 128 atom bcc Fe supercell. Four first nearest neighbors and two second nearest neighbors of impurity atom are seen in the slice. In the case of Al, Y and Zr, there is a charge accumulation in the bonding region as well as in the antibonding region. The accumulation of charge in an antibonding region is less compared to that in the bonding region. The charge is depleted from the immediate neighborhood of nuclei in a direction perpendicular to the bond direction forming a doughnut-shaped structure encircling the bond axis, which is the characteristic of covalent bonding [190]. The charge increment in the bonding region, responsible for the binding of nuclei is shared by both the nuclei and hence the interaction is covalent in nature. However, the Fe–O interaction, when oxygen is in an octahedral void of Fe lattice, is ionic in nature (*refer* Figure 3.3(d)). If we assume that Fe–O bond is ionic, Fe and O exist as Fe^+ and O^- ions and then the condition for a bond to be stable is that the force on both nuclei should be zero. The localized charge distribution should be polarized in a direction opposite to charge transfer. The same is observed in charge density

Table 3.1: Formation energies of Zr, Y, Al, and O in the bcc Fe matrix. The more positive formation energy corresponds to less solubility and vice-versa. Aluminum is the most soluble element in Fe matrix, followed by Zr, Y and then O. The data available in the literature is given in parentheses. ^a - Murali *et al.* [71], ^b - Jiang *et al.* [69], ^c - Claisse *et al.* [72], ^d - Posselt *et al.* [187], ^e - Kim *et al.* [188], ^f - Olsson *et al.* [189].

Element	Formation Energy (eV)		
	Substitutional	Octahedral	Tetrahedral
Zr	+0.26 (+0.42 ^a)	+6.81	+6.09
Y	+1.82(+1.86 ^a , +2.02 ^b , +2.12 ^c)	+4.42	+7.55
Al	-0.74 (-0.79 ^a)	+5.10	+1.22
O	+2.73	+1.33(+1.35 ^a , +1.45 ^d , +1.41 ^b)	+1.56
Vacancy	+2.11(+1.4±0.1 ^e , +2.13 ^b , +2.15 ^f)		

difference plot, (Figure 3.3.(d)).

Table 3.2: Nearest neighbor distances in Fe matrix with and without impurity atoms. (nn denotes nearest neighbor).

	Pure Fe(Å)	With Zr atom(Å)	With Al atom(Å)	With Y atom(Å)
1nn	2.45	2.54	2.49	2.58
2nn	2.81	2.83	2.78	2.84
3nn	3.97	4.02	4.00	4.03

The nearest neighbor distance table (Table 3.2) gives an idea about the strain introduced in the neighboring Fe atoms upon introduction of the impurity atom. There are 8 first nearest neighbors, 6 second nearest neighbors and 12 third nearest neighbors for an atom in bcc lattice. Yttrium and zirconium induce larger distortion than Al. After 2nn, the effect is negligible in all these cases.

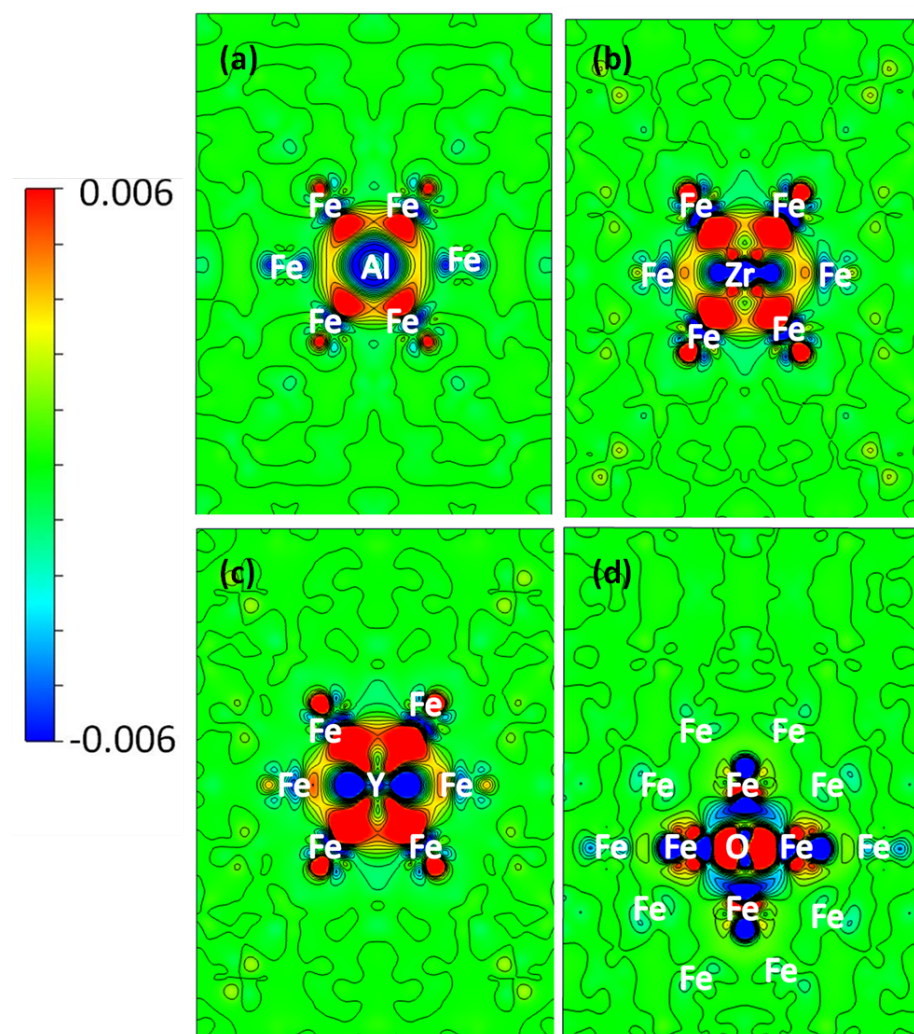


Figure 3.3: The differential charge density plot of Al, Zr, Y and O in Fe matrix in $(1\bar{1}0)$ plane of 128 atom bcc Fe supercell. Blue colour is -0.006 e/Bohr³ and red is $+0.006$ e/Bohr³. Al, Y and Zr are in substitutional position while oxygen is in octahedral interstitial site. Al, Y and Zr bind covalently with surrounding Fe atoms. Oxygen – Fe binding is ionic in nature which is evident from the polarization of Fe-O bond.

3.3.2 Solute–solute interaction

Now, if we put two similar impurity atoms in the iron matrix in the first nearest neighbor positions, the interactions are repulsive irrespective of the species considered. The binding energy values are tabulated in Table 3.3. As per literature, at the ends of the periods in the periodic table, the solute-solute binding energies in Fe are strong. But in the middle of the period, they are weakly bound [191]. The same trend is

observed here. Since the interactions are repulsive, the chances of phase separation are less. It also implies that it is unlikely that two metallic atoms will come close together in a nanocluster in the absence of oxygen or vacancy.

Table 3.3: Binding energies of two metallic atoms in Fe matrix at first and second nearest neighbor (nn) positions. (^a - Jiang *et al.* [69], ^b - Murali *et al.* [71], ^c - Posselt *et al.* [187])

Defect Species	Binding Energy (eV)	
	1nn	2nn
Zr -Zr	0.12	-0.11
Y-Y	0.18 (0.19 ^c , 0.20 ^a)	-0.06 (-0.01 ^c , 0 ^a)
Al-Al	0.12	-0.03
Zr-Y	0.16 (0.12 ^b)	-0.04
Zr-Al	0.15	-0.02
Y-Al	0.26	0.11

3.3.3 Solute–vacancy interactions and its dependence on the size of the solute atom

Vacancies are considered to be a constituent element of dispersoids in ODS steels [68, 72, 74]. Therefore, it is essential to evaluate the nature of solute vacancy interaction. Moreover, vacancy–solute binding is crucial in determining the diffusion kinetics of impurity in a matrix [192].

The solute which is least bound with the Fe matrix, the one with the largest positive formation energy, is expected to bind the most with the vacancy(□). This is due to the size effect of the solute atom. The tendency to relax towards a vacancy increase with an increase in the size of the solute atom. This expected trend is followed for Zr, Al and Y in Fe matrix, Y–□ binding being the strongest (-1.20 eV) followed by Zr–□ binding (-0.73) and Al–□ binding energy (-0.30) being the least (Table 3.5). However, oxygen binds more with vacancy than all the above owing to its magnetic nature. The magnetism of the host lattice causes confinement of O charge in the interstitial region. The presence of vacancy reduces the charge confinement by creating a new volume for charge delocalization [68].

Both yttrium and zirconium interact repulsively with Fe atoms and their size is bigger than Fe. Such a large impurity introduces strain in the matrix. The vacancies near such atoms will provide an option for them to move further away from the Fe atom relieving the strain. However, a vacancy next to a well-bound Al–Fe pair is unfavorable since the Al atom is small and interaction with vacancy requires breaking a strong Fe–Al bond. And this explains the lower vacancy binding energy of Al compared to Zr and Y.

Charge density plots for the interaction of Zr and Al with vacancy are given in Figure 3.4. It is seen that when a large atom is introduced in the matrix, the charge is redistributed in such a way that the bond with the second nearest neighbor is slightly strengthened. The calculated nearest neighbor distances indicate that Zr has moved

Table 3.4: The binding energy of Y, Al and Zr with a vacancy. (^a - Fu *et al.* [68], ^b - Posselt *et al.* [187])

Defect Species	Binding Energy (eV)	
	1nn	2nn
Y -□	-1.20(-1.45 ^b)	-0.05 (-0.26 ^b)
Al-□	-0.30	+0.05
Zr -□	-0.73	-0.06
O-□	-1.60 (-1.45 ^a)	-0.62 (-0.60 ^a)

0.31 Å towards vacancy which makes the distance to first nearest neighbor diagonally opposite to Zr atom as 2.85 Å (which was previously 2.54 Å as per Table 3.3). The distance to second nearest neighbors which was 2.83 Å has reduced to 2.60 Å and the bonds are rearranged accordingly. However, displacement of Al atom towards vacancy is only 0.10 Å. This implies that, in the case large, non magnetic solute atoms, the vacancy-solute interaction is due to strain interaction.

3.3.4 Solute–oxygen interaction

Calculated binding energies of Y, Al, Zr and vacancy with oxygen are tabulated in Table 3.5. The calculated values agree well with the available literature. There is an appreciable binding between Al and O, when they are first nearest neighbors. For Zr,

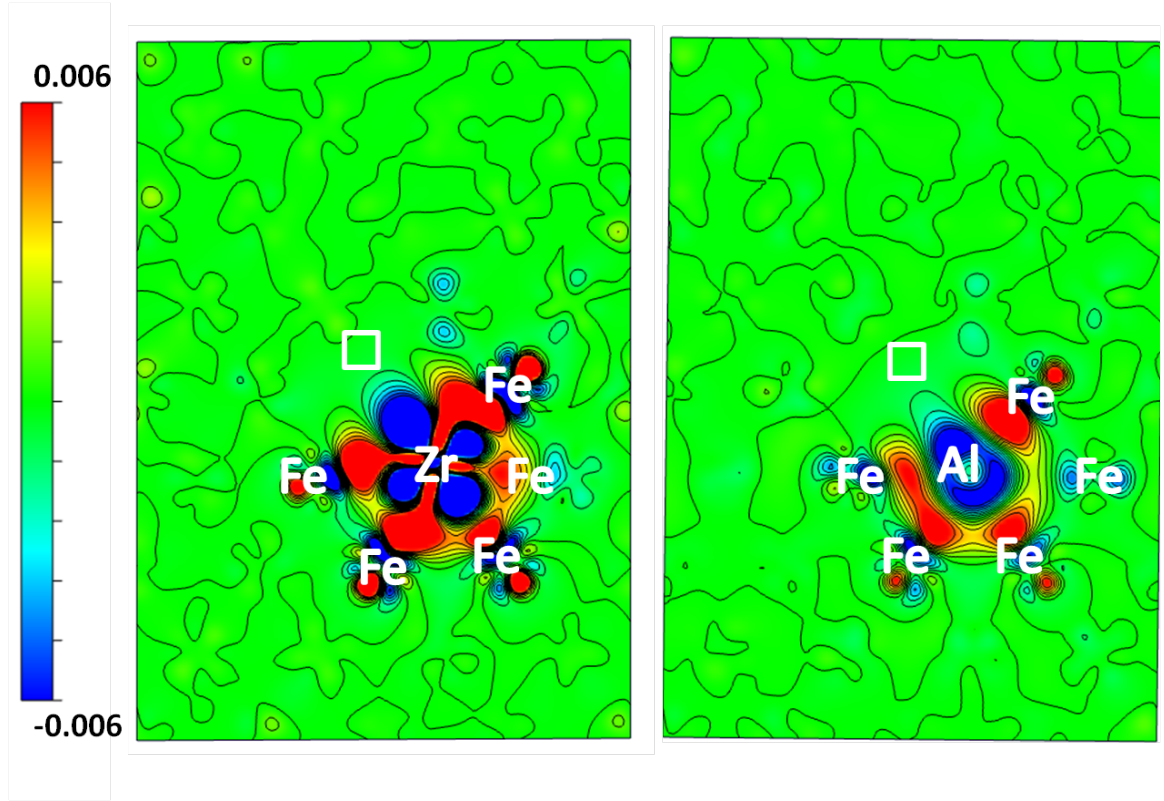


Figure 3.4: The $(\bar{1}10)$ slice of charge density difference plot of interaction of Zr and Al with a vacancy. (Vacancy is marked by a white square.)

the attraction is noticeable when they are at the second nearest neighbor position. This can be due to the larger size of Y and Zr and the resulting electron-electron repulsion between Y/Zr atom and O atom.

In free state, the bond energy of Zr–O, Al–O and Y–O is in decreasing order ($E_{Zr-O} > E_{Y-O} > E_{Al-O}$) [193]. But the calculations show that inside the Fe matrix, Y–O bond is stronger than Zr–O bond ($E_{Y-O} > E_{Zr-O} > E_{Al-O}$). In the defect-free Fe lattice, formation energies are of order $E_{Fe-Y} > E_{Fe-Zr} > E_{Fe-Al}$, which explains the anomaly. The Y atom is the least soluble (or most strained) in the Fe matrix. This resultant repulsion from the matrix makes the Y–O bonding more probable than the other two.

Figure 3.5 depicts $(02\bar{1})$ and $(\bar{1}10)$ planes of charge density difference plot of Zr–O interaction in Fe matrix. The interaction is ionic in nature. The charge is polarized towards oxygen. The polarization perturbs the Zr atom’s bonding with neighboring Fe atoms.

The charge density difference plots for Al–O interaction is given in Figure 3.6. Two

planes ($2\bar{1}0$) and ($1\bar{1}0$) are plotted for the ease of visualization. The oxygen atom is in between Al and Fe above the ($1\bar{1}0$) plane. Out of four Fe–Al covalent bonds (see Figure 3.3) otherwise present, two remain unaltered while two are broken. The ($02\bar{1}$) plane, where oxygen is in the plane, shows Fe–O and Al–O interactions, which are ionic in nature. The effect of polarization lasts till the fourth nearest-neighbor position, but the charge delocalization in atoms other than the next nearest-neighbors is less prominent compared to Zr–O interaction.

Table 3.5: Solute–oxygen binding energy in bcc Fe matrix. (^a - Jiang *et al.* [69], ^b - Murali *et al.* [71]))

Defect Species	Binding Energy (eV)	
	1nn	2nn
Y -O	+0.28 (+ 0.28 ^a , +0.35 ^b)	-0.87(-0.85 ^a , -1.01 ^b)
Al-O	-0.22	+0.08
Zr -O	+0.01	-0.74

3.3.5 Solute-oxygen-vacancy interactions

Further, oxygen and vacancy are placed next to solute atom(Al/Zr) in Fe matrix. The possible interactions are solute–oxygen, solute–vacancy and oxygen–vacancy interactions along with the interaction of matrix with solute, oxygen and vacancy. Out of five combinations possible in a bcc unitcell, which are listed in Table 3.6., one with most negative binding energy is the most stable configuration. In the table, the solute atom, the oxygen atom and the vacancy are represented by green sphere, red sphere and blue cube respectively.

From Table 3.6., the maximum binding energy for Zr–O–□ and for Al–O–□ clusters are -2.55 eV and -2.01 eV respectively. The O–□ binding is stronger than the solute–O and solute–□ binding. So the configuration in which O is nearest to the vacancy is most preferred in both Al–O–□ and Zr–O–□ clusters. However, Al–O binding is maximum when they are in 1nn position and Zr–O binding is attractive only when they are in 2nn position. So the configuration in which Zr and O are in 2nn position and Al and O in 1nn position along with minimum O–□ distance are the most stable

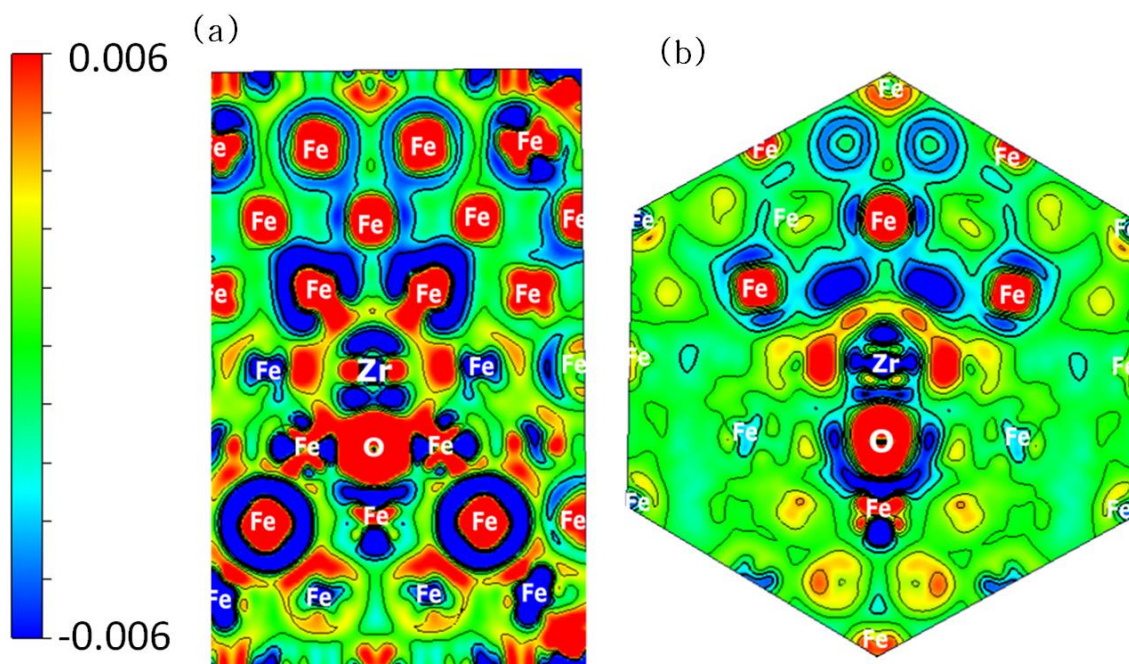


Figure 3.5: Differential charge density plot of Zr with oxygen in 128 atom Fe matrix. (a) $(02\bar{1})$ plane (b) $(1\bar{1}0)$ plane

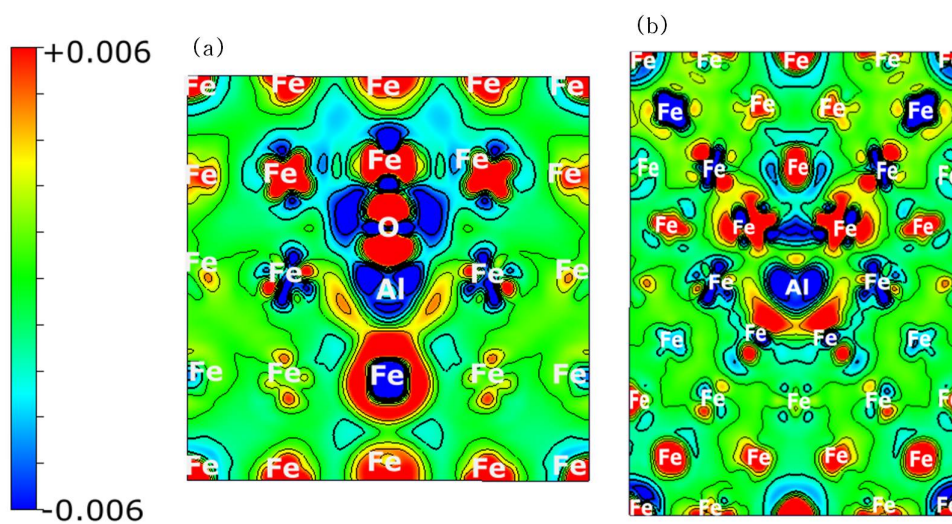
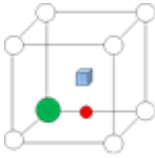
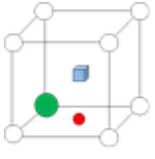
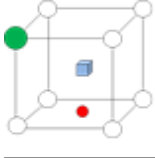
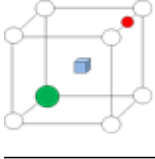
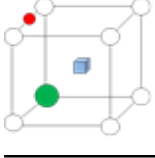


Figure 3.6: Differential charge density plot of Al with oxygen in 128 atom Fe matrix. (a) $(02\bar{1})$ plane (b) $(1\bar{1}0)$ plane

configurations. The net binding energy of Al–O–□ cluster is less than Zr–O–□ cluster because both Al–□ and Al–O binding energies are lesser than Zr–□ and Zr–O binding

Table 3.6: The solute–oxygen–vacancy binding energy in bcc Fe matrix. In the defect configurations, solute (Zr or Al) is represented by green sphere. Oxygen and vacancy are represented by red sphere and blue cube respectively.

Defect Configuration	Binding Energy (eV)	
	Zr	Al
	-0.6	-0.94
	-2.55	-1.68
	-2.30	-2.01
	-1.35	-0.90
	-1.4	-0.93

energies.

In the charge density plot of Zr–O–□ in Fe matrix (Figure 3.7), the total charge delocalization in the vicinity of Zr is less compared to that in Zr–O plot (Figure 3.5.) It is evident that the presence of vacancy helps to confine the charge delocalization caused by solute–O binding. The charge delocalization is limited within the second nearest neighbor atoms.

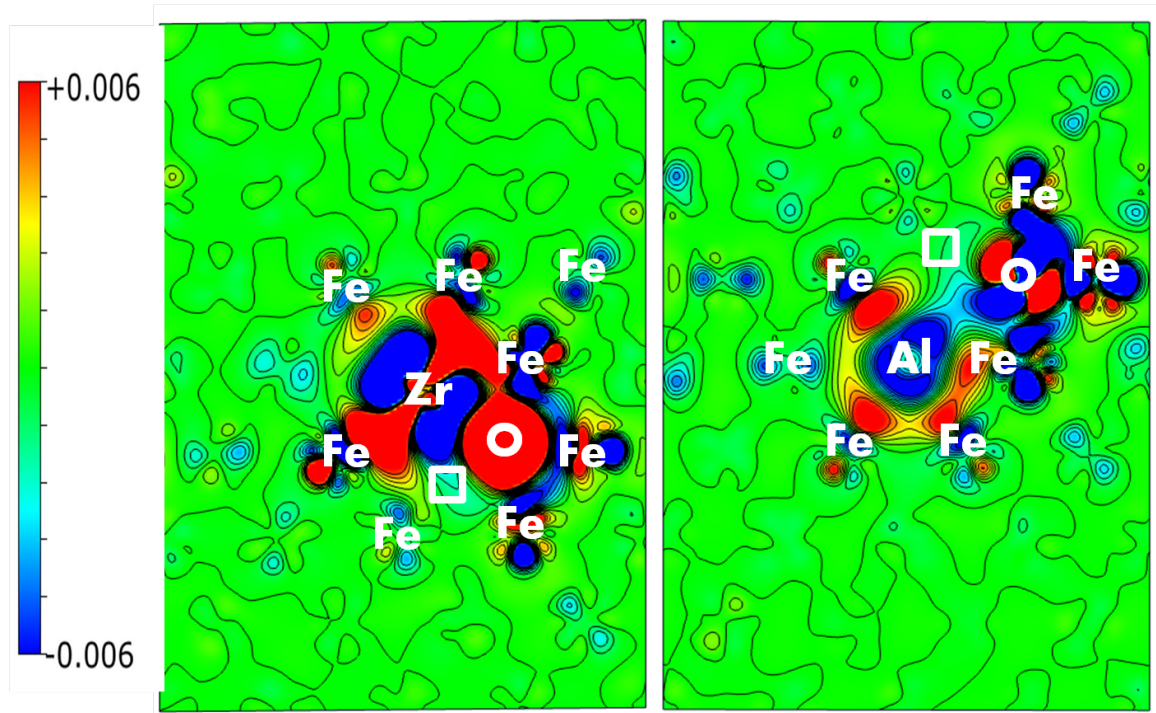


Figure 3.7: The $(1\bar{1}0)$ slice of charge density difference plot of interaction of Zr/Al with O and vacancy for the most stable configuration of Table 3.6. The vacancy is represented by a \square .

3.3.6 Effect of yttrium on solute–vacancy–oxygen interactions

Further, all the known constituents of the ODS nanocluster, yttrium, oxygen, vacancy and the solute atom are introduced in Fe matrix. First nearest neighbor pair of O and vacancy (\square) has maximum binding energy. Since the oxygen occupies interstitial position, achieving this is always possible, irrespective of other atoms present. So the clusters are chosen in such a way that O– \square remains intact at first nearest neighbor position. Such configurations with negative binding energies are listed in Table 3.7. Maximum binding energy is -3.25 eV for Y–O– \square –Al cluster and -4.16 eV for Y–O– \square –Zr cluster.

The predominant interactions present are, Y–solute, Y–O, Y– \square , solute–O, solute– \square , Y–O– \square , Y–O–solute, Y– \square –solute and solute– \square –O. The Y–solute and solute–solute interactions are repulsive. The competition with these repulsions and the remaining attractive interactions results in net binding energy. Thus the configurations in which Y and solute are in the first nearest neighbor position are the least preferred. When the repulsive species are most separated, while the distance of at least one from

vacancy and oxygen is optimum is the most preferred configuration. This is apparent from Table 3.7. Both Y–vacancy and Y–O binding energies (See Table 3.4. and 3.5) are much higher than Y–solute repulsion (Table 3.3.). Therefore Y–solute–O–□ cluster is more bound than the solute–oxygen–vacancy cluster. And it supports the experimental evidence that Y–solute–oxides are more likely to form than simple solute oxides in ODS steels.

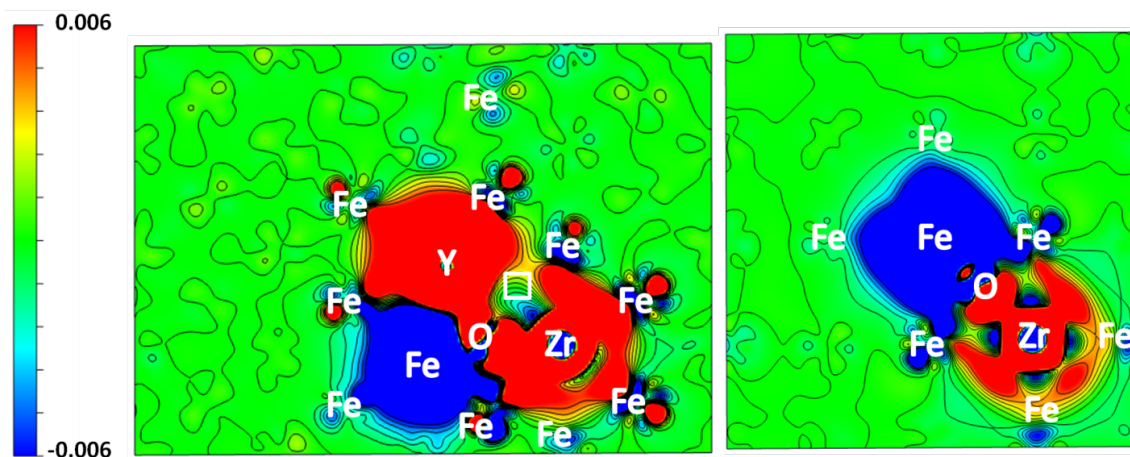


Figure 3.8: The $(1\bar{1}0)$ and $(02\bar{1})$ slices of charge density difference plot Y-Zr-□-O configuration with maximum binding energy. It can be seen that Y-O and Zr-O binding is much stronger than Fe-O binding. Also, the interaction of Fe with □ is negligible compared to the interaction of Zr and Y with vacancy.

The $(01\bar{1})$ plane of charge density plots for maximum binding energy configurations of both clusters are shown in Figure 3.8 and Figure 3.9. It contains three O–Fe, one O–solute, one Y–O ionic bonds and three solute–Fe and two Y–Fe bonds of covalent nature. The charge distortion in the matrix is minimized due to the presence of vacancy. All three metallic ions, Y, Zr and Fe bind with O atom in the matrix. Y and Zr bind strongly than Fe. Both Y and Zr relax towards the vacancy. But when Zr is replaced by Al, the Y-O and Fe-O bonds are stronger than the Al-O bond. The absence of charge distortion in neighboring Fe atoms indicates the crucial role of the vacancy in nanocluster formation. It provides volume for both charge confinement and stress relief.

Table 3.7: Binding energies of different yttrium–solute–oxygen–vacancy combinations in bcc Fe. Here, the O – vacancy positions are fixed and different configurations of Yttrium and solute around this O – vacancy pair are considered. (green circle is solute atom(Zr or Al), orange is yttrium, red is oxygen and blue cube is the vacancy.)

Defect Configuration	Binding Energy (eV)	
	Zr	Al
	-3.89	-3.03
	-3.25	-2.81
	-4.16	-3.15
	-2.86	-2.94
	-3.74	-3.25
	-3.54	-2.66
	-3.55	-2.82
	-3.57	-2.97
	-3.66	-3.01
	-3.06	-2.73

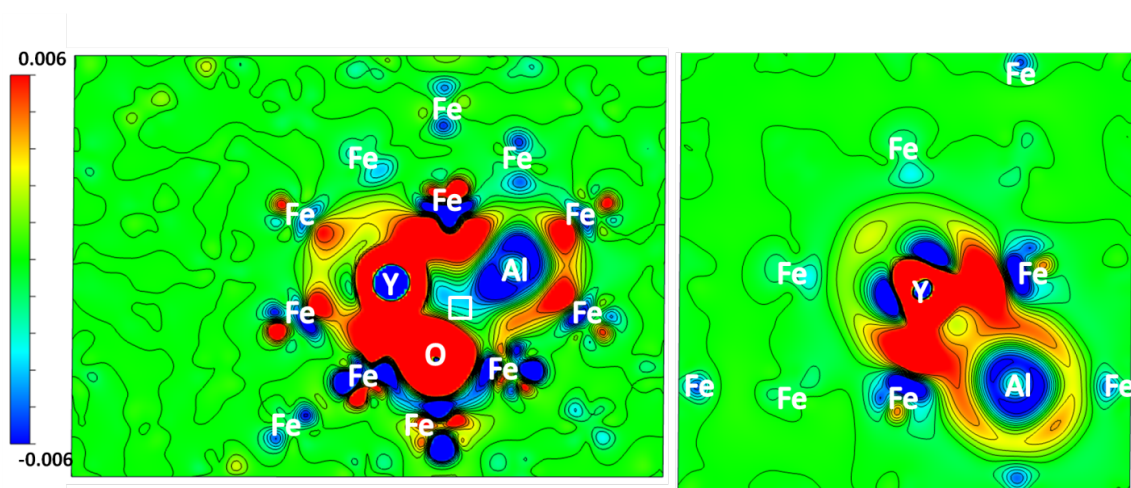


Figure 3.9: The $(1\bar{1}0)$ and $(02\bar{1})$ slices of charge density difference plot of Y-Al-O-vacancy cluster configuration with maximum binding energy. It can be seen that Y-O and Fe-O interactions are stronger than Al-O interactions.

3.3.7 Relative stability of Y-Zr-O and Y-Al-O phases in bcc Fe-matrix

The binding energies in the various stages of cluster formation are summarized in Figure 3.10. In all the configurations considered, Zr containing clusters has higher binding energy than Al containing clusters. So in ODS steels with Zr and Al as minor alloying additions, precipitation of Zr containing oxides will be favored than Al containing oxides.

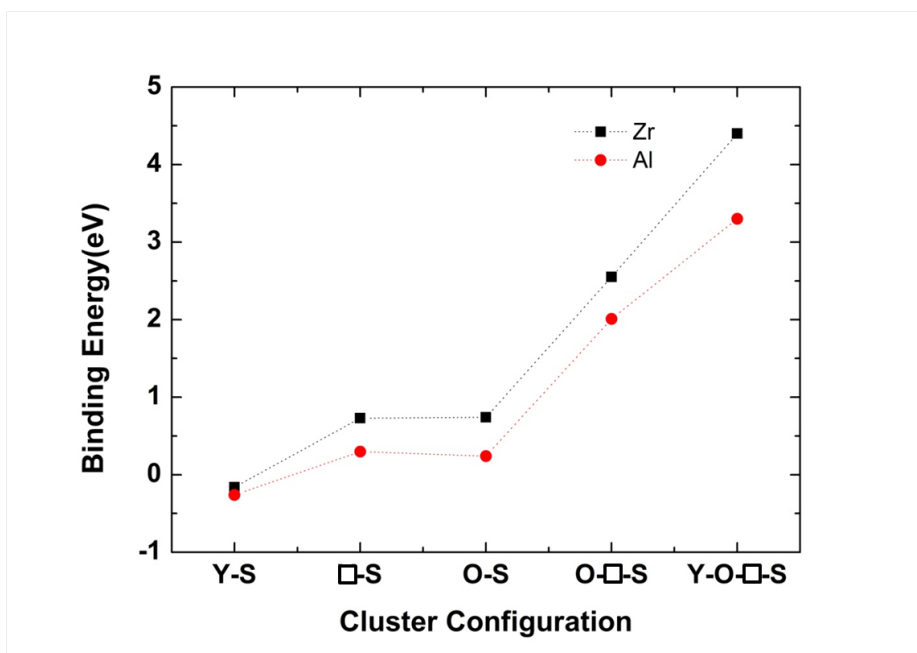


Figure 3.10: Absolute values of binding energies of Zr and Al containing clusters in bcc Fe (here S is solute: Zr/Al). The binding energy of Zr containing clusters are always higher than that of Al containing clusters.

3.4 Relative stability of pyrochlore, δ -phase and disordered fluorite in Y-Zr-O system

The most common Y-Ti-O phases in Ti-containing alloys are, $Y_2Ti_2O_7$ and Y_2TiO_5 . Incidentally, these are the most stable oxide phases of Y, Ti and O in free state [194]. The ground state formation energies are evaluated to be -36.86 eV per formula unit of $Y_2Ti_2O_7$ (3.35 eV/atom) and -27.71 eV per formula unit of Y_2TiO_5 (3.46 eV/atom) respectively. Therefore, the information about the energetically favored Y-Zr-O phase will give an insight into the most probable Y-Zr-O precipitate structures in Zr and Al-containing ODS alloys.

Therefore, *ab initio* simulations are carried out to find the most energetically favored oxide among the possible Y-Zr-O oxides. Three possible oxide structures in the Y_2O_3 - ZrO_2 system, pyrochlore, disordered fluorite and δ -phase are chosen and their formation energies are computed. A brief description about the pyrochlore, δ -phase and disordered fluorite structures are given below:

3.4.1 Crystal structures of pyrochlore, δ -phase and disordered fluorite phases

Delta(δ)-phase

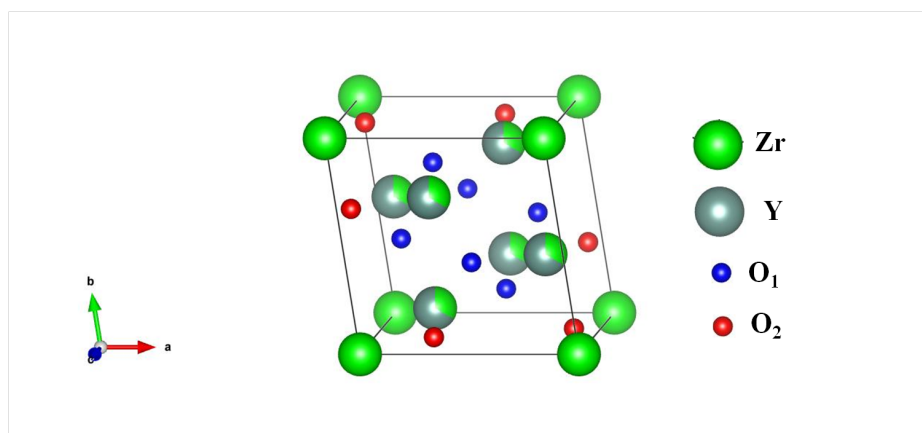


Figure 3.11: $Y_4Zr_3O_{12}$ unitcell

The stacking arrangement of the metal ions in δ -phase remains the same as fluorite structure, except for the slight displacement of ions out of the fcc (111) planes. The phase $Y_4Zr_3O_{12}$ was identified by Scott [195], Ray and Stubican [196] in 1970s. Its structure is similar to R_7O_{12} and MR_6O_{12} (M being U, W or Mo and R a rare earth), belonging to $R\bar{3}$ space group with inversion triad along [111] direction of the rhombohedron [197]. The structure is shown in Figure 3.11. It has two ordered structural vacancies in 6c positions along its inversion triad. Oxygen gets occupied in two sets of $18f$ general positions. Both sets of oxygen form octahedrons one being centered at the body center (denoted as O_I) and the second (denoted as O_{II}) at $3a$ cation octahedron. Consequently, the cation in $3a$ position is co-ordinated to six oxygen atoms and that in $18f$ positions are coordinated to 7 oxygen atoms. The exact ordering of cations in $18f$ and $3a$ positions cannot be determined directly from X-ray or neutron diffraction data because Y and Zr have similar scattering factors.

Pyrochlore

Pyrochlores are another class of fluorite-related structures that have a wide variety of applications in ionic conductivity, nuclear waste immobilization, high-temperature

thermal barrier coatings, solid oxide fuel cell, luminescence, etc. A pyrochlore structure (Space group: $Fd\bar{3}m$) can be derived from cubic fluorite structure (space group $Fm\bar{3}m$) by removing one-eighth of the oxygen atom and ordering the A and B cations along the $\langle 110 \rangle$ direction (see Figure 3.12) [198]. In $Y_2Zr_2O_7$ pyrochlore, Y and Zr are in $16d$ and $16c$ sites. One set of oxygen is in $48f$ sites (shown in red), surrounded by two Y and Zr ions each and the second set of oxygen is in $8b$ site surrounded by four Y ions (shown in blue). Vacancy is at $8a$ site enclosed by four Zr ions. The unitcell has 88 atoms and four formula units.

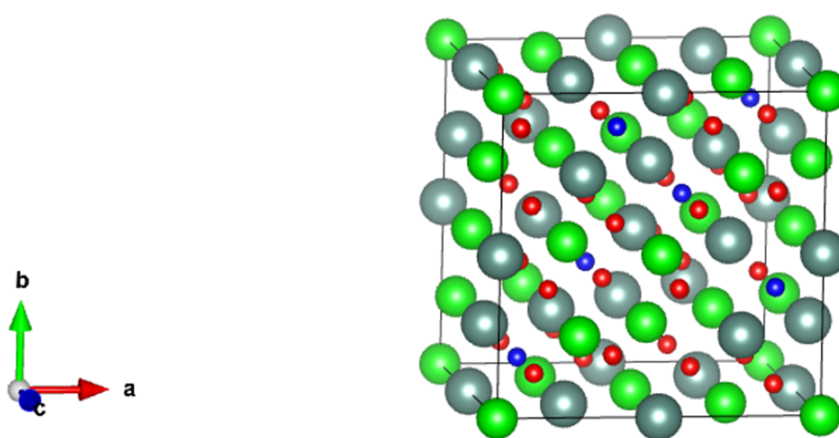


Figure 3.12: An 88 atom unitcell of pyrochlore structure.

Disordered Fluorite

A disordered fluorite structure is a pyrochlore structure without long-range order [198]. The cations can occupy $16d$ or $16c$ sites and anion vacancies do not possess a symmetry, as shown in Figure 3.13. There is a 50 % chance of Zr or Y being in a cation site and a 12.5% chance for an anion site to be vacant. Special quasi- random structure (SQS) is generally used to calculate electronic and thermodynamic properties of random structures [199]. It is a periodic structure whose distinct correlation functions match with the ensemble average of the truly random structure. To mimic fully disordered cubic fluorite structure, an 88 atom SQS constructed by Jiang *et al.* [200] is used in this calculation.

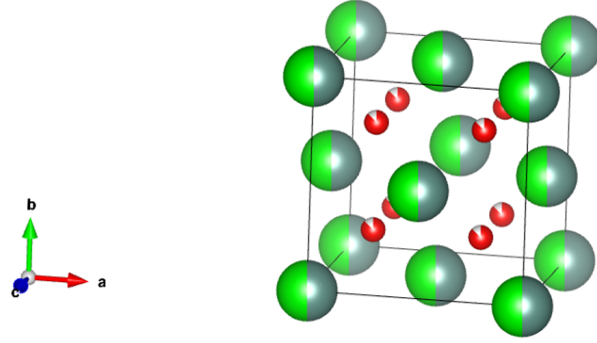


Figure 3.13: A defect fluorite unitcell. The anion positions have 50% occupancy and one-eighth of the cation position is vacant.

3.4.2 Formation energies of different phases in Y-Zr-O system

The relative stability of pyrochlore, disordered fluorite and δ -phase structures are compared by determining their formation energies with respect to Y_2O_3 and ZrO_2 using density functional theory. Similar study has been done before in $La_2Ce_2O_7$ to find the relative stability between pyrochlore and disordered fluorite structures [201]. Structural optimization is carried out for each structure and the calculated lattice parameter values are found to be in agreement with previously reported values.

The formation energies per atom of different structures are calculated as [201]:

$$\begin{aligned}
 E_{Y_2Zr_2O_7} &= \frac{(E_{tot} - E_{Y_2O_3} - 2E_{ZrO_2})}{N_f} \\
 E_{Y_4Zr_3O_{12}} &= \frac{(E_{tot} - 2E_{Y_2O_3} - 3E_{ZrO_2})}{N_f}
 \end{aligned} \tag{3.8}$$

$E_{Y_2O_3}$ and E_{ZrO_2} are the bulk energies of Y_2O_3 and ZrO_2 respectively and N_f is the number of atoms the supercell contain.

The calculated formation energies are tabulated in Table 3.8. The formation energies of both pyrochlores are almost similar irrespective of their oxygen vacancy environment, which is due to similar ionic radii of Y and Zr. Of the four systems considered, $Y_4Zr_3O_{12}$ has the most favoured energy of formation and hence is energetically preferred to form (Figure 3.14).

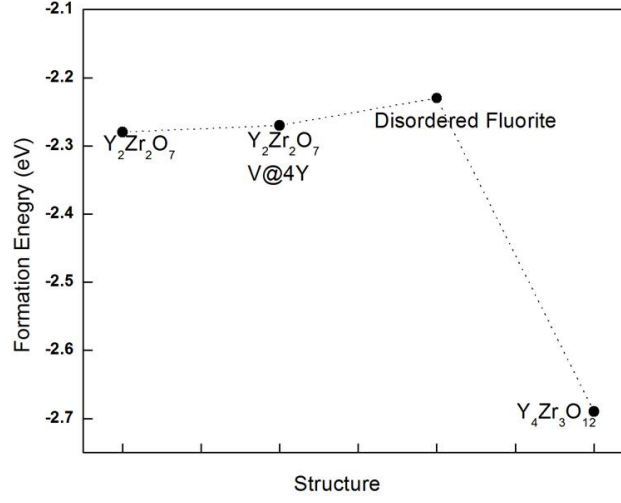


Figure 3.14: The formation energy/atom of delta-phase, pyrochlore and disordered fluorite structure in Y-Zr-O system.

Table 3.8: The formation energy/atom for pyrochlore, δ -phase and SQS structures.

Structure	O-vacancy Environment	Space Group	Formation energy/atom (eV)
Y ₂ Zr ₂ O ₇ - 1	4Zr	$Fd\bar{3}m$	-2.28
Y ₂ Zr ₂ O ₇ - 2	4Y	$Fd\bar{3}m$	-2.27
SQS	-	-	-2.23
δ -phase	2Zr2Y	$R\bar{3}$	-2.69

The simulation results are perfectly in agreement with earlier studies based on the ionic radius ratio of cations in fluorite related structures. In the compositional dependence structural stability mapped by C. R. Stanek *et al.* [202], the experimentally observed δ -phase series of compounds exist within a triangular compositional range drawn with vertices at Sc³⁺ - Ti⁴⁺, Sc³⁺ - Zr⁴⁺ and Yb³⁺ - Zr⁴⁺. According to them, when radius ratio ($\frac{R_{A^{3+}}}{R_{B^{4+}}}$) is in between 1.21 and 1.42 δ - phase is the most stable structure. The radius ratio, $\frac{R_{Y^{3+}}}{R_{Zr^{4+}}}$ is 1.415 and is right on the middle of δ -phase and pyrochlore. The DFT calculations confirm that the δ -phase is more probable than

pyrochlore or disordered fluorite.

3.5 Conclusions

Ab initio simulations are used to forecast the structure and chemistry of the dispersoids in Zr and Al containing ODS steels. As a starting point, the formation energies of constituent elements of nanoclusters in Zr and Al containing ODS alloys were computed and it is found that Zr, Al and Y prefer substitutional site whereas O prefers the octahedral interstitial site in the bcc Fe matrix. The formation energy values are directly related to the solubility of solutes in the matrix. Al has the lowest formation energy and highest solubility among the solute elements considered.

Moving on to the solute-vacancy binding energies, for the substitutional solutes, one with the largest positive formation energy has maximum binding energy with the vacancy. Y-vacancy binding is the strongest (-1.20 eV) followed by Zr-vacancy binding (-0.73) and Al-vacancy binding (-0.30). Therefore, vacancy solute interaction energies depend on how strained is the solute atom in the matrix. Likewise, the solute-oxygen binding energy is determined by the formation energy of the solute in the matrix. Even though Zr-oxygen bond energy is more than Y-oxygen bond energy in the free state, the binding energy trend is reversed inside the matrix, because of the higher formation energy of Y in bcc Fe.

Further, among all the selected configurations of the Zr-O-□, Y-Zr-O-□, Al-O-□ and Y-Al-O-□ clusters, Zr containing clusters have higher binding energy compared to Al containing clusters, which signify that when both Zr and Al are present in a ferrite matrix with yttrium and oxygen, the formation of Y-Zr-O-vacancy clusters are favored as compared to that of Y-Al-O-vacancy clusters.

Out of the major possible Y-Zr-O compounds, pyrochlore, δ -phase and disordered fluorite structure, δ -phase has the lowest formation energy per atom. Therefore, the Y-Zr-O precipitates in Zr and Al containing ODS steels is likely to have $Y_4Zr_3O_{12}$, δ -phase structure.

With these outcomes in mind, we now proceed to experimentally verify these theoretical predictions by synthesizing and characterizing Zr and Al containing ODS steels.

Synthesis and Characterization of ODS steels containing Zr and Al

4.1 Introduction

The first principle calculations in the previous chapter predicted formation of Y-Zr-O precipitates, preferably $Y_4Zr_3O_{12}$, in ODS steels containing Zr and Al. There are a few studies reporting formation of $Y_2Zr_2O_7$ [60], Y_6ZrO_{11} [61] and $Y_4Zr_3O_{12}$ [62] dispersoids in FeCrAlZr alloys along with some Y-Al-O and Y-Ti-O dispersoids. Besides the chemistry and crystal structure of the dispersoids, the details on their spatial distributions (size distribution, number density, volume fraction and inter-spacing) and metal/oxide interface structures (coherency and orientation relationships between the oxides and the bcc steel matrix) are essential to interpret the mechanical, corrosion and radiation behaviour of these ODS steels.

In this chapter, two ferritic ODS alloys of compositions Fe-14Cr-0.63Zr-0.3Y₂O₃-4Al (*named* Al-ODS) and Fe-14Cr-0.63Zr-0.3Y₂O₃ (*named* Zr-ODS) are synthesized using mechanical alloying followed by hot extrusion. The DFT predictions in the previous chapter towards preferential precipitation of $Y_4Zr_3O_{12}$ is verified using bright field, dark field and phase contrast transmission electron microscopy techniques. The grain size distributions, precipitate size distributions and different orientation relationships

are also discussed in detail.

4.2 Experimental methods

4.2.1 Synthesis of ODS steels containing Zr and Al

ODS ferritic steels are fabricated by powder metallurgy as explained in Section 1.3.1. Hot isostatic pressing and hot extrusion are conventionally used to obtain fully dense materials.

Mechanical Alloying

Two ODS steels with compositions Fe-14Cr-0.63Zr-0.3Y₂O₃-4Al (Al-ODS) and Fe-14Cr-0.63Zr-0.3Y₂O₃ (Zr-ODS) are synthesized. The details of the starting materials are provided in the Table 4.1. The alloy powders are produced by milling the elemental powders and Y₂O₃ in a high energy horizontal ball mill (Simolayer CM08 mill) for 6h under argon atmosphere. Stainless steel vial and hardened steel balls (diameter=5mm) are used for mixing. The ball to powder ratio is 10:1. In this process, the powder particles are successively deformed, broken, and cold-welded. The powder obtained after milling had a crystallite size of $\simeq 45$ nm.

Table 4.1: Details of starting elemental and Y₂O₃ powders used for ball milling.

S. No	Material	Particle size(μm)	Purity(%)
1	Fe	900	99.99
2	Cr	<10	99.99
3	Zr	300	99.7
4	Y ₂ O ₃	0.022	99.99
5	Al	60	99.99

Consolidation by Hot Extrusion

The milled powders are filled in mild steel cans, degassed at 450 °C, and sealed. The sealed cans are then forged at 1050 °C and subsequently hot extruded at 1150 °C with an extrusion ratio of 9 to get rods of diameter 16 mm. The extruded rods are further annealed at 900 °C for 1h and then water quenched. The as-prepared rods of Zr-ODS and Al-ODS are shown in Figure 4.1.



Figure 4.1: As prepared (a) Fe-14Cr-0.63Zr-4Al-0.3Y₂O₃(Al-ODS) and (b) Fe-14Cr-0.63Zr-0.3Y₂O₃(Zr-ODS) rods

4.2.2 Transmission Electron Microscopy

TEM specimens were prepared by carbon extraction replica method and by twin jet electropolishing. Discs of thickness 300 μm were sliced from the extruded rods as starting material for both methods.

Extraction replicas are made to obtain the structural information of oxides without matrix interference. The sliced as-prepared samples were polished using silicon carbide papers of successively finer grades (1000, 1200, 2400, 4000) followed by diamond polishing. Subsequently, the surface of the specimen was pre-etched using Vilella's Reagent (1gm picric acid, 10 ml HCL, and 100ml ethanol) for 2-3 minutes. Nearly 100nm thick carbon film was then deposited on the surface and the surface is etched again in the same acid solution to separate carbon films from the alloy. Finally, the film was cleaned carefully in ethanol and caught on 3 mm hexagonal copper grids with 200 mesh size.

For twin jet electropolishing, the sample discs were thinned down to $\sim 30\mu\text{m}$ and small discs of diameter 3 mm were punched out of it. The discs were then electropolished to perforation using an electrolyte of perchloric acid and ethanol in a 1:9 ratio at $-35\text{ }^\circ\text{C}$ and 25 V.

The samples obtained using both the procedures are examined using the LIBRA 200FE (Carl Zeiss) transmission electron microscope operating at 200 kV. The studies involved bright field (BF) and dark field (DF) diffraction contrast imaging and phase-contrast HRTEM imaging.

The HRTEM micrographs are thoroughly analyzed using softwares Digital Micrograph [203] and ProcessDiffraction [204–206]. The power spectra of micrographs were compared to diffraction patterns simulated using JEMS software [207] for further confirmation.

The d-spacings for oxide precipitate (d) and the matrix (d_α) are measured from HRTEM micrograph and the relative strain due to misfit at the interface is calculated as:

$$\epsilon = \left| \frac{d - d_\alpha}{d} \right| \quad (4.1)$$

When $\epsilon < 25\%$ the precipitate matrix interface is said to be semi-coherent. It is incoherent when $\epsilon > 25\%$.

4.3 Microstructure of Al/Zr ODS steels

4.3.1 Nanocrystalline grain size and its contribution to strength and radiation tolerance

The grain morphologies of the as-extruded specimen, in the extrusion direction of Al-ODS and Zr-ODS are shown in Figure 4.2. The corresponding SAED pattern is shown in Figures.4.2(c) and (d). These SAED ring patterns can be indexed for bcc Fe-Cr matrix with a lattice parameter, $a=2.859$. The average grain sizes are 234 nm and 376 nm for Zr-ODS and Al-ODS respectively. Extrusion at high temperature introduces continuous dynamic anisotropic re-crystallization resulting in grains elongated along extrusion direction [23]. Yttrium addition along with sufficient milling time is crucial in achieving grain refinement of the matrix [21]. The dissolved yttrium in the matrix

limits the grain growth resulting in nanostructured grains in both ODS alloys. It is proven that the addition of Zr further refines the grain [38].

The size of the nano-precipitates formed during consolidation also inhibits grain growth by pinning the grain boundaries, by a phenomenon known as Zener pinning [208]. The Zener limiting grain size (D_g) is directly proportional to precipitate size and inversely proportional to the volume fraction of precipitates. The smaller grain size indicates small precipitates with a high number density.

$$D_g \propto \frac{r}{f}; \quad (4.2)$$

Here D_g is the average grain size, r is the average radius of the nanoprecipitate and f is the volume fraction of the nanoprecipitates. Grain boundaries are effective sinks to trap irradiation-induced defects. Therefore, nano-grained materials have a high density of grain boundaries and hence high radiation tolerance [209]. The radiation tolerance of Zr-ODS will be more than that of Al-ODS owing to its smaller grain size.

Another important advantage of nanostructured alloys is the ability to promote selective oxidation, by providing more nucleation sites for oxides. When Al and Cr are added, to form an oxide layer, they diffuse to the surface by the grain boundary diffusion mechanism. An increase in the number of grain boundaries increases the outward diffusion of Al and Cr in the alloy. So the amount of Al required to form a continuous protective layer in a nano-grained alloy is less than the same alloy with a larger grain size [210].

The nano-grained materials also possess high strength and ductility than coarse-grained materials [211]. The grain refinement and resulting high density of grain boundaries that impede dislocation movements strengthen the material. The grain boundary strengthening mechanism is usually described by the Hall-Petch relation [212]: $\Delta\sigma \propto d^{-1/2}$, where $\Delta\sigma$ is the strength component due to grain boundary strengthening and d is the average grain diameter. Thus, the Zr-ODS is expected to have a higher contribution from grain boundary strengthening towards the total strength than Al-ODS. Altogether, it is advantageous to have nano-sized grains, along with nano precipitates, in ODS steels. Because they provide higher radiation tolerance and corrosion resistance.

4.3.2 Nature of dispersoids and verification of DFT simulations

As per various literature, during the hot-consolidation process, the dissolved minor alloying elements, re-precipitate as complex Y-Zr-O, or Y- Al-O oxides depending on the composition. The Figure 4.3 shows the bright field (BF) image and the dark field (DF) image of the oxide particles in the carbon extraction replica of Al-ODS. The contrast is arising due to mass-thickness as well as diffraction. The size distribution of the particles is presented in the Figure 4.3(d). The nanoparticle diameter ranges from 1.6 nm to 43 nm with a mean diameter of 8 nm. The size distribution of precipitates in Zr-ODS alloy ranges from 1.6 -26 nm with a mean diameter of 4 nm (Figure 4.4). The particle number densities and mean distance between the precipitates are measured from APT measurements. The mean distance between particles is 5.6 nm for Zr-ODS and 9.2 nm for Al-ODS. The number density of Zr-ODS precipitates is $1 \times 10^{24}/\text{m}^3$ and the number density of dispersoids in Al-ODS is $3.8 \times 10^{23}/\text{m}^3$. The volume fractions are 0.06 and 0.10 respectively.

The conclusions in DFT studies presented in chapter.3. pointed towards the formation of Y-Zr-O precipitates, predominantly $\text{Y}_4\text{Zr}_3\text{O}_{12}$ in Zr containing ODS steels and the Al containing precipitates are less likely to form in presence of Zr. This can be verified by analyzing the diffraction pattern of Zr and Al ODS specimens. The rings in the diffraction patterns obtained from the replicas of Al-ODS and Zr-ODS are shown in Figure 4.3(c) and Figure 4.4(c) respectively. This shows polycrystalline nature of the dispersoids and are in exact agreement with trigonal $\text{Y}_4\text{Zr}_3\text{O}_{12}$ with $a=9.738$ and $c=9.115$ in hexagonal representation (ICDD : 01-077-0743, [213]). Therefore, it is evident that the major precipitate phase is $\text{Y}_4\text{Zr}_3\text{O}_{12}$. This is in-line with the DFT predictions.

According to Hsiung *et al.* [51], the critical size for $\text{Y}_4\text{Al}_2\text{O}_9$ precipitates to possess definite structure and stoichiometry in α -Fe matrix is 2 nm. Below this critical size, they were predominantly amorphous or disordered cluster domains. But here, even the precipitate of size as small as 1.6 nm can be resolved into the structure of $\text{Y}_4\text{Zr}_3\text{O}_{12}$. So the critical size of disordered atomic clusters to grow into stoichiometric, crystalline oxide particle is ≤ 1.6 nm. It is further observed that the smaller precipitates (≤ 5 nm) have a faceted structure while larger ones tend to be spherical or elliptical.

Table 4.2: Microstructural information of as-prepared Zr ODS and Al-ODS alloys

Alloy	Grain size (nm)	Precipitate radius, r (nm)	Number Density (/m ³)	Inter-particle distance, λ (nm)	Volume Fraction, f
Zr - ODS	234	2	1.7×10^{24}	5.6	0.06
Al-ODS	376	4	3.8×10^{23}	9.2	0.10

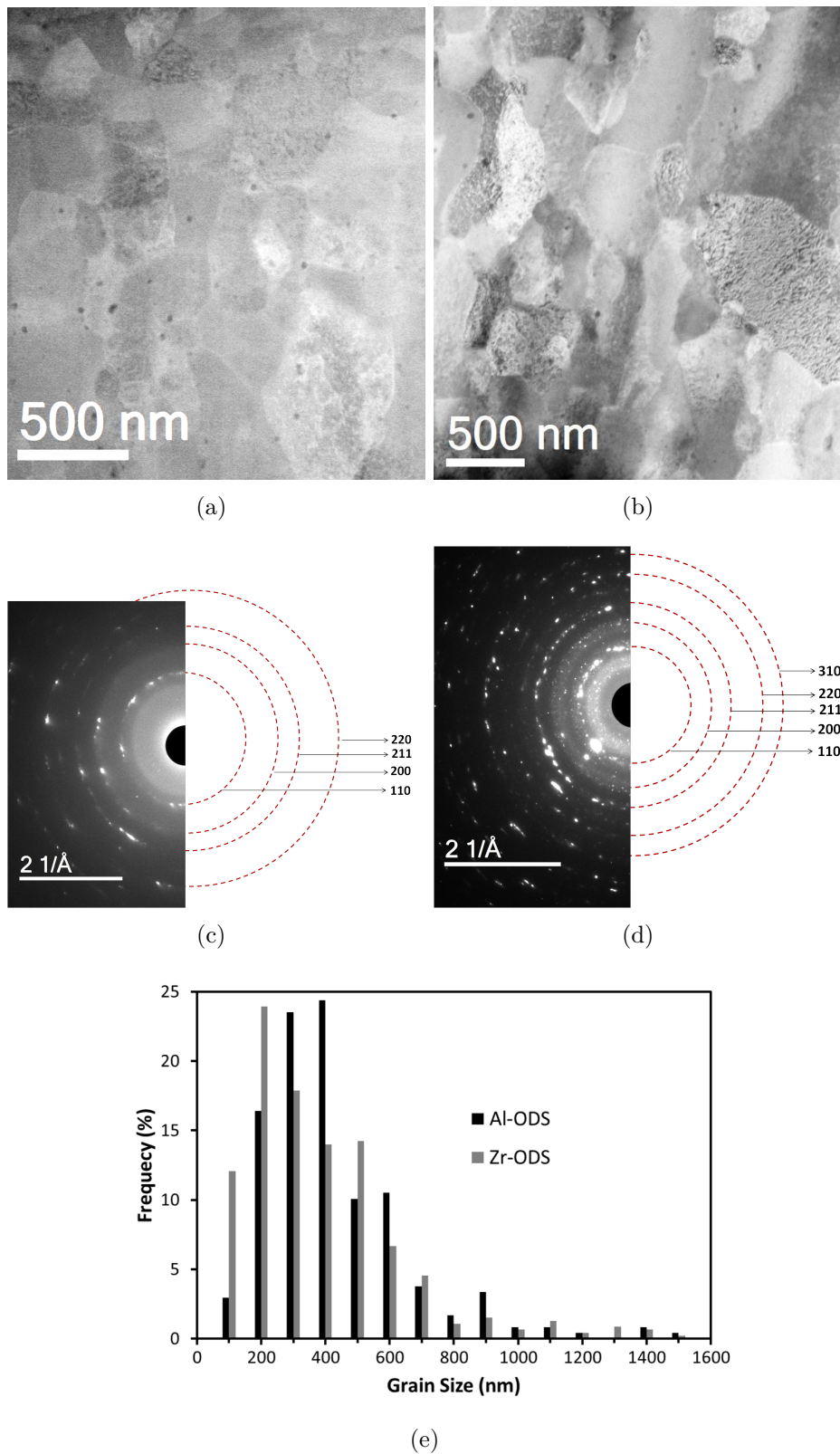


Figure 4.2: Bright Field TEM images of (a) Al - ODS and (b) Zr - ODS. (c) SAED pattern of Al-ODS sample, indexed for bcc Fe. (d) SAED pattern of Zr-ODS, indexes correspond to planes of bcc Fe. (e) Grain size distribution of Zr-ODS and Al-ODS.

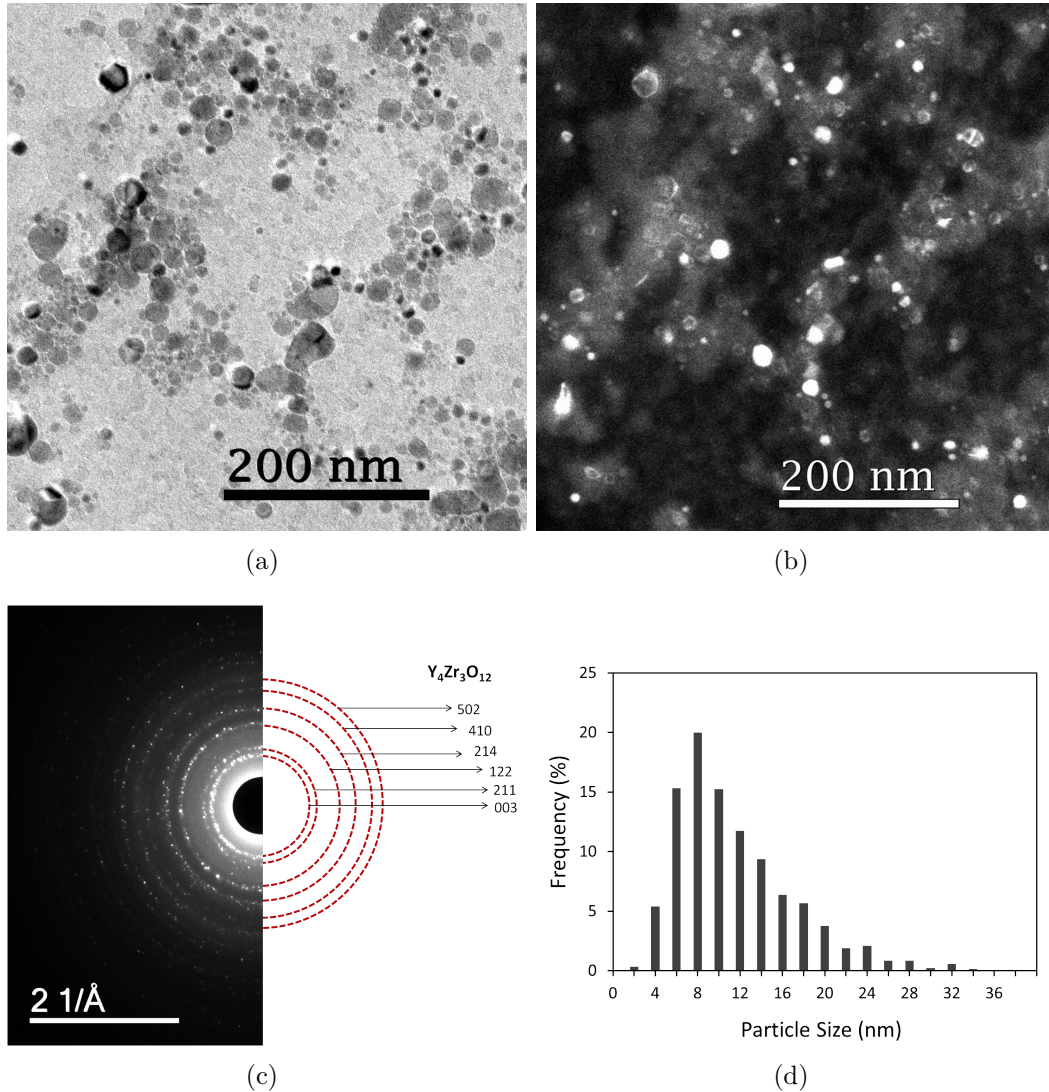


Figure 4.3: (a) Bright Field image and (b) Dark Field image of oxide particles in the carbon extraction replica of Al-ODS. (c) The SAED pattern of the extraction replica, which can be indexed for trigonal $Y_4Zr_3O_{12}$ (ICDD : 01-077-0743) (d) Particle size distribution in Al-ODS.

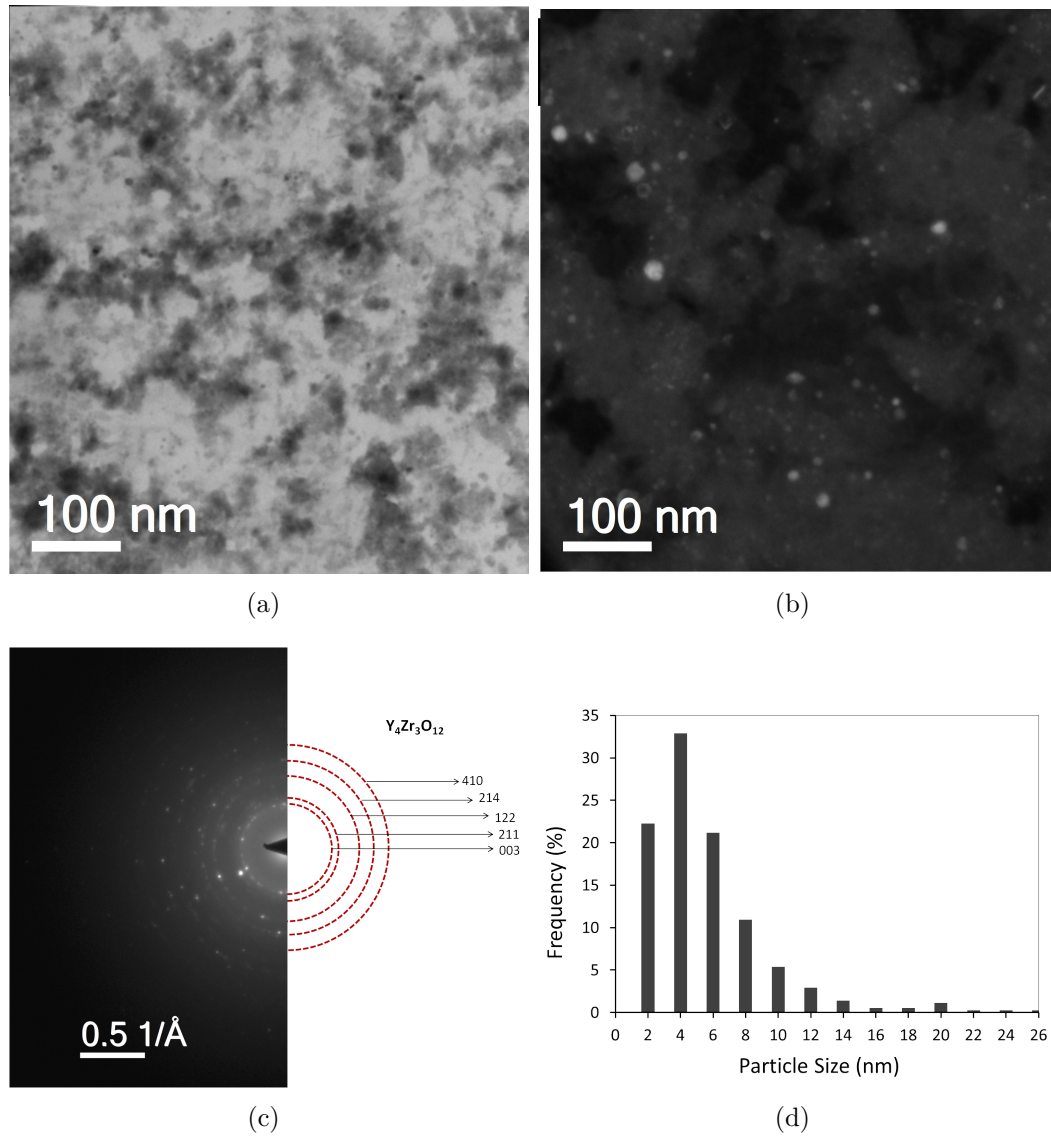


Figure 4.4: (a) Bright Field and (b) Dark Field images and (c) the SAED pattern of the extraction replica of Zr-ODS, which can be indexed for trigonal $Y_4Zr_3O_{12}$ (ICDD : 01-077-0743) and (d) particle size distribution of Zr - ODS

4.4 Strengthening mechanisms in Zr/Al-ODS steels

As discussed in Section 1.2, the strengthening of materials with fine dispersions can occur either by Orowan bypassing mechanism or by precipitate shearing mechanism [12]. The Orowan bypassing mechanism is predominant when the precipitates are incoherent or semi-coherent with the matrix while the precipitate shearing mechanism is predominant when the precipitates are coherent with the matrix. By empirical methods, it is possible to formulate a quantitative insight into the operative strengthening mechanism. That information can be used to compare the strength of the as-prepared dispersion strengthened alloys. This can also be used to predict the coherency of the precipitates formed.

For the precipitates which are incoherent with the matrix, the dispersoid strengthening mechanism is governed by Orowan dislocation bypassing mechanism. The increment in yield strength is [214]:

$$\Delta\sigma_{orowan} = M \frac{0.4Gb}{\pi\sqrt{1-\nu}} \frac{\ln(2\bar{r}/b)}{\lambda}; \bar{r} = \sqrt{\frac{2}{3}}r \quad (4.3)$$

The meaning of parameters of this equation is summarized in Table 4.3.

Table 4.3: Microstructural information of Zr and Al-ODS, used for calculating different strength contributions.

Symbol	Parameter	Value	Unit
M	Mean orientation factor	3.06, for polycrystalline, texture-free bcc metals [215, 216]	Dimensionless
G	Shear modulus	82 [216, 217]	GPa
b	Magnitude of the Burger's vector	0.25 [218]	nm
ν	Poissons Ratio	0.3 [217]	Dimensionless
α_ϵ	a constant	0.2 [217]	Dimensionless

The strength increment from orowan bypassing [219]:

$$\frac{\Delta\sigma_{orowan,Al}}{\Delta\sigma_{orowan,Zr}} = \frac{\ln(2\bar{r}_{Al}/b)}{\lambda_{b,Al}} \times \frac{\lambda_{b,Zr}}{\ln(2\bar{r}_{Zr}/b)} \quad (4.4)$$

The yield strength increment by Orowan bypass mechanism in Al-ODS is ~ 345 MPa and that for Zr-ODS is ~ 424 MPa

In the case of semi coherent precipitates, the strengthening mechanism can be Orowan bypassing or dislocation shearing mechanism. To determine the operative mechanism, the strength increment resulting from dislocation shearing has to be estimated and compared with $\Delta\sigma_{orowan}$ to find the operative mechanism. There are three factors contributing to the increase in yield strength by dislocation shearing : coherency strengthening ($\Delta\sigma_{CS}$), modulus mismatch strengthening ($\Delta\sigma_{MS}$) and order strengthening ($\Delta\sigma_{OS}$). The equations available to calculate these strength increments are [220–222]:

$$\Delta\sigma_{CS} = M \times \alpha_\epsilon \times (G\epsilon_c)^{\frac{3}{2}} \times \sqrt{\frac{rf}{0.5Gb}} \quad (4.5)$$

$$\Delta\sigma_{MS} = M \times 0.0055(\Delta G)^{\frac{3}{2}} \times \sqrt{\frac{2f}{G}} \times \left(\frac{r}{b}\right)^{\frac{3m}{2}-1} \quad (4.6)$$

$$\Delta\sigma_{OS} = M \times 0.81 \times \frac{\gamma_{apb}}{2b} \times \sqrt{\frac{3\pi f}{8}} \quad (4.7)$$

The larger of ($\Delta\sigma_{CS} + \Delta\sigma_{MS}$) or $\Delta\sigma_{OS}$ is the total strength increment from shearing mechanism.

As mentioned in Table 4.4., the $Y_4Zr_3O_{12}$ has a trigonal structure with $a=9.738$ Å and $c=9.115$ Å in its hexagonal representation. The constrained effective coherent misfit strain, ϵ_c is defined as [223]:

$$\epsilon_c = \frac{1}{3} \times \left(\frac{1+\nu}{1-\nu}\right) \times \left(\frac{\epsilon_{eff}}{1 + \frac{4G}{3B_c}}\right) \quad (4.8)$$

where, B_c is the bulk modulus of the precipitate. ϵ_{eff} is the effective scalar coherency strain:

$$\epsilon_{eff} = \frac{\sqrt{2}}{3} \left[(\epsilon_{11} - \epsilon_{22})^2 + (\epsilon_{22} - \epsilon_{33})^2 + (\epsilon_{33} - \epsilon_{11})^2 \right]^{\frac{1}{2}} \quad (4.9)$$

where

$$\epsilon_{11} = \frac{a_p}{a_m} - 1; \quad \epsilon_{22} = \frac{\sqrt{3}a_p}{\sqrt{2}a_m} - 1; \quad \epsilon_{33} = \frac{c_p}{\sqrt{2}a_m} - 1 \quad (4.10)$$

a_m is the lattice parameter of the Fe- matrix, 2.869 Å. a_p and c_p are the lattice parameters of the precipitate.

The calculated strength component due to coherency strengthening ($\Delta\sigma_{CS}$) is ~ 710 MPa for Al-ODS and ~ 558 MPa for Zr-ODS. In both cases, $\Delta\sigma_{orowan} < \Delta\sigma_{CS}$. The component with smaller value is the predominant operating mechanism [220]. Therefore Orowan bypassing mechanism is the predominant strengthening mechanism in ODS steels. This also imply that most of the precipitates are either incoherent or semi-coherent with the matrix.

4.5 Crystal structure and orientation relationships of dispersoids

Detailed HRTEM investigation was carried out to determine structure and orientation of the precipitates in Zr and Al- ODS steels. Nearly one hundred precipitates from each alloy were analyzed. Power spectrum of micrograph containing precipitate is obtained. The d-spacings and angles between the planes measured from the power spectrum is compared with those values obtained from simulated diffraction pattern of different compounds in different zone axes. The major oxide phases considered are: $Y_4Zr_3O_{12}$, ZrO_2 (cubic, monoclinic and tetragonal), Y_6ZrO_{11} , $Y_2Ti_2O_7$, Al_2O_3 (trigonal, monoclinic), $Y_4Al_2O_9$, $Y_3Al_5O_{12}$, Cr_2O_3 , Fe_2O_3 , Fe_3Al and Y_2O_3 (cubic, monoclinic). The space group and lattice parameters of of predominant structures are tabulated in Table 4.4.

Detailed analysis of different structures and orientation relationships of precipitates are presented in the following sections.

4.5.1 Existence of novel bcc/trigonal orientation relationship in Zr-containing ODS steels

A high resolution lattice image of the distribution of dispersoids in Zr-ODS can be seen in Figure 4.5(a), where the precipitates are indicated by arrows. The precipitate

Table 4.4: The details of crystal structures used for analyzing HRTEM micrographs.

Structure	Space Group	a(Å)	b(Å)	c(Å)	$\alpha(^{\circ})$	$\beta(^{\circ})$	$\gamma(^{\circ})$
$\text{Y}_4\text{Zr}_3\text{O}_{12}$ [195]	$R\bar{3}$	9.738	9.738	9.115	90	90	120
Monoclinic ZrO_2 [224]	$P2_1/c$	5.14	5.20	5.31	90	99.197	90
Tetragonal ZrO_2 [225]	$P4_2/nmc$	3.64	3.64	5.27	90	90	90
Cubic ZrO_2 [226]	$Fm\bar{3}m$	4.925	4.925	4.925	90	90	90
Fe-Cr Matrix (α) [227]	$Im\bar{3}m$	2.859	2.859	2.859	90	90	90

sizes range from 1.6 nm to 8 nm. The power spectrum of the entire region is shown in 4.5(b). The zone axis of the matrix (α - Fe) is [111]. The matrix spots are marked with red arrows and indexed. The precipitate spots are seen almost parallel to the matrix spots. The precipitate spots are marked in yellow arrows. The inverse Fourier transform image is constructed using precipitate spots alone and it is shown in 4.5(c). It can be seen that all the precipitates have the same orientation. And there is a predominant matrix-precipitate orientation relationship in Zr-ODS.

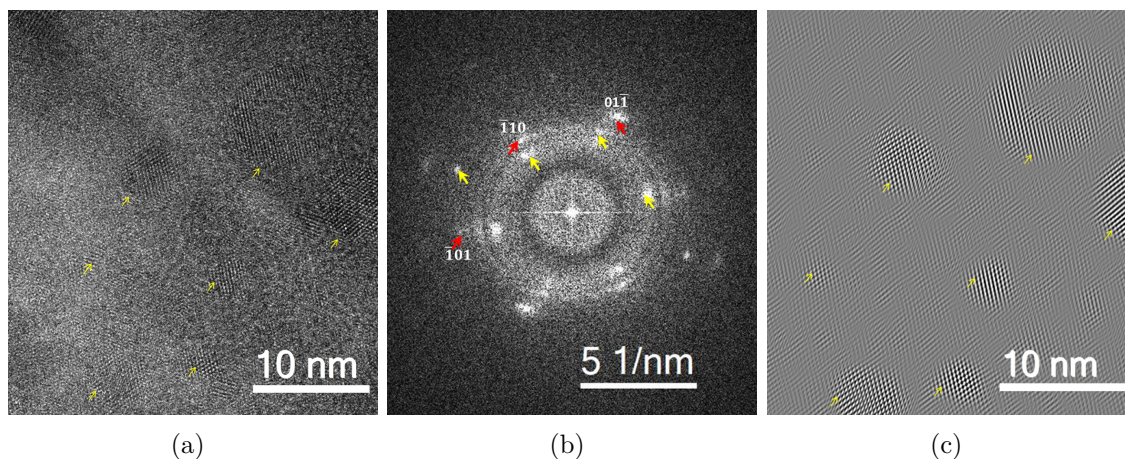


Figure 4.5: (a) HRTEM image showing distribution of dispersoids in the matrix of as prepared Zr-ODS steel. The dispersed precipitates in the micrograph have diameter ranging from 1.6 nm to 8 nm (b) Power spectrum of the micrograph in (a). Matrix spots are marked with red arrows and indexed for [111] zone axis of Fe. The diffraction spots corresponding to precipitates are marked with yellow arrows. (c) The image reconstructed using diffraction spots corresponding to precipitates. The nanoclusters are indicated by yellow arrows in (a) and (c).

Magnified view of a dispersoid of same orientation as in Figure 4.5 is shown in Figure 4.6. The power spectrum of 4.6(a) is shown in 4.6(b). The matrix and precipitate diffraction spots are marked. The spots in power spectrum corresponding to the precipitate match with simulated diffraction pattern in $[2\bar{1}0]$ zone axis (Miller notation) of $Y_4Zr_3O_{12}$ (refer to Figure 4.6(c)). In Miller - Bravais notation, this is equivalent to $[5\bar{4}\bar{1}0]$ direction. The d values are measured and compared with d-values calculated using the ICDD data. The measured and calculated values of d-spacings and angles of precipitate and matrix is tabulated in Table 4.5. From this a precipitate matrix orientation relationship can be deduced:

$$[111]_{\alpha} \parallel [2\bar{1}0]_{Y_4Zr_3O_{12}} \text{ and } (\bar{1}10)_{\alpha} \parallel (122)_{Y_4Zr_3O_{12}} \quad (4.11)$$

All the precipitates in Figure 4.5. and 86% of the precipitates analyzed in this study possess this orientation relationship. The existence of a predominant precipitate-matrix relationship points to the fact that the oxide powders completely dissolves in the matrix during the ball milling process and nucleates as new phase in a preferred direction of the matrix. The (122) plane of precipitate is oriented parallel to $(\bar{1}10)$ plane of α -Fe. The angle between these two planes is $\sim 0.3^\circ$. The most commonly reported ORs in hcp/bcc precipitate-matrix interfaces are: Burger's OR [228], Pitsche-Schrader OR [229], Potter's OR [229, 230], Zheng's OR [231] and Crawley's OR [232].

Burgers OR: $\{110\}_{bcc} \parallel \{0001\}_{hcp}$ and $[111]_{bcc} \parallel [11\bar{2}0]_{hcp}$

Pitsche-Schrader OR: $\{110\}_{bcc} \parallel \{0001\}_{hcp}$ and $[001]_{bcc} \parallel [11\bar{2}0]_{hcp}$

Potter's OR : $\{110\}_{bcc} \parallel \{01\bar{1}1\}_{hcp}$ and $[011]_{bcc}$ from $[0001]_{hcp}$ 2°

Zheng's OR : $\{303\}_{bcc} \parallel \{11\bar{2}0\}_{hcp}$ and $[\bar{1}\bar{3}1]_{bcc} \parallel [0001]_{hcp}$

Crawley's OR : $\{111\}_{bcc} \parallel \{0001\}_{hcp}$ and $[\bar{2}11]_{bcc} \parallel [11\bar{2}0]_{hcp}$

A well-known fact about common ORs like Burger's OR is that the close-packed planes of both the precipitate and the matrix structures tend to be parallel [233]. The six $\{110\}$ planes are the close-packed planes in the bcc structure. As per the X-ray diffraction data in the reference [196], (003), $(12\bar{1})$, (122), $(12\bar{4})$, (140), (125) and (143) reflections are very strong. These are the close-packed planes in $Y_4Zr_3O_{12}$. The (003) plane is nearly parallel to the $(01\bar{1})$ plane of the matrix, with an angle $\sim 5.3^\circ$. The angle between $(12\bar{1})$ plane of the precipitate and the $(1\bar{1}0)$ plane of the matrix is $\sim 2^\circ$. Therefore, this orientation relationship is peculiar because the six close-packed

planes of the matrix are nearly parallel to six close-packed planes of the $Y_4Zr_3O_{12}$ precipitate. Since nearly 86% of the observed $Y_4Zr_3O_{12}$ precipitates in the Fe matrix possess this orientation, this could be the most energetically favored orientation in Zr-containing ODS alloy.

The zone axes, $[\bar{2}10]$, $[\bar{1}\bar{3}0]$, $[130]$, $[1\bar{2}0]$, $[\bar{1}20]$, $[310]$, $[\bar{3}\bar{1}0]$, $[320]$ and $[\bar{3}\bar{2}0]$ of $Y_4Zr_3O_{12}$ also have same diffraction pattern as $[2\bar{1}0]$. These directions are related by $R\bar{3}$ symmetry of $Y_4Zr_3O_{12}$ and can be generated from $[2\bar{1}0]$ direction using the six space group generators $(1, 3^+0, 0, z; 3^-0, 0, z; -10, 0, 0; -3^+0, 0, z; -3^-0, 0, z)$ of $R\bar{3}$ space group.

The alternate ways to write this orientation relationship are (here δ is used as a subscript to indicate rhombohedral $Y_4Zr_3O_{12}$ phase) :

$$[130]_{\delta} \parallel [111]_{\alpha} \text{ and } (3\bar{1}\bar{2})_{\delta} \parallel (\bar{1}10)_{\alpha}; \quad (4.12)$$

$$[310]_{\delta} \parallel [111]_{\alpha} \text{ and } (1\bar{3}\bar{2})_{\delta} \parallel (\bar{1}10)_{\alpha}; \quad (4.13)$$

$$[\bar{3}\bar{1}0]_{\delta} \parallel [111]_{\alpha} \text{ and } (\bar{1}32)_{\delta} \parallel (\bar{1}10)_{\alpha}; \quad (4.14)$$

$$[\bar{1}\bar{3}0]_{\delta} \parallel [111]_{\alpha} \text{ and } (\bar{3}12)_{\delta} \parallel (\bar{1}10)_{\alpha}; \quad (4.15)$$

$$[\bar{2}10]_{\delta} \parallel [111]_{\alpha} \text{ and } (122)_{\delta} \parallel (\bar{1}10)_{\alpha}; \quad (4.16)$$

$$[1\bar{2}0]_{\delta} \parallel [111]_{\alpha} \text{ and } (2\bar{1}2)_{\delta} \parallel (\bar{1}10)_{\alpha}; \quad (4.17)$$

$$[\bar{1}20]_{\delta} \parallel [111]_{\alpha} \text{ and } (21\bar{2})_{\delta} \parallel (\bar{1}10)_{\alpha}; \quad (4.18)$$

$$[320]_{\delta} \parallel [111]_{\alpha} \text{ and } (2\bar{3}2)_{\delta} \parallel (\bar{1}10)_{\alpha}; \quad (4.19)$$

$$[\bar{3}\bar{2}0]_{\delta} \parallel [111]_{\alpha} \text{ and } (23\bar{2})_{\delta} \parallel (\bar{1}10)_{\alpha}; \quad (4.20)$$

$$[\bar{2}\bar{3}0]_{\delta} \parallel [111]_{\alpha} \text{ and } (3\bar{2}2)_{\delta} \parallel (\bar{1}10)_{\alpha}; \quad (4.21)$$

$$[230]_{\delta} \parallel [111]_{\alpha} \text{ and } (\bar{3}2\bar{2})_{\delta} \parallel (\bar{1}10)_{\alpha} \quad (4.22)$$

Since the bcc structure has four equivalent $[111]$ directions, at least 32 equivalent combinations for Eq. 4.11. are probable, each one is referred to as a *variant*. A combined stereo-graphic projection of $[2\bar{1}0]_{\delta}$ and $[111]_{\alpha}$ with $(122)_{\delta} \parallel (\bar{1}10)_{\alpha}$ is given in Figure 4.7.

Misfit dislocations and strain contrast at the precipitate matrix interface

The relationship between the planes of the $Y_4Zr_3O_{12}$ and Fe matrix in orientation relationship described by equation 4.11 is: $5d_{\bar{1}10,M} \simeq 4d_{122,\delta}$, which makes it semi-coherent with the matrix. The lattice mismatch, $\Delta = \left| \frac{d_{\delta,122} - d_{M,\bar{1}10}}{d_{\delta,122}} \right| = 22.3\%$.

The precipitate matrix interface is shown in Figure 4.8. The simulated HREM map for precipitate and matrix is in agreement with the observed HRTEM image. The simulated patterns are shown in regions marked (a) and (b). Periodic array of geometric dislocations can be seen at the precipitate - matrix interface, which are marked in yellow. Some precipitate matrix planes are perfectly coinciding. After a set of three such coinciding planes, two matrix ($\bar{1}10$) planes terminate on both sides of a (122) precipitate plane, creating a dislocation doublet. Each dislocation doublet is separated by a distance of ~ 0.6 nm. The strain due to lattice mismatch is accommodated by these misfit dislocations. And the strain contrast is observed in precipitate image as ripples along $[\bar{1}10]$ direction. It is reported that the orthogonal strains for bcc/hcp orientation relationships are along $\langle 001 \rangle$ and $\langle 110 \rangle$ directions. From the direction of the ripples in Figure 4.8., it can be concluded that this observation holds well for trigonal/bcc relationship also.

4.5.2 Orientation related by rotation to preferred orientation

The most frequently reported ORs, Burger's, Potters and Pitsche-Schrader ORs are connected to each other by a small relative rotation [234]. A rotation of 5.26 degrees of Pitsche-Schrader OR brings two new low index planes in coincidence, and the resulting OR is called the Burger's OR [233]. This angle is independent of the lattice parameter of the crystals involved. In the stereogram Figure 4.7., it is evident that the angle between $(003)_\delta$ and $(\bar{1}01)_\alpha$ is 5.26° . On rotating by 5.26° with respect to $[111]_\alpha || [2\bar{1}0]_\delta$ will bring $(003)_\delta$ and $(\bar{1}01)_\alpha$ in coincidence. A few precipitates with this orientation, with the same directional relationship as the most preferred orientation but different parallel planes, are also observed in Zr-ODS.

A $Y_4Zr_3O_{12}$ precipitate with $[2\bar{1}0]_\delta || [111]_\alpha$ and $(003)_\delta || (\bar{1}01)_\alpha$ is shown in the Figure 4.9(a). The power spectrum of the precipitate and the matrix is shown in Figure 4.9(b). The combined diffraction pattern of $[2\bar{1}0]_\delta$ and $[111]_\alpha$ is shown in Figure 4.9(b). The mismatch with matrix d-value ($d_{\bar{1}01} = 2.02 \text{ \AA}$) and the precipitate d-value

($d_{300} = 3.03$) is 33.33%. It can be noted that an offset of 5.26° between the close packed planes in the most preferred OR (Eq. 4.22) reduces the strain by $\sim 10\%$. The orientation relationships equivalent to $[2\bar{1}0]_\delta || [111]_\alpha$ and $(00\bar{3})_\delta || (\bar{1}01)_\alpha$ are:

$$[130]_\delta || [111]_\alpha \text{ and } (00\bar{3})_\delta || (\bar{1}01)_\alpha; \quad (4.23)$$

$$[310]_\delta || [111]_\alpha \text{ and } (00\bar{3})_\delta || (\bar{1}01)_\alpha; \quad (4.24)$$

$$[\bar{3}\bar{1}0]_\delta || [111]_\alpha \text{ and } (00\bar{3})_\delta || (\bar{1}01)_\alpha; \quad (4.25)$$

$$[\bar{1}\bar{3}0]_\delta || [111]_\alpha \text{ and } (00\bar{3})_\delta || (\bar{1}01)_\alpha; \quad (4.26)$$

$$[\bar{2}10]_\delta || [111]_\alpha \text{ and } (00\bar{3})_\delta || (\bar{1}01)_\alpha; \quad (4.27)$$

$$[1\bar{2}0]_\delta || [111]_\alpha \text{ and } (00\bar{3})_\delta || (\bar{1}01)_\alpha; \quad (4.28)$$

$$[2\bar{1}0]_\delta || [111]_\alpha \text{ and } (00\bar{3})_\delta || (\bar{1}01)_\alpha; \quad (4.29)$$

$$[\bar{1}20]_\delta || [111]_\alpha \text{ and } (00\bar{3})_\delta || (\bar{1}01)_\alpha; \quad (4.30)$$

$$[320]_\delta || [111]_\alpha \text{ and } (00\bar{3})_\delta || (\bar{1}01)_\alpha; \quad (4.31)$$

$$[\bar{3}\bar{2}0]_\delta || [111]_\alpha \text{ and } (00\bar{3})_\delta || (\bar{1}01)_\alpha; \quad (4.32)$$

$$[\bar{2}\bar{3}0]_\delta || [111]_\alpha \text{ and } (00\bar{3})_\delta || (\bar{1}01)_\alpha; \quad (4.33)$$

$$[230]_\delta || [111]_\alpha \text{ and } (00\bar{3})_\delta || (\bar{1}01)_\alpha \quad (4.34)$$

Just like in the case of precipitates with OR in Eq.4.11., this orientation in bcc Fe also have 32 possible variants. The periodicity of the dislocations in the interface and the strain relaxation is different than the previous OR.

4.5.3 Random orientations of precipitates in the matrix

In addition to the predominant ORs mentioned so far, two random precipitate-matrix orientations are also observed in Zr-ODS. These orientations also possess a relationship with matrix-plane and can be expressed in the form of complete orientation relationships. The HRTEM image of one such precipitate in Zr-ODS is shown in Figure 4.10. The measured and calculated d- spacings of both the particles and matrix are tabulated in Table 4.7. The precipitate is $Y_4Zr_3O_{12}$ with zone axis $[\bar{4}7\ 10]$. The $(\bar{1}10)$

plane of matrix is parallel to $(12\bar{1})$ plane of $Y_4Zr_3O_{12}$. The d-values of these planes are 2.04 and 3.00 respectively. The lattice misfit at the interface is, $\left| \frac{d_{42\bar{3}} - d_{\alpha, \bar{1}10}}{d_{12\bar{1}}} \right| = 33.33\%$. The lattice mismatch is similar to the mismatch for OR in equations 4.34-4.23. The relationship between the planes is: $3d_{101, \alpha} = 2d_{12\bar{1}, \delta}$. This OR is very rare, being only 2% of the precipitate analyzed. The angle between $[2\bar{1}0]$ and $[\bar{4}7\ 10]$ directions are $\sim 47^\circ$. Extensive twinning of the precipitate planes can be observed at the precipitate matrix interface. This can be explained due to the high rotational angle between the closed packed directions [233]. Due to the symmetry of matrix and precipitates, this orientation relationship can be written in 12 different ways.

$$[\bar{4}7\ 10]_\delta || [111]_\alpha \text{ and } (12\bar{1})_\delta || (\bar{1}10)_\alpha; \quad (4.35)$$

$$[4\bar{7}\ \bar{1}0]_\delta || [111]_\alpha \text{ and } (12\bar{1})_\delta || (\bar{1}10)_\alpha; \quad (4.36)$$

$$[\bar{7}\bar{4}\ \bar{1}0]_\delta || [111]_\alpha \text{ and } (211)_\delta || (\bar{1}10)_\alpha; \quad (4.37)$$

$$[\bar{7}\bar{4}\ 10]_\delta || [111]_\alpha \text{ and } (211)_\delta || (\bar{1}10)_\alpha; \quad (4.38)$$

$$[11\ 4\ 10]_\delta || [111]_\alpha \text{ and } (\bar{2}31)_\delta || (\bar{1}10)_\alpha; \quad (4.39)$$

$$[\bar{1}\bar{1}\ \bar{4}\ \bar{1}0]_\delta || [111]_\alpha \text{ and } (\bar{2}31)_\delta || (\bar{1}10)_\alpha; \quad (4.40)$$

$$[\bar{4}\ \bar{1}\bar{1}\ 10]_\delta || [111]_\alpha \text{ and } (\bar{3}21)_\delta || (\bar{1}10)_\alpha; \quad (4.41)$$

$$[4\ 11\ \bar{1}0]_\delta || [111]_\alpha \text{ and } (\bar{3}21)_\delta || (\bar{1}10)_\alpha \quad (4.42)$$

$$[\bar{7}\ \bar{1}\bar{1}\ 10]_\delta || [111]_\alpha \text{ and } (12\bar{1})_\delta || (\bar{1}10)_\alpha; \quad (4.43)$$

$$[7\ 11\ \bar{1}0]_\delta || [111]_\alpha \text{ and } (12\bar{1})_\delta || (\bar{1}10)_\alpha; \quad (4.44)$$

$$[\bar{7}\ \bar{1}\bar{1}\ \bar{1}0]_\delta || [111]_\alpha \text{ and } (211)_\delta || (\bar{1}10)_\alpha; \quad (4.45)$$

$$[11\ 7\ 10]_\delta || [111]_\alpha \text{ and } (211)_\delta || (\bar{1}10)_\alpha; \quad (4.46)$$

These 12 orientations along with 12 possible $(\bar{1}10)/[111]$ pairs in bcc matrix, a total of 32 variants are probable.

The Figure 4.11.(a). shows a spherical $Y_4Zr_3O_{12}$ precipitate of diameter ~ 12 nm. Careful analysis of power spectrum reveals that the spots marked in 4.11.(b). are in agreement with the simulated pattern displayed in 4.10(c). The zone axis is

$[\bar{4}1 \bar{1}1]$. The $(31\bar{1})$ plane of the precipitate ($d=2.26$) is parallel to $(\bar{1}10)$ plane of the matrix($d=2.04$). The lattice mismatch is $\sim 9.7\%$. In this orientation, The equivalent ORs are:

$$[\bar{4}1 \bar{1}1]_{\delta} || [111]_{\alpha} \text{ and } (31\bar{1})_{\delta} || (\bar{1}10)_{\alpha}; \quad (4.47)$$

$$[4\bar{1} 11]_{\delta} || [111]_{\alpha} \text{ and } (31\bar{1})_{\delta} || (\bar{1}10)_{\alpha}; \quad (4.48)$$

$$[\bar{1}\bar{4} 11]_{\delta} || [111]_{\alpha} \text{ and } (131)_{\delta} || (\bar{1}10)_{\alpha}; \quad (4.49)$$

$$[\bar{1}4 11]_{\delta} || [111]_{\alpha} \text{ and } (131)_{\delta} || (\bar{1}10)_{\alpha}; \quad (4.50)$$

$$[1 5 11]_{\delta} || [111]_{\alpha} \text{ and } (4\bar{3}1)_{\delta} || (\bar{1}10)_{\alpha}; \quad (4.51)$$

$$[\bar{1} \bar{5} \bar{1}1]_{\delta} || [111]_{\alpha} \text{ and } (4\bar{3}1)_{\delta} || (\bar{1}10)_{\alpha}; \quad (4.52)$$

$$[\bar{5} \bar{1} 11]_{\delta} || [111]_{\alpha} \text{ and } (3\bar{4}1)_{\delta} || (\bar{1}10)_{\alpha}; \quad (4.53)$$

$$[5 1 \bar{1}1]_{\delta} || [111]_{\alpha} \text{ and } (3\bar{4}1)_{\delta} || (\bar{1}10)_{\alpha}; \quad (4.54)$$

$$[5 4 \bar{1}1]_{\delta} || [111]_{\alpha} \text{ and } (\bar{1}41)_{\delta} || (\bar{1}10)_{\alpha}; \quad (4.55)$$

$$[\bar{5} \bar{4} 11]_{\delta} || [111]_{\alpha} \text{ and } (\bar{1}41)_{\delta} || (\bar{1}10)_{\alpha}; \quad (4.56)$$

$$[4 5 11]_{\delta} || [111]_{\alpha} \text{ and } (\bar{4}11)_{\delta} || (\bar{1}10)_{\alpha}; \quad (4.57)$$

$$[\bar{4} \bar{5}; \bar{1}1]_{\delta} || [111]_{\alpha} \text{ and } (\bar{4}11)_{\delta} || (\bar{1}10)_{\alpha}; \quad (4.58)$$

The orientation relationships and their nature, nature of interface and frequency of occurrence is tabulated in Table 4.8. It is interesting to find that all the precipitates are semi-coherent with the matrix, with at-least one precipitate d-spacing parallel to a matrix d-spacing. This precipitate-matrix correlation in atomic scale is a conclusive evidence to the fact that the Y_2O_3 is dissolving fully during the milling and it is re-precipitating as Y-Zr-O phase during hot-consolidation.

Table 4.8: Summary of the orientation relationships found in as prepared Zr-ODS steel.

Sl.No.	Orientation Relationships	Nature of interface	Relationship between planes	Frequency of occurrence(%)
1	$[2\bar{1}0]_{\delta} \parallel [111]_{\alpha}$	semi-coherent	$5d_{101,\alpha} = 4d_{122,\delta}$	86
2	$[2\bar{1}0]_{\delta} \parallel [111]_{\alpha}$	semi-coherent	$3d_{101,\alpha} = 2d_{003,\delta}$	10
3	$[\bar{4}7\ 10]_{\delta} \parallel [111]_{\alpha}$	semi-coherent	$3d_{101,\alpha} = 2d_{12\bar{1},\delta}$	2
4	$[\bar{4}1\ \bar{1}\bar{1}]_{\delta} \parallel [111]_{\alpha}$	semi-coherent	$d_{101,\alpha} = d_{31\bar{1},\delta}$	2

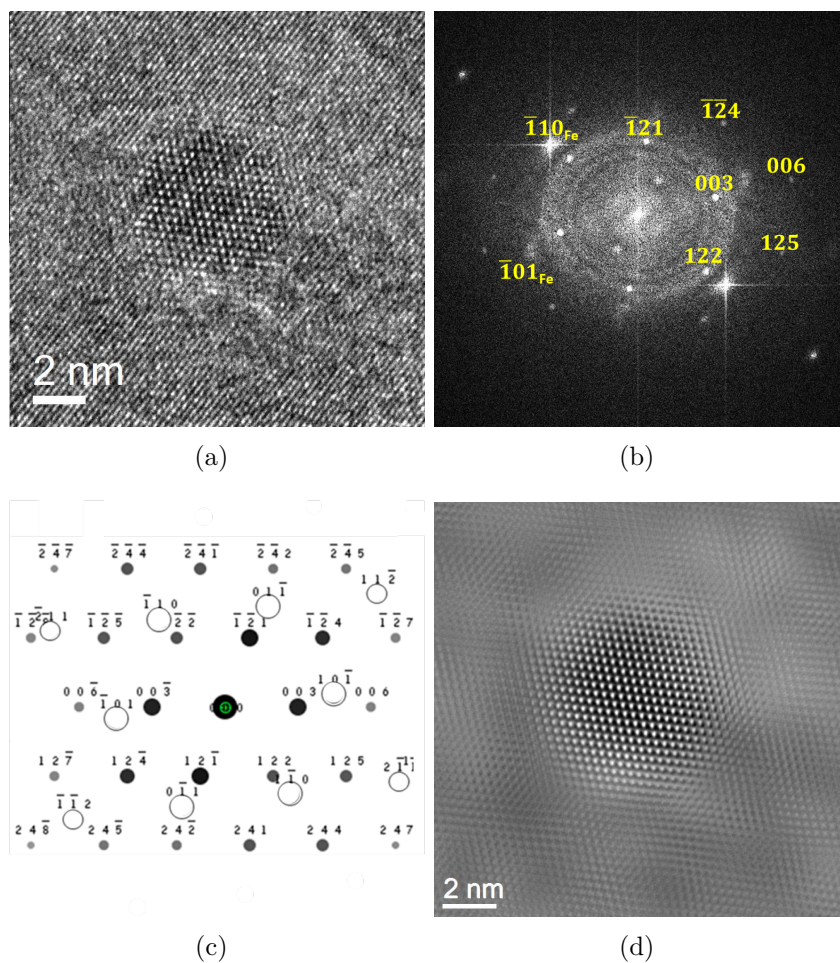


Figure 4.6: (a) HRTEM micrograph of a faceted $Y_4Zr_3O_{12}$ precipitate in Zr-ODS matrix. (b) Power spectrum of the image. The spots corresponding to the matrix are indexed with subscript Fe. (c) Simulated diffraction pattern corresponding to the orientation relationship $(10\bar{1})_{\alpha} || (122)_{\delta}$ and $[111]_{\alpha} || [2\bar{1}0]_{\delta}$ which can be derived from the power spectrum. The open circles indicate matrix-spots and filled circles indicate precipitate-spots. (d) The image reconstructed using precipitate spots of (b).

Table 4.5: Inter-planar distances (d) and angles (α) of the nanoparticle of Figure 4.6

		$d(\text{\AA}), \alpha(^{\circ})$	d_1	d_2	d_3	α_{12}	α_{13}	α_{23}
Particle	Measured		3.00	1.85	2.61	35	53	88
	Planes		$(00\bar{3})$	$(12\bar{4})$	$(\bar{1}2\bar{2})$	-	-	-
	Calculated		3.03	1.85	2.61	35.56	55.03	90.5
Matrix	Measured		2.04	2.04	2.04	60	120	60
	Planes		$(01\bar{1})$	$(10\bar{1})$	$(\bar{1}10)$	-	-	-
	Calculated		2.02	2.02	2.02	60	120	60

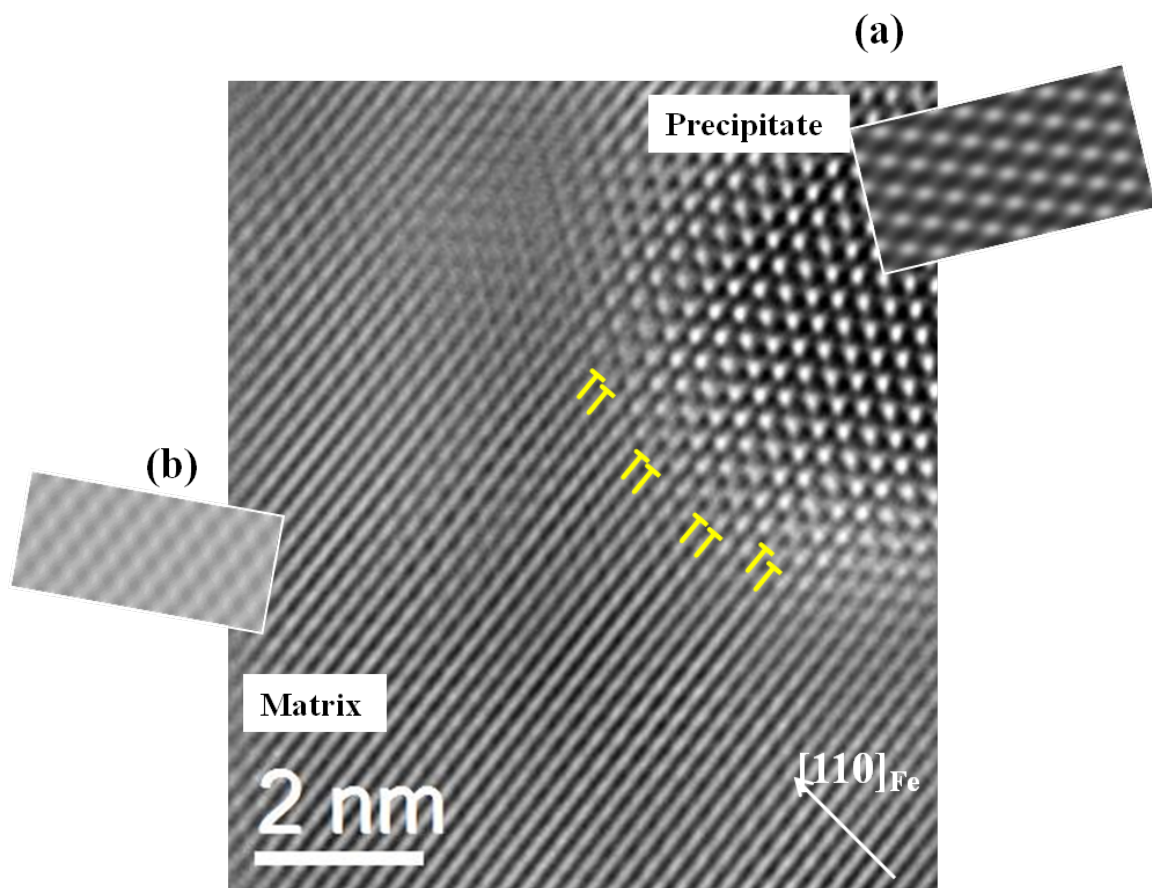


Figure 4.8: The precipitate matrix interface of precipitate in Figure 4.6. The simulated HREM map of precipitate and matrix is shown in regions marked (a) and (b) respectively. The precipitate matrix interface has a periodic array of dislocations, marked in yellow.

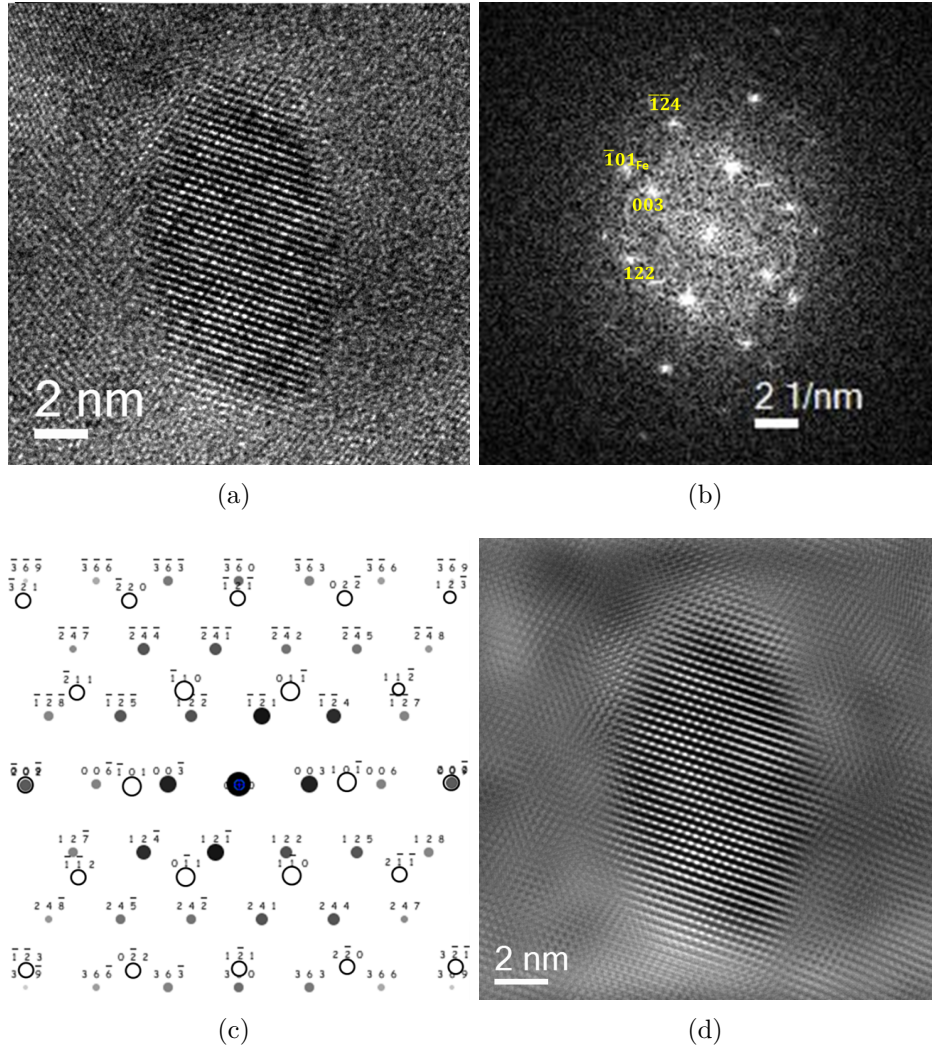


Figure 4.9: (a) HRTEM micrograph of a $Y_4Zr_3O_{12}$ precipitate (b) The power spectrum of (a). (c) A combined diffraction pattern of $[111]_{Fe} || [2\bar{1}0]_{\delta}$ with $(110)_{Fe} || (00\bar{3})_{\delta}$. The matrix spots are shown as open circles. (d) The inverse FFT generated using the precipitate spots of the power spectrum.

Table 4.6: Inter-planar distances (d) and angles (α) of the nanoparticle of Figure 4.9

		$d(\text{\AA}), \alpha(^{\circ})$	d_1	d_2	d_3	α_{12}	α_{13}	α_{23}
Particle	Measured		3.00	1.85	2.61	35.2	54.6	90
	Planes		$(00\bar{3})$	$(12\bar{4})$	$(\bar{1}2\bar{2})$	-	-	-
	Calculated		3.03	1.85	2.61	35	55	90.59
Matrix	Measured		2.04	2.04	2.04	60	120	60
	Planes		$(01\bar{1})$	$(10\bar{1})$	$(\bar{1}10)$	-	-	-
	Calculated		2.02	2.02	2.02	60	120	60

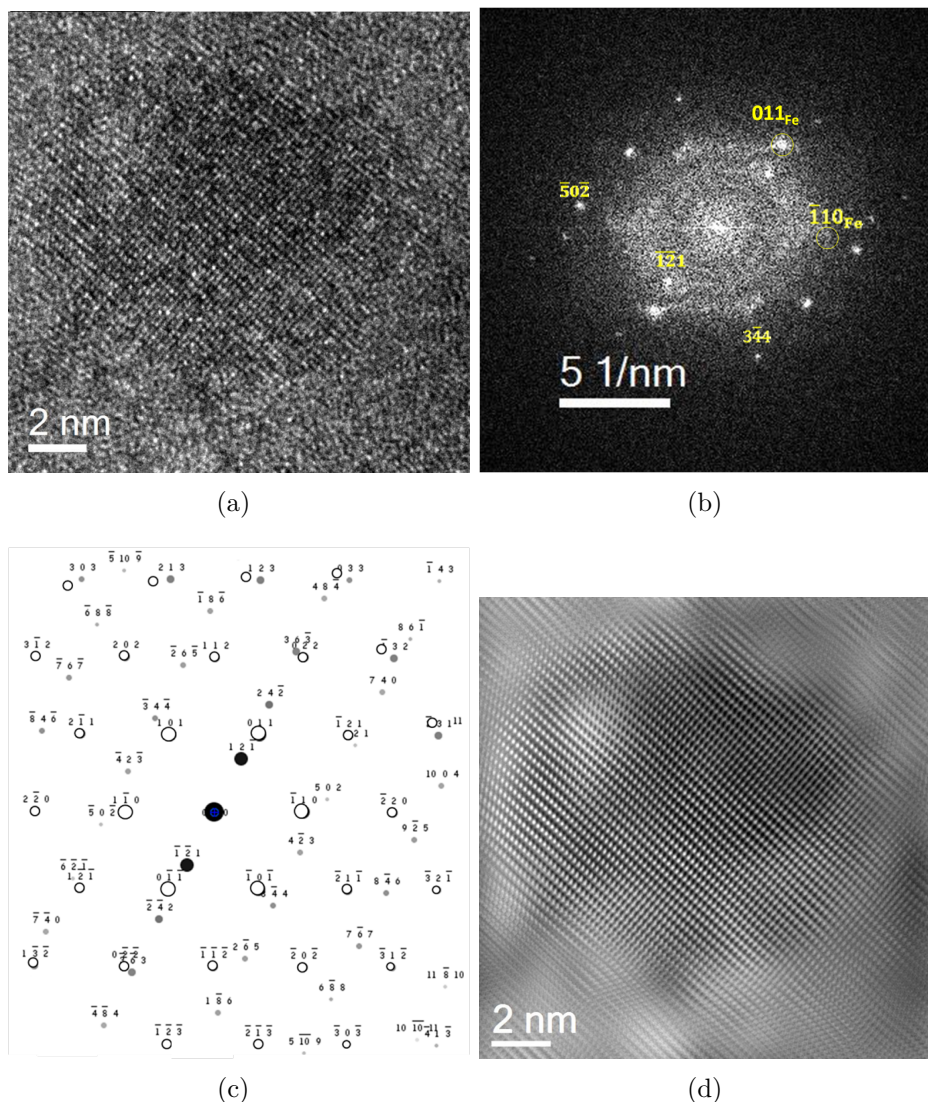


Figure 4.10: (a) HRTEM micrograph of a $Y_4Zr_3O_{12}$ particle in Zr-ODS. (b) Power spectrum of the micrograph with corresponding (hkl) values. The zone axis is $[\bar{4}7\ 10]$ (c) Simulated diffraction pattern of the $[\bar{4}7\ 10]$ zone axis of $Y_4Zr_3O_{12}$ with $[111]$ zone axis of α -Fe. The open circles corresponds to matrix spots and the filled circles corresponds to precipitate spots (d) IFFT constructed from power spectrum using precipitate spots.

Table 4.7: Inter-planar distances (d) and angles (α) of the nanoparticle of Figure 4.10

$d(\text{\AA}), \alpha(^{\circ})$	d_1	d_2	d_3	α_{12}	α_{13}	α_{23}
Measured	1.56	3.0	1.91	56.0	31.2	88
Planes	$(\bar{5}0\bar{2})$	$(\bar{1}\bar{2}1)$	$(\bar{4}2\bar{3})$	-	-	-
Calculated	1.58	3.01	1.90	56.3	31.7	88.01

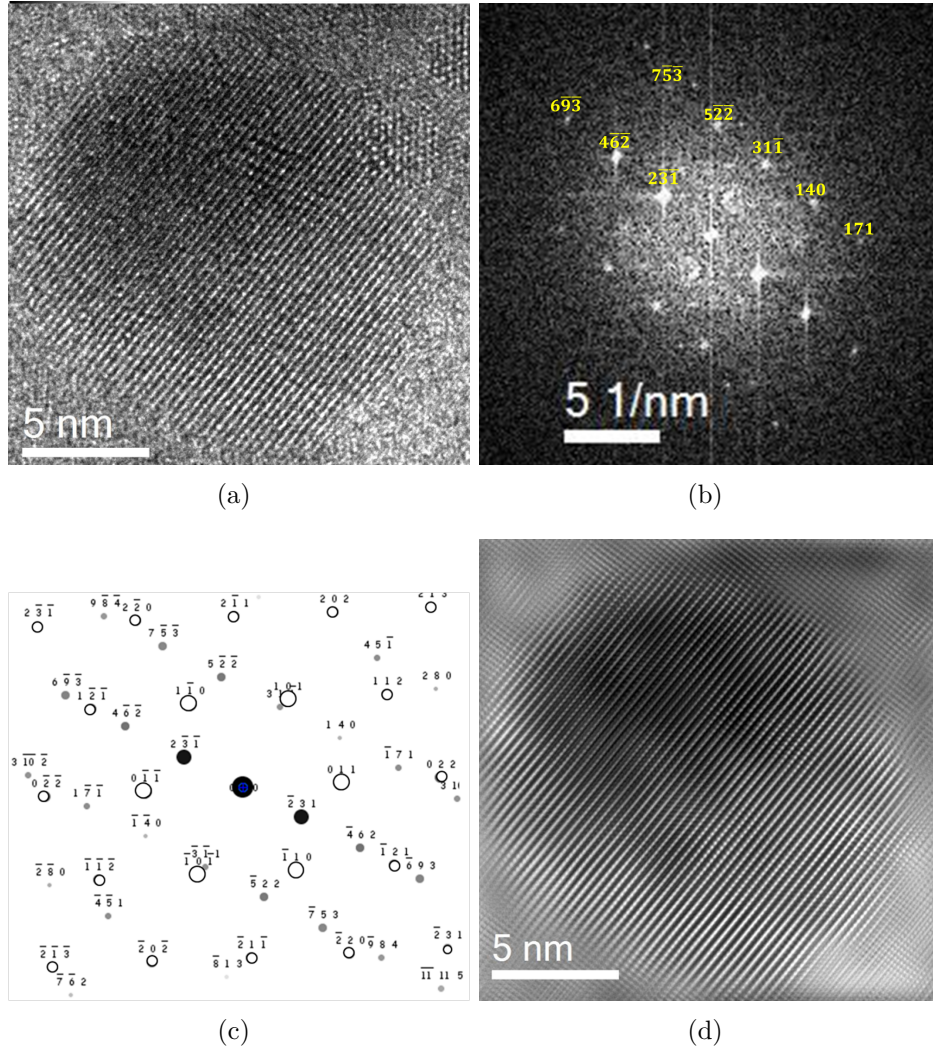


Figure 4.11: The HRTEM micrograph and its power spectrum of a precipitate in Zr-ODS is shown in (a) and (b). The spots marked in (b) correspond to $[\bar{4}1\bar{1}]$ zone axis of $Y_4Zr_3O_{12}$. The theoretical diffraction pattern and noise-filtered image (inverse FFT) is shown in (c) and (d).

Table 4.9: Inter-planar distances (d) and angles (α) of the nanoparticle of Figure 4.11

$d(\text{\AA}), \alpha(^{\circ})$	d_1	d_2	d_3	α_{12}	α_{13}	α_{23}
Measured	1.9	1.59	3.0	56	88	32
Planes	$(\bar{4}2\bar{3})$	$(50\bar{2})$	$(\bar{1}\bar{2}1)$	-	-	-
Calculated	1.9	1.58	3.0	56	88	32

4.5.4 Chemistry of dispersoids in Al-ODS

Most of the precipitates in Al-ODS were spherical and well-formed. There is no sign of core-shell structure in the micrographs. One precipitate with $[2\bar{1}0]$ orientation shown in Figure 4.13. The precipitate is spherical, fully crystallized with a diameter ~ 13 nm. The power spectrum of the micrograph, simulated diffraction pattern and image reconstructed using the diffraction spots are shown in 4.13(b), (c) and (d) respectively. The measured and calculated d-spacings are tabulated in the Table 4.11. Nearly 74% of the precipitates examined have this orientation and are in the size range of 2-15 nm. Most of them have a diameter of less than 10 nm. This could be because it has a preferred orientation in the Al -ODS matrix, similar to the Zr-ODS matrix.

A relatively large precipitate, of diameter ~ 28 nm is presented in Figure 4.16. The structure of this precipitate is $Y_4Zr_3O_{12}$ and the zone axis is $[0\bar{5}\bar{2}]$. The power spectrum and simulated pattern is presented in 4.16 (b), (c) and (d).

Another $Y_4Zr_3O_{12}$ precipitate, of diameter ~ 13 nm is shown in Figure 4.17. The precipitate is oriented along $[\bar{4}1\ \bar{1}\bar{1}]$, which is also a zone axis of $Y_4Zr_3O_{12}$ in Zr -ODS (*refer to* Figure 4.7). The precipitates with this orientation are $\sim 10 - 15$ nm in dimension, which is consistent in the case of Al-ODS also. The power spectrum, simulated diffraction pattern and inverse FFT of $[\bar{4}7\ 10]$ direction of $Y_4Zr_3O_{12}$ is presented in 4.17(b), (c) and (d).

Unlike Zr-ODS, which contained only $Y_4Zr_3O_{12}$ precipitates, there are signatures of monoclinic, tetragonal, and cubic ZrO_2 precipitates in Al-ODS. An example of monoclinic ZrO_2 oriented along $[111]$ zone axis is included in the Figure 4.18. along with the power spectrum, theoretical pattern, and the FFT filtered image.

The tetragonal ZrO_2 are more common than monoclinic ZrO_2 precipitates. They are spherical with well-defined boundaries and have a size range of 10 - 20 nm. A tetragonal ZrO_2 precipitate is shown in Figure 4.14, which is aligned with $[101]$ zone axis. The simulated pattern and FFT filtered image are also included along with the diffraction pattern and HRTEM. Figure 4.12 shows a tetragonal ZrO_2 precipitate of zone axis $[201]$. The d-spacings are listed in Table 4.10.

Cubic ZrO_2 structure is rare(2%), like monoclinic ZrO_2 . HRTEM micrograph of a nearly spherical cubic- ZrO_2 precipitate of diameter ~ 10 nm is presented in the Figure 4.15. The power spectrum of the precipitate shown in 4.15(b) matches well

with the simulated diffraction pattern of cubic ZrO_2 structure along [001] zone axis. The precipitate image reconstructed using spots in 4.15(b) is shown in 4.15(d).

In short, in Al-containing ODS steel, majority (78%) of the nanoparticles are consistent with trigonal-rhombohedral $\text{Y}_4\text{Zr}_3\text{O}_{12}$ structure. A few monoclinic, tetragonal and cubic ZrO_2 precipitates were also found. Earlier, P. Dou *et al.* [66], has observed $\sim 87.4\%$ of precipitates belonged to Y-Zr-O structures, 5.7% were Y-Ti-O, 3.5% were Y-Al-O structures and 3.4% were monoclinic/tetragonal/cubic ZrO_2 . But in the current study, Al-containing phases were completely absent, which is in agreement with the simulation results of Chapter 3., that in an alloy with Y, Al, Zr, and O, Zr containing phases are more probable. In alloys with lower Zr content, the fraction of Y-Ti-O and Y-Al-O phases were much larger. Thus 0.63% Zr seems to be optimum for getting the desired precipitate size in Al-containing ODS steels.

During ball milling, fragmentation and dissolution of Y_2O_3 ($\text{Y}_2\text{O}_3 \rightarrow 2[\text{Y}] + 3[\text{O}]$) has been reported earlier. In presence of Zr, which readily oxidises to ZrO_2 ($\text{Zr} + 2[\text{O}] \rightarrow \text{ZrO}_2$), a complex internal oxidation reaction ($2\text{Y}_2\text{O}_3 + 3\text{ZrO}_2 \rightarrow \text{Y}_4\text{Zr}_3\text{O}_{12}$) occurs during hot consolidation which may be resulting in precipitation as $\text{Y}_4\text{Zr}_3\text{O}_{12}$. The presence of ZrO_2 is supportive to this hypothesis.

Zirconia (ZrO_2) exists as different polymorphs, depending on the temperature, pressure, and size of the atomic cluster forming the precipitate. In its bulk form, ZrO_2 exhibits a monoclinic structure at ambient conditions [235]. The transition from monoclinic to tetragonal structure occurs at 1170°C , however, the transition temperature is a function of grain size. Tetragonal to cubic structural transformation occurs at 2450°C to 2675°C . It is well known that even though tetragonal and cubic polymorphs of ZrO_2 cannot be quenched to room temperature, the phases can be stabilized by the addition of large cations like lanthanides and yttrium. Here, in the Al-ODS matrix, with the heat treatment at 1050°C , the presence of yttrium and the small size of the precipitates is playing a major role in stabilizing cubic and tetragonal ZrO_2 phases at room temperature along with the monoclinic phase. The precipitate phases found in Al-ODS are tabulated in the Table 4.17

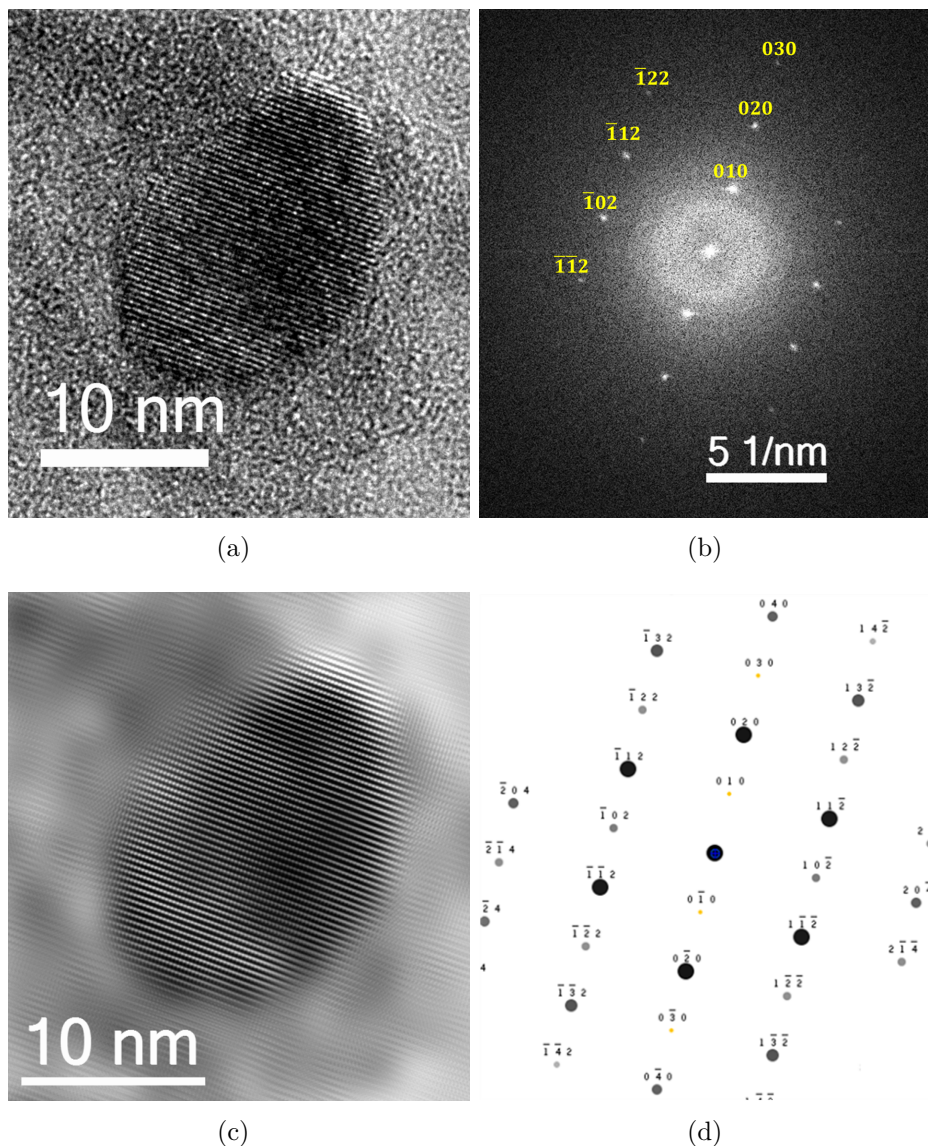


Figure 4.12: (a) HRTEM micrograph of a tetragonal ZrO₂ precipitate in Al-ODS, (b) power spectrum of micrograph with corresponding (hkl) values, zone axis is identified to be [201] (c) IFFT constructed using the spots in (b) and (d) The simulated diffraction pattern of [201] zone axis of tetragonal ZrO₂ as per ICDD: 00-065-0729.

Table 4.10: Inter-planar distances (d) and angles (α) of the monoclinic ZrO₂ nanoparticle of Figure 4.12. The zone-axis is [201]

$d(\text{\AA}), \alpha(^{\circ})$	d_1	d_2	d_3	α_{12}	α_{13}	α_{23}
Measured	1.85	2.10	1.81	30.3	61.2	30.3
Planes	$(\bar{1}12)$	$(\bar{1}02)$	$(\bar{1}\bar{1}2)$	-	-	-
Calculated	1.82	2.10	1.81	31.6	60.59	29.6

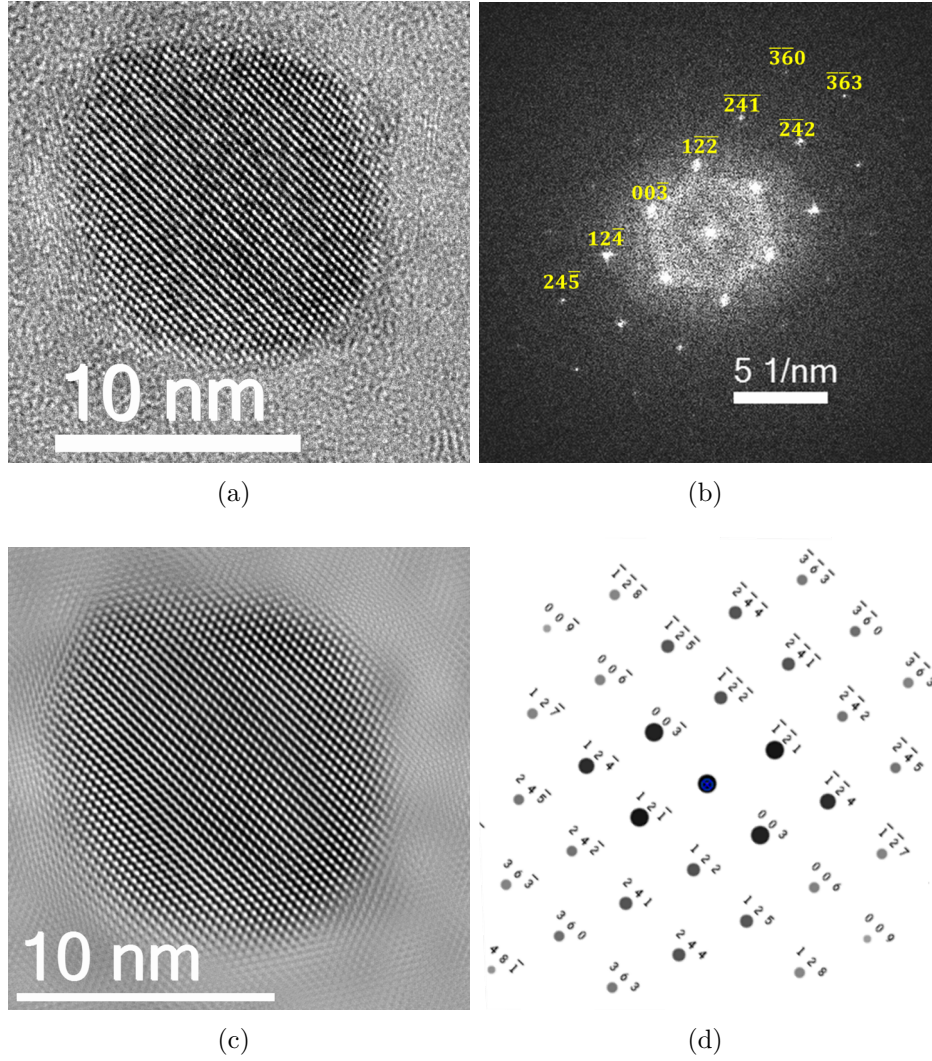


Figure 4.13: The HRTEM image of a $Y_4Zr_3O_{12}$ nanoprecipitate of diameter ~ 13 nm found in Al-ODS steel. The power spectrum of precipitate in (a) is shown in (b). The power spectrum is compared with simulated diffraction pattern shown in (c) and zone axis is $[2\bar{1}0]$. The precipitate image reconstructed using spots in (b) is shown in (d).

Table 4.11: Inter-planar distances (d) and angles (α) of the $Y_4Zr_3O_{12}$ nanoparticle in Figure 4.13 with zone-axis $[2\bar{1}0]$

$d(\text{\AA}), \alpha(^{\circ})$	d_1	d_2	d_3	α_{12}	α_{13}	α_{23}
Measured	3.0	2.95	1.76	69	36	34
Planes	(003)	$(\bar{1}\bar{2}\bar{2})$	$(\bar{1}\bar{2}\bar{4})$	-	-	-
Calculated	3.0	3.03	1.85	70.7	35.55	35.1

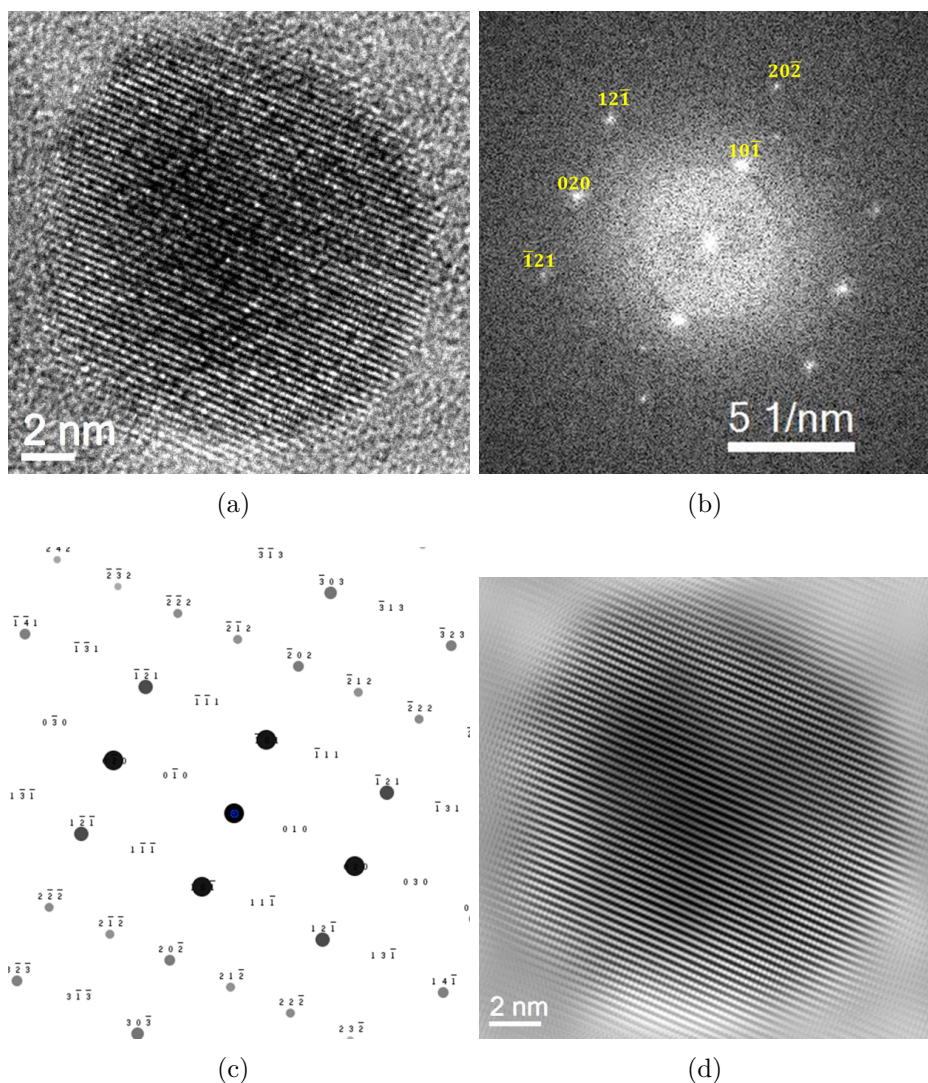


Figure 4.14: HRTEM micrograph of a nearly spherical tetragonal ZrO_2 precipitate in Al-ODS. The power spectrum of the precipitate shown in (b) matches well with the simulated diffraction pattern of tetragonal ZrO_2 structure along $[101]$ zone axis (ICDD: 00-065-0729). The precipitate image reconstructed using spots in (b) is shown in (d).

Table 4.12: Inter-planar distances (d) and angles (α) of the ZrO_2 nanoparticle in Figure 4.14. The structure is tetragonal with zone-axis $[101]$

$d(\text{\AA}), \alpha(^{\circ})$	d_1	d_2	d_3	α_{12}	α_{13}	α_{23}
Measured	1.56	2.95	1.80	58.6	31.5	90
Planes	$(12\bar{1})$	$(10\bar{1})$	(020)	-	-	-
Calculated	1.536	2.95	1.798	58.67	31.33	90

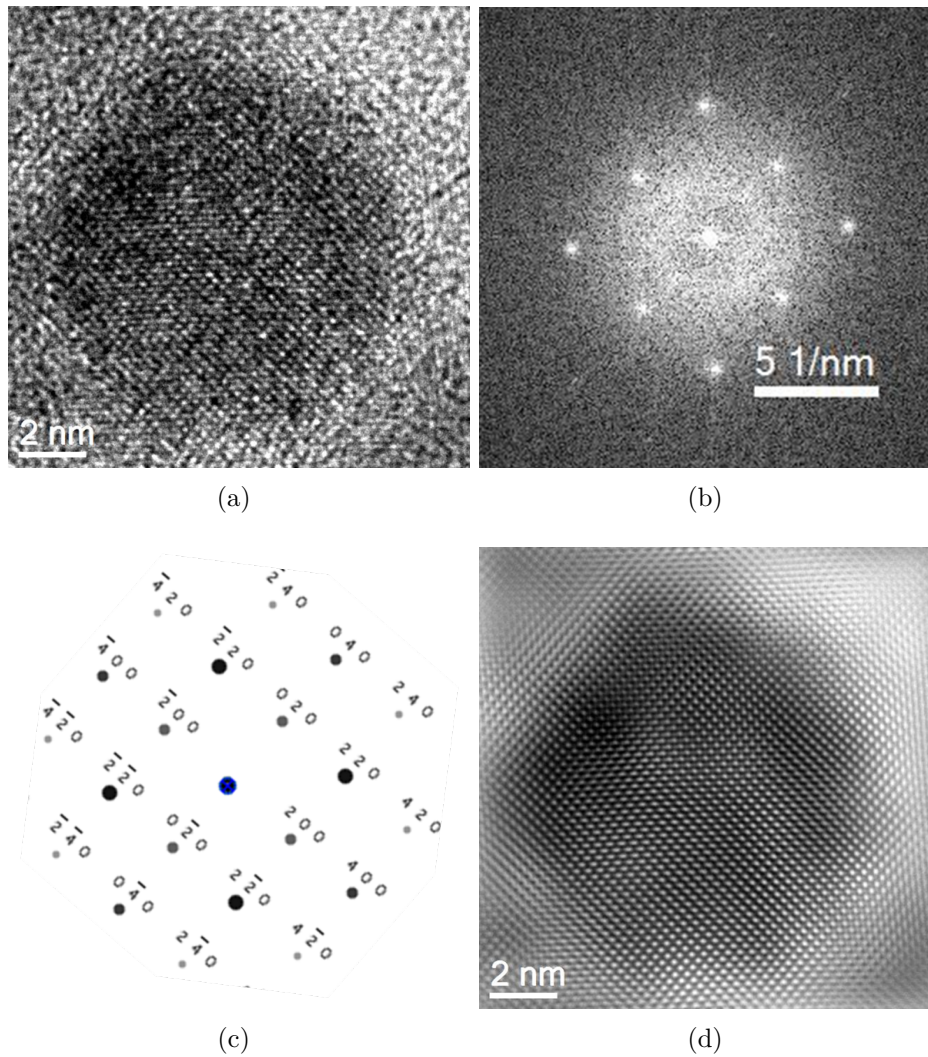


Figure 4.15: HRTEM micrograph of a nearly spherical cubic -ZrO_2 precipitate of diameter ~ 10 nm. The power spectrum of the precipitate shown in (b) matches well with the simulated diffraction pattern of cubic ZrO_2 structure along $[001]$ zone axis. The precipitate image reconstructed using spots in (b) is shown in (d).

Table 4.13: Inter-planar distances (d) and angles (α) of the ZrO_2 nanoparticle in Figure 4.15. The structure is face centered cubic with zone-axis $[001]$

$d(\text{\AA}), \alpha(^{\circ})$	d_1	d_2	d_3	α_{12}	α_{13}	α_{23}
Measured	1.76	2.49	1.76	45	90	45
Planes	$(\bar{2}20)$	$(\bar{2}00)$	$(\bar{2}\bar{2}0)$	-	-	-
Calculated	1.74	2.46	1.74	45	90	45

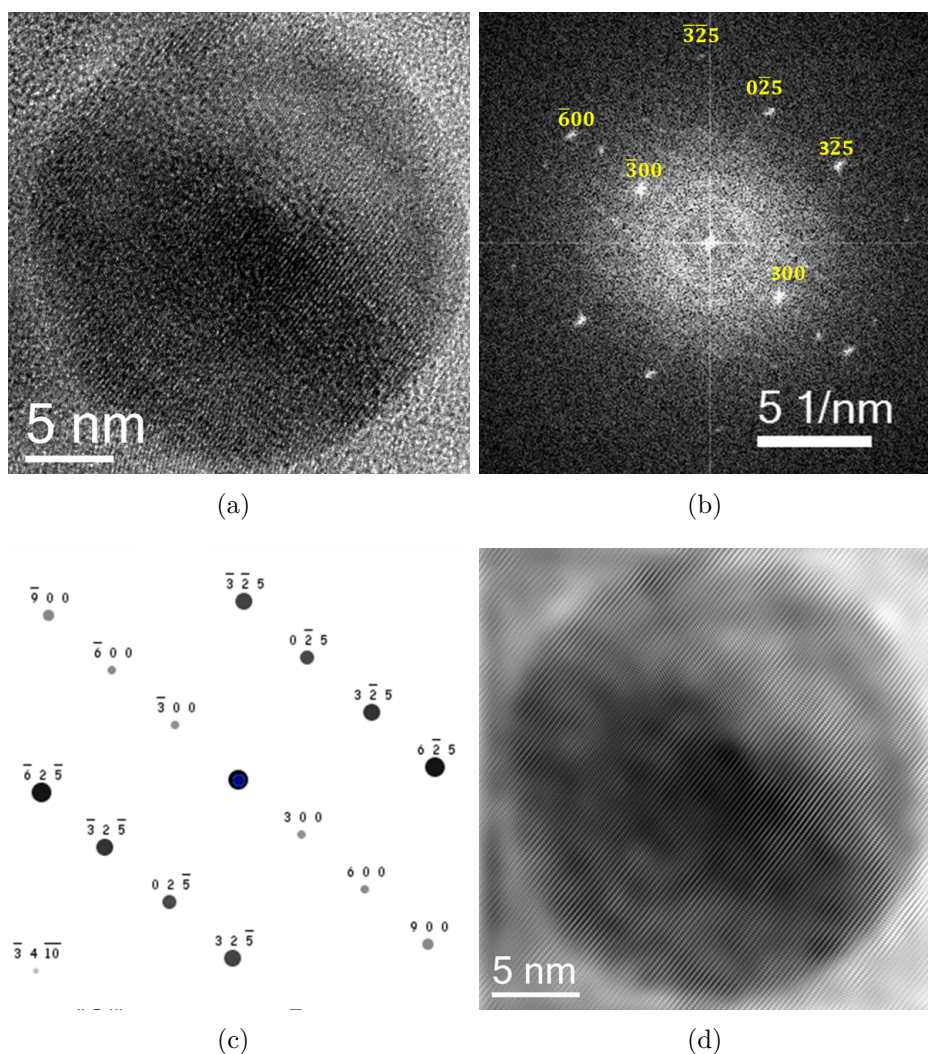


Figure 4.16: (a) shows a $Y_4Zr_3O_{12}$ precipitate of diameter ~ 28 nm. The power spectrum can be identified as $[0\bar{5}2]$ zone axis and is in agreement with the simulated pattern shown in (c). The FFT filtered image is presented in (d).

Table 4.14: Inter-planar distances (d) and angles (α) of the $Y_4Zr_3O_{12}$ nanoparticle in Figure 4.16.

$d(\text{\AA}), \alpha(^{\circ})$	d_1	d_2	d_3	α_{12}	α_{13}	α_{23}
Measured	1.63	1.55	2.60	73	33.6	106.6
Planes	$(\bar{3}1\bar{1})$	$(\bar{3}00)$	$(0\bar{1}1)$	-	-	-
Calculated	1.68	1.58	2.81	68	33.5	101.5

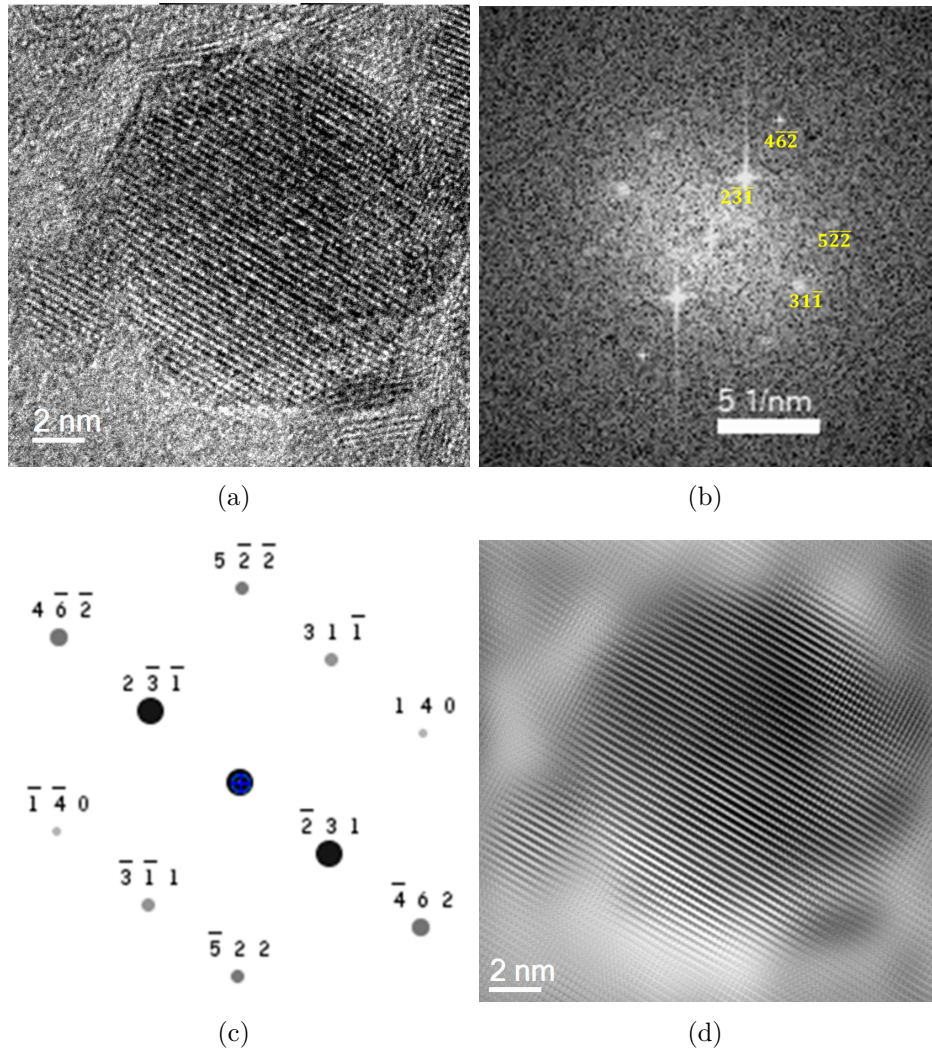


Figure 4.17: (a) shows a $Y_4Zr_3O_{12}$ precipitate of diameter ~ 13 nm. The power spectrum can be identified as $[\bar{4}1\bar{1}]$ zone axis and is in agreement with the simulated pattern shown in (c). The FFT filtered image is presented in (d).

Table 4.15: Inter-planar distances (d) and angles (α) of the $Y_4Zr_3O_{12}$ nanoparticle in Figure 4.17.

$d(\text{\AA}), \alpha(^{\circ})$	d_1	d_2	d_3	α_{12}	α_{13}	α_{23}
Measured	3.0	2.13	1.76	58.9	34.6	89.1
Planes	$(\bar{3}1\bar{1})$	$(\bar{3}00)$	$(0\bar{1}1)$	-	-	-
Calculated	3.0	2.26	1.78	97.49	56.67	88.04

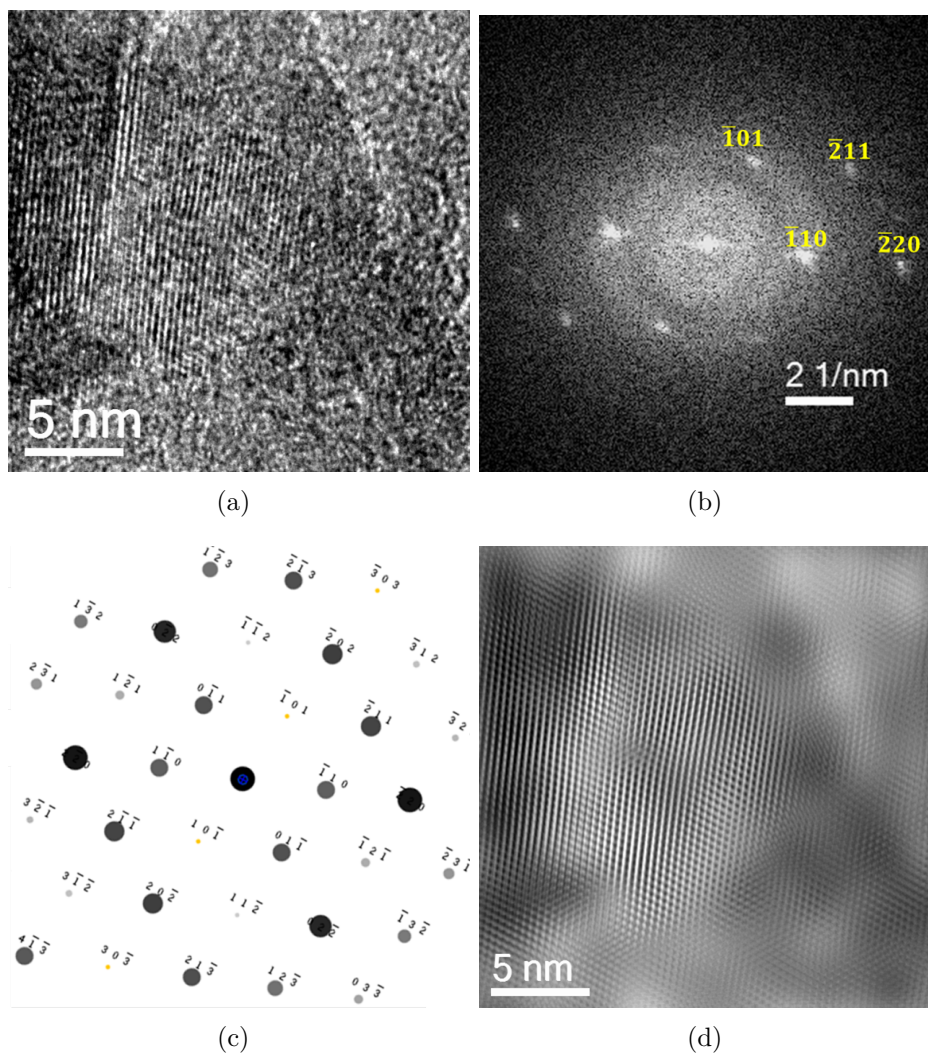


Figure 4.18: (a) HRTEM micrograph of a monoclinic ZrO_2 precipitate in Al-ODS steel. (b) The power spectrum generated from (a). The zone axis is identified to be $[111]$. (c) Simulated diffraction spots along $[111]$ direction of monoclinic ZrO_2 (ICDD 00-036-0420). (d) The inverse FFT generated using the spots in (b).

Table 4.16: d-spacings and angles of the monoclinic ZrO_2 nanoparticle of Figure 4.18.

$d(\text{\AA}), \alpha(^{\circ})$	d_1	d_2	d_3	α_{12}	α_{13}	α_{23}
Measured	3.73	2.19	3.61	32.4	29.9	61.7
Planes	$(\bar{1}01)$	$(\bar{2}11)$	$(\bar{1}10)$	-	-	-
Calculated	3.98	2.21	3.63	32.40	30.3	62.4

Table 4.17: The chemistry of precipitates in Al-ODS steel.

S.No	Structure	Frequency of occurrences(%)
1	$Y_4Zr_3O_{12}$	78
2	ZrO ₂ -M	2
3	ZrO ₂ -T	18
4	ZrO ₂ -C	2

4.6 Conclusions

In the present chapter, the *ab initio* predictions on the chemistry of the dispersoids, previously discussed in Chapter 3. have been substantiated using experimental investigations. As a starting point, the ODS steels with compositions Fe-14Cr-0.3Y₂O₃-0.63Zr (Zr-ODS) and Fe-14Cr-0.3Y₂O₃-0.63Zr-4Al (Al-ODS) are successfully synthesized by mechanical alloying and hot extrusion. TEM observations show that both the alloys have nano-sized grains, 234 nm for Zr-ODS and 376 nm for Al-ODS. This nano-metric grain size is expected to contribute towards the enhanced corrosion resistance and radiation tolerance of these alloys.

The average precipitate size in Al-ODS is higher than that in Zr-ODS. The fine sized, high number density of dispersoids in Zr-ODS will be responsible for increased tolerance for radiation-induced defects. The empirical analysis shows that in both the alloys Orowan bypassing mechanism is predominant than the dislocation shearing mechanism of the precipitation strengthening. This also implies that the majority of the precipitates are either semi-coherent or incoherent with the matrix.

There is a predominant precipitate(δ)-matrix (α) orientation relationship, $[2\bar{1}0]_{\delta}||[111]_{\alpha}$ and $(122)_{\delta}||(\bar{1}01)_{\alpha}$ in Zr-ODS steel. This is similar to Pitsche-Shrader (PS) orientation relationship in bcc/hcp interface. Just as Burger's OR can be deduced from PS OR by a rotation of $\sim 5.3^{\circ}$, a new OR can be deduced from the predominant OR for trigonal/bcc interface. This new OR is: $[2\bar{1}0]_{\delta}||[111]_{\alpha}$ and $(122)_{\delta}||(\bar{1}0\bar{3})_{\alpha}$. Along with these two ORs, two random ORs, $[\bar{4}1\bar{1}]_{\delta}||[111]_{\alpha}$ and $(31\bar{1})_{\delta}||(\bar{1}10)_{\alpha}$ and $[\bar{4}7\ 10]_{\delta}||[111]_{\alpha}$ and $(12\bar{1})_{\delta}||(\bar{1}10)_{\alpha}$; are also observed. A rough analysis estimates 32 possible variants in each OR. The existence of predominant OR is conclusive of

the fact that that the oxide powder gets completely dissolved in the matrix during milling and precipitates in a preferred way during the hot-consolidation process. All the precipitates have semi-coherent interface, testifying the empirical calculations.

All the precipitates in Zr -ODS have $Y_4Zr_3O_{12}$ structure. Al-ODS contains monoclinic, tetragonal and cubic ZrO_2 precipitates along with $Y_4Zr_3O_{12}$. However, the precipitates containing Al are absent in both the alloys. This is in exact agreement with the simulation results presented in Chapter 3. This also affirms the significance of first principle simulations as a predictive tool for precipitation kinetics in multi-component alloys.

Now that we have synthesized and characterized Zr-ODS and Al-ODS alloys, our next task is to evaluate the radiation response of these alloys. The information obtained on the micro-structure and precipitate chemistry of these alloys might come handy in interpreting the irradiation behaviour of these alloys.

Study of vacancy defects in self-ion irradiated Zr and Al containing ODS steels

5.1 Introduction

In previous chapter, it is observed that the as-prepared Al-ODS and Zr-ODS steels have nanometric grains and high density of fine dispersoids, predominantly $Y_4Zr_3O_{12}$. The radiation stability of these materials is important for future applications and ion irradiation is commonly employed as a convenient way to emulate the neutron irradiation inside the reactor. Irradiations using self-ions do not introduce any foreign atom into the matrix, and therefore they are a preferred choice to study the damage and vacancy defects. There are several studies showing that the presence of dispersoids in Ti-containing ODS effectively prevents the formation and clustering of vacancies. However, similar data on Zr and Al containing ODS steels are unavailable in the existing literature.

The positron annihilation spectroscopic techniques are an indispensable aid in examining the creation and evolution of vacancy related defects in materials. Therefore, in the present work, positron annihilation spectroscopy is employed to characterize the inherent and irradiation-induced open volume defects in Zr-ODS and Al-ODS steels. At first positron lifetime components are deduced using positron lifetime spectroscopy,

which are fitted to positron trapping model to predict the nature and number density of defects in the pristine materials. Further, both the alloys are irradiated with 1.6 MeV Fe⁺ ions at room temperature and high-temperature with different doses using 1.6 MV Tandetron accelerator (mentioned in Section 2.4.1). The irradiation-induced open volume defects in the alloys are studied using depth-resolved positron beam spectroscopy (*refer to* Section 2.5.).

5.2 Experimental methods

Positron annihilation lifetime spectroscopy (PALS) provides quantitative information about the defects in the sample. The room-temperature positron lifetime spectra are obtained for as-prepared Zr-ODS and Al-ODS steels from the experimental set-up described in Chapter 2. After subtracting the corrections due to the source and instrumental resolution, the measured lifetime spectra were analyzed for different lifetime components and intensities using LT09 software [236].

Further, the samples were irradiated by 1.6 MeV Fe⁺ ions using the 1.7 MV tandem accelerator. The damage profile is simulated using Stopping Range of Ions in Matter (SRIM) software [237]. The SRIM damage and implanted ion profile for 1.6 MeV Fe⁺ in Fe for a full cascade simulation of $\sim 10^6$ Fe ions is presented in Figure 5.1. The projected range of the ion is ~ 560 nm and the peak damage occurs at ~ 480 nm. The electronic and nuclear stopping powers are ~ 200 eV/Å and ~ 72 eV/Å respectively. It should be noted that the SRIM calculations are done at 0K. This implies that the diffusion, annealing and clustering of vacancy and interstitial defects, which will occur during irradiation, are not taken into account in these calculations. The implantation is done at a vacuum of $\sim 10^{-7}$ mbar with a fixed current of 200 nA. The Al-ODS and Zr-ODS specimen were irradiated to a displacement damage of 100 dpa at room temperature as well as 340 °C. Further, the Zr-ODS samples were irradiated to 150 dpa. The dose rate is maintained at 2.1×10^{-3} dpa/s.

Positron beam measurements are carried out by tuning the energy of positrons from 0.2 to 22 keV in steps of 0.5 keV, using a magnetically guided system [175]. A Doppler broadened spectrum of $\sim 10^6$ counts is collected in each energy step using an HPGe detector. The S and W-parameters were deduced from the Doppler broadened

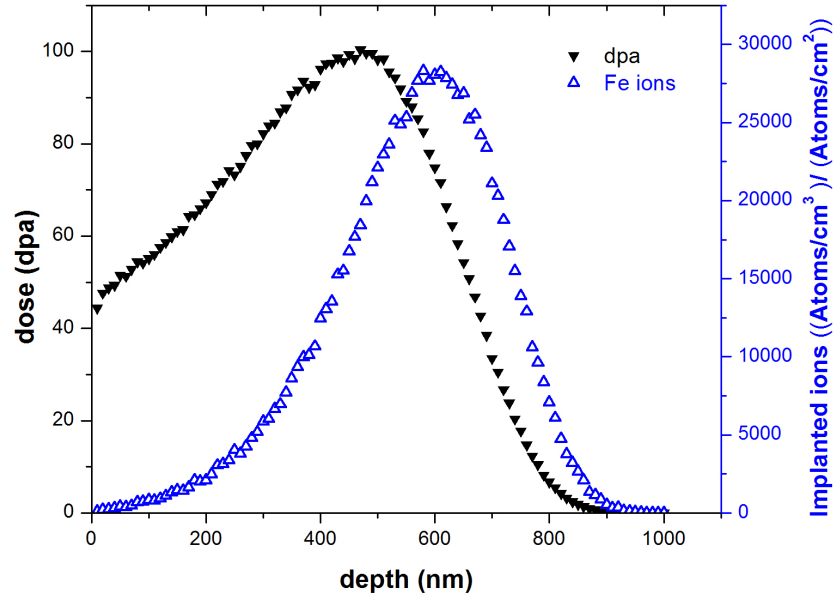


Figure 5.1: Depth distribution of displacement damage and implanted ions in 1.6 MeV Fe^+ irradiated Fe, calculated using SRIM. The peak damage is 100 dpa at 480 nm.

spectrum. The variation of the S-parameter with positron beam energies are analyzed using VEPFIT program [238]. The VEPFIT program separates the contributions to S-parameter from the surface, defect and bulk states, by solving the positron diffusion equation. Using this program, the experimental spectrum ($S(E)$) can be de-convoluted as:

$$S(E) = f_s S_s + f_{d1} S_{d1} + f_{d2} S_{d2} + \dots + f_b S_b \quad (5.1)$$

where f_s , f_d and f_b are the fraction of positrons annihilating at the surface, defect and bulk states respectively and S_s , S_d and S_b are corresponding S-parameters. Further, the simulated and experimental curves are compared to calculate the S-parameter values at various positron states, diffusion lengths of positrons and thickness of the damage layers created.

5.3 Estimation of defect concentration in as-prepared Zr/Al - ODS alloys using positron annihilation lifetime spectroscopy

Both Al-ODS and Zr-ODS show two positron lifetime components. Two-component analysis requires three parameters to fit, τ_1 , τ_2 and I_1 . The two lifetime components for Al-ODS and Zr-ODS are tabulated in the Table 5.1. These lifetime values are consistent with earlier reports on ODS steels [78, 88, 239, 240].

The PALS measurements can provide information on the nature, size and concentration of the defects. In Fe, the defect-free lifetime is 110 ps, while the lifetime associated with mono-vacancy is approximately 175 ps [241]. The lifetime values in the range 140-170 ps which are considerably higher than the bulk lifetime, but lower than the lifetime of mono-vacancies, are attributed to dislocations in the matrix [242, 243]. The lifetime of 200-500 ps is reported to be arising from three-dimensional vacancy clusters [239, 241, 243, 244]. The lifetime in a vacancy cluster increases with an increase in the number of constituent vacancies [245]. Di-vacancies give a lifetime of 188 ps and voids consisting of 177 vacancies are associated with positron lifetime of 435 ps [246]. Also, there are reports with long lifetime $\sim (360 \pm 30)$ ps in nanograined (6 nm) iron, attributed to nanovoids at grain intersections [243]. Ultra-pure Fe with high speed deformation exhibited a long lifetime of ~ 340 ps due to vacancy clusters [245]. Positron lifetimes are longer in some oxides. In TiO_2 the lifetime is ~ 180 ps [239]. The lifetime in Y_2O_3 is 240 ps [247] and in $\text{TiZnBiNb}_2\text{O}_7$ pyrochlores, it is 300 ps [248].

On the basis of these literature [78, 239], the lifetime τ_1 can be ascribed to dislocations in the matrix. The second lifetime component, τ_2 can be arising due to nano-features in the matrix or vacancy clusters resulting from mechanical alloying.

According to standard two-component trapping model [249]:

$$\frac{1}{\tau_1} = \frac{1}{\tau_b} + \kappa = \lambda_b + \kappa; \quad (5.2)$$

$$\tau_2 = \frac{1}{\lambda_d} = \tau_d; \quad (5.3)$$

$$\kappa = \frac{I_2}{I_1}(\lambda_b - \lambda_d) \quad (5.4)$$

Table 5.1: PALS lifetimes and corresponding intensities of Zr-ODS and Al-ODS steels.

Sample	$\tau_1(ps)$	I_1	$\tau_2(ps)$	I_2
Zr-ODS	156±8	94.2%	301±12	5.8%
Al-ODS	161±7	91%	380±18	9%

where κ is the trapping rate, λ_b and λ_d are the annihilation rates in the bulk matrix and trapping sites respectively. For defect free Fe matrix, $\tau_b = 110$ ps [246].

This model, however does not provide satisfactory results when the first component is well above the bulk value and the second component is well separated from the first component [78, 239, 241]. Therefore, the first component can be assumed as the weighted average of bulk and a shorter lifetime trap, like dislocations. The longer lifetime is often attributed to vacancy clusters and nanoprecipitates in the matrix. In such cases, trapping rates are given by [241]:

$$\kappa_{d_1} = \frac{\tau_1(\lambda_b - I_2\lambda_{d_2}) - I_1}{\tau_{d_1} - \tau_1} = \mu_{d_1}N_{d_1} \quad (5.5)$$

$$\kappa_{d_2} = \frac{I_2}{I_1}(\lambda_b - \lambda_{d_2} + \kappa_{d_1}) = \mu_{d_2}N_{d_2} \quad (5.6)$$

The $\tau_{d_1} = 170$ ps, which is a fixed value for dislocations from literature [78]. $\mu_{d_1} = (0.6 \pm 0.2) \times 10^{-4}$ m²/s, is the trapping coefficient for dislocations [250] and $\mu_{d_2} = (1.3 \pm 0.2) \times 10^{-14}$ m³/s is the trapping coefficient for mono vacancies [239, 241]. N_{d_1} is the number density of dislocations and N_{d_2} is the number density of vacancy clusters or nanofeatures.

For vacancy clusters the positron trapping rate is given by [241]:

$$\kappa_{vc} = n\mu_{d_1}N_{vc} \quad (5.7)$$

where n is the number of vacancies(n), N_{vc} (m⁻³) is the number density of the clusters and μ_{d_1} is the trapping coefficient for monovacancies. For nanoprecipitates, the

positron trapping is diffusion limited and is given by [174, 239]:

$$\kappa_{nf} = 4\pi r D_+ N_{nf}; \quad D_+ = \frac{L_+^2}{\tau_1} \quad (5.8)$$

Here, r is the radius of the precipitate and D_+ is the diffusivity of the positron. L_+ is the positron diffusion length. The positron diffusion length deduced from S-E plot for pristine samples presented in Figure 5.3 using VEPFIT analysis. The calculated values of positron diffusion length for Al-ODS and Zr-ODS are 132.06 ± 8.47 nm and 150.75 ± 7.58 nm respectively. The corresponding diffusivity in Al-ODS and Zr-ODS are 1.45 cm²/s and 1.08 cm²/s respectively, which are in line with previously reported values [251].

If we assume that the second lifetime component is arising from the nanoprecipitates, solving the Eqns.5.6. and 5.8 yields a number density of $6.7 \times 10^{20}/\text{m}^3$ for Zr-ODS and $1.9 \times 10^{21}/\text{m}^3$ for Al-ODS. These values are much smaller than the measured particle number density values presented in Chapter 4, ie., $1.7 \times 10^{24}/\text{m}^3$ for Zr-ODS and $3.8 \times 10^{23}/\text{m}^3$ for Al-ODS. Thus the second longer lifetime components can be attributed only to vacancy clusters. Moreover, the calculated lifetime values of V_6 and V_{15} vacancy clusters in Fe are 304 ps and 386 ps respectively [244]. These values are very similar to the longer lifetime components in this study. Thus, in the present study, τ_2 values of Zr-ODS can be correlated with V_6 clusters and that of Al-ODS can be attributed to V_{15} clusters.

Also, the individual fractions of positron trapping [78]:

$$f_1 = \frac{1}{1 + \tau_b(\kappa_{d_1} + \kappa_{d_2})} \quad (5.9)$$

$$f_{d_1/vc} = \frac{\tau_b \kappa_{d_1/vc}}{1 + \tau_b(\kappa_{d_1} + \kappa_{d_2})} \quad (5.10)$$

Here, f_1 is the fraction of positron annihilating in the bulk, f_{d_1} and f_{vc} are the fraction annihilating in dislocations and vacancy clusters respectively. The calculated values of rate constants and defect densities in Zr-ODS and Al-ODS are presented in Table 5.2.

The dislocation density in Al-ODS are higher than that of Zr-ODS. In Chapter 4, it has already been found out that the precipitates in Al-ODS and Zr-ODS are mostly semi-coherent with the matrix. The matrix-precipitate interface has misfit dislocations

Table 5.2: Rate constants, dislocation densities, vacancy cluster densities and individual fractions of positron trapping values calculated from PALS lifetime using standard trapping model.

Sample	$k_{d_1}(s^{-1})$	$N_{d_1}(m^{-2})$	$k_{vc}(s^{-1})$	$N_{vc}(m^{-3})$	f_1	f_{d_1}	f_{vc}
Zr-ODS	3.4×10^{10}	5.7×10^{14}	2.4×10^9	3.6×10^{22}	20%	74.2%	5.8%
Al-ODS	6.2×10^{10}	1×10^{15}	5.9×10^9	3.1×10^{22}	11%	80%	8%

in order to accommodate the strain. These misfit dislocations are identified to be efficient traps for positron annihilation [252]. Larger the precipitates, higher the strain field around them and larger the number of misfit dislocations. Thus the higher dislocation density in Al-ODS might be due to the larger size of the precipitates.

There is a long held debate about the role of vacancy clusters in nucleation and growth of precipitates in the ODS alloys. Some studies have pointed out that the vacancies produced during mechanical alloying is crucial in bringing atoms together to form oxides. And thus the nanoclusters will have a lot of vacancies in them in addition to constituent elements. There are supporting APT studies and positron studies enforcing this hypothesis [77, 240, 253]. However, one group of authors have reported the probability of nanocluster formation by oxygen mediated mechanisms without the help of vacancies [73]. Though the TEM studies find the dispersoids to be of crystalline, the APT studies identify the dispersoids as cluster of atoms rather than stoichiometric oxides [46]. Earlier studies in ODS EUROFER97 steels by Barotsova *et al.* [253], the longest lifetime component ($\tau = 265$ ps) is ascribed to vacancy clusters consisting of four vacancies. Those vacancy clusters were absent in EUROFER base material without Y_2O_3 addition. Thus they concluded that the vacancy clusters are associated with Y_2O_3 precipitates. In the present study, the vacancy cluster size and their number density observed in Al-ODS and Zr-ODS scale up with respect to the precipitate size (*refer to* Table 5.2). These alloys are made in same conditions. The dependence of second lifetime component on the precipitate size indicate that these vacancy clusters might be present inside the precipitate or in the precipitate matrix boundary.

5.4 Coincidence Doppler broadening spectroscopy

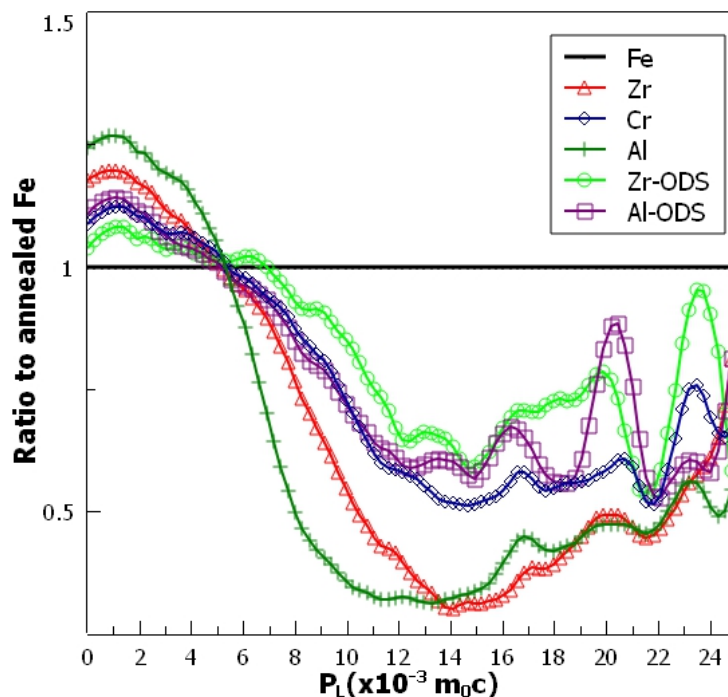


Figure 5.2: CDB ratio curves for Al-ODS and Zr-ODS alloys, normalized with respect to the pure Fe. The ratio curves for Zr, Cr and Al are also shown for comparison.

The normalized Coincidence Doppler broadening (CDB) ratio curves for Zr-ODS and Al-ODS are shown in the Figure 5.2 along with ratio curves of major alloying elements (Fe, Cr, Zr and Al). All the curves are normalized with respect to Fe (annealed at 800 °C and 10^{-6} mbar), which is the predominant element of the alloy. Al-ODS and Zr - ODS shows similar behavior in ratio curves. There is a dip in the intermediate P_L values and a peak at low P_L values. This is in agreement with earlier reported data in different ODS alloys [88, 92, 239]. The high concentration of Cr in ODS alloys responsible for the depletion in the high-momentum region, compared to the Fe CDB spectrum. This dip is observed to increase with an increase in yttria content and HIPing temperature. The increase in the dip is ascribed to increased positron trap sink strength arising from nanostructures and vacancy clusters [92, 239].

5.5 Vacancy defects in self-ion irradiated Zr/Al ODS alloys: Effect of dose and temperature

The variation of S-parameter of Zr-ODS and Al-ODS with mean positron implantation depth (calculated from the positron energy) is plotted in Figure 5.3. The data points were fitted using the multi-layer model in the VEPFIT program and the fitted profile is shown as solid lines in the plot. The S parameter, calculated as the ratio of counts in the low-momentum region ($< 2.5 \times 10^{-3} m_0 c$, where m_0 is the electron mass and c is the light velocity) to the total number of counts, is sensitive to vacancy-type defects. Thus the high value of the S-parameter is an indication of a high concentration of vacancy type defects. The S-parameters of both the pristine samples are high at the surface due to the presence of surface positron traps, which may be induced by polishing or due to surface contaminants. This can result from positronium formation at the metallic surface [254]. With the increase in energy, S-parameter decreases, saturates and attain bulk value. The almost constant S-parameter values in the bulk indicate that positron traps are distributed uniformly. The bulk S-parameter of Al-ODS is higher than that of Zr-ODS. This may be attributed to the dislocations in the matrix, as evident from the lifetime analysis in the previous section. The larger size of vacancy clusters and high dislocation density in Al-ODS, together contribute towards the high bulk S-parameter value of the Al-ODS compared to Zr-ODS. Figure 5.4. shows the S-W correlation plots of both the Zr - ODS and Al - ODS samples. These plots are useful for revealing the presence of different positron traps or different chemical surroundings of the positron annihilation sites. All the data points, which lie on a straight line in the S-W plot represent the same type of defect. If the change in the slope of the S-W plot is due to a change in W, which is related to positron annihilation with the core electrons, then the chemical environments of the annihilation defects are different. The Al-ODS and Zr-ODS have different slopes in the S-W plot, which is an indication of the difference either in the chemical surrounding or in the size of the open volume defects in these alloys. The major differences of Al-ODS from Zr-ODS are: (i) the presence of Al-rich oxide layer in (ii) higher amount of dissolved Al in the matrix and (iii) larger size of the precipitates. Factors (ii) and (iii) will be contributing towards the high number of defects that are not present in Zr-ODS.

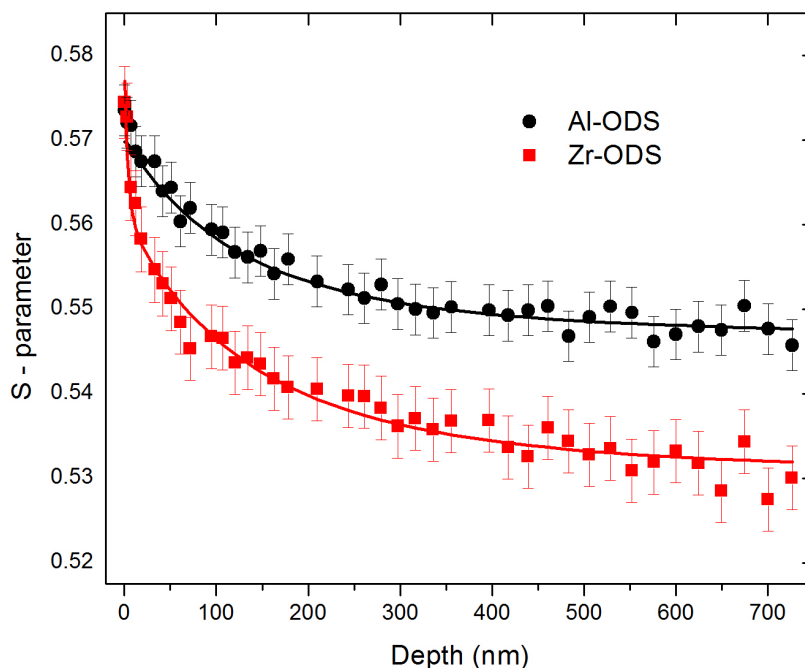


Figure 5.3: The variation of S-parameter with mean positron implantation depth for pristine Zr-ODS and Al-ODS alloys. The solid lines are obtained from VEPFIT analysis. The S-parameter values for both the alloys decrease with depth and attain bulk value.

The samples are further annealed for 1 hr at 800 °C in vacuum (1×10^{-6} mbar) for eliminating pre-existing defects. It is well known that the dislocations and vacancy clusters in ODS alloys are stable up to ~ 1000 °C. So the annealed and pristine samples do not show any change in the S-parameter values. Further, the samples are irradiated to a displacement damage of 100 dpa using 1.6 MeV Fe^+ ions at room temperature and elevated temperature of 340 °C. The irradiated samples are again characterized by depth-resolved Doppler broadening spectroscopy. Variation of S-parameter for Al-ODS with positron implantation depth is shown in Figure 5.5. For a dose of 100 dpa at room temperature, there is an increase in the S-parameter compared to the un-irradiated bulk, and hence an increase in open volume defects. However, the high-temperature irradiated sample shows a similar S-parameter curve as the unirradiated sample, indicating defect annealing. At 300 °C, in ferritic steel, the concentration of irradiation-induced vacancies is much higher than the thermal vacancies [255].

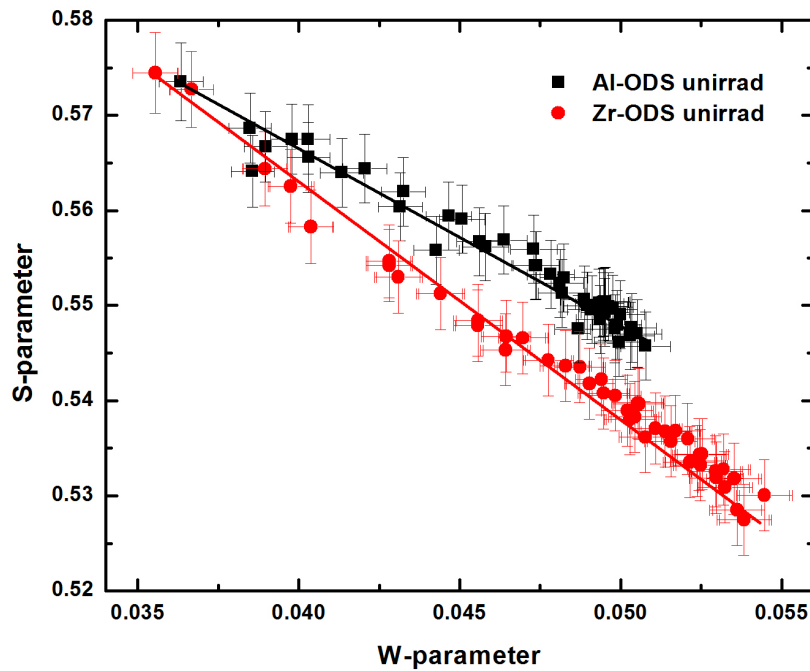


Figure 5.4: The S-W plot of the Al-ODS and Zr-ODS, which allows a direct comparison of defect types. The nature of defects in Zr-ODS and Al-ODS are dissimilar.

However, the interstitial mobility is enhanced at this temperature, leading to quick recombinations and annealing of irradiation-induced vacancy-defects. This explains the observed trend of decreasing the S- parameters of the 340°C sample to that of the unirradiated sample.

The S-W plot of pristine and irradiated Al-ODS are shown in Figure 5.6(a). The unirradiated specimen has a single slope, which most probably is associated with dislocations, as observed from the lifetime measurements. The room-temperature irradiated sample shows a deviation in its slope, indicating the evolution of different types of defects during ion irradiation. In the irradiated specimen, the defects could be arising due to irradiation-induced vacancies, dissociation of pre-existing vacancies or dissolution of precipitates in the matrix. However, the high-temperature irradiated specimen has the same kind of defects as the unirradiated specimen consistent with the S-parameter variation shown in Figure 5.4. So we can conclude that the defects produced during irradiation are vacancies which annihilate at a higher rate at high

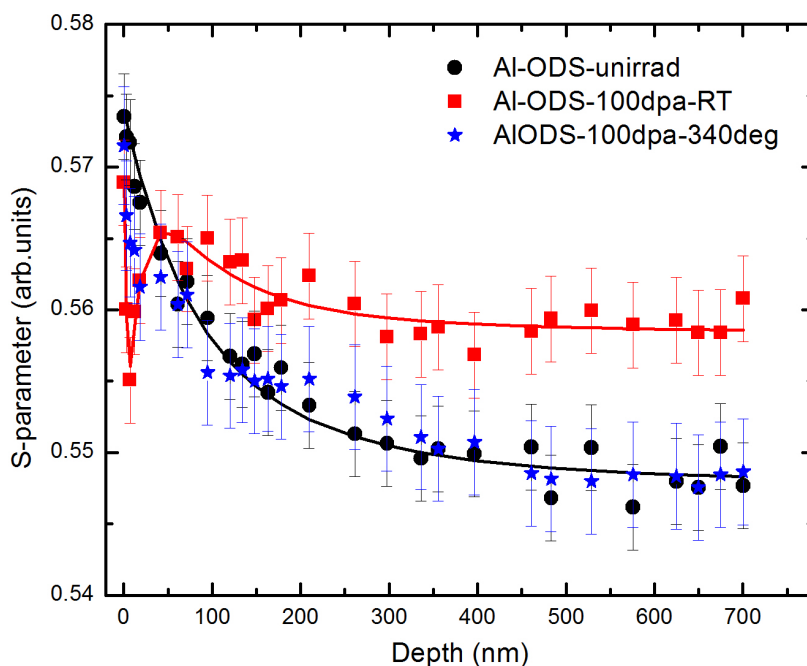


Figure 5.5: Depth distribution of vacancy defects in pristine and 1.6 MeV Fe^+ ion irradiated Al-ODS samples obtained by VLEPB studies. The solid lines are obtained by VEPFIT analysis. There is an increment in the S-parameter value for 100 dpa, RT irradiated specimens. Whereas, the 100 dpa HT irradiated specimens do not show any change in S-parameter.

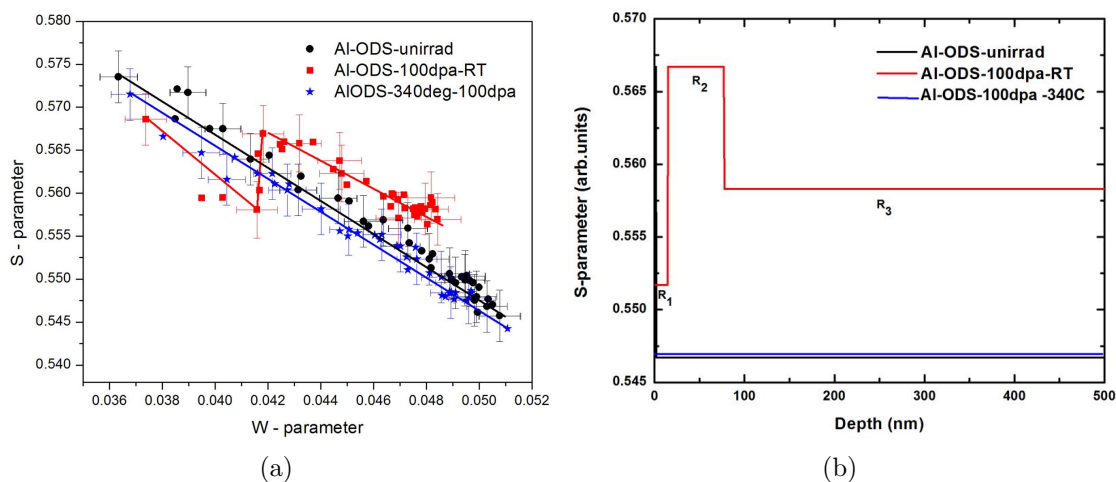


Figure 5.6: (a) S-W correlation plot for pristine and ion-irradiated Al-ODS. The 100 dpa, RT- irradiated specimen shows 3 slopes in the S-W plot (b) The depth profile obtained from VEPFIT analysis. R_1 is the surface layer, R_2 and R_3 are defect layers.

temperature compared to room temperature.

The multi-layer fitting model for irradiated and unirradiated specimens, deduced using VEPFIT program is displayed in Figure 5.6(b). A three-layer fit yielded meaningful physical parameters with the lowest variance. The layers are marked R_1 , R_2 and R_3 . The first layer (R_1) is a surface oxide layer and the remaining two layers (R_2 and R_3) are defect layers created by irradiation. The width of the surface layer is ~ 15 nm. The first defect layer is ~ 60 nm wide and the second defect layer extends beyond 500 nm. This means that the open volume defects are detected much beyond the range predicted by SRIM. This is due to the fact that SRIM does not consider the diffusion of irradiation-induced vacancies, while in many cases vacancies diffuse to longer distances than the projected range to form stable defect complexes.

As observed in Figure 5.7, the Zr-ODS samples do not show variation in S-parameter from the pristine sample for 100 dpa self-ion implantation at room temperature as well as high temperature. However, there is an increase in S-parameter and hence an increase in open volume defect concentration for a room temperature irradiation of 150 dpa. The as-prepared and 100 dpa irradiated samples of Zr-ODS show a single slope in the S-W plot, which is associated with dislocations as per the lifetime analysis results. But upon inducing a damage of 150 dpa, the S-W plot (Figure 5.8 (a)) shows a similar behavior as Al-ODS irradiated to a dose of 100 dpa at room-temperature, with three distinct slopes.

A two-layer fit gives the minimum variance as shown in the Figure 5.8(b). The surface layer has a width of 140 nm (marked as R_1 in Figure 5.8(b)). The defect layer is more than 800 nm further deep from the surface layer and marked as R_2 in the figure. From the S-W plots, it is evident that the irradiation response of both Al-ODS and Zr-ODS have similar behavior. However, the onset of the open volume defects in the Zr-ODS occurs at a higher dose than the Al-ODS. As observed in Chapter 4., Zr ODS has a smaller grain size, lower precipitate diameter and high precipitate number density compared to Al-ODS. Therefore the chances of recombination of irradiation-induced defects are high in Zr-ODS, leading to high radiation tolerance.

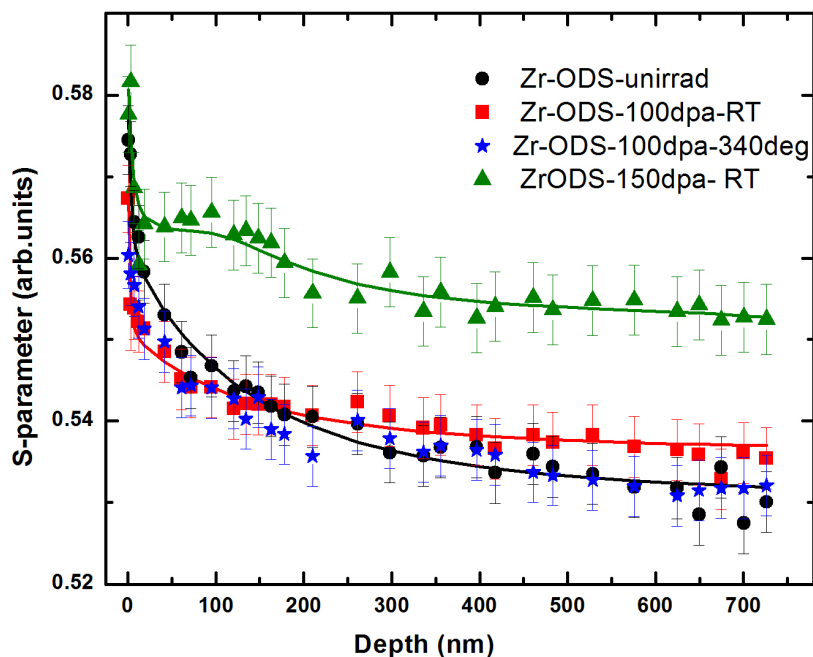


Figure 5.7: The S - parameter as a function of positron implantation depth in pristine and self ion- irradiated Zr-ODS alloy. There is no change in S-parameter for displacement damage of 100 dpa at room temperature as well as high temperature. An increment in S-parameter is observed for a damage of 150 dpa at room temperature.

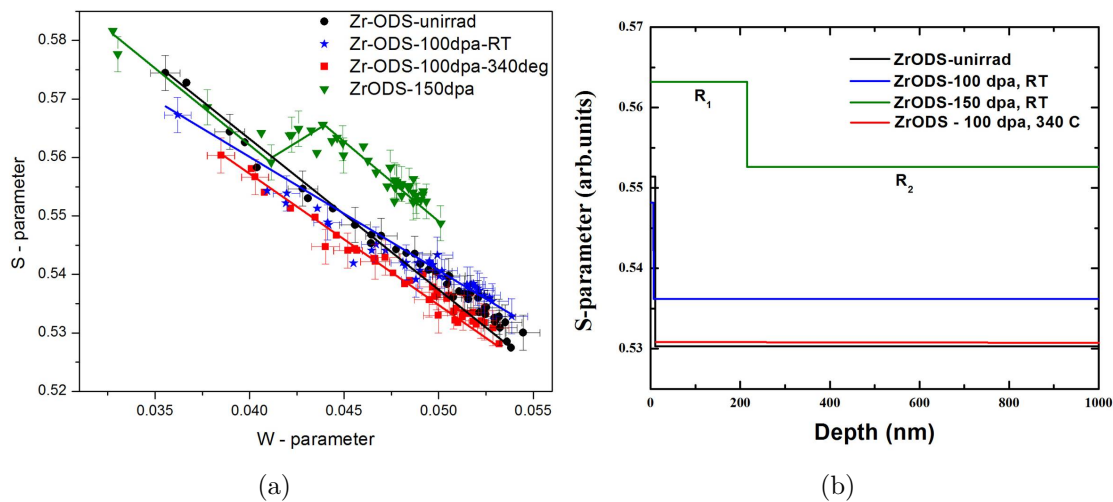


Figure 5.8: (a) S-W correlation plot for pristine and ion irradiated Zr-ODS steels. The 150 dpa, RT irradiated specimen show 3 slopes. (b) The depth profile obtained from VEPFIT analysis. R_1 and R_2 are the defect levels

5.6 Conclusions

In this chapter, positron lifetime spectroscopy techniques, PALS, CDB and VLEPB, are utilized to draw information about intrinsic and radiation-induced open volume defects in as-prepared Zr-ODS and Al-ODS alloys. Each of the alloys has two positron lifetime components, which can be attributed to the presence of dislocations and vacancy clusters respectively. From this, the dislocation number densities and number densities of vacancy clusters in the alloys have been computed using two-component trapping model. The Al-ODS has a more dislocation dense microstructure compared to Zr-ODS. The number densities of vacancy clusters are in the same range, however the size of vacancy clusters in Al-ODS is larger than that of Zr-ODS. These vacancy clusters are most probably associated with the precipitates. Therefore Al-ODS has a defect-rich microstructure compared to Zr-ODS to start with.

The ion irradiation with 1.6 MeV Fe^+ ions at room temperature and high temperature introduced vacancies in the alloys. In room-temperature irradiated specimens, Al-ODS showed the presence of open volume defects, and hence an increase in S-parameter for a dose of 100 dpa. But Zr-ODS does not show a significant increment in S-parameter for this dose. So the onset of defect production in Zr-ODS occurs at a higher dose than the Al-ODS. This is the consequence of smaller sized, higher number densities of dispersoids in Zr-ODS, compared to Al-ODS, as inferred in the previous chapter. Both the alloys do not show the presence of open volume defects upon irradiation at 340 °C.

Understanding the stability of the oxide nanoclusters under irradiation is critical for their future deployment, therefore we now advance to evaluate the radiation resistance of $\text{Y}_4\text{Zr}_3\text{O}_{12}$, the precipitate phase in Al-ODS and Zr-ODS.

Threshold displacement energies and defect formation energies of $Y_4Zr_3O_{12}$

6.1 Introduction

The dispersoids are believed critical to the high temperature strength and potential radiation resistance of ODS alloys and hence the long-term stability of these dispersoids under irradiation is of enormous interest. The major dispersoid phase in Zr-ODS and Al-ODS, the $Y_4Zr_3O_{12}$, belongs to fluorite related class, along with cubic pyrochlores, disordered fluorites and monoclinic pyrochlores. These compounds are widely known for their remarkable resistance to radiation induced amorphization. A brief review of the radiation resistance of these compounds is given in Section 1.4. The $Y_4Zr_3O_{12}$, also known as δ -phase belongs to $R\bar{3}$ space group, in which the $3a$ site is entirely occupied by Zr and $18f$ site has Zr and Y with a Y-occupancy of 66.66%. Two sets of oxygen are arranged in two sets of $18f$ positions. Further details on the crystal structure of $Y_4Zr_3O_{12}$ is given in Section 3.4.1.

Threshold displacement energies and defect formation energies are the most fundamental quantities governing the radiation response of a material. Therefore, in the present chapter, as the first step towards studying the radiation resistance of the dispersoid phase in ODS steels, threshold displacement energies of Y, Zr, and

O in $Y_4Zr_3O_{12}$ δ - phase compound are computed along three main crystallographic directions using *ab initio* Molecular Dynamics (AIMD) simulations and the defects formed and the displacement mechanisms involved in each case are analyzed in detail. Further, the defect formation energies of $Y_4Zr_3O_{12}$ are computed and the role of these defects and their formation energies in the possible rhombohedral to cubic transformation of $Y_4Zr_3O_{12}$ is discussed in comparison with existing data on cubic pyrochlores.

6.2 Computational Details

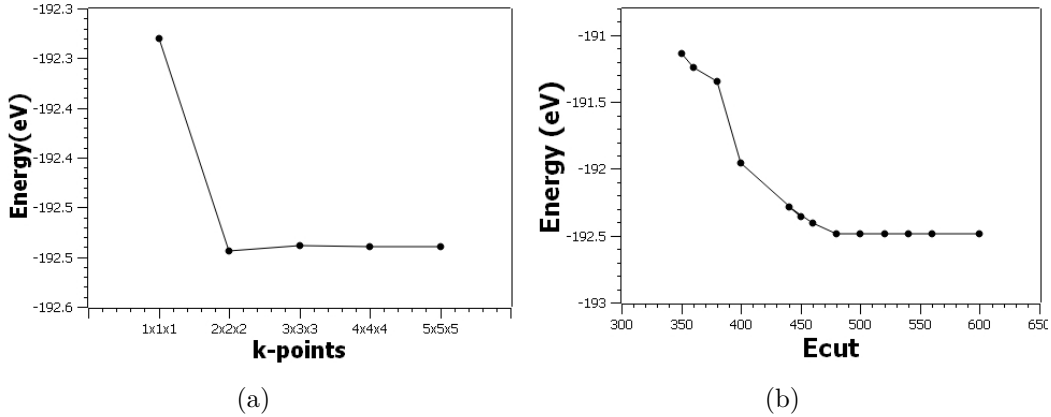


Figure 6.1: Convergence of energy in $Y_4Zr_3O_{12}$ supercell. Variation of total energy with respect to (a) k-point mesh and (b) cut-off energy.

The calculations are done using Vienna ab-initio simulation package (VASP) [161] with pseudopotentials generated with the projected augmented wave approach (PAW) [161]. For exchange-correlation functional, the generalized gradient approximation as parameterized by Perdew, Burke and Ernzerhof (PBE) [147] is used. For static calculations a dense k point $5 \times 5 \times 5$ Monkhorst-Pack [178] mesh is used and the simulation cell of 152 atoms is fully relaxed (atom positions and cell volume) until the force on each atom is less than $0.001 \text{ eV}/\text{\AA}$ for both ideal structures and defect structures. The variation of energy with respect to k-point mesh and E_{cut} are given in Figure 6.1. The Energy cut-off value is 500 eV.

For AIMD calculations, plane wave energy cut-off of 500 eV and automatic $1 \times 1 \times 1$ mesh with their origin at the Γ - point is used. An orthogonal supercell containing

456 atoms (shown in Figure 6.2.) is constructed from rhombohedral unitcell using the transformation matrix $(-2,1,2; 2,1,2; 0,-2,2)$. The $[100]$ direction in the original unitcell is equivalent to the $[322]$ direction in the transformed supercell. The supercell size is chosen in such a way that the image interactions are minimized.

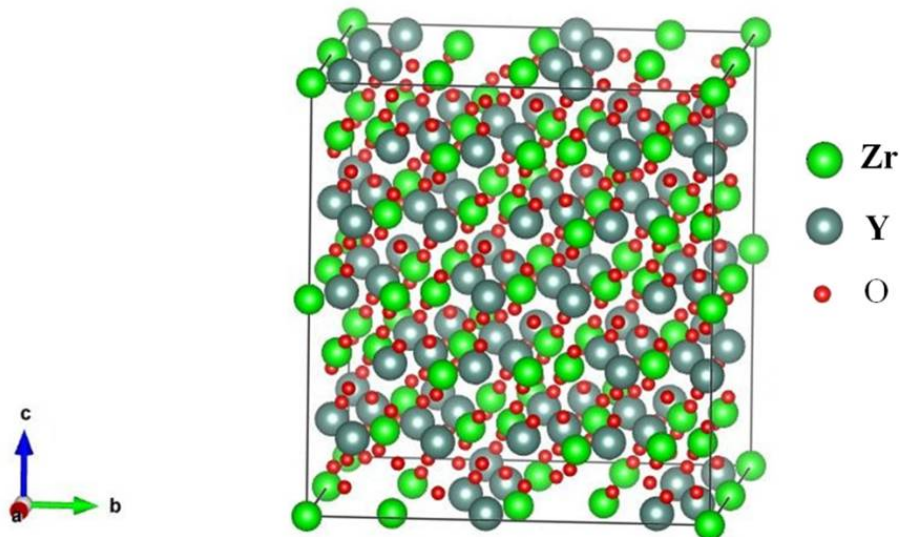


Figure 6.2: Orthogonal cell of the $Y_4Zr_3O_{12}$, containing 456 atoms. It is constructed from rhombohedral unitcell using the transformation matrix: $(-2,1,2; 2,1,2; 0,-2,2)$. The lattice parameters are: $a = 19.44 \text{ \AA}$, $b = 16.84 \text{ \AA}$, $c = 18.18 \text{ \AA}$, $\alpha = \beta = \gamma = 90^\circ$. This cell is used for AIMD calculations.

The simulations were carried out in NVE ensemble with periodic boundary conditions imposed along all three axes. The supercells were first equilibrated at 300K for 4000 time steps (400 fs). The variation of temperature with time-step is plotted in Figure 6.3. The temperature remains in the range of $300 \pm 20 \text{ K}$. A Nosé–Hoover thermostat algorithm is employed for maintaining a constant temperature. After the temperature of the entire system reaching to steady-state, the system is kept as a microcanonical or NVE ensemble and there is no heat exchange between the system and its boundary. The only process is the exchange of potential and kinetic energy inside the ensemble, with total energy being conserved.

An atom (Zr_{3a} , Y_{18f} , Zr_{18f} or O_{18f}) is chosen as a primary knock-on atom (PKA) and energy is given to it in three main crystallographic directions. After giving energy for a particular PKA in a particular crystallographic direction, the system is made to evolve in time with a variable time step method starting from 0.1 to 2 fs. The atom

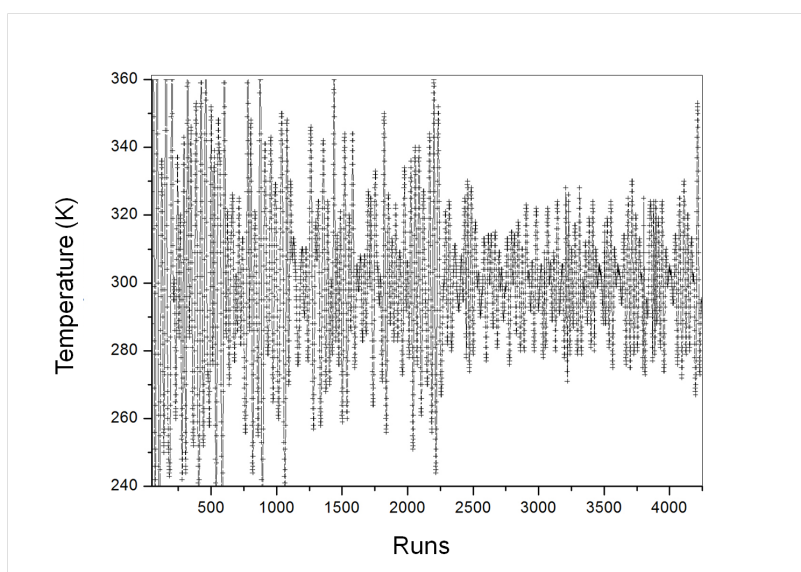


Figure 6.3: Variation in temperature of $Y_4Zr_3O_{12}$ supercell with time steps. The equilibrated temperature remains in the range of 300 ± 20 K.

trajectories are traced for at least 2 ps. If the PKA is not returned to its original position after the end of simulations (2 ps) it is assumed to be a displaced atom. Here we study only primary damage creation and ignore the effects of long-term defect annealing. Displacement energy is determined by ensuring that the Frenkel pair or cation antisite defect is formed and is stable over sufficient time. All visualizations are done using VESTA [256].

6.3 Preferential distribution of Y and Zr in $18f$ sites of $Y_4Zr_3O_{12}$ unitcell

The details about the crystal structure of $Y_4Zr_3O_{12}$ can be found in Section 3.4.1. It belongs to $R\bar{3}$ space group with inversion triad along $[111]$ direction of the rhombohedron [197], similar to R_7O_{12} and MR_6O_{12} (M being U, W or Mo and R a rare earth). The structure is shown in Figure 3.11. It has two ordered structural vacancies in $6c$ positions along its inversion triad. Oxygen gets occupied in two sets of $18f$ general positions. Both sets of oxygen form two octahedron one being centered at the body center (denoted as O_I) and the second (denoted as O_{II}) at $3a$ cation octahedron. Consequently, the cation in $3a$ position is co-ordinated to six oxygen atoms and that

in $18f$ positions are coordinated to 7 oxygen atoms. The exact ordering of cations in $18f$ and $3a$ positions cannot be determined directly from X-ray or neutron diffraction data because Y and Zr have similar scattering factors.

In 2001, Bogicevic *et al.* [257] searched lowest energy configurations of $Y_4Zr_3O_{12}$ using ab initio simulations and lattice algebra techniques and found that the six-fold coordinated cation site ($3a$) is occupied solely by Zr. By a combination of pair potential Monte Carlo simulations with DFT, the ordered cation structure of a range of δ -phase compounds were computed and concluded that the ground state of $Y_4Zr_3O_{12}$ contains only one formula unit per unitcell.

In the present work, in order to find the most energetically probable configuration, six different cation distributions are considered (*refer to* Table 6.1). The total energies for these 19 atom unitcells are compared. The systems with Zr in $3a$ position has the lower energy compared to Y in $3a$ position and among the $18f$ cation positions, the two Zr occupying the diagonally opposite positions of the cation octahedron has lower energy compared to other combinations. The lowest energy structure is used for our further calculations. The configurations and corresponding formation energies per formula unit are summarized in Table 6.1 and plotted in Figure 6.4.

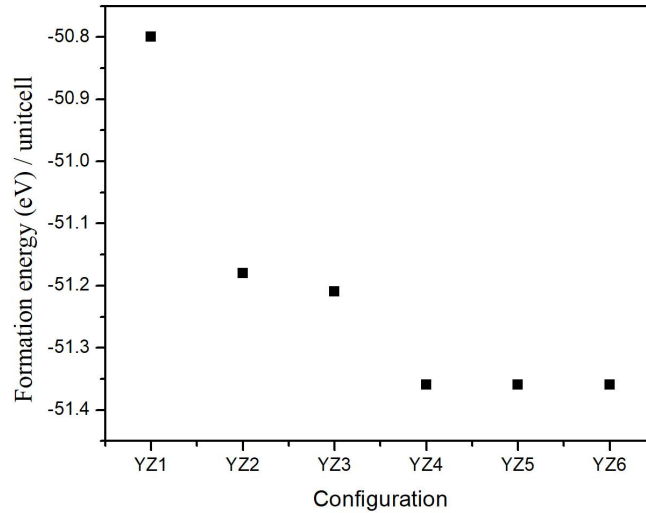
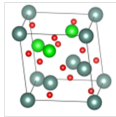
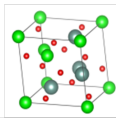
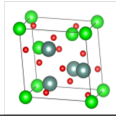
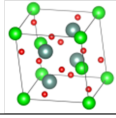
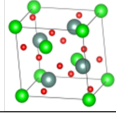
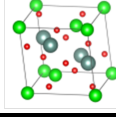


Figure 6.4: Formation energies for different configurations of $Y_4Zr_3O_{12}$ unitcell

Table 6.1: Formation energies/unitcell for different configurations of Y and Zr in $18f$ positions of $Y_4Zr_3O_{12}$ structure.

Configuration		Formation energy/ unitcell (eV)
YZ-1		-50.80
YZ-2		-51.18
YZ-3		-51.21
YZ-4		-51.36
YZ-5		-51.36
YZ-6		-51.36

6.4 Threshold displacement energies of $Y_4Zr_3O_{12}$

An orthogonal supercell of 456 atoms is constructed as shown in Figure 6.2. For a chosen PKA atom and a particular crystallographic direction, the system is evolved for 2 ps with variable time-steps, as explained in the previous section. The simulations are repeated with incremental PKA energy in steps of 1 eV. The minimum initial energy of the PKA atom, which finally results in its displacement, is considered as the threshold displacement energy (TDE). The threshold displacement energies of anions and cations along with resulting defect configurations are tabulated in Table 6.2 and 6.3 respectively. It can be noted that in low energy displacement events, the number

of anion defects is more than cation defects, suggesting that anion disorder might be predominant in $Y_4Zr_3O_{12}$ during irradiation.

Table 6.2: The threshold displacement energies of O_I and O_{II} in $Y_4Zr_3O_{12}$ structure along with final defect configurations and separation between defects after simulation for 2 ps. (A_B is A atom occupying site of B atom.)

Direction	E_d (eV)	Defect Configurations	Separation between defects (\AA)
O_I [100]	13	$O_{I,int} + O_{I,vac}$	3.2
O_I [110]	20	$O_{I,int} + O_{I,vac}$	2.35
O_I [111]	13	$O_{I,int} + O_{I,vac} + O_{II,int} + O_{II,vac}$	2.0
O_{II} [100]	16	$O_{II,int} + O_{II,vac}$	2.0
O_{II} [110]	22	$O_{II,int} + O_{II,vac}$	2.1
O_{II} [111]	26	$O_{II,int} + O_{II,vac}$	2.3

Table 6.3: The threshold displacement energies of Y and Zr in $Y_4Zr_3O_{12}$ structure along with final defect configurations and separation between defects after simulation for 2 ps. (A_B is A atom occupying site of B atom.)

Direction	E_d (eV)	Defect Configurations	Separation between defects (\AA)
$Zr_{3a}[100]$	65	Zr_Y	3.6
		$O_{II, \text{int}} + O_{II, \text{vac}}$	3.7
$Zr_{3a}[110]$	60	Zr_Y	5.0
		$O1_{O2}$	3.0
		$O_{II, \text{int}} + O_{\text{vac}}$	2.8
$Zr_{3a}[111]$	28	$Zr_{3a\text{-int}} + Zr_{3a\text{-vac}}$	4.7
$Zr_{18f}[100]$	65	Zr_{Zr}	4.6
		Zr_{int}	2.4
		$O_{II, \text{int}} + O_{II, \text{vac}}$	2.4
		$O_{II, \text{int}} + O_{II, \text{vac}}$	2.8
$Zr_{18f}[110]$	69	Zr_{Zr}	5.3
		$O1_{O2}$	3.38
		$O2_{O2}$	3.56
		$O_{I, \text{vac}} + O_{II, \text{int}}$	2.8
		Zr_{int}	3.41
$Zr_{18f}[111]$	40	$Zr_{\text{int}} + Zr_{18f\text{-vac}}$	5.12
		$O2_{O2}$	4.4
		$O_{II, \text{vac}} + O_{II, \text{int}}$	3.3
		$O_{I, \text{vac}} + O_{I, \text{int}}$	2.8
$Y[100]$	65	Y_Y	3.9
		$O_{I, \text{vac}} + O_{I, \text{int}}$	3.2
		$O_{II, \text{vac}} + O_{II, \text{int}}$	2.6
$Y[110]$	50	Y_{3a} $Y_{\text{vac}} + Zr_{\text{int}}$	5.4
$Y[111]$	62	$Y_{\text{int}} + Y_{\text{vac}}$	5.2
		$O_{I, \text{int}} + O_{I, \text{vac}}$	5.3
		$O_{I, \text{int}} + O_{I, \text{vac}}$	3.8

6.5 Nature of defects produced during threshold displacement events

Figure 6.5(a) shows the events occurring after imparting threshold energy along the [100] to Zr atom at $3a$ position. When the kinetic energy of 65 eV is imparted to Zr_{3a} atom along the [100] direction, it repulsively interacts with Y_{18f} atom situated at 3.6 Å along this direction. The energy transferred to Y_{18f} is sufficient to knock it out of its equilibrium position and form a cation antisite defect. Further, the path of Y_{18f} recoil atom deviates from [100] direction to [631] direction, and it stabilizes at a bridge site between Zr_{3a} and Y_{18f} atoms, 2.9 Å away from its equilibrium site. An O_{II} atom, which is initially bonded to secondary recoil atom (Y_{18f}), also gets displaced by 3.6 Å along $[5\bar{1}1]$ direction forming the O_{II} Frenkel pair. The net defects produced are: Y_{Zr} antisite, an O_{II} Frenkel pair, a Y_{18f} interstitial, and a vacancy at $3a$ site.

For a Zr_{3a} PKA with E_d of 60 eV along [110] direction (Figure 6.5 (b)), the mechanism is similar as that in the [100] direction. It initially collides and replaces the Y atom in its path. The secondary recoil atom (SRA) moves further along [110] direction and stabilizes in the bridge site between Zr_{3a} and Y_{18f} atoms. The distance moved by SRA is 3.5 Å. O_I atom which is initially bonded with PKA migrates by 3 Å along the same direction and knocks out an O_{II} atom and occupies its position. The anion interstitial thus formed moves 2.8 Å away from its initial position and occupies vacant $6c$ site. At this events the following defect are produced: Zr_{3a} vacancy, Zr_Y antisite, $O_{O_{II}}$ antisite, O_{II} Frenkel pair and a Y interstitial.

The lowest displacement energy of (28 eV) Zr in $3a$ position is along [111] direction (Figure 6.5.(c)), the direction in which the structural anion vacancies are aligned. The only defect produced is a Zr interstitial - vacancy pair, separated by 4.7 Å which stabilizes at the body center. There is no cation antisite formation or anion migration. The two vacancies aligned in this direction makes it easier to move for the Zr atom and stabilize at the center of anion octahedron where it has a similar anion environment as $3a$ site. Four out of six O_{II} atoms move 0.6 Å away from the equilibrium position in order to accommodate the Zr atom. The Zr forms new bonds with neighboring O_I atoms and the average Zr-O distance is ~ 2.3 Å.

When displacement energy of 65 eV is imparted to the Zr_{18f} along [100] direction

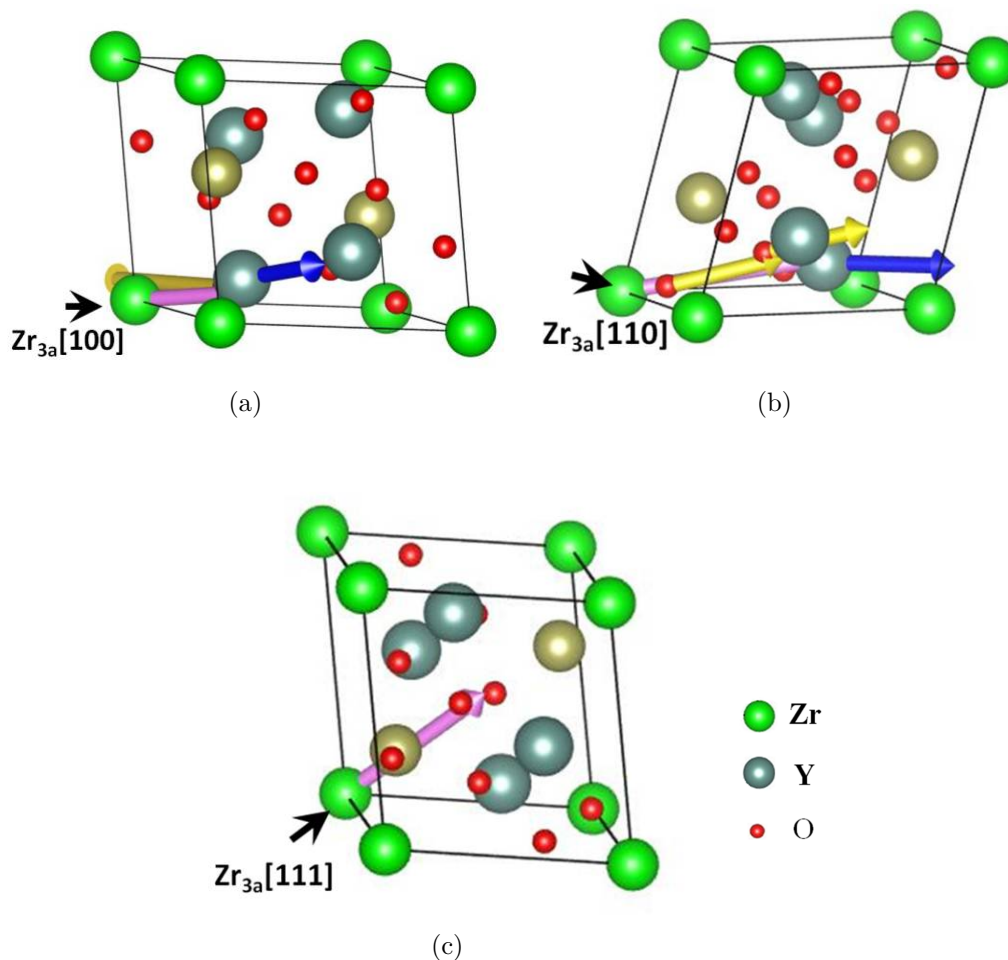
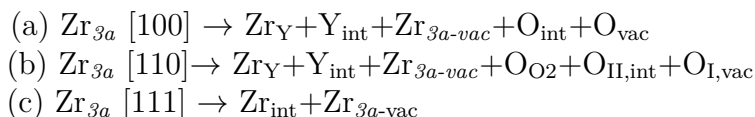


Figure 6.5: Defects produced when Zr_{3a} atom is given energy along (a) [100], (b) [110] and (c) [111] directions. The direction in which energy is given, is marked by a black arrow. The purple arrow indicates Zr displacement direction, the blue arrow indicates Y displacement direction and the yellow arrow indicates oxygen displacement direction. Here, the green atoms are Zr_{3a} , the yellow atoms are Zr_{18f} , the blue atoms are Y_{18f} , and the red atoms are oxygen.



(Figure 6.6. (a)): the PKA repulsively interacts with two Y atom in the direction and changes its path, knocks off Zr_{18f} atom in that direction, situated at the farthest point of the cation-octahedron forming a Zr interstitial. The secondary recoil atom gets moved to 2.4 Å away from its site. Two O_{II} atoms which are in the direction of motion of the PKA are displaced by 2.3 Å and 2.8 Å respectively producing Frenkel

pairs.

For Zr_{18f} PKA along [110] direction (Figure 6.6.(b)), the threshold displacement energy is determined to be 69 eV. The PKA moves through the center of the cation octahedron, collides with another Zr_{18f} atom, and replaces it. The recoiled Zr migrates 3.4 Å from its equilibrium position and occupies vacant $6c$ site. O_I which was initially bound to PKA moves 3.4 Å along [110] direction and replaces O_I atom. The displaced O_I atom continues moving in the same direction eventually displacing an O_{II} atom and occupies its position. The displaced O_{II} atom moves 2.8 Å to form an interstitial. Zr_{18f} atom has minimum threshold displacement energy of 40 eV along [111] direction (Figure 6.6.(c)). The Zr_{18f} PKA moves along [111] direction and stabilizes as an interstitial at the bridge site between Zr_{3a} and Y atom of the next cell, 5.12 Å away from its original position. The PKA also knocks out an O_{II} atom situated in [111] direction. The knocked-out oxygen eventually moves along [111] direction, replacing another O_{II} atom on its way. The recoiled O_{II} atom migrates along the direction and eventually occupies one of the vacant $6c$ site (structural vacancy). The distance between the first O_{II} atom displaced by PKA and the now occupied $6c$ site 3.3 Å. Another O_{II} atom initially bonded to the PKA moves 2.8 Å from its original site and stabilizes in $6c$ site of a nearby cell.

A similar approach has been employed for Y recoils. For Y PKA along [100] direction (Figure 6.7(a)), the calculated threshold displacement energy is 65 eV. The Y PKA initially collides with another Y atom in [100] direction and occupies its site. The SRA moves further along [100] direction to form a stable interstitial at the face of the rhombohedral structure, at a distance of 3.2 Å. During this process, O_I atom which was initially bound to PKA, moves along by 3.9 Å towards $6c$ site in the next cell. Another O_{II} atom which was initially bonded with PKA moves by 2.6 Å along [100] direction to form a Frenkel pair.

For Y recoil along [110] direction((Figure 6.7(b))), the threshold displacement energy is determined to be 50 eV. The Y PKA moves along [110] direction, eventually knocking off Zr_{3a} atom at a distance of 5.06 Å in its path and occupying its position to form an antisite. The recoiled Zr atom form a stable interstitial at a distance 3.6 Å away from its original position, in the midpoint of O_I octahedron. There is no anion present in this direction of the cell and the anion environment of O_I octahedron is similar to that of $3a$ site. So no anion disorder is observed in this case.

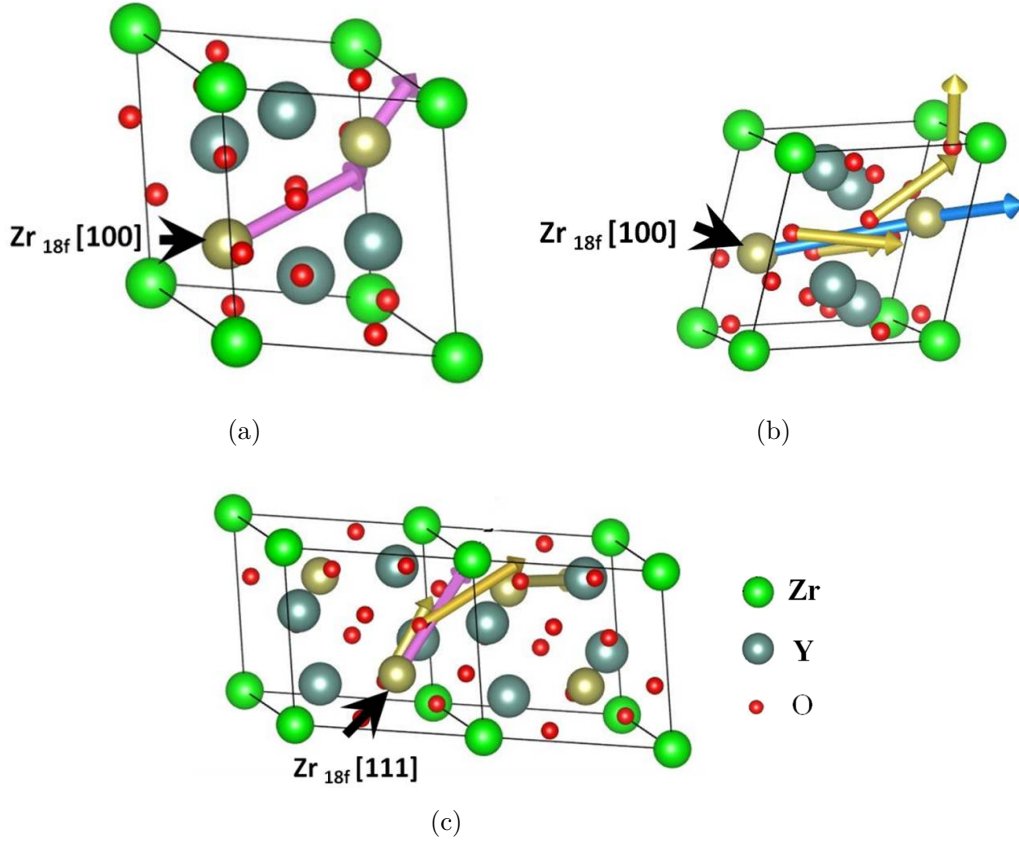
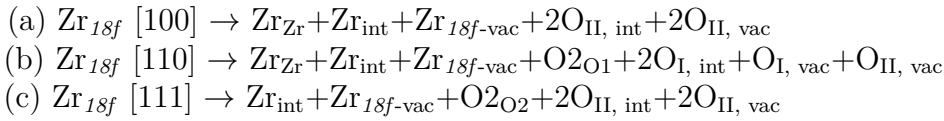


Figure 6.6: Defects generated by imparting threshold displacement energy to Zr_{18f} atom along (a) [100] (b) [110] and (c) [111] directions. The purple arrow indicates Zr displacement direction, the blue arrow indicates Y displacement direction and the yellow arrow indicates oxygen displacement direction. Here, the green atoms are Zr_{3a} , the yellow atoms are Zr_{18f} , the blue atoms are Y_{18f} , and the red atoms are oxygen.



The calculated threshold displacement energy for Y recoil along [111] direction ((Figure 6.7(c))) is 62 eV. This value is higher than that of Zr_{3a} and Zr_{18f} PKA along the [111] direction. The Y PKA moves along [111] direction to form a stable cation interstitial at the bridge site between Zr_{3a} and Y_{18f} atoms in the nearby cell. The distance of separation of cation Frenkel pair is 5.3 Å. While tracing its path, the PKA knocks out an O_{II} atom occupied along [111] direction, which recoils along the same direction forming an anion antisite with an O_I atom at a distance of 5.2 Å. The

recoiled O_I atom moves by 3.80 \AA to form an anion interstitial.

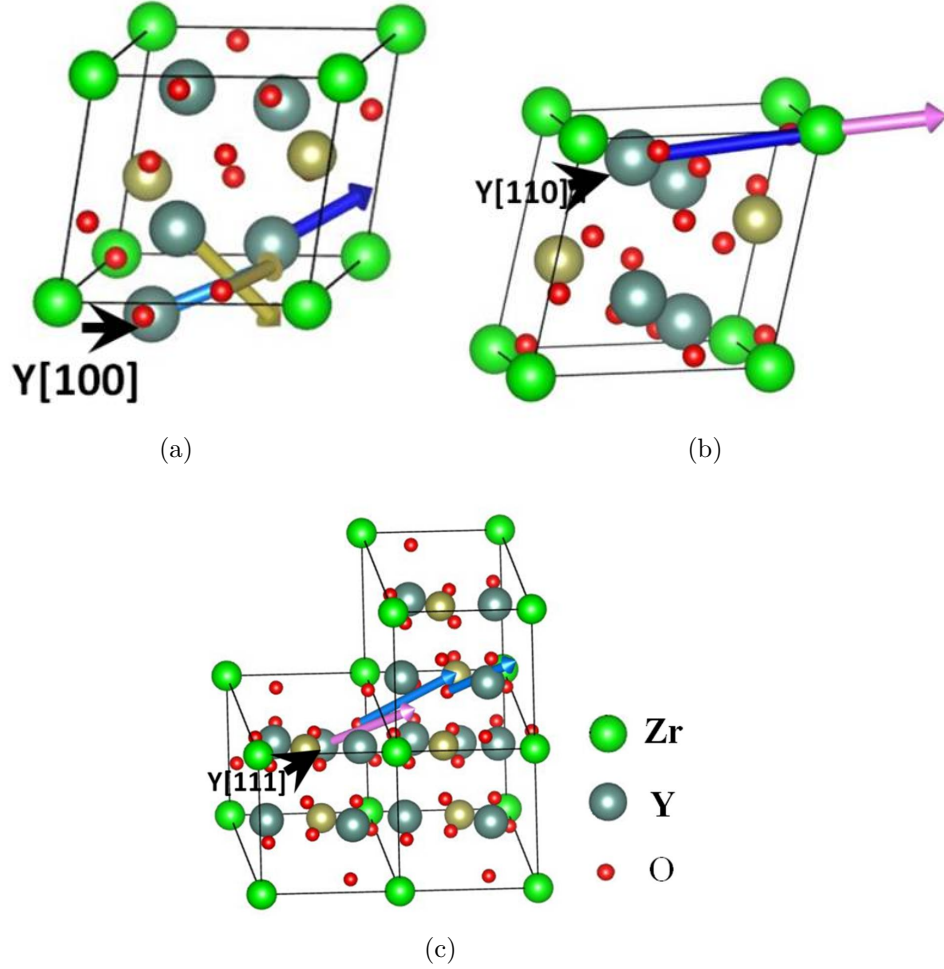
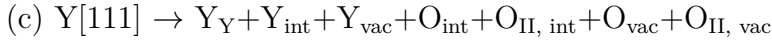
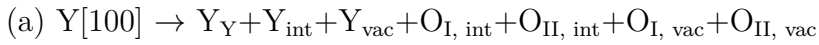


Figure 6.7: Defects generated by imparting energy to Y atom along (a) [100] (b)[110] and (c)[111] directions.



Anions have lower threshold displacement energy compared to cations (see Figure 6.8). At 300K, 13 eV is required for the O_I atom to move along [100] direction and produce a Frenkel pair separated by 2.5 \AA . The cation sublattice remains unaltered. Along [110] direction the displacement energy is slightly higher (20 eV) and the Frenkel pair separation distance is 2 \AA . Oxygen interstitials produced by PKAs in the [100] and [110] incident directions get stabilized in the vacant $6c$ site. When energy is given along [111], the O_I PKA which moves along the [111] direction, occupies the O_{II} site in

the nearest cell, with the movement of O_{II} to $6c$ site. The process can be summarized as:

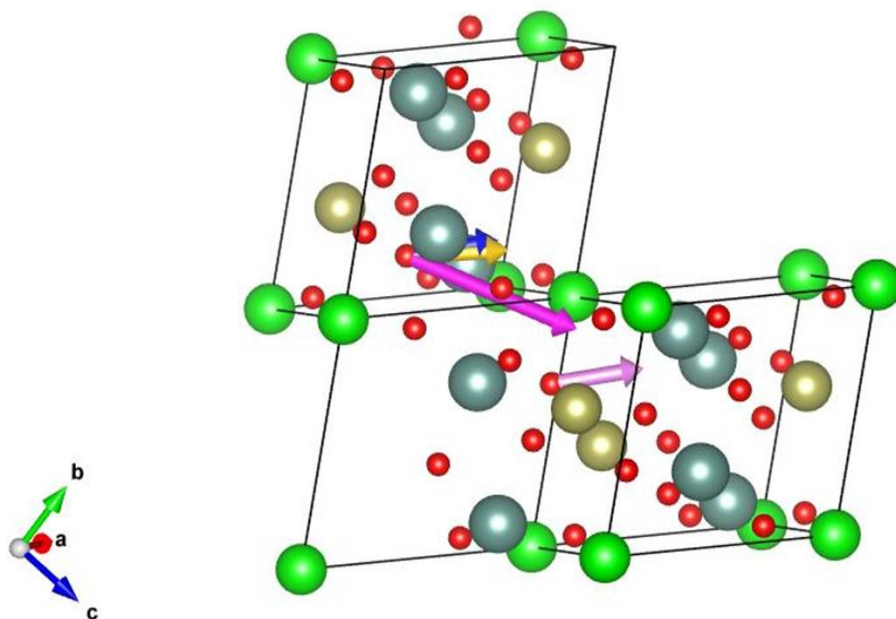
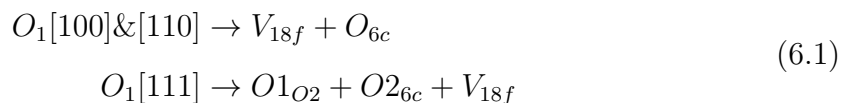


Figure 6.8: The displacements of O_I atom when incident energy is given along $[100]$ (Blue arrow), $[110]$ (Yellow arrow) and $[111]$ (Purple arrow) directions. The first two result in FP with interstitial occupied in $6c$ site and third one results in an anion antisite pair and FP with interstitial in $6c$ site. Here green atoms are Zr_{3a} , Yellow atoms are Zr_{18f} , blue atoms are Y and red atoms are oxygen.

O_{II} PKA requires 17 eV to move along $[100]$ direction and produce a Frenkel pair separated by 2.0 Å. During this process, the cation sublattice and other atoms of anion sublattice remain unaffected. In $[110]$ and $[111]$ directions, Frenkel pairs separated by 2.1 Å and 2.3 Å are formed.

6.6 Defect formation energies in $Y_4Zr_3O_{12}$ and its role in radiation resistance

Generally, the O-D transformation in fluorite related structures is defined by two reactions: (i) antisite defects in cation sublattice and (ii) Frenkel pair formation in

anion sublattice. These two defect reactions are termed as the order to disorder defect reaction pair [102]. The lower the O-D reaction pair energy, the higher the radiation tolerance of the defect fluorite structure. In previous defect studies on pyrochlore structures, [125, 258, 259] the cation antisite defect is found to have the lowest formation energy, and the anion Frenkel pair formation energies are significantly reduced in the presence of cation antisite defects.

The O-D reaction pair energy is considered as a good indicator of radiation tolerance in δ - phase structures also [102]. However, the defect formation energies on the $Y_4Zr_3O_{12}$ δ -phase structure is not available in any literature so far. Therefore we have attempted to study the formation of vacancies, interstitials, antisites, and Frenkel pairs in $Y_4Zr_3O_{12}$ and tried to correlate O-D pair energy to the possible transformation of $Y_4Zr_3O_{12}$ to disordered fluorite structure. The calculated values are tabulated in Table 6.4.

The vacancy formation energies in $Y_4Zr_3O_{12}$ are calculated as:

$$E_{vac}^X = (E_{def} + E_x) - E_{total} \quad (6.2)$$

where E_{total} is the total energy of the supercell of the ideal δ -phase structure, E_{def} is the total energy of supercell with the vacancy in it and E_x is the reference energy calculated with respect to equilibrium phase of X, ie., ground state crystalline phases of Y and Zr and the gas phase of oxygen molecule. The vacancy formation energies are found to be 16.04 eV, 13.73 eV, 6.94 eV and 7.27 eV respectively for zirconium at $3a$, yttrium at $18f$ and oxygen at two sets of $18f$ positions. The vacancy formation energies are comparable to that of $Y_2Ti_2O_7$ pyrochlores where 14.64 eV, 16.59 eV, 6.53 eV and 8.93 eV are required for forming Y, Ti, O_{48f} and O_{8b} vacancies respectively [124].

Formation energies of yttrium, zirconium and oxygen interstitials at a vacant $6c$ site are also considered. The interstitial defect formation energies are calculated as

$$E_{int}^X = E_{def} - (E_{total} + E_x) \quad (6.3)$$

where E_{def} is the energy of the supercell containing an interstitial X atom, E_{total} and E_x are the total energy of supercell and reference energy respectively as in the earlier case. The formation energies for interstitials are lower than those for vacancies as in the case of pyrochlores [124]. Though the $6c$ site is an anion vacancy, yttrium

and zirconium are also found to be stable in that site. The cation interstitials are stable in the center of anion octahedron, Y being more stable than Zr by 0.1 eV. It is observed that in low energy recoil events of Table 6.3., the displaced anion atoms tend to stabilize at the vacant $6c$ site and cations are stable at body center position.

Table 6.4: Formation energies of vacancy and interstitial defects in $Y_4Zr_3O_{12}$

Species	Formation Energy (eV)
Vacancy	
O_I	6.94
Y	13.72
Zr	16.04
O_{II}	7.27
Interstitial	
O_{6c}	2.85
Y_{6c}	4.54
Zr_{6c}	4.29
Y_{center}	3.75
Zr_{center}	3.65
$O_{6c} + O_{6c}$	0.64

Now, energy expenditure to form cation antisite defects, formed by replacing $18f$ atom with $3a$ atom and vice versa are calculated. The formation energy of A in B site is given by

$$E_B^A = E_{def} - (E_{total} + E_A - E_B) \quad (6.4)$$

where E_{def} is the energy of a supercell with A in one B site, E_A and E_B are the energies of the supercell with A in A-site and B in B-site. Due to the similarity in cation radii, antisite pair defects are the most stable defect species in δ -phase. An additional zirconium in an $18f$ yttrium site is more probable than an additional Y due to its slightly smaller radius. Likewise, the yttrium in a $3a$ site is less stable than the other two configurations, due to its larger ionic radius.

The antisite pair defect is introduced by exchanging neighboring $18f$ and $3a$ atoms.

The energy liberated or absorbed during an antisite pair formation is :

$$E_{AS} = E_{def} - E_{total} \quad (6.5)$$

where E_{def} is the energy of supercell with an antisite pair. Antisite formation energy is 0.54 eV. Antisite pair formation between $18f$ cation sites is negligibly small as the structure suggests. This considerably reduces the O-D defect reaction pair energy compared to other pyrochlores.

The calculated Frenkel pair energy values show that two sets of oxygen have different vacancy formation energies and Frenkel pair formation energies due to their different chemical environments.

Table 6.5: Antisite and Frenkel pair formation energies of $Y_4Zr_3O_{12}$

Species	Formation Energy (eV)
Antisite	
Y_{3a}	2.76
Zr_{18f}	2.03
Y_{18f}	2.50
AS_{pair}	0.54
Frenkel Pairs	
$O_{6c} + O_{1,vac}$	1.12
$Zr_{6c} + Zr_{3a,vac}$	7.76
$Y_{6c} + Y_{vac}$	7.37
$O_{6c} + O_{2,vac}$	3.21

6.7 Discussions

The minimum E_d values of $Y_4Zr_3O_{12}$ are found to be 28 eV for Zr_{3a} PKA, 40 eV for Zr_{18f} and 50 eV for Y recoils. For O_I and O_{II} minimum values are 13 eV and 16 eV respectively. Zr_{3a} , Zr_{18f} and O_I have the least E_d values along [111] direction. Yttrium

has a minimum E_d along [110] direction and O_{II} has minimum value along [100] direction. The directions except for direction in which inherent structural vacancies are aligned, cation tends to occupy another cation site. Anions tend to stabilize at vacant $6c$ site. The body center position, inside anion octahedron, also is a stable site for Zr cation.

Threshold displacement energies of anions are found to be dependent on the atomic environment and nature of the chemical bond [118, 260]. The O_I has the atomic environment of Y_4 tetrahedron and O_{II} has the atomic environment of Y_3ZrO trigonal bipyramid. The minimum displacement energy of O_{II} is 3 eV higher than that of O_I . The Zr-O distance in coordination polyhedron is smaller than Y-O distance suggesting that the Zr-O bond is more covalent in nature [123] and hence the difficulty in displacing O_{II} compared to O_I .

Threshold displacement energies of $Y_2Ti_2O_7$, which is the oxide precipitate in conventional Ti containing ODS steels, has been computed by H. Y. Xiao *et al.* in detail [124]. The minimum E_d values of Y, Ti, O_{48f} and O_{8b} are 35.1 eV, 35.4 eV, 13 eV and 20 eV respectively. The E_d values of cations are lower than that of $Y_4Zr_3O_{12}$ computed in this paper and those of anions are similar. A material with high displacement energy is expected to have higher radiation tolerance because of the smaller number of initial defects upon irradiation [260, 261]. The enhanced irradiation resistance of GaN compared to GaAs is attributed to the higher threshold displacement energy of GaN [262]. In fluorite-structured oxides, ThO_2 and CeO_2 , calculated threshold displacement energy of Th is more than that of Ce and those of oxygen are comparable (For ThO_2 , $E_{d,Th} = 53.5$ eV, $E_{d,O} = 17.5$ and for CeO_2 , $E_{d,Ce} = 46$ eV and $E_{d,O} = 20$ eV) [119]. The experimental evidence shows that defect accumulation and radiation damage are more in CeO_2 [263].

There is a counter-argument by Xiao *et al.* [123] and Wang *et al.* [122] that in pyrochlores, the higher the threshold displacement energy, higher the energy barrier for O- D transformation. So the pyrochlores with higher displacement energy tend to amorphize faster than those with lower displacement threshold. Experimentally, $Gd_2Zr_2O_7$ is the most radiation resistant zirconate pyrochlore. But the ab initio molecular dynamics simulations give higher values for threshold displacement energies ($E_{d,Gd} = 31$ eV, $E_{d,Zr} = 39$ eV, $E_{d,O_{8b}} = 13$ eV, $E_{d,O_{48f}} = 9.5$ eV) [264] compared to $La_2Zr_2O_7$ ($E_{d,La} = 29.5$ eV, $E_{d,Zr} = 39.5$ eV, $E_{d,O_{8b}} = 10.5$ eV $E_{d,O_{48f}} = 15.5$ eV),

$\text{Nd}_2\text{Zr}_2\text{O}_7$ ($E_{d,\text{Nd}} = 21.5$ eV, $E_{d,\text{Zr}} = 27$ eV, $E_{d,\text{O}48f} = 6.5$ eV, $E_{d,\text{O}8b} = 3.0$ eV) and $\text{Sm}_2\text{Zr}_2\text{O}_7$ ($E_{d,\text{Nd}} = 21.5$ eV, $E_{d,\text{Zr}} = 26.5$ eV, $E_{d,\text{O}48f} = 7.0$ eV, $E_{d,\text{O}8b} = 3.0$ eV), which are comparatively less radiation resistant [123]. So the argument of higher radiation resistance for lower threshold displacement energy is not valid in these cases.

The E_d value is an important input parameter for SRIM (Stopping Range of Ions in Matter) simulations [107]. SRIM is a collection of software used to simulate ion beam interactions with matter. It is widely used by the ion-implantation research and technology community and in other branches of radiation material science for the calculation of ion ranges and evaluation of ion beam induced mixing, sputtering, and damage production. The main part of the SRIM is TRIM (Transport of Ions in Matter), which seeks the Kinchin-Pease analytical solution [104] for target damage using a Monte-Carlo simulation method namely Binary Collision Approximation (BCA) [237]. When experimental and simulated data of E_d values are unavailable for a certain element in the periodic table, SRIM universally takes $E_d=25$ eV. For a SRIM simulation for 1MeV He^+ ions in $\text{Y}_4\text{Zr}_3\text{O}_{12}$, the error between peak damage value for default values in SRIM and the calculated E_d values in this chapter is $\sim 33\%$.

Table 6.6: O-D defect reaction pair energies of Zr containing δ – phases. (* - current study; ** - values obtained from Figure 3. of reference [102])

Delta phase	O-D defect reaction pair energy (eV)
$\text{Y}_4\text{Zr}_3\text{O}_{12}$	1.66*
$\text{Dy}_4\text{Zr}_3\text{O}_{12}$	2.5**
$\text{Er}_4\text{Zr}_3\text{O}_{12}$	2.58**
$\text{Yb}_4\text{Zr}_3\text{O}_{12}$	2.62**
$\text{Lu}_4\text{Zr}_3\text{O}_{12}$	2.64**
$\text{In}_4\text{Zr}_3\text{O}_{12}$	2.72**
$\text{Sc}_4\text{Zr}_3\text{O}_{12}$	2.76**

The defect formation energies are compared to previously calculated values of pyrochlore structures. The cation antisite pair formation energy (0.54 eV for $3a$ - $18f$ cation swap) lower than that of all the pyrochlores data available so far (1.77 $\text{Y}_2\text{Ti}_2\text{O}_7$),

1.97 [259] ($Y_2Sn_2O_7$), 1.9 [265] ($Gd_2Ti_2O_7$) 1.8 [265] ($Gd_2Zr_2O_7$)) and anion Frenkel pair formation energies are less than $Y_2Ti_2O_7$ but more than $Gd_2Zr_2O_7$.

The study by Sickafus *et al.* includes the O-D pair formation energy for δ -phase structures like $Dy_4Zr_3O_{12}$, $Lu_4Zr_3O_{12}$ and $Sc_4Zr_3O_{12}$. At cryogenic temperature, $Dy_4Zr_3O_{12}$ possess highest radiation resistance (stable up to 55 dpa) followed by $Lu_4Zr_3O_{12}$ (stable up to 30 dpa) and then $Sc_4Zr_3O_{12}$ (up to 22 dpa). The values of their defect reaction pair energies presented in Sickafus *et al.* are tabulated in Table 6.6. The trend in radiation resistance of δ - phases is in accordance with their O-D pair formation energies. The least O-D pair formation energy corresponds to the best radiation tolerance and vice versa. But it is not clear that which oxygen Frenkel pair formation was considered in reference [102], the O_I Frenkel pair, or the O_{II} Frenkel pair. If we consider O_I Frenkel pair, the O-D transformation energy for $Y_4Zr_3O_{12}$ is 1.66 eV which is lower than all the data on Zr containing pyrochlores and δ -phases studied so far [102, 259, 263–265]. This suggests a rapid transformation of $Y_4Zr_3O_{12}$ to disordered fluorite structure and hence more resistance to amorphization for $Y_4Zr_3O_{12}$ compared to other similar structures. These results convey that Zr/Al - ODS alloys which have better corrosion resistance properties compared to the conventional Ti-ODS alloys may also possess superior radiation resistance.

6.8 Conclusions

The *ab-initio* based molecular dynamics simulation technique has been extended to study the low energy recoil events and defect formation energies in $Y_4Zr_3O_{12}$. As a first step, the density functional theory calculations are carried out to show that among available $18f$ sites in the δ -phase structure, the Zr atoms in $Y_4Zr_3O_{12}$ prefer to occupy the farthest corners of cation octahedron. Further, the threshold displacement energies are found to be anisotropic, strongly dependent on the incident direction. The minimum threshold displacement energies of Zr_{3a} , Zr_{18f} , and Y_{18f} are 28 eV, 40 eV, and 50 eV respectively. Anions have smaller threshold displacement energies than cations, 13 eV for O_I and 16 eV for O_{II} . The defect generation mechanisms of cations involve more number of defects, suggesting that anion disorder is more probable than cation disorder.

Furthermore, the formation energies for vacancy, interstitial, antisites and Frenkel pairs in $Y_4Zr_3O_{12}$ are calculated using DFT simulations. The Y – Zr_{18f} antisite formation energy has the least value among defect formation energies considered. Therefore upon irradiation, the 18f atoms can interchange position and continue to be in the δ - phase structure before transforming into the defect fluorite phase, indicating the possibility for enhanced radiation tolerance of this phase compared to other fluorite-related structures.

An in-depth understanding on the defects in $Y_4Zr_3O_{12}$ can be obtained using ion beam induced luminescence spectroscopic studies, which constitute our final chapter of the thesis.

Ion beam induced luminescence in $\text{Y}_4\text{Zr}_3\text{O}_{12}$ and the role of anion defects

7.1 Introduction

The origin and evolution of point defects in $\text{Y}_4\text{Zr}_3\text{O}_{12}$ and its importance in understanding radiation resistance of that material is discussed in the previous chapter. From the threshold displacement energy calculations it is inferred that the anion-related defects are more likely to form in $\text{Y}_4\text{Zr}_3\text{O}_{12}$ in a radiation environment. This conjuncture is experimentally validated in the present chapter.

Luminescence is a very effective experimental tool to analyze the intrinsic and extrinsic defects in a material. Ionoluminescence (IL) is a branch of luminescence in which the photon emission occurs from a target upon ion beam irradiation. Irradiation by light ions mainly introduces isolated point defects. These defects introduce levels in the bandgap influencing charge carrier lifetime and mobility [130]. The damage may accumulate and transform into complex defect clusters at higher fluences. Ionoluminescence is similar to cathodoluminescence. Hence the studies in cathodoluminescence can be used for comparison and interpretation of the results. Fluorites are well known to exhibit luminescence for a wide range of wavelengths. Light emission from fluorites originates from impurities and a variety of color centers [134]. They are shown to

have bands in IL-spectrum, each containing many sub-bands [133].

In the present chapter, the dispersed oxide in as-prepared ODS steels, $Y_4Zr_3O_{12}$ phase, is synthesized by the solid-state method and characterized using XRD, Raman spectroscopy and UV-Vis Spectroscopy. Further, for the in-depth understanding of the irradiation-induced defects, the ion beam induced luminescence spectra of $Y_4Zr_3O_{12}$ are acquired. The defect levels associated with anion vacancies and color centers are simulated using DFT-HSE06 calculations. The bands in IL spectra are correlated with the radiative electronic transitions involving the calculated defect levels.

7.2 Experimental methods

7.2.1 Synthesis of $Y_4Zr_3O_{12}$

The $Y_4Zr_3O_{12}$ phase can be prepared from Y_2O_3 and ZrO_2 precursors by solid state method. The chemical reaction is:



Required amount of ZrO_2 (*Alfa aesar*, purity: 99.9%) and Y_2O_3 (*Alfa aesar*, purity: 99.9%) are mixed in a ball mill for 8 hours. The milled powder is further sintered at 1300 °C for \sim 120 hours. The phase formation was confirmed using powder-XRD data taken in the INEL equinox diffractometer. Raman measurements were carried out using micro-Raman spectrometer (WITec Alpha RA 300) using Nd-YAG laser having an excitation wavelength of 532 nm and laser power of 0.5 mW.

7.2.2 Ionoluminescence

The as-prepared $Y_4Zr_3O_{12}$ is made into pellet and irradiated by He^+ ions of energy 100 keV. The projected range of He^+ ions in $Y_4Zr_3O_{12}$ is \sim 415 nm which is calculated using SRIM software with the threshold displacement values computed in Chapter 6. The vacancy profiles of Y, Zr and O for a full cascade SRIM calculation of 10^5 He ions are shown in Figure 7.1. It can be seen that the number of oxygen vacancies per ion-Å are \sim 75% higher than the number of Zr and Y vacancies combined. Nuclear energy loss (197 eV/Å) is higher than the electronic energy loss (34.51 eV/Å) in this energy.

During the experiment, the vacuum is maintained at 10^{-6} mbar. The beam diameter is 10 mm. The beam current is kept constant at $1 \mu\text{A}$. The surface of the pellet was covered with a steel mesh to avoid the current-fluctuations and luminescence due to accumulated charge. The flux is increased up to 1×10^{17} ions/cm² and the luminescence during ion irradiation is recorded at definite intervals. The initial few IL spectra were acquired in the wavelength range of 300-800 nm. There was no peak outside the range of 300 - 470 nm. Therefore, further acquisitions were carried out in the 300 - 470 nm range. The 470-800 nm wavelength region was periodically checked for signatures, but no other peak emerged during the course of the experiment.

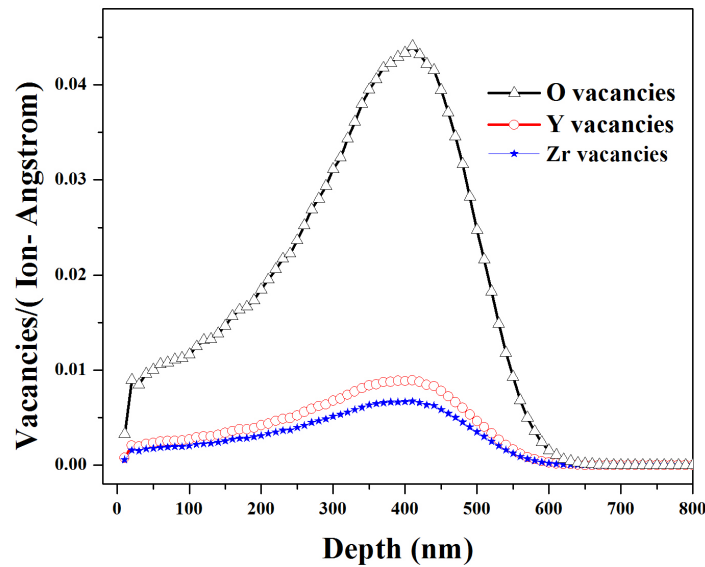


Figure 7.1: The vacancy profile of Y, Zr and O in 100 keV He^+ ion irradiated $\text{Y}_4\text{Zr}_3\text{O}_{12}$, calculated using SRIM.

7.2.3 Calculation of defect-levels

In addition to the structural relaxations presented in the Chapter 6, the extent of charge localization is tested for charged defects, using HSE06 hybrid xc functional [150] and DFT-GGA which was previously used. All the calculations are done in a supercell of 152 atoms. The initial structural relaxations are done using DFT-GGA and the relaxed structure is used as the starting point for HSE06 calculations. A flexible automatic k-point mesh generation method implemented in VASP [161], based on the

Monkhorts pack [178] is used for k-point generation. The calculations are continued up to an energy convergence of 0.01 meV/atom.

7.3 X-Ray Diffraction of as-prepared $Y_4Zr_3O_{12}$

The typical XRD pattern of as-synthesized powder is presented in Figure 7.2. Reflections related to the parent compounds, Y_2O_3 and ZrO_2 are not observed. All the reflections can be indexed for $Y_4Zr_3O_{12}$, as per references [195, 196]. The $Y_4Zr_3O_{12}$ belongs to the trigonal crystal system, which can be represented using hexagonal axes and rhombohedral axes. In Hexagonal representation, the unit-cell ($a=b=9.78$ Å, $c=9.11$ Å, $\alpha = \beta = 90^\circ$, $\gamma = 120^\circ$) contains three formula units. In rhombohedral representation the unit-cell ($a=b=c=6.38$ Å, $\alpha = \beta = \gamma = 99.298^\circ$) contains one formula unit. This structure is also related to the fluorite structure and pyrochlore structure. In Figure 7.2, the pattern is indexed with respect to hexagonal axes. The

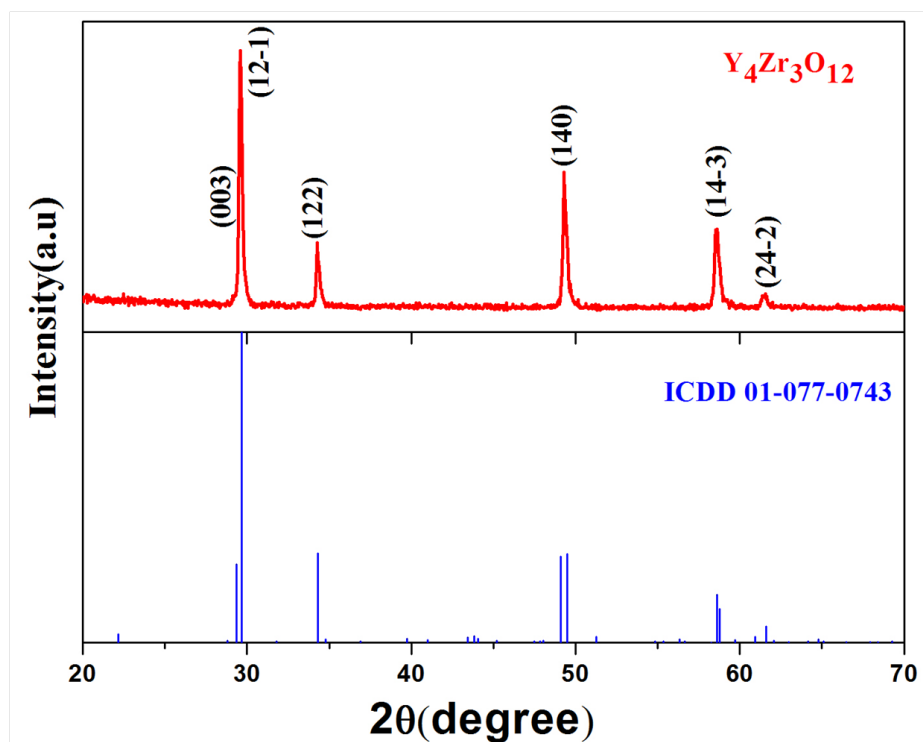


Figure 7.2: The XRD spectrum of as-prepared $Y_4Zr_3O_{12}$. Corresponding ICDD data (ICDD 01-077-0743) is also shown.

predominant reflection (211) is equivalent to $(20\bar{1})$ plane in rhombohedral represen-

tation. This is related to cation ordering and is less sensitive to anion ordering. It is equivalent to (311) plane in the fluorite related structures (pyrochlore), which is a fundamental reflection corresponding to the fluorite structure. The (122) plane, is equivalent to $(21\bar{1})$ plane in rhombohedral axes. It constitutes $3a$ cations and O_{II} anions. In cubic axes, it is equivalent to (222) plane, which again is an indication of fluorite superstructure. The plane, (214) in hexagonal axes ((310) in rhombohedral axes) is sensitive to $3a$ cations, $18f$ cations, and anions. The fourth reflection in the spectrum, indexed as (413) plane is equivalent to $(40\bar{1})$ in rhombohedral axes. This plane is an indication of anion ordering in $Y_4Zr_3O_{12}$. As per the threshold displacement energy calculations in Chapter 6., this reflection is most sensitive to irradiation-induced changes.

7.4 Raman spectroscopy and simulation of Raman modes in $Y_4Zr_3O_{12}$

The fluorite-related structures, pyrochlore, δ -phase, and defect fluorite structure exhibit similar XRD patterns since the structure differ mainly by anion arrangement. The superstructure reflections of the cations are so intense that the reflections from the cation sublattice are indistinguishable from the background. Vibrational spectroscopic techniques like Raman and FTIR spectroscopy are often used to distinguish these species.

The Raman spectra of as-prepared $Y_4Zr_3O_{12}$ is shown in Figure 7.3. It is similar to the spectra reported earlier in literature [266]. The peaks are broad due to pre-existing oxygen vacancies and strong luminescence background in the system. The spectrum can be divided into three regions marked I, II, and III. There is no reported literature explaining different modes responsible for these bands. So it is necessary to proceed with ab initio simulations on vibrational modes of $Y_4Zr_3O_{12}$.

Raman modes in perfect $Y_4Zr_3O_{12}$ structure can be simulated using Density Functional Theory calculations. A periodic cell with 152 atoms is used for the calculations. The simulations are done using VASP non-spin-polarized calculations with projector augmented wave pseudopotentials, the Perdew-Burke-Ernzerhof exchange-correlation functional [148], a plane-wave energy cutoff of 500 eV, and a $10 \times 10 \times 10$ k-point

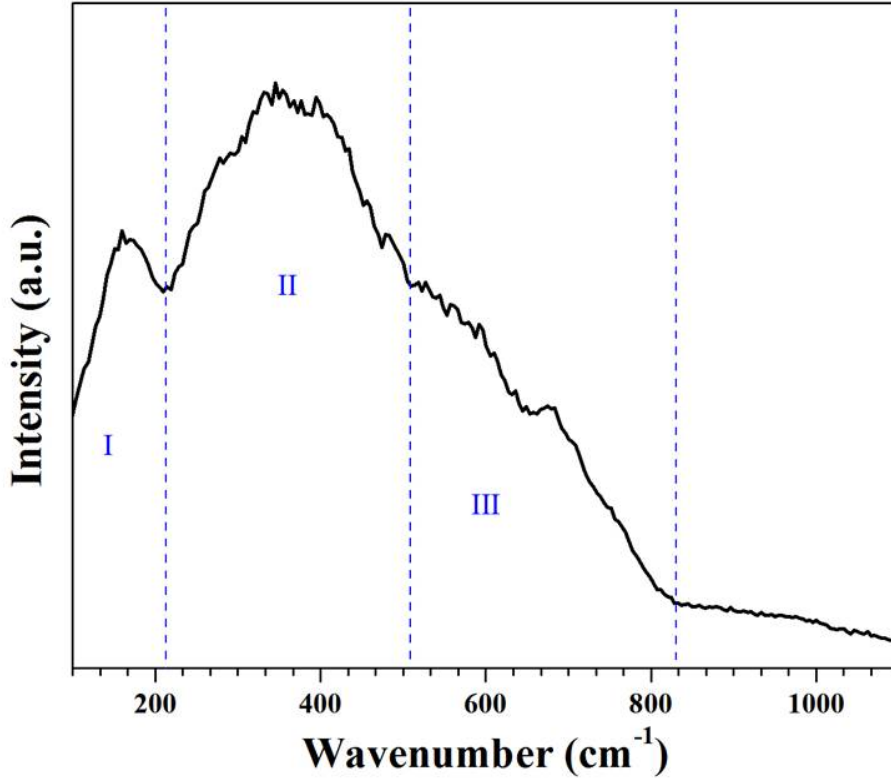


Figure 7.3: The Raman spectrum of $Y_4Zr_3O_{12}$. The spectrum can be divided into three bands I, II, and III. The band-I, II and III have 6, 7 and 4 sub bands respectively. (refer to Table 7.1)

mesh. Since partial occupancies of atoms cannot be implemented in VASP without changing symmetry, ZrY_6O_{12} unit-cell is used for the simulations. Using the density functional perturbation theory (DFPT) method [267] as implemented in the VASP. The PHONOPY code [268, 269] is used to extract the the phonon frequencies and normal modes at the Γ point.

The $Y_4Zr_3O_{12}$ belongs to point group C_3^i [270]. From factor group analysis [271], the irreducible representations for $Y_4Zr_3O_{12}$ crystal is:

$$\Gamma_{crystal} = 9A_g + 9E_g + 10A_u + 10E_u \quad (7.1)$$

Here A_u and A_g modes are non-degenerate, while E_g and E_u modes are doubly degenerate resulting in a total of 57 total modes. Out of these 57 modes, there are

three acoustic modes and 54 (3N-3) optic modes.

$$\Gamma_{acoustic} = A_u + E_u \quad (7.2)$$

$$\Gamma_{optical} = 9A_g + 9E_g + 9A_u + 9E_u \quad (7.3)$$

Based on the selection rules, A_g and E_g modes are Raman active while A_u and E_u modes are IR active. Thus there are 27 Raman active vibrations and 27 IR active vibrations.

The calculated modes, their frequency and Raman activity are tabulated in Table 7.1. The first band in Figure 7.3 has 6 modes in it, numbered 5, 7, 9, 10, 12 and 13 in the Table 7.1. The broad band centered at 350 cm^{-1} is comprised of seven Raman active modes in the wavenumber range 293 cm^{-1} to 454 cm^{-1} . The tail region marked III consists of four Raman active modes numbered 32, 33, 36 and 37 in the table.

Table 7.1: The calculated vibrational modes, their frequencies and Raman activity in $Y_4Zr_3O_{12}$

Sl.No	Mode	Frequency	Raman activity
1	A_u	0	
2	E_u	0	
3	A_u	118.95	
4	E_u	122.30	
5	A_g	125.06	R
6	A_u	150.33	
7	E_g	158.75	R
8	E_u	172.56	
9	A_g	188.67	R
10	E_g	191.00	R
11	E_u	214.60	
12	A_g	220.74	R
13	E_g	226.79	R
14	A_u	244.71	
15	E_u	255.41	
16	$E_g + A_u$	283.00	
17	A_g	293.48	R
18	E_g	311.95	R
19	A_u	329.19	
20	E_u	331.87	
21	A_g	347.84	R
22	A_u	372.80	
23	E_u	377.23	
24	E_g	387.51	R
25	A_u	414.94	
26	E_u	415.50	
27	A_g	417.57	R
28	A_g	451.88	R
29	E_g	454.21	R
30	E_u	503.35	
31	A_u	510.77	
32	A_g	516.09	R
33	E_g	516.60	R
34	A_u	524.52	
35	E_u	567.33	
36	E_g	592.94	R
37	A_g	658.13	R

7.5 Bandgap energy of $Y_4Zr_3O_{12}$

The bandgap energy of $Y_4Zr_3O_{12}$ is measured using UV-vis absorption spectroscopy. The measured bandgap values are compared with bandgap obtained using DFT calculations.

7.5.1 Estimation of bandgap using UV-Vis spectroscopy

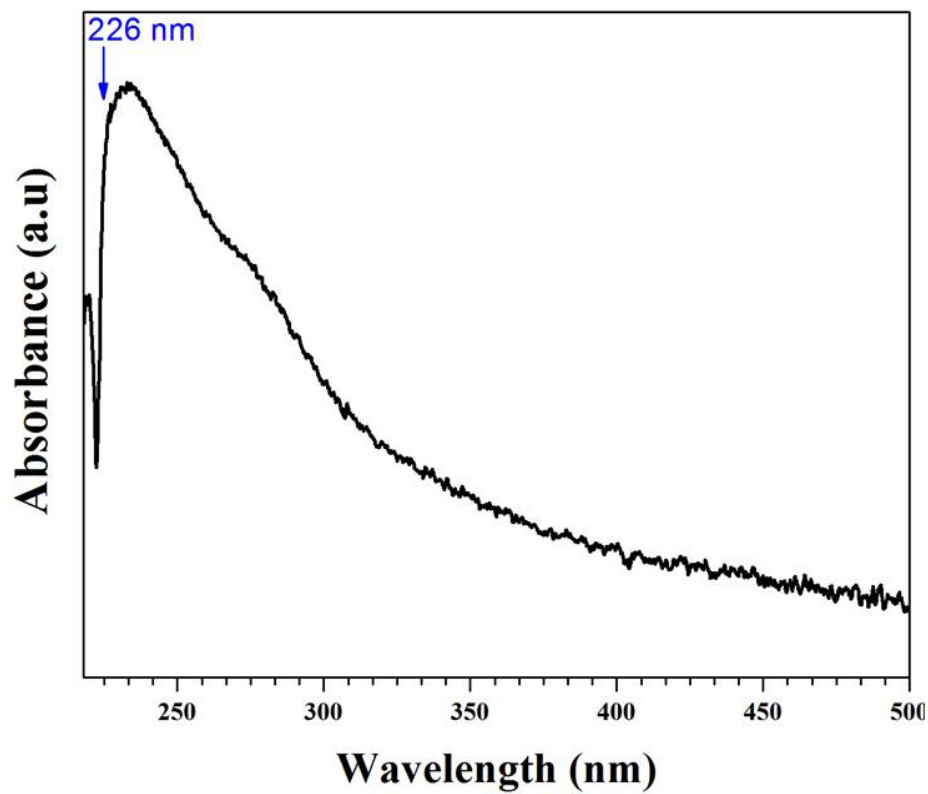
In 1966, Tauc proposed a method to determine the bandgap energy from the experimentally determined energy-dependent absorption coefficient of the material [272]. The Tauc equation is:

$$(\alpha.h\nu)^{\frac{1}{n}} = B(h\nu - E_g) \quad (7.4)$$

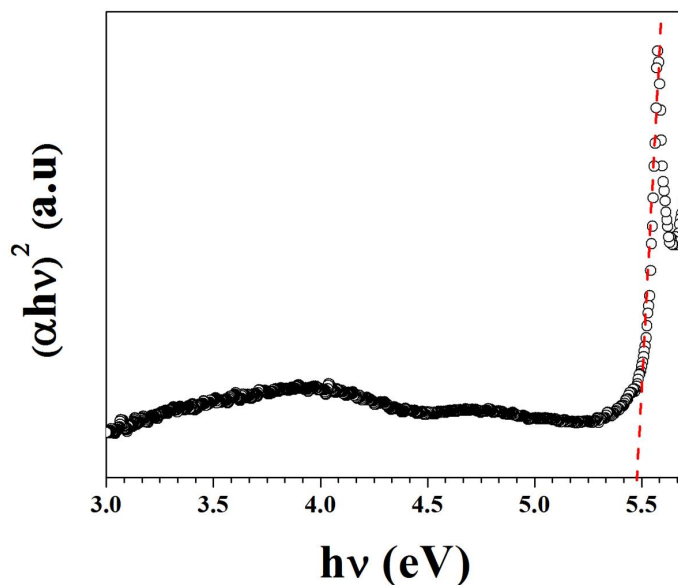
where h is the Planck constant, α is the absorbance, ν is the photon frequency, E_g is the bandgap energy and B is a constant. The n -factor depends on the nature of the electronic transition and its value is 1/2 and 2 for direct and indirect transitions respectively.

The Figure 7.4 shows the UV-visible absorption spectra of the as-prepared $Y_4Zr_3O_{12}$. The absorption is high at the UV region and exponentially decreases in the visible region. This exponential nature of decay is due to pre-existing defect states in the bandgap region and is a characteristic nature of nanoceramics [266]. The absorption edge gives a rough estimate of the bandgap. The absorption edge is at ~ 226 nm, which corresponds to the bandgap energy of ~ 5.48 eV. The absorption band is wide, owing to the presence of oxygen vacancies in the material.

The Tauc plot is plotted from the absorbance spectra of $Y_4Zr_3O_{12}$ and is presented in Figure 7.4(b). The value of n is chosen to be 1/2. As per Eq.7.4., the linear region of $(\alpha.h\nu)^2-h\nu$ plot can be extrapolated to $h\nu$ axis to find the bandgap. The bandgap energy determined from Tauc plot is 5.47 eV. It is slightly higher than earlier reported value of 5.4 eV, which is calculated from reflectance spectra [266]. The results indicate that $Y_4Zr_3O_{12}$ is a wide bandgap material.



(a)



(b)

Figure 7.4: (a) The UV-vis absorption spectrum of $Y_4Zr_3O_{12}$. The absorption edge is at 226 nm. (b) The Tauc plot. The bandgap calculated from the Tauc plot is 5.47 eV.

7.5.2 Calculation of bandgap using PBE-GGA and HSE06 xc functionals

In DFT calculations, the bandgap is calculated as:

$$E_g = E^- + E^+ - 2E^0 \quad (7.5)$$

Here E^0 is the total energy of the perfect neutral structure. E^+ and E^- are the total

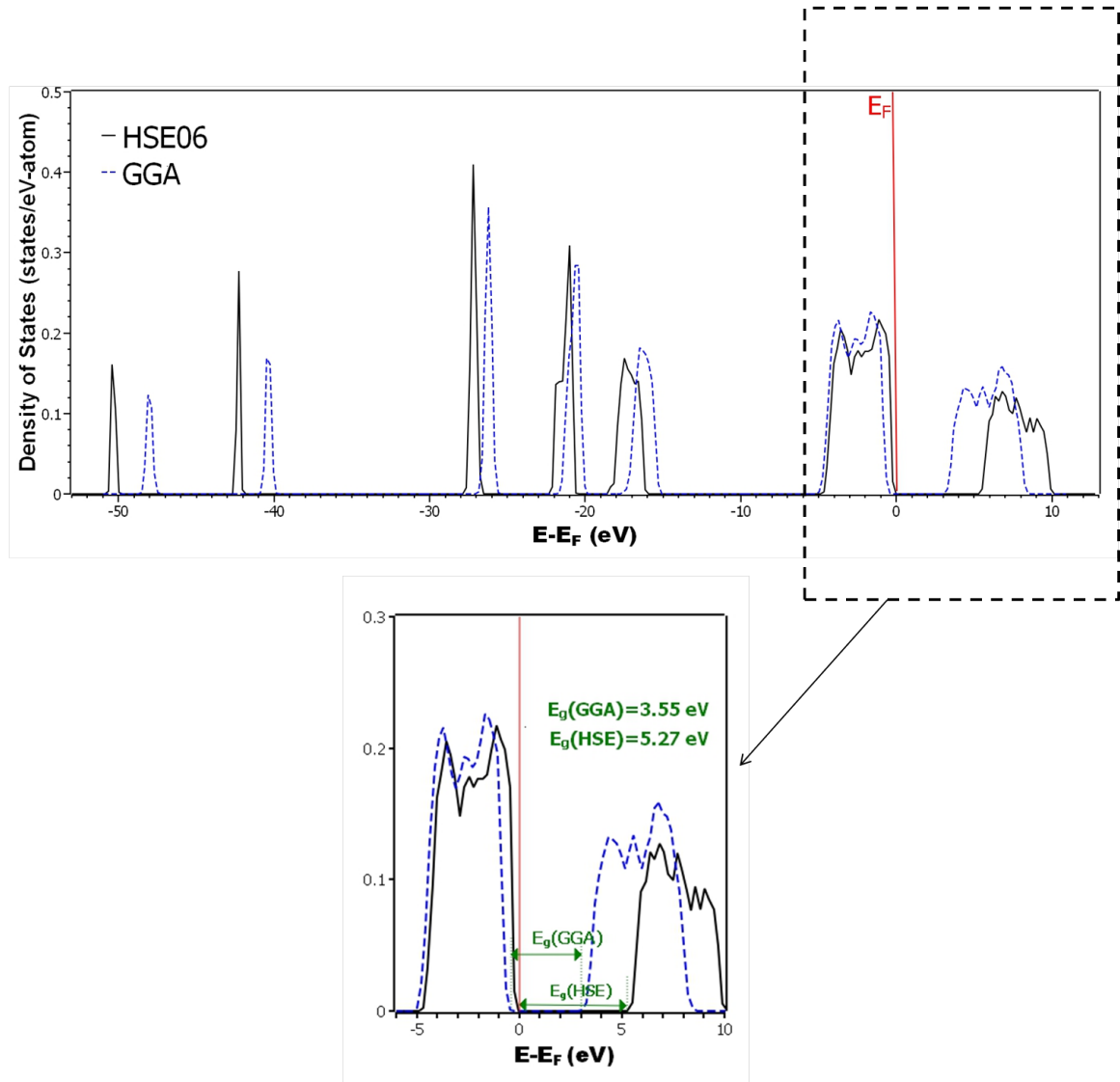


Figure 7.5: Total Density of states (TDOS) of $Y_4Zr_3O_{12}$, calculated using PBE-GGA (blue, dashed line) and HSE06 hybrid functional (black solid line). The red line indicates the Fermi level. The calculated bandgap is 5.27 eV for HSE06 and 3.55 eV for PBE-GGA calculations.

energy of the structure with one electron added and removed respectively. Normal PBE-DFT calculations of $Y_4Zr_3O_{12}$ estimate the bandgap as 3.55 eV, which is lower than the experimentally observed value. The partial and total density of states plot of ideal $Y_4Zr_3O_{12}$ crystal is shown in Figure 7.5.(blue, dotted line). The valence band is comprised of p orbitals of O and d orbitals of Y and Zr and the conduction band has some d and f states from Y and Zr. The error in bandgap value is due to the self-interaction error within the occupied states, which over delocalize them and forces them up in energy, consequently reducing bandgap.

A hybrid exchange-correlation functional is a combination of Hartree-Fock (HF) and LDA (or GGA) functionals [273]. The amount of HF to be mixed is determined by the 'mixing parameter'. The bandgap calculations of $Y_4Zr_3O_{12}$ were repeated using HSE06 functional [150], and the resulting DOS plot is presented in Figure 7.5.(solid line). The screening parameter is fixed to 0.2\AA^{-1} . The calculated bandgap is 5.27 eV, which has a better agreement with the experimentally determined value. Crystal field splitting of bands is the same irrespective of the potential used.

7.6 Ionoluminescence spectroscopy of $Y_4Zr_3O_{12}$

The ionoluminescence (IL) spectra of $Y_4Zr_3O_{12}$ pellet acquired for various fluences of 100 keV He^+ ion irradiations are presented in Figure 7.6.

The IL spectra consist of two major peaks centered at 330 nm (3.72 eV) and 415 nm (2.98 eV) respectively. The intensity of the first peak is nearly 3 times the intensity of the second one. The intensity of both peaks decreases with an increase in fluence. At a fluence of 4×10^{16} ions/cm², the intensity of both the peaks drop by 40% and remains the same up to 1×10^{17} ions/cm². The variation of peak intensities with fluence is plotted in Figure 7.7. The intensity of the second peak is observed to decrease at a slightly higher rate compared to the intensity of the first peak. In order to find the origin of IL peaks in $Y_4Zr_3O_{12}$, first-principle calculations of different luminescence centers and corresponding defect levels are carried out using HSE06 hybrid functional.

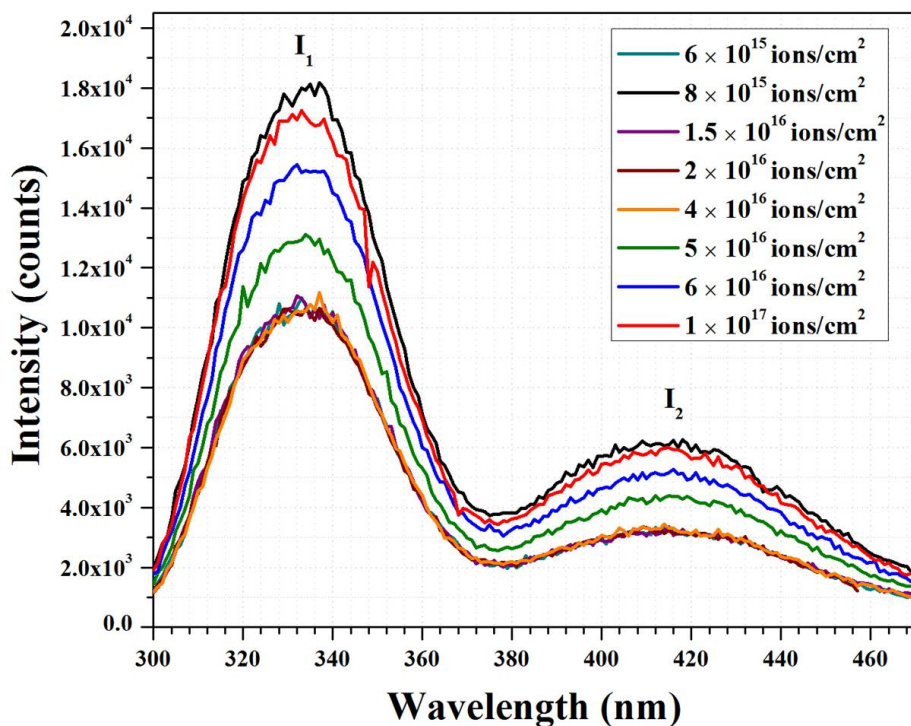


Figure 7.6: The ionoluminescence spectra of $Y_4Zr_3O_{12}$ acquired during irradiation with 100 keV He^+ ion at various fluences. The two bands observed in the spectra are marked as I_1 and I_2 .

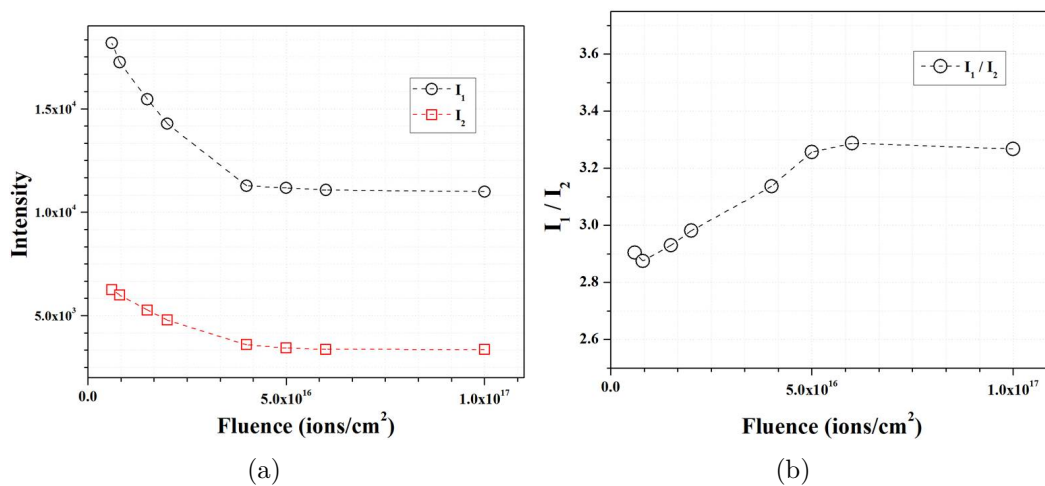


Figure 7.7: (a) Intensity variation of ionoluminescence bands with fluence. I_1 is the intensity of band centered at 330 nm and I_2 is the intensity of band centered at 415 nm. Both intensities decrease exponentially with fluence. (b) The ratio of intensities of first and second peaks. It shows that the second band is quenching faster than the first band.

7.7 *Ab initio* simulation of anion-related defect levels in $Y_4Zr_3O_{12}$ using HSE06 functional

As seen from Chapter 6, oxygen vacancies are the most probable defects in $Y_4Zr_3O_{12}$ under irradiation. The SRIM simulations (Figure 7.1.) also indicate that number of oxygen vacancies is high. Role of oxygen vacancy related defects in light emission has been reported in MgO , ZrO_2 , Al_2O_3 etc [134–137]. The irradiation-induced defects and color-centers produce defect levels within the bandgap. The optical transitions involving these localized states might be primarily responsible for ion beam induced luminescence [130, 274]. The simplest defects created are F-centers. An F-center is an anion vacancy filled by $2(O^{2-}$ or $F^{2-})$, $1(O^-$ or $F^-)$, or 0 (O-vacancy or α -center) electrons [275]. At high fluences, defect concentration increases resulting in clustering and formation of more complex defect clusters, therefore quenching the luminescence centers.

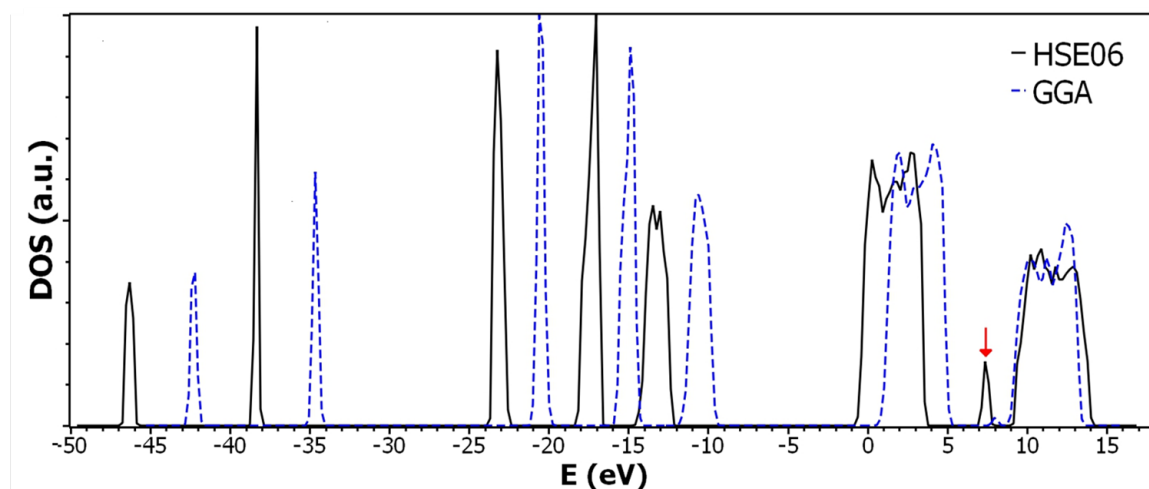


Figure 7.8: Total density of states for O vacancy in $Y_4Zr_3O_{12}$, in GGA (blue, dashed line) and HSE06 (black, solid line) functionals. O vacancy creates a localized defect state at 3.51 eV above the valence band maximum.

As we have discussed earlier, oxygen occupies two different sets of $18f$ positions in $Y_4Zr_3O_{12}$, denoted by O_I and O_{II} . These two types of oxygen have different chemical environments and formation energies. Removal of these oxygen atoms creates a localized defect levels within the bandgap. The DOS obtained after HSE06 and GGA calculations on O_I vacancy is shown in Figure 7.8. In HSE06 calculations, the defect

state is at 3.51 eV from the valence band maximum. In GGA calculation, the defect level is located at 2.62 eV away from the valence band maximum.

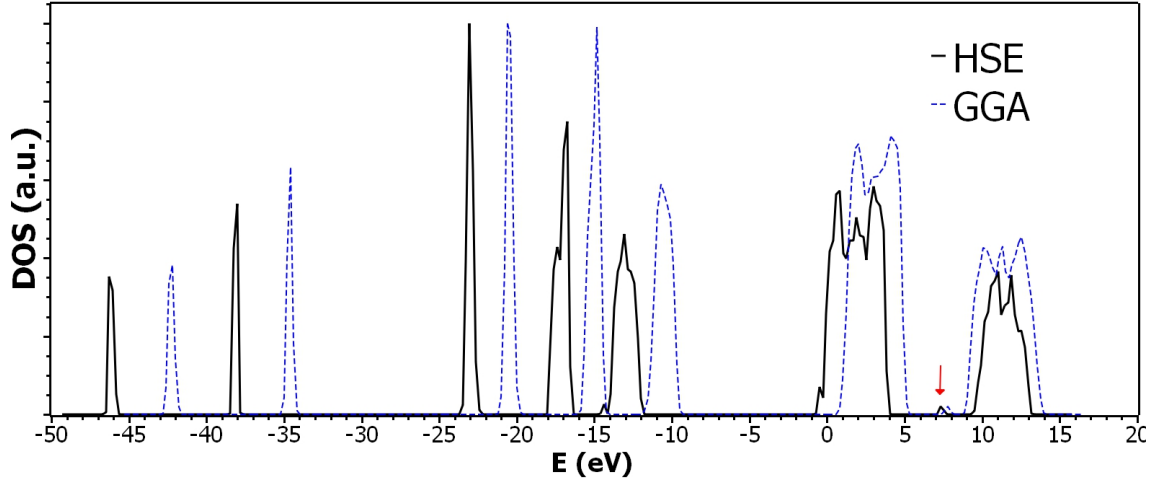


Figure 7.9: The DOS plot for O_{II} vacancy in $Y_4Zr_3O_{12}$. It produces a localized defect level at 2.9 eV from the valence band maximum.

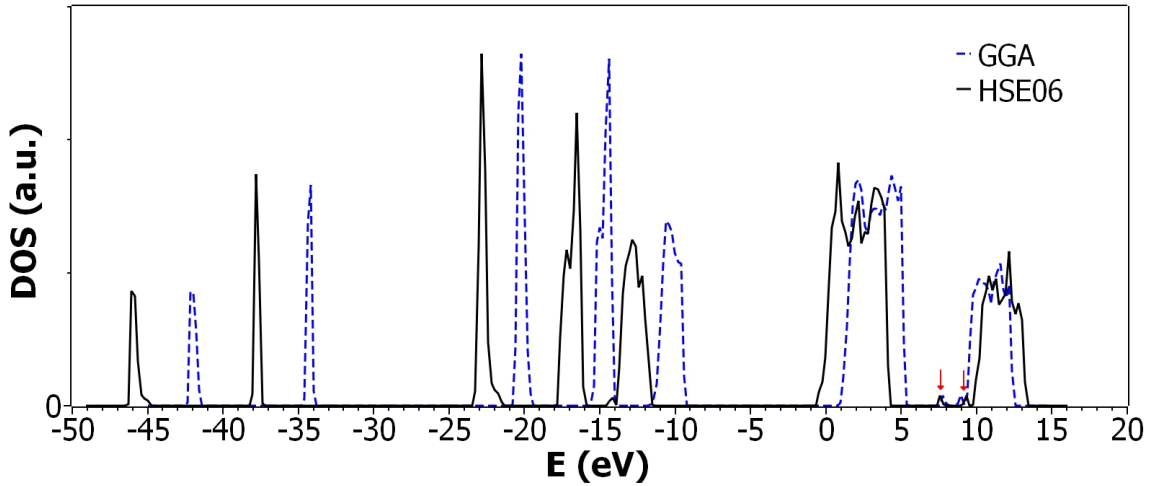


Figure 7.10: Total density of states for O vacancy with a trapped negative charge in $Y_4Zr_3O_{12}$, in GGA and HSE06 functionals. There are two defect levels at 3 eV and 4.5 eV above the valence band, marked using red arrows.

In order to correlate with the experimentally observed bandgap, the defect level position can be estimated as : $\frac{3.51}{5.27} \times 5.47 \text{ eV} = 3.64 \text{ eV}$. The transition involving this defect state to conduction band will have a emission at $\sim 340 \text{ nm}$. Thus the relaxation from O_1 vacancy defect state might be a constituent in the first band of ionoluminescence spectra of $Y_4Zr_3O_{12}$ (Figure 7.6).

An O_2 vacancy in the lattice creates a level at 2.9 eV from the conduction band edge. The DOS plot for O_2 vacancy is shown in Figure 7.9. When we scale up this to the experimentally observed bandgap value, the defect falls at ~ 3.02 eV. The transition involving this level and the conduction band will be at ~ 411 nm. This defect might be responsible for the second peak observed in the IL spectra.

An O^- vacancy (or F^- center) is formed when either O_1 or O_2 vacancy traps an electron. F^- center is an IL active color-center in fluorite crystals [129]. To examine the effect of O^- vacancy in IL spectra of $Y_4Zr_3O_{12}$, HSE06 and GGA calculations were performed. The TDOS plot for O_1^- vacancy is presented in Figure 7.10. An O_1^- vacancy introduces two narrow defect states in the bandgap at 3 eV and 4.5 eV respectively. When we scale up to the experimental bandgap, these defect bands will be at 3.13 eV and 4.69 eV respectively. The transitions involving these defect states and valence band will have signatures at ~ 400 nm and ~ 264 nm respectively.

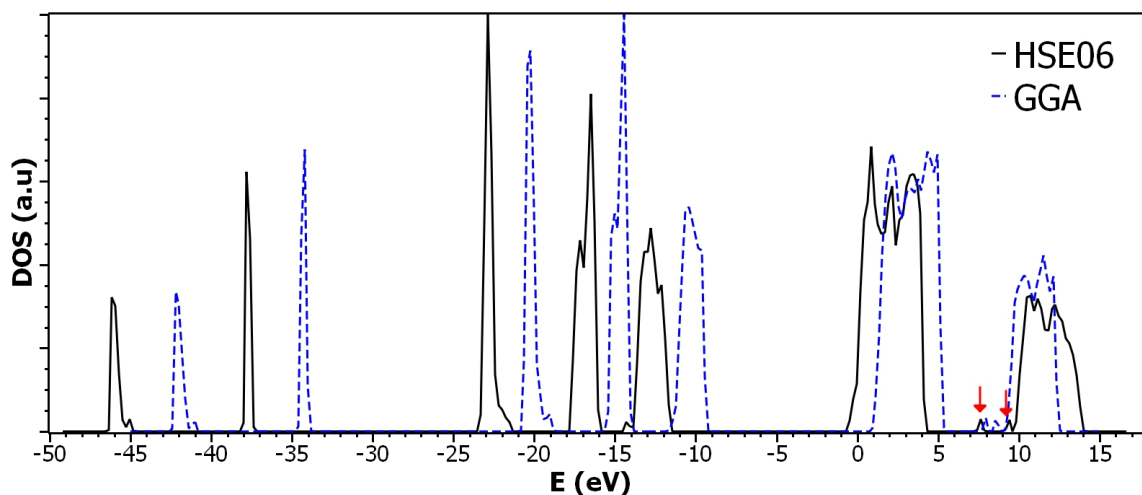


Figure 7.11: TDOS plot for O_{II}^- vacancy in $Y_4Zr_3O_{12}$, calculated using GGA and HSE06 functionals. There are two defect levels at 3.2 eV and 4.6 eV respectively. The red arrows indicate the position of defect levels.

The F^+ center is an electron deficient oxygen vacancy. It is responsible for the 415 nm transition in IL spectrum of sapphire. The change in TDOS for an O_1^+ vacancy formation is presented in Figure 7.12. It creates a level at 3.5 eV away from the conduction band edge. Likewise, O^+ vacancy creates defect-level at 3.46 eV from the conduction band edge (see Figure 7.13). These are constituents of the first band of IL spectra.

The $3a$ and $18f$ cation vacancies create defect levels very close to the valence band.

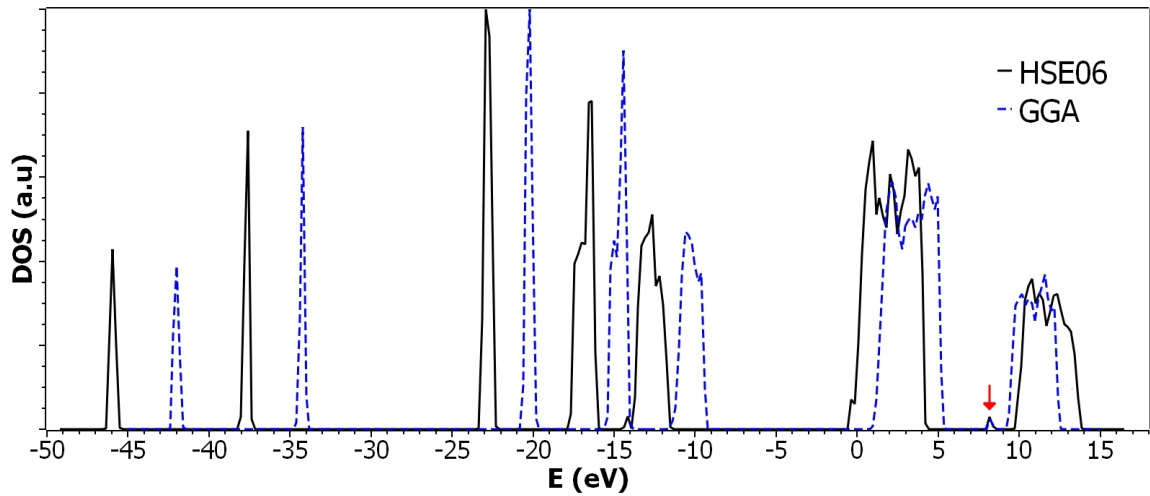


Figure 7.12: TDOS plot for O_1^+ vacancy. The defect band created by O_1^+ vacancy is situated at 3.55 eV from the valence band maximum.

So they may not be contributing to the transitions associated with luminescence.

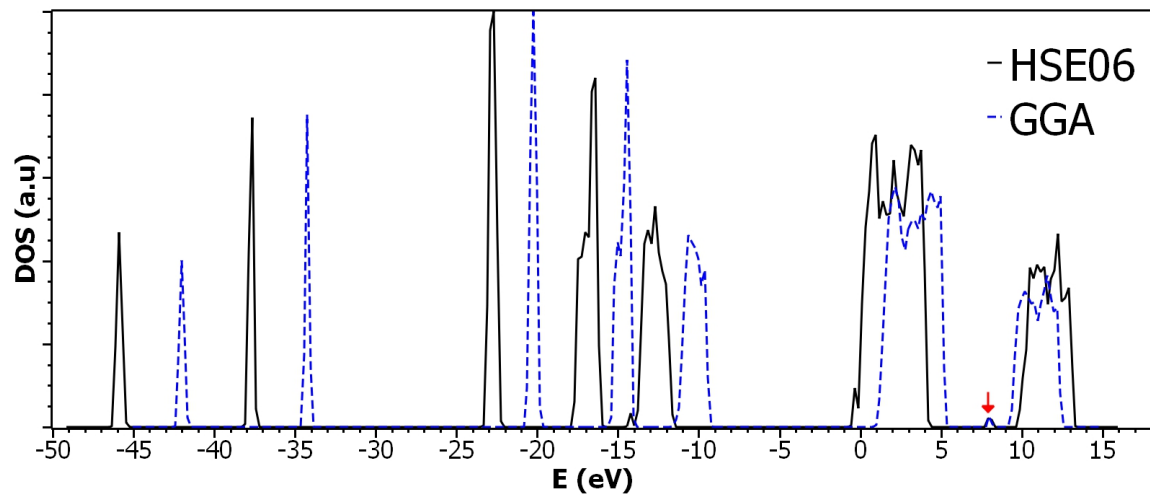


Figure 7.13: TDOS plot for O_2^+ vacancy. The defect band created by O_2^+ vacancy is half filled and is situated at 3.46 eV from the conduction band edge.

Similarly, O_2^{2+} and O_1^{2+} creates defect levels at 4.2 eV and 4.3 eV respectively. These energies are close to the first band in IL spectra.

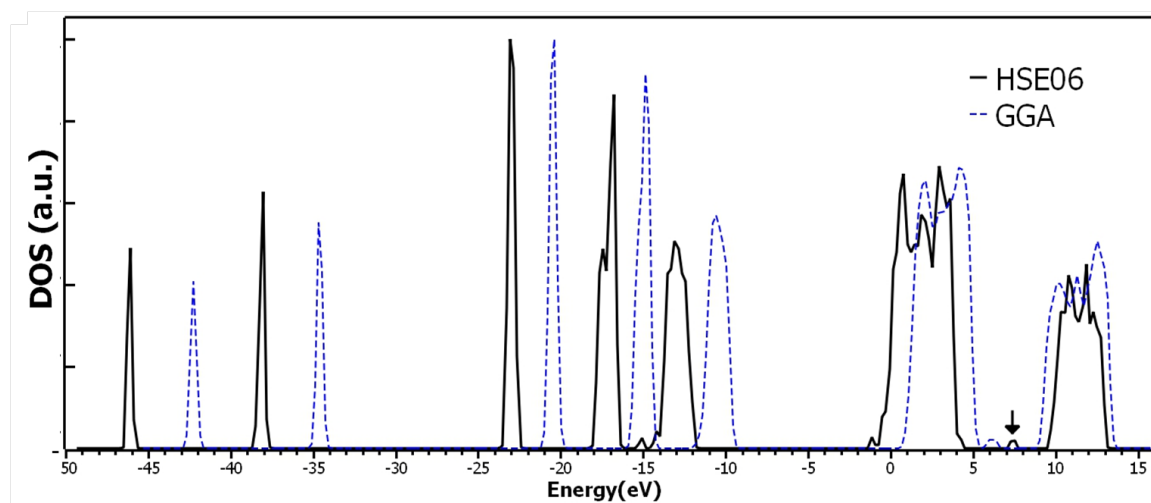


Figure 7.14: TDOS plot for Oxygen interstitial in $6c$ site in $Y_4Zr_3O_{12}$, calculated using GGA and HSE06 functionals. The defect level is at 2.9 eV from valence band edge.

7.8 Correlation between IL spectra and simulated defect levels

It is evident that the IL bands in Figure 7.6. are far away from the band edge (5.5 eV). Therefore, these bands can be due to deep level emission (DBE) from the defect levels created by irradiation [136]. Excitation by ion beams creates electron-hole pairs, which get trapped in different metastable energy states within the bandgap contributing to the luminescence. The broad luminescence emissions are a result of overlapping sub-bands resulting from different defect centers [276]. The defect levels associated with $3a$ vacancy and $18f$ vacancy are close to the valence band and hence belong to much lower wavelengths. Moreover many photoluminescence, ionoluminescence and cathodoluminescence studies attribute the luminescence of fluorite related structures to oxygen vacancy related defects [133, 136, 276, 277]. Therefore it is feasible to correlate the ion beam induced luminescence spectra to oxygen-related defects.

The IL spectra of CaF_2 mainly consist of two wide bands, centered at ~ 300 nm and ~ 580 nm. The band at 300 nm includes a small peak at ~ 410 nm. These emissions are explained using intrinsic crystal defects and self-trapped excitons (STEs) [133, 278]. An STE is a V_k center with an electron. Various configurations of STEs with various luminescence properties are also studied [277]. A wide emission band due to F_2

centers (sometimes called M- centers) at ~ 580 nm is also observed in fluorites [130]. Even though $Y_4Zr_3O_{12}$ is a fluorite related structure, the IL peak at ~ 580 nm is not observed even after irradiation up to 1×10^{17} ions/cm². Further, the calculations show that the F_2 centers in $Y_4Zr_3O_{12}$ create doublet levels near to the oxygen mono vacancy levels. Therefore it is unlikely to have the luminescence bands due to F_2 centers far away from monovacancy-related bands.

Ionoluminescence is in many ways similar to cathodoluminescence(CL). Hence the CL studies are widely used to compare and interpret IL spectra. The similarity between IL and CL spectra of CaF_2 enforces this argument [130,279]. The cathodoluminescence (CL) of ZrO_2 related materials are usually discussed in association with oxygen vacancies. The CL intensity of Y-doped ZrO_2 is reported to decrease with an increase in oxygen vacancies [280]. A strongly localized, electron-deficient vacancy readily accepts an electron and recombines radiatively. This is the major component in CL emission of ZrO_2 and IL emission in sapphire also [135]. Deconvolution of CL spectra of CeO_2 emission from F-centers are predominant compared to F^+ centers and there is a quenching of intensity after critical oxygen vacancy concentration [281]. The CL emission from HfO_2 is also ascribed to the radiative recombination emission caused by oxygen vacancies [282]. The doping of HfO_2 by Sc leads to a decrease of the intensity of cathodoluminescence spectra by passivating the adjacent oxygen vacancies [283]. The luminescence properties of yttria stabilized zirconia system, which is similar to $Y_4Zr_3O_{12}$, has been studied extensively by many groups [280,284]. According to their reports, there are at least three types of defects in it: an intrinsic neutral oxygen vacancy, F^- center and F^{2-} center. It exhibits three distinct CL bands at 460 nm, 550 nm and 600 nm. In YSZ samples with monoclinic polymorph, a band at 330 nm is observed, which is ascribed to oxygen vacancies [281].

The defect levels in $Y_4Zr_3O_{12}$, of O_I and O_{II} in different charge states as per the HSE06 calculations are summarized in Figure 7.15. This Figure is scaled up for the experimental bandgap value and is shown in Figure 7.16. A detailed understanding of the contribution of different color centers towards the luminescence spectra in Figure 7.6 can be obtained from these diagrams.

From the defect levels computed, it is evident that the energy gap between valence band and energy level positions of O_I (339 nm), O_I^+ (335 nm) and O_{II}^+ (343 nm) fall on the wavelength range of first band (centered at 330 nm) of IL spectra. A free

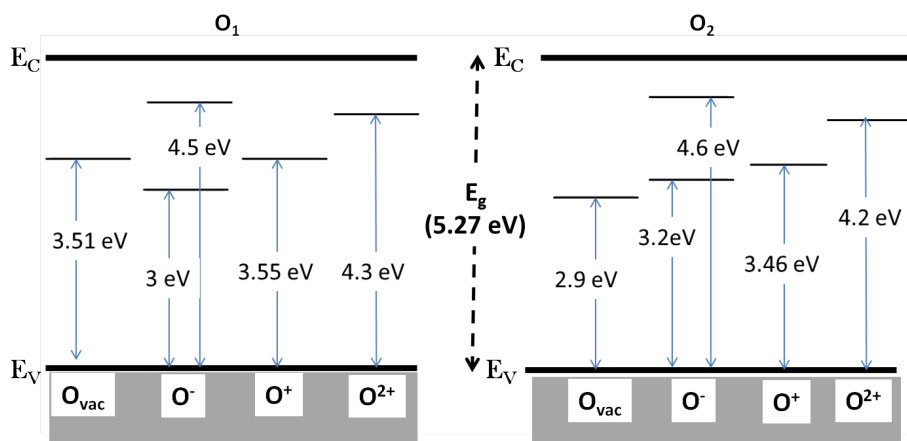


Figure 7.15: The defect levels in $Y_4Zr_3O_{12}$ simulated using HSE06 hybrid functional for two types of oxygen, O_I and O_{II} , in different charge states. E_V and E_C are valence band maximum and conduction band minimum respectively.

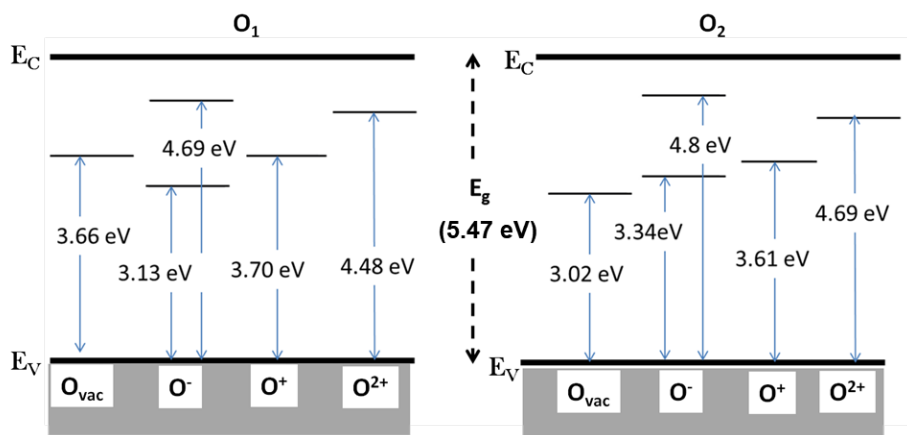


Figure 7.16: The simulated defect levels in $Y_4Zr_3O_{12}$, scaled-up to experimentally observed bandgap, $E_g = 5.47$ eV

electron is captured by these bands will undergo recombination and simultaneous photon emission of energy ~ 3.7 eV. In addition to this, there might be contributions from polarons associated with the thermal activation energy of trapping of the defects. Similarly, the radiative recombinations associated with neutral O_{II} (413 nm), O_I^- (371 nm) vacancies and oxygen interstitial at $6c$ site (411 nm) will be contributing to the second band at 415 nm.

The decrease in intensity is due to an increase in the annihilation rate resulting in the quenching of luminescence centers. Jardin *et al.* [135] has reported similar ionoluminescence spectra in sapphire ($\alpha-Al_2O_3$) using 2 MeV He^+ ion beam. Sapphire also has IL peaks at 360 nm and 400 nm along with a peak at ~ 695 nm. The peak at

300 nm and 400 nm were attributed to F^+ - centers and F^- - centers respectively. There was an initial increase in IL intensity due to the creation of defects and quenching in intensity after 2×10^{16} ions/cm². In some cathodoluminescence studies of fluorite related structures, the reduction in intensity is attributed to the de-localization of lattice strain upon irradiation and is referred to as the 'strained lattice hypothesis'. According to another argument, the 'charge trap hypothesis', an increased number of oxygen vacancies act as charge traps, thereby decreasing the number of available electrons and reducing the CL intensity. These hypotheses could be extended in the case of $Y_4Zr_3O_{12}$ also.

7.9 Conclusions

In previous chapter, low energy recoil events and defect formation energies in $Y_4Zr_3O_{12}$ have been studied using the *ab initio* molecular dynamics simulations. The main inference from the study is that anion defects are more probable to form than cation defects in irradiated $Y_4Zr_3O_{12}$. We revisited this problem using various experimental techniques, including X-ray Diffraction, Raman Spectroscopy, UV-vis spectroscopy, Ionoluminescence spectroscopy and simulations based on DFT-HSE06 hybrid functional.

The $Y_4Zr_3O_{12}$ oxide synthesized by solid-state route showed well-resolved peaks, which are in exact agreement with previously reported data. The observed and simulated Raman spectra of the as-prepared compound showed 17 Raman-active modes, within three predominant bands. Further, the bandgap measured using UV-vis spectroscopy and hybrid-potential based electronic structure calculation are 5.27 eV and 5.47 eV respectively, which indicate it is a wide bandgap material. Here, the shortcomings of conventional DFT techniques on estimating the bandgap are compensated by selecting a suitable hybrid exchange-correlation functional.

The ionoluminescence spectra acquired during 100 keV He^+ ion irradiation shows two prominent bands, centered at wavelengths 330 nm and 415 nm respectively, which can be attributed to radiative electronic transitions involving anion-related defect levels within the bandgap. The defect levels calculated using DFT-HSE06 simulations are in-line with the bands observed in the IL spectra. The O_I , O_I^+ and

O_{II}^+ vacancy defects contribute to the band at 330 nm and neutral O_{II} , O_I^- vacancies and O interstitial at $6c$ site contribute to the band at 415 nm. This correspondence is substantial proof for the AIMD simulations discussed earlier.

Summary and scope for future work

This chapter summarizes the important results in the present thesis and proposes relevant future work.

8.1 Summary of the thesis

The present thesis has focused on the detailed investigation of microstructure, precipitation kinetics and radiation response Zr-containing ODS alloys with and without Al. During the course of this work, *ab initio* simulations are used to predict the formation of nanoclusters. The theoretical predictions are further experimentally verified using transmission electron microscopic techniques. The enhanced radiation tolerance of these alloys is also established using various positron annihilation spectroscopic techniques. Further, the radiation response of the nanocluster phase, $Y_4Zr_3O_{12}$, is explored by means of *ab-initio* molecular dynamics simulations. The inferences from molecular dynamics simulations are substantiated by interpreting ion beam induced luminescence spectra of $Y_4Zr_3O_{12}$. While exploring these aspects, many fundamental problems were also addressed with systematic theoretical and experimental investigations.

One of the key outcome of the thesis is the *ab initio* simulations on the binding energies of different nanoclusters in bcc Fe matrix which shows the Zr-Y-O-vacancy

containing clusters have higher binding energy compared to Y-Al-O-vacancy containing clusters. The study also concluded that the DFT formation energies per atom for $Y_4Zr_3O_{12}$ is lower than pyrochlore and defect fluorite structure of the same composition. These calculations pointed towards the preferential formation of Y-Zr-O precipitates, most probably $Y_4Zr_3O_{12}$ (also known as δ -phase), in Zr and Al containing ferritic ODS steels.

The first-principle predictions are in exact agreement with experimental results obtained by high resolution transmission electron microscopy (HRTEM) studies in as-prepared Zr and Al containing ODS alloys. All precipitates in as-prepared Zr-ODS (Fe - 14Cr - 0.3Y₂O₃ - 0.63Zr) and $\sim 80\%$ of precipitates in Al-ODS (Fe - 14Cr - 0.3Y₂O₃ - 0.63Zr - 4Al) possess $Y_4Zr_3O_{12}$ structure. Some precipitates in Al-containing ODS steels were consistent with monoclinic, tetragonal and cubic ZrO₂ structure. Al- containing phases were completely absent in both the alloys. The size and the number density of the precipitates in these alloys were comparable to conventional Ti - containing ODS alloys.

It is further observed that there is a predominant precipitate (δ)-matrix (α) orientation relationship, $[2\bar{1}0]_{\delta}||[111]_{\alpha}$ and $(122)_{\delta}|| (011)_{\alpha}$. This novel trigonal/bcc orientation relationship established in this study is similar to Pitsche- Shrader relationship in hcp/bcc system. The existence of a predominant OR indicates that the Y₂O₃ phase is dissolving in the matrix during the ball milling process and it is precipitating as $Y_4Zr_3O_{12}$ during the hot consolidation.

A detailed investigation on self-ion irradiated Al-ODS and Zr-ODS showed that they possess exceptional radiation tolerance due to the high number density of finely dispersed $Y_4Zr_3O_{12}$ precipitates. At room temperature, Al-ODS successfully resists the formation and clustering of open volume defects up to a self-ion induced damage of 100 dpa. The Zr-ODS is more resistant to vacancy formation, up to 150 dpa at room temperature, owing to its smaller size and higher number densities of dispersoids compared to Al-ODS. At 340 °C, both Al-ODS and Zr-ODS are tolerant to damage up to 100 dpa.

It is well known that the radiation response of the ODS steels depends on the radiation resistance of its constituent nanoclusters. Now that the presence of $Y_4Zr_3O_{12}$ is confirmed on both the alloys, the study further focused on the radiation response of $Y_4Zr_3O_{12}$ by calculating its threshold displacement energies and defect formation

energies. The threshold displacement energies of $Y_4Zr_3O_{12}$ are found to be anisotropic, strongly dependent on the incident direction. Anions have smaller threshold displacement energies than cations and defect generation mechanisms of cations involve more number of displacements, suggesting that anion disorder is more probable than cation disorder in irradiated $Y_4Zr_3O_{12}$. The lower Y – Zr_{18f} antisite formation energy suggests that the *18f* atoms can interchange position and continue to be in the δ -phase structure before transforming into the defect fluorite phase. The low defect reaction pair energy, the sum of cation antisite formation energy and anion Frenkel pair formation energy, of $Y_4Zr_3O_{12}$ infers its superior radiation tolerance compared to pyrochlores.

The ion beam induced luminescence spectra of $Y_4Zr_3O_{12}$ and related first principle calculations on defect levels point to the fact that the anion defects are readily produced during ion-irradiation which is in agreement with *ab initio* molecular dynamics simulations of the preceding chapter. The bands in the IL spectrum, located at 330 nm and 415 nm are at lower energies than the bandgap emission of $Y_4Zr_3O_{12}$ and hence they can be attributed to deep band emissions (DBE) from defect-related levels within the bandgap. Each band is a superposition of defect-related sub-bands. These bands are ascribed to anion vacancies and related color centers (anion vacancies with trapped charge). By comparing the experimental IL spectra and the anion-related defect levels simulated using DFT-HSE06 hybrid functional, it can be concluded that the O_I , O_I^+ and O_{II}^+ vacancy defects contribute to the IL band at 330 nm and O_{II} and O_I^- vacancies and O interstitial at *6c* site contribute to the band at 415 nm.

8.2 Future scope

ODS steels of different compositions and microstructures are an active area of research in the realm of nuclear structural materials. There is a huge scope for future work in this area, related to the findings in the present thesis. The major possibilities are mentioned below:

- The first principle study discussed in the first chapter can be extended to find the energetics of different precipitate-matrix orientation relationships. This information will be useful for finding the reason behind the existence of predominant

OR between $Y_4Zr_3O_{12}$ and the matrix. This will also help to gain an insight into the precipitate - matrix interface structure also.

- The TEM studies mentioned in the fourth chapter can be extended to the characterization of the surface oxide layer formed on Zr and Al containing ODS alloys. The change in the amount of Al and its effect on thickness and composition of the surface layer can also be explored.
- It is well known that the grain sizes parallel and perpendicular to the extrusion direction tend to be different in ODS alloys produced by extrusion. The implications of this bimodal grain size distribution on the radiation resistance and corrosion resistance of these alloys have to be unveiled.
- The ODS alloys synthesized by HIP and hot extrusion are different in terms of grain size. It will be interesting to synthesize an alloy of the same composition by HIP and compare the microstructure and precipitate chemistry.
- Helium along with heavy-ion dual ion implantation is widely used to predict the behaviour of the nuclear materials in in-service conditions. Likewise, dual and triple ion irradiation studies can be conducted, followed by TEM investigation to find out the micro and macro structural changes of Zr and Al containing ODS steels.
- The molecular dynamics method can be explored to simulate the irradiation response of the precipitates in Al-ODS and Zr-ODS. The dissolution of different elements of the precipitates upon irradiation and their diffusion through the matrix also can be studied.
- The order to disorder transition of δ -phase compounds has gained interest in recent times. The δ -phase to disordered fluorite transition of $Y_4Zr_3O_{12}$ and its critical amorphization dose and critical amorphization temperatures are yet to be found.

Sincere efforts have been made in this thesis to provide a significant contribution towards the understanding the formation kinetics, microstructure and irradiation stability of Zr and Al containing ODS steels and its constituent precipitates using DFT simulations, diffraction contrast and phase contrast imaging, positron annihilation

spectroscopy, molecular dynamics simulations and ion beam induced luminescence spectroscopy. The results discussed and conclusions drawn during the course of the thesis can be used to analyze the applicability of Zr and Al containing ODS steels as candidate structural materials of future nuclear reactors.

Bibliography

- [1] S. Jain, *Nuclear Power - an alternative*, NPCIL. Retrieved **27** (2012).
- [2] S. Mannan, S. Chetal, B. Raj, and S. Bhoje, *Selection of materials for Prototype Fast Breeder Reactor*, Transactions-Indian Institute of Metals **56**, 155 (2003).
- [3] G. Odette, M. Alinger, and B. Wirth, *Recent developments in irradiation-resistant steels*, Annu. Rev. Mater. Res. **38**, 471 (2008).
- [4] P. Rodriguez, *Nuclear reactor materials: Irradiation effects*, (2001).
- [5] F. Wiffen, P. Maziasz, E. Bloom, J. Stiegler, and M. Grossbeck, *Behavior of Type 316 stainless steel under simulated fusion reactor irradiation*, Technical report, Oak Ridge National Lab., Tenn.(USA), 1978.
- [6] A. R. Laborne, P. Gavaille, J. Malaplate, C. Pokor, and B. Tanguy, *Correlation of radiation-induced changes in microstructure/microchemistry, density and thermo-electric power of type 304L and 316 stainless steels irradiated in the Phénix reactor*, Journal of Nuclear Materials **460**, 72 (2015).
- [7] B. Rouxel, C. Bisor, Y. De Carlan, A. Courcelle, and A. Legris, *Influence of the austenitic stainless steel microstructure on the void swelling under ion irradiation*, EPJ Nuclear Sciences & Technologies **2**, 30 (2016).
- [8] A.-A. Tavassoli, E. Diegele, R. Lindau, N. Luzginova, and H. Tanigawa, *Current status and recent research achievements in ferritic/martensitic steels*, Journal of Nuclear Materials **455**, 269 (2014).
- [9] K. Laha, S. Saroja, A. Moitra, R. Sandhya, M. Mathew, T. Jayakumar, and E. R. Kumar, *Development of India-specific RAFM steel through optimization of tungsten and tantalum contents for better combination of impact, tensile, low cycle fatigue and creep properties*, Journal of Nuclear Materials **439**, 41 (2013).
- [10] N. Baluc, D. Gelles, S. Jitsukawa, A. Kimura, R. Klueh, G. Odette, B. Van der Schaaf, and J. Yu, *Status of reduced activation ferritic/martensitic steel development*, Journal of Nuclear Materials **367**, 33 (2007).
- [11] A. De Bremaecker, *Past research and fabrication conducted at SCK• CEN on ferritic ODS alloys used as cladding for FBR's fuel pins*, Journal of nuclear materials **428**, 13 (2012).

- [12] G. E. Dieter and D. J. Bacon, *Mechanical Metallurgy*, volume 3, McGraw-hill New York, 1986.
- [13] N. Mott and F. Nabarro, *Dislocation theory and transient creep*, Physical Society Bristol Conference Report , 1 (1948).
- [14] A. Rollett, G. Rohrer, and J. Humphreys, *Recrystallization and Related Annealing Phenomena*, Newnes, 2017.
- [15] C. Zener, *Theory of growth of spherical precipitates from solid solution*, Journal of Applied Physics **20**, 950 (1949).
- [16] T. Gladman, *On the theory of the effect of precipitate particles on grain growth in metals*, Proceedings of the Royal Society of London. Series A. Mathematical and Physical Sciences **294**, 298 (1966).
- [17] J. Benjamin and T. Volin, *The mechanism of mechanical alloying*, Metallurgical Transactions **5**, 1929 (1974).
- [18] P. Gilman and J. Benjamin, *Mechanical alloying*, Annual Review of Materials Science **13**, 279 (1983).
- [19] J. J. Fischer, *Dispersion strengthened ferritic alloy for use in Liquid-Metal Fast Breeder Reactors (LMFBRs)*, 1978, US Patent 4,075,010.
- [20] M. Alinger, G. Odette, and D. Hoelzer, *On the role of alloy composition and processing parameters in nanocluster formation and dispersion strengthening in nanostructured ferritic alloys*, Acta Materialia **57**, 392 (2009).
- [21] S. Ukai, M. Harada, H. Okada, M. Inoue, S. Nomura, S. Shikakura, K. Asabe, T. Nishida, and M. Fujiwara, *Alloying design of oxide dispersion strengthened ferritic steel for long life FBRs core materials*, Journal of Nuclear Materials **204**, 65 (1993).
- [22] S. Ukai, T. Nishida, T. Okuda, and T. Yoshitake, *R&D of oxide dispersion strengthened ferritic martensitic steels for FBR*, Journal of Nuclear Materials **258**, 1745 (1998).
- [23] S. Ukai, T. Nishida, H. Okada, T. Okuda, M. Fujiwara, and K. Asabe, *Development of oxide dispersion strengthened ferritic steels for FBR core application,(I)*, Journal of Nuclear Science and Technology **34**, 256 (1997).
- [24] J. H. Kim, K. M. Kim, T. S. Byun, D. W. Lee, and C. H. Park, *High-temperature oxidation behavior of nano-structured ferritic oxide dispersion-strengthened alloys*, Thermochemica Acta **579**, 1 (2014).
- [25] T. R. Allen, J. Gan, J. I. Cole, M. K. Miller, J. T. Busby, S. Shutthanandan, and S. Thevuthasan, *Radiation response of a 9 chromium oxide dispersion strengthened steel to heavy ion irradiation*, Journal of Nuclear Materials **375**, 26 (2008).

- [26] R. Lindau, A. Möslang, M. Schirra, P. Schlossmacher, and M. Klimenkov, *Mechanical and microstructural properties of a hiped RAFM ODS-steel*, Journal of Nuclear Materials **307**, 769 (2002).
- [27] C. Cayron, E. Rath, I. Chu, and S. Launois, *Microstructural evolution of Y_2O_3 and $MgAl_2O_4$ ODS EUROFER steels during their elaboration by mechanical milling and hot isostatic pressing*, Journal of Nuclear Materials **335**, 83 (2004).
- [28] M. Miller, E. Kenik, K. Russell, L. Heatherly, D. Hoelzer, and P. Maziasz, *Atom probe tomography of nanoscale particles in ODS ferritic alloys*, Materials Science and Engineering: A **353**, 140 (2003).
- [29] M. Alinger, G. Odette, and D. Hoelzer, *The development and stability of Y–Ti–O nanoclusters in mechanically alloyed Fe–Cr based ferritic alloys*, Journal of Nuclear Materials **329**, 382 (2004).
- [30] H. Wen, T. D. Topping, D. Isheim, D. N. Seidman, and E. J. Lavernia, *Strengthening mechanisms in a high-strength bulk nanostructured Cu–Zn–Al alloy processed via cryomilling and spark plasma sintering*, Acta materialia **61**, 2769 (2013).
- [31] J. H. Kim and C. H. Park, *Effect of milling temperature on nanoclusters and ultra fine grained microstructure of oxide dispersion strengthened steel*, Journal of Alloys and Compounds **585**, 69 (2014).
- [32] T. Hayashi, P. Sarosi, J. H. Schneibel, and M. J. Mills, *Creep response and deformation processes in nanocluster-strengthened ferritic steels*, Acta Materialia **56**, 1407 (2008).
- [33] J.-O. Andersson and B. Sundman, *Thermodynamic properties of the Cr–Fe system*, Calphad **11**, 83 (1987).
- [34] B. Weiss and R. Stickler, *Phase instabilities during high temperature exposure of 316 austenitic stainless steel*, Metallurgical and Materials Transactions B **3**, 851 (1972).
- [35] E. Brown, M. Burnett, P. Purtscher, and G. Krauss, *Intermetallic phase formation in 25Cr–3Mo–4Ni ferritic stainless steel*, Metallurgical Transactions A **14**, 791 (1983).
- [36] A. L. Rouffié, J. Crépin, M. Sennour, B. Tanguy, A. Pineau, D. Hamon, P. Wident, S. Vincent, V. Garat, and B. Fournier, *Effect of the thermal ageing on the tensile and impact properties of a 18% Cr ODS ferritic steel*, Journal of Nuclear Materials **445**, 37 (2014).
- [37] Z. Oksiuta, M. Lewandowska, K. J. Kurzydowski, and N. Baluc, *Effect of vanadium addition on the microstructure and mechanical properties of the ODS ferritic steels*, Journal of Nuclear Materials **442**, S84 (2013).

- [38] R. Rahmanifard, H. Farhangi, and A. J. Novinrooz, *Effect of zirconium and tantalum on the microstructural characteristics of 12YWT ODS steel nanocomposite*, Journal of Alloys and Compounds **622**, 948 (2015).
- [39] S. Ukai and S. Ohtsuka, *Nano-mesoscopic structure control in 9Cr-ODS ferritic steels*, Energy Materials **2**, 26 (2007).
- [40] M. Alinger and G. Odette, *On the precipitation kinetics, thermal stability and strengthening mechanisms of nanometer scale Y-Ti-O clusters in nanostructured ferritic alloys*, Fusion Mater. Semiannu. Prog. Rep. DOE-ER-03 13/37 61 **69** (2005).
- [41] M. Alinger, G. Odette, and D. Hoelzer, *On the role of alloy composition and processing variables in nanofeature formation and dispersion strengthening in nanostructured ferritic alloys*, Fusion Mater. Semiannu. Prog. Rep. DOE-ER-0313 **43** (2008).
- [42] M. Hamilton et al., *Fabrication technological development of the oxide dispersion strengthened alloy MA957 for fast reactor applications*, Technical report, Pacific Northwest National Lab., 2000.
- [43] Y. Wu, J. Ciston, S. Kräemer, N. Bailey, G. R. Odette, and P. Hosemann, *The crystal structure, orientation relationships and interfaces of the nanoscale oxides in nanostructured ferritic alloys*, Acta Materialia **111**, 108 (2016).
- [44] D. Larson, P. Maziasz, I.-S. Kim, and K. Miyahara, *Three-dimensional atom probe observation of nanoscale titanium-oxygen clustering in an oxide-dispersion-strengthened Fe-12Cr-3W-0.4 Ti-Y₂O₃ ferritic alloy*, Scripta Materialia **44**, 359 (2001).
- [45] M. Miller, K. Russell, and D. Hoelzer, *Characterization of precipitates in MA/ODS ferritic alloys*, Journal of Nuclear Materials **351**, 261 (2006).
- [46] A. London, S. Santra, S. Amirthapandian, B. Panigrahi, R. Sarguna, S. Balaji, R. Vijay, C. Sundar, S. Lozano-Perez, and C. Grovenor, *Effect of Ti and Cr on dispersion, structure and composition of oxide nano-particles in model ODS alloys*, Acta Materialia **97**, 223 (2015).
- [47] M. Miller, D. Hoelzer, E. Kenik, and K. Russell, *Stability of ferritic MA/ODS alloys at high temperatures*, Intermetallics **13**, 387 (2005).
- [48] A. Kimura et al., *Development of Al added high-Cr ODS steels for fuel cladding of next generation nuclear systems*, Journal of Nuclear Materials **417**, 176 (2011).
- [49] S. Ohtsuka, T. Kaito, M. Inoue, T. Asayama, S. Kim, S. Ukai, T. Narita, and H. Sakasegawa, *Effects of aluminum on high-temperature strength of 9Cr-ODS steel*, Journal of Nuclear Materials **386**, 479 (2009).

- [50] R. Gao, T. Zhang, X. Wang, Q. Fang, and C. Liu, *Effect of zirconium addition on the microstructure and mechanical properties of ODS ferritic steels containing aluminum*, Journal of Nuclear Materials **444**, 462 (2014).
- [51] L. Hsiung, M. Fluss, S. Tumey, J. Kuntz, B. El-Dasher, M. Wall, B. Choi, A. Kimura, F. Willaime, and Y. Serruys, *HRTEM study of oxide nanoparticles in K3-ODS ferritic steel developed for radiation tolerance*, Journal of Nuclear Materials **409**, 72 (2011).
- [52] P. W. Atkins and J. De Paula, *Physical chemistry: Thermodynamics and kinetics*, Recording for the Blind & Dyslexic, 2007.
- [53] K. R. Lawless, *The oxidation of metals*, Reports on Progress in Physics **37**, 231 (1974).
- [54] J. Ejenstam, M. Thuvander, P. Olsson, F. Rave, and P. Szakalos, *Microstructural stability of Fe–Cr–Al alloys at 450–550° C*, Journal of Nuclear Materials **457**, 291 (2015).
- [55] J. Isselin, R. Kasada, and A. Kimura, *Corrosion behaviour of 16% Cr–4% Al and 16% Cr ODS ferritic steels under different metallurgical conditions in a supercritical water environment*, Corrosion Science **52**, 3266 (2010).
- [56] J. Lee, R. Kasada, A. Kimura, T. Okuda, M. Inoue, S. Ukai, S. Ohnuki, T. Fujisawa, and F. Abe, *Influence of alloy composition and temperature on corrosion behavior of ODS ferritic steels*, Journal of Nuclear Materials **417**, 1225 (2011).
- [57] L. L. Hsiung, M. J. Fluss, S. J. Tumey, B. W. Choi, Y. Serruys, F. Willaime, and A. Kimura, *Formation mechanism and the role of nanoparticles in Fe–Cr ODS steels developed for radiation tolerance*, Physical Review B **82**, 184103 (2010).
- [58] H. Xu, Z. Lu, D. Wang, and C. Liu, *Microstructure refinement and strengthening mechanisms of a 9Cr oxide dispersion strengthened steel by zirconium addition*, Nuclear Engineering and Technology **49**, 178 (2017).
- [59] J. Ren, L. Yu, Y. Liu, C. Liu, H. Li, and J. Wu, *Effects of Zr addition on strengthening mechanisms of Al-alloyed high-Cr ODS steels*, Materials **11**, 118 (2018).
- [60] C. Yu, H. Oka, N. Hashimoto, and S. Ohnuki, *Development of damage structure in 16Cr–4Al ODS steels during electron-irradiation*, Journal of Nuclear Materials **417**, 286 (2011).
- [61] S. Ohnuki, N. Hashimoto, S. Ukai, A. Kimura, M. Inoue, T. Kaito, T. Fujisawa, T. Okuda, and F. Abe, *Super ODS steels R&D for fuel cladding of next generation nuclear systems: Effect of minor alloying elements*, Proceedings of the ICAPP 2009 , 2195 (2009).

- [62] P. Dou, A. Kimura, R. Kasada, T. Okuda, M. Inoue, S. Ukai, S. Ohnuki, T. Fujisawa, and F. Abe, *TEM and HRTEM study of oxide particles in an Al-alloyed high-Cr oxide dispersion strengthened steel with Zr addition*, Journal of Nuclear Materials **444**, 441 (2014).
- [63] L. Zhang, L. Yu, Y. Liu, C. Liu, H. Li, and J. Wu, *Influence of Zr addition on the microstructures and mechanical properties of 14Cr ODS steels*, Materials Science and Engineering: A **695**, 66 (2017).
- [64] P. Dou, S. Jiang, L. Qiu, and A. Kimura, *Effects of contents of Al, Zr and Ti on oxide particles in Fe-15Cr-2W-0.35 Y₂O₃ ODS steels*, Journal of Nuclear Materials **531**, 152025 (2020).
- [65] H. Dong, L. Yu, Y. Liu, C. Liu, H. Li, and J. Wu, *Effect of hafnium addition on the microstructure and tensile properties of aluminum added high-Cr ODS steels*, Journal of Alloys and Compounds **702**, 538 (2017).
- [66] P. Dou et al., *TEM and HRTEM study of oxide particles in an Al-alloyed high-Cr oxide dispersion strengthened ferritic steel with Hf addition*, Journal of Nuclear Materials **485**, 189 (2017).
- [67] P. Dou, Q. Ye, and A. Kimura, *Crystal and metal/oxide interface structures of nanoparticles in 15Cr-2W-0.1 Ti-4Al-0.6 Hf-0.35 Y₂O₃ ODS steel*, Journal of Nuclear Materials , 152029 (2020).
- [68] C. L. Fu, M. Krčmar, G. S. Painter, and X.-Q. Chen, *Vacancy mechanism of high oxygen solubility and nucleation of stable oxygen-enriched clusters in Fe*, Physical Review Letters **99**, 225502 (2007).
- [69] Y. Jiang, J. R. Smith, and G. Odette, *Formation of Y-Ti-O nanoclusters in nanostructured ferritic alloys: A first-principles study*, Physical Review B **79**, 064103 (2009).
- [70] D. Murali, B. Panigrahi, M. Valsakumar, and C. Sundar, *Diffusion of Y and Ti/Zr in bcc iron: A first principles study*, Journal of Nuclear Materials **419**, 208 (2011).
- [71] D. Murali, B. Panigrahi, M. Valsakumar, S. Chandra, C. Sundar, and B. Raj, *The role of minor alloying elements on the stability and dispersion of yttria nanoclusters in nanostructured ferritic alloys: An ab initio study*, Journal of Nuclear Materials **403**, 113 (2010).
- [72] A. Claisse and P. Olsson, *First-principles calculations of (Y, Ti, O) cluster formation in body centred cubic iron-chromium*, Nuclear Instruments and Methods in Physics Research Section B: Beam Interactions with Materials and Atoms **303**, 18 (2013).

- [73] L. Barnard, G. Odette, I. Szlufarska, and D. Morgan, *An ab initio study of Ti–Y–O nanocluster energetics in nanostructured ferritic alloys*, *Acta Materialia* **60**, 935 (2012).
- [74] L. Barnard, N. Cunningham, G. Odette, I. Szlufarska, and D. Morgan, *Thermodynamic and kinetic modeling of oxide precipitation in nanostructured ferritic alloys*, *Acta Materialia* **91**, 340 (2015).
- [75] P. Dou, A. Kimura, T. Okuda, M. Inoue, S. Ukai, S. Ohnuki, T. Fujisawa, and F. Abe, *Polymorphic and coherency transition of Y–Al complex oxide particles with extrusion temperature in an Al-alloyed high-Cr oxide dispersion strengthened ferritic steel*, *Acta Materialia* **59**, 992 (2011).
- [76] C. Zhang, A. Kimura, R. Kasada, J. Jang, H. Kishimoto, and Y. Yang, *Characterization of the oxide particles in Al-added high-Cr ODS ferritic steels*, *Journal of Nuclear Materials* **417**, 221 (2011).
- [77] Z. Zhang, L. Yao, X.-L. Wang, and M. K. Miller, *Vacancy-controlled ultrastable nanoclusters in nanostructured ferritic alloys*, *Scientific reports* **5**, 1 (2015).
- [78] V. Krsjak, Z. Szaraz, and P. Hähner, *Positron annihilation lifetime study of oxide dispersion strengthened steels*, *Journal of Nuclear Materials* **428**, 160 (2012).
- [79] B. Zhang, L. Lu, and M. Lai, *Evolution of vacancy densities in powder particles during mechanical milling*, *Physica B: Condensed Matter* **325**, 120 (2003).
- [80] P. Song, D. Morrall, Z. Zhang, K. Yabuuchi, and A. Kimura, *Radiation response of ODS ferritic steels with different oxide particles under ion-irradiation at 550° C*, *Journal of Nuclear Materials* **502**, 76 (2018).
- [81] H. Kishimoto, K. Yutani, R. Kasada, and A. Kimura, *Helium cavity formation research on oxide dispersed strengthening (ODS) ferritic steels utilizing dual-ion irradiation facility*, *Fusion Engineering and Design* **81**, 1045 (2006).
- [82] I.-S. Kim, J. Hunn, N. Hashimoto, D. Larson, P. Maziasz, K. Miyahara, and E. Lee, *Defect and void evolution in oxide dispersion strengthened ferritic steels under 3.2 MeV Fe⁺ ion irradiation with simultaneous helium injection*, *Journal of Nuclear Materials* **280**, 264 (2000).
- [83] C. Liu, C. Yu, N. Hashimoto, S. Ohnuki, M. Ando, K. Shiba, and S. Jitsukawa, *Micro-structure and micro-hardness of ODS steels after ion irradiation*, *Journal of Nuclear Materials* **417**, 270 (2011).
- [84] K. Yutani, H. Kishimoto, R. Kasada, and A. Kimura, *Evaluation of Helium effects on swelling behavior of oxide dispersion strengthened ferritic steels under ion irradiation*, *Journal of Nuclear Materials* **367**, 423 (2007).

- [85] P. Song, Z. Zhang, K. Yabuuchi, and A. Kimura, *Helium bubble formation behavior in ODS ferritic steels with and without simultaneous addition of Al and Zr*, *Fusion Engineering and Design* **125**, 396 (2017).
- [86] P. Song, A. Kimura, K. Yabuuchi, P. Dou, H. Watanabe, J. Gao, and Y.-J. Huang, *Assessment of phase stability of oxide particles in different types of 15Cr-ODS ferritic steels under 6.4 MeV Fe ion irradiation at 200° C*, *Journal of Nuclear Materials* **529**, 151953 (2020).
- [87] C. He, M. Barthe, P. Desgardin, S. Akhmadaliev, M. Behar, and F. Jomard, *Positron studies of interaction between yttrium atoms and vacancies in bcc iron with relevance for ODS nanoparticles formation*, *Journal of Nuclear Materials* **455**, 398 (2014).
- [88] Y. Ortega, V. De Castro, M. Monge, A. Muñoz, T. Leguey, and R. Pareja, *Positron annihilation characteristics of ODS and non-ODS EUROFER isochronally annealed*, *Journal of Nuclear Materials* **376**, 222 (2008).
- [89] R. Domínguez-Reyes, M. Auger, M. Monge, and R. Pareja, *Positron annihilation study of the vacancy clusters in ODS Fe–14Cr alloys*, *Philosophical Magazine* **97**, 833 (2017).
- [90] I. Bartošová, A. Bouhaddane, M. Dománková, V. Slugeň, D. Wall, and F. Selim, *Study of radiation damage in ODS steels by positron annihilation spectroscopy*, in *Journal of Physics: Conference Series*, volume 674, page 012011, 2016.
- [91] P. Gao, X. Ju, Y. Xin, Q. Cao, Z. Guo, L. Guo, and B. Wang, *Helium-Implanted ODS-Fe Alloy Investigated by Positron-Annihilation Spectroscopy*, *IEEE Transactions on Plasma Science* **44**, 1631 (2016).
- [92] P. Parente, T. Leguey, V. De Castro, T. Gigl, M. Reiner, C. Hugenschmidt, and R. Pareja, *Characterization of ion-irradiated ODS Fe–Cr alloys by doppler broadening spectroscopy using a positron beam*, *Journal of Nuclear Materials* **464**, 140 (2015).
- [93] M. Šćepanović, V. de Castro, I. García-Cortés, F. Sánchez, T. Gigl, C. Hugenschmidt, and T. Leguey, *Characterisation of open volume defects in Fe–Cr and ODS Fe–Cr alloys after He⁺ and Fe⁺ ion irradiations*, *Journal of Nuclear Materials* , 152230 (2020).
- [94] M. Šćepanović, T. Leguey, I. García-Cortés, F. Sánchez, C. Hugenschmidt, M. Auger, and V. de Castro, *Sequential ion irradiations on Fe–Cr and ODS Fe–Cr alloys*, *Nuclear Materials and Energy* **25**, 100790 (2020).
- [95] R. Kögler, W. Anwand, A. Richter, M. Butterling, A. Mücklich, X. Ou, H. Reuther, C. L. Chen, and A. Wagner, *Investigation of dual-beam-implanted oxide-dispersed-strengthened FeCrAl alloy by positron annihilation spectroscopy*, in *Defect and Diffusion Forum*, volume 331, pages 149–163, Trans Tech Publ, 2012.

- [96] K. Sickafus, L. Minervini, R. Grimes, J. Valdez, M. Ishimaru, F. Li, K. McClellan, and T. Hartmann, *Radiation tolerance of complex oxides*, *Science* **289**, 748 (2000).
- [97] J. Lian, J. Chen, L. Wang, R. C. Ewing, J. M. Farmer, L. A. Boatner, and K. Helean, *Radiation-induced amorphization of rare-earth titanate pyrochlores*, *Physical Review B* **68**, 134107 (2003).
- [98] S. Wang, L. Wang, R. Ewing, and K. G. Kutty, *Ion irradiation of rare-earth- and yttrium-titanate-pyrochlores*, *Nuclear Instruments and Methods in Physics Research Section B: Beam Interactions with Materials and Atoms* **169**, 135 (2000).
- [99] J. Lian, X. Zu, K. G. Kutty, J. Chen, L. Wang, and R. Ewing, *Ion-irradiation-induced amorphization of $La_2Zr_2O_7$ pyrochlore*, *Physical Review B* **66**, 054108 (2002).
- [100] M. Tang, P. Kluth, J. Zhang, M. Patel, B. Uberuaga, C. O. Reichhardt, and K. Sickafus, *Swift heavy ion irradiation-induced microstructure modification of two delta-phase oxides: $Sc_4Zr_3O_{12}$ and $Lu_4Zr_3O_{12}$* , *Nuclear Instruments and Methods in Physics Research Section B: Beam Interactions with Materials and Atoms* **268**, 3243 (2010).
- [101] J. Valdez, M. Tang, and K. Sickafus, *Radiation damage effects in δ - $Sc_4Zr_3O_{12}$ irradiated with Kr^{2+} ions under cryogenic conditions*, *Nuclear Instruments and Methods in Physics Research Section B: Beam Interactions with Materials and Atoms* **250**, 148 (2006).
- [102] K. E. Sickafus, R. W. Grimes, J. A. Valdez, A. Cleave, M. Tang, M. Ishimaru, S. M. Corish, C. R. Stanek, and B. P. Uberuaga, *Radiation-induced amorphization resistance and radiation tolerance in structurally related oxides*, *Nature Materials* **6**, 217 (2007).
- [103] M. Tang, K. Holliday, C. Jiang, J. Valdez, B. Uberuaga, P. Dickerson, R. Dickerson, Y. Wang, K. Czerwinski, and K. Sickafus, *Order-to-disorder phase transformation in ion irradiated uranium-bearing delta-phase oxides $RE_6U_1O_{12}$ ($RE = Y, Gd, Ho, Yb, and Lu$)*, *Journal of Solid State Chemistry* **183**, 844 (2010).
- [104] G. Kinchin and R. Pease, *The displacement of atoms in solids by radiation*, *Reports on Progress in Physics* **18**, 1 (1955).
- [105] K. Nordlund et al., *Primary radiation damage: A review of current understanding and models*, *Journal of Nuclear Materials* **512**, 450 (2018).
- [106] M. Norgett, M. Robinson, and I. Torrens, *A proposed method of calculating displacement dose rates*, *Nuclear Engineering and Design* **33**, 50 (1975).

- [107] J. F. Ziegler, M. D. Ziegler, and J. P. Biersack, *SRIM—The stopping and range of ions in matter (2010)*, Nuclear Instruments and Methods in Physics Research Section B: Beam Interactions with Materials and Atoms **268**, 1818 (2010).
- [108] K. Yasunaga, K. Yasuda, S. Matsumura, and T. Sonoda, *Electron energy-dependent formation of dislocation loops in CeO₂*, Nuclear Instruments and Methods in Physics Research Section B: Beam Interactions with Materials and Atoms **266**, 2877 (2008).
- [109] K. L. Smith, M. Colella, R. Cooper, and E. R. Vance, *Measured displacement energies of oxygen ions in titanates and zirconates*, Journal of Nuclear Materials **321**, 19 (2003).
- [110] M. Robinson, N. Marks, K. Whittle, and G. Lumpkin, *Systematic calculation of threshold displacement energies: Case study in rutile*, Physical Review B **85**, 104105 (2012).
- [111] J. Morris, B. J. Cowen, S. Teyseyre, and A. A. Hecht, *Molecular dynamics investigation of threshold displacement energies in CaF₂*, Computational Materials Science **172**, 109293 (2020).
- [112] P. Olsson, C. Becquart, and C. Domain, *Ab initio threshold displacement energies in iron*, Materials Research Letters **4**, 219 (2016).
- [113] M. Jiang, H. Xiao, S. Peng, G. Yang, Z. Liu, and X. Zu, *A comparative study of low energy radiation response of AlAs, GaAs and GaAs/AlAs superlattice and the damage effects on their electronic structures*, Scientific Reports **8**, 1 (2018).
- [114] M. Sayed, J. Jefferson, A. Walker, and A. Cullis, *Computer simulation of atomic displacements in Si, GaAs, and AlAs*, Nuclear Instruments and Methods in Physics Research Section B: Beam Interactions with Materials and Atoms **102**, 232 (1995).
- [115] E. Holmström, A. Kuronen, and K. Nordlund, *Threshold defect production in silicon determined by density functional theory molecular dynamics simulations*, Physical Review B **78**, 045202 (2008).
- [116] E. Holmström, K. Nordlund, and A. Kuronen, *Threshold defect production in germanium determined by density functional theory molecular dynamics simulations*, Physica Scripta **81**, 035601 (2010).
- [117] H. Xiao, F. Gao, X. T. Zu, and W. J. Weber, *Threshold displacement energy in GaN: Ab initio molecular dynamics study*, Journal of Applied Physics **105**, 123527 (2009).
- [118] B. Liu, H. Xiao, Y. Zhang, D. S. Aidhy, and W. J. Weber, *Ab initio molecular dynamics simulations of threshold displacement energies in SrTiO₃*, Journal of Physics: Condensed Matter **25**, 485003 (2013).

- [119] H. Y. Xiao, Y. Zhang, and W. J. Weber, *Ab initio molecular dynamics simulations of low-energy recoil events in ThO_2 , CeO_2 , and ZrO_2* , Physical Review B **86**, 054109 (2012).
- [120] B. Petersen, B. Liu, W. J. Weber, and Y. Zhang, *Ab initio molecular dynamics simulations of low energy recoil events in MgO* , Journal of Nuclear Materials **486**, 122 (2017).
- [121] Y. Yuan, M. Jiang, F. Zhao, H. Chen, H. Gao, H. Xiao, X. Xiang, and X. Zu, *Ab initio molecular dynamics simulation of low energy radiation responses of $\alpha\text{-Al}_2\text{O}_3$* , Scientific reports **7**, 1 (2017).
- [122] X. Wang, H. Y. Xiao, X. Zu, Y. Zhang, and W. J. Weber, *Ab initio molecular dynamics simulations of ion–solid interactions in $\text{Gd}_2\text{Zr}_2\text{O}_7$ and $\text{Gd}_2\text{Ti}_2\text{O}_7$* , Journal of Materials Chemistry C **1**, 1665 (2013).
- [123] H. Y. Xiao, W. J. Weber, Y. Zhang, and X. Zu, *Ab initio molecular dynamics simulations of ion–solid interactions in zirconate pyrochlores*, Acta Materialia **87**, 273 (2015).
- [124] H. Y. Xiao, F. Gao, and W. J. Weber, *Threshold displacement energies and defect formation energies in $\text{Y}_2\text{Ti}_2\text{O}_7$* , Journal of Physics: Condensed Matter **22**, 415801 (2010).
- [125] Y. Li, P. M. Kowalski, G. Beridze, A. R. Birnie, S. Finkeldei, and D. Bosbach, *Defect formation energies in $\text{A}_2\text{B}_2\text{O}_7$ pyrochlores*, Scripta Materialia **107**, 18 (2015).
- [126] D. J. Vogel and D. S. Kilin, *First-principles treatment of photoluminescence in semiconductors*, The Journal of Physical Chemistry C **119**, 27954 (2015).
- [127] T. Perevalov and D. Islamov, *Atomic and electronic structure of oxygen polyvacancies in ZrO_2* , Microelectronic Engineering **178**, 275 (2017), Special issue of Insulating Films on Semiconductors (INFOS 2017).
- [128] H. Jiang, R. I. Gomez-Abal, P. Rinke, and M. Scheffler, *Electronic band structure of zirconia and hafnia polymorphs from the GW perspective*, Physical Review B **81**, 085119 (2010).
- [129] H. Calvo del Castillo, A. Millán, P. Beneítez, J. L. Ruvalcaba-Sil, and T. Calderón, *Proton induced luminescence of minerals*, Revista mexicana de física **54**, 93 (2008).
- [130] V. Veligura and G. Hlawacek, *Ionoluminescence*, in *Helium Ion Microscopy*, pages 325–351, Springer, 2016.
- [131] V. Vil’Kotskii and V. Y. Pivovarov, *Cathodoluminescence of gallium phosphide containing residual defects and radiation-induced defects*, Journal of Applied Spectroscopy **19**, 1604 (1973).

- [132] C. White, *Ion induced optical emission for surface and depth profile analysis*, Nuclear Instruments and Methods **149**, 497 (1978).
- [133] J. H. Beaumont, A. L. Harmer, and W. Hayes, *An investigation of (100) and (110) oriented F_2 -centres in CaF_2 and SrF_2 (Zero-phonon lines)*, Journal of Physics C: Solid State Physics **5**, 1475 (1972).
- [134] S. Srivastava, P. Gangopadhyay, S. Chinnathambi, and P. Magudapathy, *Ion-beam induced luminescence and optical response measurement setup at IGCAR: First experimental results*, AIP Advances **10**, 095228 (2020).
- [135] C. Jardin, B. Canut, and S. Ramos, *The luminescence of sapphire subjected to the irradiation of energetic hydrogen and helium ions*, Journal of Physics D: Applied Physics **29**, 2066 (1996).
- [136] E. Epie and W. Chu, *Ionoluminescence study of Zn- and O- implanted ZnO crystals: An additional perspective*, Applied Surface Science **371**, 28 (2016).
- [137] D. B. Perea, *Ion Beam Induced Luminescence in MgO*, in *Ion-Irradiation-Induced Damage in Nuclear Materials*, pages 151–167, Springer, 2018.
- [138] J.-M. Combes, P. Duclos, and R. Seiler, *The Born-Oppenheimer approximation*, in *Rigorous atomic and molecular physics*, pages 185–213, Springer, 1981.
- [139] P. Hohenberg and W. Kohn, *Inhomogeneous electron gas*, Physical Review B **136**, B864 (1964).
- [140] D. Sholl and J. A. Steckel, *Density functional theory: A practical introduction*, John Wiley & Sons, 2011.
- [141] W. Koch and M. C. Holthausen, *A chemist's guide to density functional theory*, John Wiley & Sons, 2015.
- [142] M. Levy, *Universal variational functionals of electron densities, first-order density matrices, and natural spin-orbitals and solution of the v -representability problem*, Proceedings of the National Academy of Sciences **76**, 6062 (1979).
- [143] W. Kohn, A. Savin, and C. A. Ullrich, *Hohenberg–Kohn theory including spin magnetism and magnetic fields*, International Journal of Quantum Chemistry **101**, 20 (2005).
- [144] W. Kohn and L. J. Sham, *Self-consistent equations including exchange and correlation effects*, Physical Review B **140**, A1133 (1965).
- [145] D. M. Ceperley and B. J. Alder, *Ground state of the electron gas by a stochastic method*, Physical Review Letters **45**, 566 (1980).

- [146] J. P. Perdew, J. A. Chevary, S. H. Vosko, K. A. Jackson, M. R. Pederson, D. J. Singh, and C. Fiolhais, *Atoms, molecules, solids, and surfaces: Applications of the generalized gradient approximation for exchange and correlation*, Physical Review B **46**, 6671 (1992).
- [147] J. P. Perdew, K. Burke, and M. Ernzerhof, *Generalized gradient approximation made simple*, Physical Review Letters **77**, 3865 (1996).
- [148] J. P. Perdew, *Density functional theory and the band gap problem*, International Journal of Quantum Chemistry **28**, 497 (1985).
- [149] P. J. Hasnip, K. Refson, M. I. Probert, J. R. Yates, S. J. Clark, and C. J. Pickard, *Density functional theory in the solid state*, Philosophical Transactions of the Royal Society A: Mathematical, Physical and Engineering Sciences **372**, 20130270 (2014).
- [150] J. Heyd, G. E. Scuseria, and M. Ernzerhof, *Hybrid functionals based on a screened Coulomb potential*, The Journal of Chemical Physics **118**, 8207 (2003).
- [151] A. D. Becke, *Density-functional exchange-energy approximation with correct asymptotic behavior*, Physical Review A **38**, 3098 (1988).
- [152] C. Lee, W. Yang, and R. G. Parr, *Development of the Colle-Salvetti correlation-energy formula into a functional of the electron density*, Physical Review B **37**, 785 (1988).
- [153] S. H. Vosko, L. Wilk, and M. Nusair, *Accurate spin-dependent electron liquid correlation energies for local spin density calculations: A critical analysis*, Canadian Journal of Physics **58**, 1200 (1980).
- [154] J. P. Perdew, M. Ernzerhof, and K. Burke, *Rationale for mixing exact exchange with density functional approximations*, The Journal of Chemical Physics **105**, 9982 (1996).
- [155] C. Adamo and V. Barone, *Toward reliable density functional methods without adjustable parameters: The PBE0 model*, The Journal of Chemical Physics **110**, 6158 (1999).
- [156] Y. Zhao and D. G. Truhlar, *The M06 suite of density functionals for main group thermochemistry, thermochemical kinetics, noncovalent interactions, excited states, and transition elements: Two new functionals and systematic testing of four M06-class functionals and 12 other functionals*, Theoretical Chemistry Accounts **120**, 215 (2008).
- [157] A. V. Krukau, O. A. Vydrov, A. F. Izmaylov, and G. E. Scuseria, *Influence of the exchange screening parameter on the performance of screened hybrid functionals*, The Journal of Chemical Physics **125**, 224106 (2006).

- [158] J. C. Phillips, *Energy-band interpolation scheme based on a pseudopotential*, Physical Review **112**, 685 (1958).
- [159] P. E. Blöchl, *Projector augmented-wave method*, Physical Review B **50**, 17953 (1994).
- [160] G. Kresse and D. Joubert, *From ultrasoft pseudopotentials to the projector augmented-wave method*, Physical Review B **59**, 1758 (1999).
- [161] G. Kresse and J. Furthmüller, *Efficient iterative schemes for ab initio total-energy calculations using a plane-wave basis set*, Physical Review B **54**, 11169 (1996).
- [162] G. Kresse and J. Furthmüller, *Efficiency of ab-initio total energy calculations for metals and semiconductors using a plane-wave basis set*, Computational Materials Science **6**, 15 (1996).
- [163] J. Hafner, *Ab-initio simulations of materials using VASP: Density-functional theory and beyond*, Journal of Computational Chemistry **29**, 2044 (2008).
- [164] M. Tuckerman, *Statistical mechanics: Theory and molecular simulation*, Oxford University Press, 2010.
- [165] G. Kresse and J. Hafner, *Ab initio molecular dynamics for liquid metals*, Physical Review B **47**, 558 (1993).
- [166] F. Jensen, *Introduction to computational chemistry*, John Wiley & Sons, 2017.
- [167] J. Grotendorst, *Modern methods and algorithms of quantum chemistry*, volume 1, NIC, 2000.
- [168] R. Car and M. Parrinello, *Structural, dynamical, and electronic properties of amorphous silicon: An ab initio molecular-dynamics study*, Physical Review Letters **60**, 204 (1988).
- [169] C. B. Carter and D. B. Williams, *Transmission electron microscopy: Diffraction, imaging, and spectrometry*, Springer, 2016.
- [170] J. Frank, *Three-dimensional electron microscopy of macromolecular assemblies: visualization of biological molecules in their native state*, Oxford University Press, 2006.
- [171] C. David, *Application of ion accelerators in defect studies and investigation of non linear effects due to molecular ion implantation*, PhD thesis, Madras University, 2013.
- [172] P. Jegadeesan, *Radiation effects in oxides used in nuclear applications*, PhD thesis, Homi Bhabha National Institute, 2019.

- [173] P. Balasaritha, *Inert gas ion irradiation effects on microstructural and optical properties of monoclinic zirconia*, PhD thesis, Homi Bhabha National Institute, 2019.
- [174] R. Krause-Rehberg and H. S. Leipner, *Positron annihilation in semiconductors: Defect studies*, volume 127, Springer Science & Business Media, 1999.
- [175] G. Amarendra, B. Viswanathan, G. V. Rao, J. Parimala, and B. Purniah, *Variable low energy positron beams for depth resolved defect spectroscopy in thin film structures*, Current Science , 409 (1997).
- [176] R. Renjith, *Study of irradiation effects in reduced activation ferritic/martensitic steel using positron beam based doppler broadening spectroscopy*, PhD thesis, Homi Bhabha National Institute, 2019.
- [177] B. D. Cullity, *Elements of X-ray Diffraction*, Addison-Wesley Publishing, 1956.
- [178] H. J. Monkhorst and J. D. Pack, *Special points for Brillouin-zone integrations*, Physical Review B **13**, 5188 (1976).
- [179] F. Murnaghan, *The compressibility of media under extreme pressures*, Proceedings of the National Academy of Sciences of the United States of America **30**, 244 (1944).
- [180] W. P. Davey, *Precision measurements of the lattice constants of twelve common metals*, Physical Review **25**, 753 (1925).
- [181] F. Soisson and C.-C. Fu, *Cu-precipitation kinetics in α -Fe from atomistic simulations: Vacancy-trapping effects and Cu-cluster mobility*, Physical Review B **76**, 214102 (2007).
- [182] M. Palm, *Concepts derived from phase diagram studies for the strengthening of Fe-Al-based alloys*, Intermetallics **13**, 1286 (2005).
- [183] C. Servant, C. Gueneau, and I. Ansara, *Experimental and thermodynamic assessment of the Fe-Zr system*, Journal of Alloys and Compounds **220**, 19 (1995).
- [184] O. Kubaschewski, *Iron—Binary phase diagrams*, Springer Science & Business Media, 2013.
- [185] B. J. Lee, *Thermodynamic calculation for stability of oxides in steel systems*, Journal of the Korean Institute of Metals and Materials **36**, 217 (1998).
- [186] V. Raghavan, *Phase diagrams of ternary iron alloys. I*, ASM International , 226 (1987).
- [187] M. Posselt, D. Murali, and B. Panigrahi, *Energetics, structure and composition of nanoclusters in oxide dispersion strengthened Fe-Cr alloys*, Modelling and Simulation in Materials Science and Engineering **22**, 085003 (2014).

- [188] S. Kim and W. Buyers, *Vacancy formation energy in iron by positron annihilation*, Journal of Physics F: Metal Physics **8**, L103 (1978).
- [189] P. Olsson, C. Domain, and J. Wallenius, *Ab initio study of Cr interactions with point defects in bcc Fe*, Physical Review B **75**, 014110 (2007).
- [190] R. Bader and T. Nguyen-Dang, *Quantum theory of atoms in molecules–Dalton revisited*, in *Advances in Quantum Chemistry*, volume 14, pages 63–124, Elsevier, 1981.
- [191] E. A. Devi, R. Chinnappan, and C. Sundar, *First-principles study of interaction energies of atomic defects in bcc ferromagnetic iron*, Physical Review B **98**, 144104 (2018).
- [192] D. Shin and C. Wolverton, *First-principles study of solute–vacancy binding in magnesium*, Acta Materialia **58**, 531 (2010).
- [193] Y. Luo and J. Cheng, *Bond dissociation energies in CRC Handbook of Chemistry and Physics*, 2015.
- [194] Y. Jiang, J. R. Smith, and G. R. Odette, *Prediction of structural, electronic and elastic properties of $Y_2Ti_2O_7$ and Y_2TiO_5* , Acta Materialia **58**, 1536 (2010).
- [195] H. Scott, *The yttria–zirconia δ phase*, Acta Crystallographica Section B: Structural Crystallography and Crystal Chemistry **33**, 281 (1977).
- [196] S. Ray and V. Stubican, *Fluorite related ordered compounds in the ZrO_2 – CaO and ZrO_2 – Y_2O_3 systems*, Materials Research Bulletin **12**, 549 (1977).
- [197] H. Rossell, *Crystal structures of some fluorite-related M_7O_{12} compounds*, Journal of Solid State Chemistry **19**, 103 (1976).
- [198] B. C. Chakoumakos, *Systematics of the pyrochlore structure type, ideal $A_2B_2X_6Y$* , Journal of Solid State Chemistry **53**, 120 (1984).
- [199] A. Zunger, S.-H. Wei, L. Ferreira, and J. E. Bernard, *Special quasirandom structures*, Physical Review Letters **65**, 353 (1990).
- [200] C. Jiang, C. Stanek, K. Sickafus, and B. Uberuaga, *First-principles prediction of disordering tendencies in pyrochlore oxides*, Physical Review B **79**, 104203 (2009).
- [201] D. E. Vanpoucke, P. Bultinck, S. Cottenier, V. Van Speybroeck, and I. Van Driessche, *Density functional theory study of $La_2Ce_2O_7$: disordered fluorite versus pyrochlore structure*, Physical Review B **84**, 054110 (2011).
- [202] C. Stanek, C. Jiang, B. Uberuaga, K. Sickafus, A. Cleave, and R. Grimes, *Predicted structure and stability of $A_4B_3O_{12}$ δ -phase compositions*, Physical Review B **80**, 174101 (2009).

- [203] B. Schaffer, *Digital Micrograph*, in *Transmission Electron Microscopy*, pages 167–196, Springer, 2016.
- [204] J. L. Lábár, *Electron diffraction based analysis of phase fractions and texture in nanocrystalline thin films, Part I: Principles*, *Microscopy and Microanalysis* **14**, 287 (2008).
- [205] J. L. Lábár, *Electron diffraction based analysis of phase fractions and texture in nanocrystalline thin films, Part II: Implementation*, *Microscopy and Microanalysis* **15**, 20 (2009).
- [206] J. L. Lábár, *Consistent indexing of a (set of) single crystal SAED pattern (s) with the ProcessDiffraction program*, *Ultramicroscopy* **103**, 237 (2005).
- [207] P. Stadelmann, *JEMS electron microscopy software*, V4, EPFL, Lausanne, Switzerland (2012).
- [208] E. Nes, N. Ryum, and O. Hunderi, *On the Zener drag*, *Acta Metallurgica* **33**, 11 (1985).
- [209] C. Du et al., *Ultrastrong nanocrystalline steel with exceptional thermal stability and radiation tolerance*, *Nature Communications* **9**, 1 (2018).
- [210] P. Tortorelli and K. Natesan, *Critical factors affecting the high-temperature corrosion performance of iron aluminides*, *Materials Science and Engineering: A* **258**, 115 (1998).
- [211] A. Lasalmonie and J. Strudel, *Influence of grain size on the mechanical behaviour of some high strength materials*, *Journal of Materials Science* **21**, 1837 (1986).
- [212] N. Hansen, *Hall–Petch relation and boundary strengthening*, *Scripta Materialia* **51**, 801 (2004).
- [213] V. Red'ko and L. Lopato, *Crystal structure of the compounds $M_4Zr_3O_{12}$ and $M_4Hf_3O_{12}$ (where M is a rare earth element)*, *Inorganic Materials* **27**, 1609 (1991).
- [214] W. Zhang, Z. Zhao, J. Fang, P. He, Z. Chao, D. Gong, G. Chen, and L. Jiang, *Evolution and strengthening mechanism of metastable precipitates in Cu-2.0 wt% Be alloy*, *Journal of Alloys and Compounds* , 157601 (2020).
- [215] A. Keh, *Work hardening and deformation sub-structure in iron single crystals deformed in tension at 298 K*, *Philosophical Magazine* **12**, 9 (1965).
- [216] N. Kamikawa, K. Sato, G. Miyamoto, M. Murayama, N. Sekido, K. Tsuzaki, and T. Furuhashi, *Stress–strain behavior of ferrite and bainite with nano-precipitation in low carbon steels*, *Acta Materialia* **83**, 383 (2015).
- [217] G. W. C. Kaye and T. H. Laby, *Tables of physical and chemical constants and some mathematical functions*, Longmans, Green and Company, 1911.

- [218] Y. Ijiri, N. Oono, S. Ukai, S. Ohtsuka, T. Kaito, and Y. Matsukawa, *Oxide particle–dislocation interaction in 9Cr-ODS steel*, Nuclear Materials and Energy **9**, 378 (2016).
- [219] P. Hirsch and F. Humphreys, *Physics of strength and plasticity*, MIT Press, Cambridge (1969).
- [220] K. Ma, H. Wen, T. Hu, T. D. Topping, D. Isheim, D. N. Seidman, E. J. Lavernia, and J. M. Schoenung, *Mechanical behavior and strengthening mechanisms in ultrafine grain precipitation-strengthened aluminum alloy*, Acta Materialia **62**, 141 (2014).
- [221] L. Brown and R. Ham, *Strengthening methods in crystals*, Applied Science, London **9** (1971).
- [222] R. Kahn and P. Hassen, *Physical Metallurgy*, Elsevier, Science, 1996.
- [223] J.-S. Wang, M. Mulholland, G. B. son, and D. N. Seidman, *Prediction of the yield strength of a secondary-hardening steel*, Acta Materialia **61**, 4939 (2013).
- [224] J. Adam and M. Rogers, *The crystal structure of ZrO_2 and HfO_2* , Acta Crystallographica **12**, 951 (1959).
- [225] G. Teufer, *The crystal structure of tetragonal ZrO_2* , Acta Crystallographica **15**, 1187 (1962).
- [226] D. Wang, Y. Guo, K. Liang, and K. Tao, *Crystal structure of zirconia by Rietveld refinement*, Science in China Series A: Mathematics **42**, 80 (1999).
- [227] P. Olsson, I. A. Abrikosov, L. Vitos, and J. Wallenius, *Ab initio formation energies of Fe–Cr alloys*, Journal of Nuclear Materials **321**, 84 (2003).
- [228] W. Burgers, *On the process of transition of the cubic-body-centered modification into the hexagonal-close-packed modification of zirconium*, Physica **1**, 561 (1934).
- [229] W. Rong and G. Dunlop, *The crystallography of secondary carbide precipitation in high speed steel*, Acta Metallurgica **32**, 1591 (1984).
- [230] D. Potter, *The structure, morphology and orientation relationship of V_3N in α -vanadium*, Journal of the Less Common Metals **31**, 299 (1973).
- [231] O. Zheng, J. Zhou, D. Zhao, J. Wang, R. Wang, J. Gui, D. Xiong, and Z. Sun, *The crystallography of continuous precipitates with a newly observed orientation relationship in an Mg–Al-based alloy*, Scripta Materialia **60**, 791 (2009).
- [232] A. Crawley and B. Lagowski, *Effect of two-step aging on the precipitate structure in magnesium alloy AZ91*, Metallurgical Transactions **5**, 949 (1974).
- [233] U. Dahmen, *Orientation relationships in precipitation systems*, Acta Metallurgica **30**, 63 (1982).

- [234] Y. Matsukawa, *Crystallography of Precipitates in Metals and Alloys:(1) Analysis of Crystallography*, in *Crystallography*, IntechOpen, 2019.
- [235] C. Howard, R. Hill, and B. Reichert, *Structures of ZrO₂ polymorphs at room temperature by high-resolution neutron powder diffraction*, Acta Crystallographica Section B: Structural Science **44**, 116 (1988).
- [236] J. Kansy, *Microcomputer program for analysis of positron annihilation lifetime spectra*, Nuclear Instruments and Methods in Physics Research Section A: Accelerators, Spectrometers, Detectors and Associated Equipment **374**, 235 (1996).
- [237] M. T. Robinson and I. M. Torrens, *Computer simulation of atomic-displacement cascades in solids in the binary-collision approximation*, Physical Review B **9**, 5008 (1974).
- [238] A. Van Veen, H. Schut, M. Clement, J. De Nijs, A. Kruseman, and M. Ijpma, *VEPFIT applied to depth profiling problems*, Applied Surface Science **85**, 216 (1995).
- [239] M. Alinger, S. Glade, B. Wirth, G. Odette, T. Toyama, Y. Nagai, and M. Hasegawa, *Positron annihilation characterization of nanostructured ferritic alloys*, Materials Science and Engineering: A **518**, 150 (2009).
- [240] J. Xu, C. Liu, M. Miller, and H. Chen, *Nanocluster-associated vacancies in nanocluster-strengthened ferritic steel as seen via positron-lifetime spectroscopy*, Physical Review B **79**, 020204 (2009).
- [241] A. Vehanen, P. Hautojärvi, J. Johansson, J. Yli-Kauppila, and P. Moser, *Vacancies and carbon impurities in α -iron: Electron irradiation*, Physical Review B **25**, 762 (1982).
- [242] C. Hidalgo, G. González-Doncel, S. Linderoth, and J. San Juan, *Structure of dislocations in Al and Fe as studied by positron-annihilation spectroscopy*, Physical Review B **45**, 7017 (1992).
- [243] H.-E. Schaefer, R. Würschum, R. Birringer, and H. Gleiter, *Structure of nanometer-sized polycrystalline iron investigated by positron lifetime spectroscopy*, Physical Review B **38**, 9545 (1988).
- [244] M. Puska and R. Nieminen, *Defect spectroscopy with positrons: A general calculational method*, Journal of Physics F: Metal Physics **13**, 333 (1983).
- [245] Y. Nagai, K. Takadate, Z. Tang, H. Ohkubo, H. Sunaga, H. Takizawa, and M. Hasegawa, *Positron annihilation study of vacancy-solute complex evolution in Fe-based alloys*, Physical Review B **67**, 224202 (2003).

- [246] H. Ohkubo, Z. Tang, Y. Nagai, M. Hasegawa, T. Tawara, and M. Kiritani, *Positron annihilation study of vacancy-type defects in high-speed deformed Ni, Cu and Fe*, Materials Science and Engineering: A **350**, 95 (2003).
- [247] L. Damonte, M. Taylor, J. Desimoni, and J. Runco, *PALS study on the defect structure of yttria-stabilized zirconia*, Radiation Physics and Chemistry **76**, 248 (2007).
- [248] H. Du, X. Yao, X. Zhang, and H. Weng, *Defect structure and dielectric properties of Bi-based pyrochlores probed by positron annihilation*, Applied Surface Science **253**, 1856 (2006).
- [249] R. West, *Positron studies of lattice defects in metals*, in *Positrons in solids*, pages 89–144, Springer, 1979.
- [250] Y.-K. Park, J. T. Waber, M. Meshii, C. Snead Jr, and C. Park, *Dislocation studies on deformed single crystals of high-purity iron using positron annihilation: Determination of dislocation densities*, Physical Review B **34**, 823 (1986).
- [251] R. Paulin, R. Ripon, and W. Brandt, *Diffusion constant and surface states of positrons in metals*, Applied physics **4**, 343 (1974).
- [252] R. Rajaraman, P. Gopalan, and S. Venkadesan, *Positron trapping at precipitates in titanium-modified stainless steels*, Materials Letters **24**, 243 (1995).
- [253] I. Bartošová, J. Čížek, F. Lukáč, and V. SLUGENĚ, *Vickers Hardness and Positron Annihilation Study of EUROFER97 and ODS EUROFER.*, Acta Physica Polonica, A. **125** (2014).
- [254] R. Renjith, C. David, P. Magudapathy, R. Rajaraman, R. Govindaraj, and G. Amarendra, *Study of defect complexes and their evolution with temperature in hydrogen and helium irradiated RAFM steel using positron annihilation spectroscopy*, Fusion Engineering and Design **142**, 55 (2019).
- [255] V. Pereira, H. Schut, and J. Sietsma, *A study of the microstructural stability and defect evolution in an ODS Eurofer steel by means of Electron Microscopy and Positron Annihilation Spectroscopy*, Journal of Nuclear Materials **540**, 152398 (2020).
- [256] K. Momma and F. Izumi, *VESTA: A three-dimensional visualization system for electronic and structural analysis*, Journal of Applied Crystallography **41**, 653 (2008).
- [257] A. Bogicevic, C. Wolverton, G. M. Crosbie, and E. B. Stechel, *Defect ordering in aliovalently doped cubic zirconia from first principles*, Physical Review B **64**, 014106 (2001).

- [258] Z. Chen, H. Xiao, X. T. Zu, and F. Gao, *First-principles calculation of defect formation energies and electronic properties in stannate pyrochlores*, Journal of Applied Physics **104**, 093702 (2008).
- [259] W. R. Panero, L. Stixrude, and R. C. Ewing, *First-principles calculation of defect-formation energies in the $Y_2(Ti, Sn, Zr)_2O_7$ pyrochlore*, Physical Review B **70**, 054110 (2004).
- [260] K. Trachenko, *Understanding resistance to amorphization by radiation damage*, Journal of Physics: Condensed Matter **16**, R1491 (2004).
- [261] D. Simeone, J. M. Costantini, L. Luneville, L. Desgranges, P. Trocellier, and P. Garcia, *Characterization of radiation damage in ceramics: Old challenge new issues?*, Journal of Materials Research **30**, 1495 (2015).
- [262] J. Nord, K. Nordlund, and J. Keinonen, *Molecular dynamics study of damage accumulation in GaN during ion beam irradiation*, Physical Review B **68**, 184104 (2003).
- [263] R. I. Palomares, J. Shamblin, C. L. Tracy, J. Neuefeind, R. C. Ewing, C. Trautmann, and M. Lang, *Defect accumulation in swift heavy ion-irradiated CeO_2 and ThO_2* , Journal of Materials Chemistry A **5**, 12193 (2017).
- [264] J. A. Purton and N. L. Allan, *Displacement cascades in $Gd_2Ti_2O_7$ and $Gd_2Zr_2O_7$: A molecular dynamics study*, Journal of Materials Chemistry **12**, 2923 (2002).
- [265] F. Zhang, J. Wang, J. Lian, M. Lang, U. Becker, and R. Ewing, *Phase stability and pressure dependence of defect formation in $Gd_2Ti_2O_7$ and $Gd_2Zr_2O_7$ pyrochlores*, Physical Review Letters **100**, 045503 (2008).
- [266] R. Rejith, R. R. Krishnan, A. John, J. K. Thomas, and S. Solomon, *Structural optical and electrical properties of $RE_4Zr_3O_{12}$ ($RE = Dy, Y, Er, \text{ and } Yb$) nanoceramics*, Ionics **25**, 5091 (2019).
- [267] X. Gonze and C. Lee, *Dynamical matrices, Born effective charges, dielectric permittivity tensors, and interatomic force constants from density-functional perturbation theory*, Physical Review B **55**, 10355 (1997).
- [268] A. Togo and I. Tanaka, *First principles phonon calculations in materials science*, Scripta Materialia **108**, 1 (2015).
- [269] A. Togo, L. Chaput, and I. Tanaka, *Distributions of phonon lifetimes in Brillouin zones*, Physical Review B **91**, 094306 (2015).
- [270] E. B. Wilson, J. C. Decius, and P. C. Cross, *Molecular vibrations: The theory of infrared and Raman vibrational spectra*, Courier Corporation, 1980.
- [271] W. Fetteley, F. Dollish, N. McDevitt, and F. Bentley, *Infrared and Raman selection rules for molecular and lattice vibrations*, 1972.

- [272] J. Tauc, *Optical properties and electronic structure of amorphous Ge and Si*, Materials Research Bulletin **3**, 37 (1968).
- [273] A. Arbuznikov, *Hybrid exchange correlation functionals and potentials: Concept elaboration*, Journal of Structural Chemistry **48**, S1 (2007).
- [274] E. P. Chinkov and V. F. Shtan'ko, *Luminescence of self-trapped excitons in calcium fluoride under pulsed electron irradiation*, Physics of the Solid State **40**, 1117 (1998).
- [275] T. V. Perevalov and D. R. Islamov, *Oxygen polyvacancies as conductive filament in zirconia: First principle simulation*, ECS Transactions **80**, 357 (2017).
- [276] M. Boffelli, W. Zhu, M. Back, G. Sponchia, T. Francese, P. Riello, A. Benedetti, and G. Pezzotti, *Oxygen hole states in zirconia lattices: Quantitative aspects of their cathodoluminescence emission*, The Journal of Physical Chemistry A **118**, 9828 (2014).
- [277] M. Adair, C. Leung, and K. Song, *Equilibrium configuration of the self-trapped exciton in CaF_2 and SrF_2* , Journal of Physics C: Solid State Physics **18**, L909 (1985).
- [278] R. Williams, M. Kabler, W. Hayes, and J. Stott, *Time-resolved spectroscopy of self-trapped excitons in fluorite crystals*, Physical Review B **14**, 725 (1976).
- [279] D. Rao and H. Bose, *Cathodoluminescence of CaF_2* , Physica **52**, 371 (1971).
- [280] N. Petrik, D. Taylor, and T. Orlando, *Laser-stimulated luminescence of yttria-stabilized cubic zirconia crystals*, Journal of Applied Physics **85**, 6770 (1999).
- [281] T. Thajudheen, A. G. Dixon, S. Gardonio, I. Arcon, and M. Valant, *Oxygen vacancy-related cathodoluminescence quenching and polarons in CeO_2* , The Journal of Physical Chemistry C **124**, 19929 (2020).
- [282] V. A. Gritsenko, D. R. Islamov, T. V. Perevalov, V. S. Aliev, A. P. Yelisseyev, E. E. Lomonova, V. A. Pustovarov, and A. Chin, *Oxygen vacancy in hafnia as a blue luminescence center and a trap of charge carriers*, The Journal of Physical Chemistry C **120**, 19980 (2016).
- [283] V. V. Kaichev, E. V. Ivanova, M. V. Zamoryanskaya, T. P. Smirnova, L. V. Yakovkina, and V. A. Gritsenko, *XPS and cathodoluminescence studies of HfO_2 , Sc_2O_3 and $(\text{HfO}_2)_{1-x}(\text{Sc}_2\text{O}_3)_x$ films*, The European Physical Journal Applied Physics **64**, 10302 (2013).
- [284] H. Nakajima and T. Mori, *Photoluminescence excitation bands corresponding to defect states due to oxygen vacancies in yttria-stabilized zirconia*, Journal of Alloys and Compounds **408**, 728 (2006).